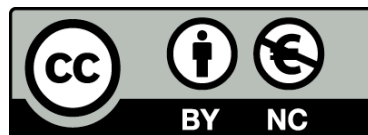




UNIVERSITAT DE
BARCELONA

A new classification of gamma-ray bursts and its cosmological implications

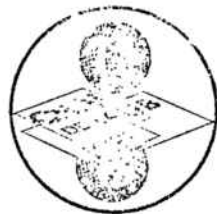
Andreu Balastegui Manso



Aquesta tesi doctoral està subjecta a la llicència [Reconeixement- NoComercial 4.0. Espanya de Creative Commons](#).

Esta tesis doctoral está sujeta a la licencia [Reconocimiento - NoComercial 4.0. España de Creative Commons](#).

This doctoral thesis is licensed under the [Creative Commons Attribution-NonCommercial 4.0. Spain License](#).



UNIVERSITAT DE BARCELONA
DEPARTAMENT D'ASTRONOMIA I METEOROLOGIA



U
UNIVERSITAT DE BARCELONA



A new classification of gamma-ray bursts and its cosmological implications



UNIVERSITAT DE BARCELONA



Memòria presentada per
Andreu Balastegui Manso
per optar al grau de
Doctor en Ciències Físiques

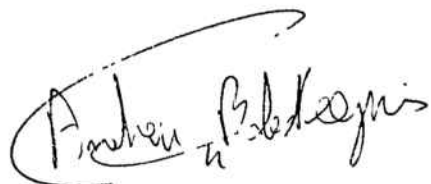
Barcelona, desembre de 2005



PROGRAMA DE DOCTORAT D'ASTRONOMIA I METEOROLOGIA

BIENNI 1999–2001

Memòria presentada per **Andreu Balastegui Manso** per optar al
grau de Doctor en Ciències Físiques

A handwritten signature in black ink, appearing to read "Andreu Balastegui". The signature is fluid and cursive, with a large, open loop at the top left.

DIRECTORS DE LA TESI

Dr. Ramon Canal i Masgoret Dra. María del Pilar Ruiz-Lapuente

Contents

Resum	i
0.1 Història	ii
0.2 Energies	iv
0.3 Estructura temporal	iv
0.4 Distribució espacial	vi
0.4.1 Isotropia	vi
0.4.2 Inhomogeneïtat	vi
0.5 La bola de foc	viii
0.6 L' <i>afterglow</i>	ix
0.7 Progenitors	x
0.7.1 Col·lapse d'estrelles massives	xi
0.7.2 Fusions d'objectes compactes	xii
0.8 Aquesta tesi	xiii
0.9 Conclusions	xiv
1 Introduction	1
1.1 History	2
1.2 Energetics	4
1.3 Temporal structure	5
1.4 Spatial distribution	7
1.4.1 Isotropy	7
1.4.2 Inhomogeneity	9
1.5 The fireball	11
1.6 The afterglow	12
1.7 Progenitors	15

1.7.1	Collapse of massive stars	15
1.7.2	Mergings	16
1.8	This thesis	17
 I Classification of gamma-ray bursts		
2	The GRB catalogue	21
2.1	The Compton gamma-ray observatory	21
2.1.1	OSSE	23
2.1.2	COMPTEL	24
2.1.3	EGRET	24
2.1.4	BATSE	25
2.2	BATSE catalogue	28
2.2.1	The Basic catalogue	29
2.2.2	The Flux and Fluence catalogue	30
2.2.3	The Duration catalogue	32
2.2.4	The CMAX/CMIN catalogue	33
3	Automatic classification algorithms	37
3.1	Principal component analysis	38
3.2	Cluster analysis	41
3.3	Neural networks	44
3.3.1	Kohonen self-organizing map	48
4	Reclassification of gamma-ray bursts	51
4.1	Principal component analysis	52
4.2	Cluster analysis classification	53
4.3	Neural network classification	62
4.4	The maximum redshift	67
4.5	Hardness evolution	72
4.6	Conclusions	75

II Cosmology with gamma-ray bursts

5 The gamma-ray burst intensity distribution	81
5.1 Introduction	81
5.2 Historical review	83
5.3 The $\log N - \log P$ distribution	84
5.3.1 The Hubble constant	85
5.3.2 The cosmological parameters Ω_M , Ω_Λ , and Ω_K	86
5.3.3 The comoving distance	88
5.3.4 The explosion rate	88
5.3.5 The luminosity function	94
5.3.5.1 Luminosity evolution	95
5.3.6 The spectrum	98
5.3.7 The peak flux	98
5.4 Building the observational intensity distributions	100
5.5 Fitting the intensity distribution	106
5.5.1 The minimization	109
6 The $\log N - \log P$ fits	111
6.1 The best fits	111
6.2 The gamma-ray burst explosion rate	118
6.2.1 The gamma-ray burst redshift distribution	129
6.3 The gamma-ray burst luminosity function	133
6.3.1 Luminosity evolution	138
6.4 Measuring the cosmological parameters	143
6.5 Simulations	153
6.5.1 The best fits	154
6.5.2 The cosmological parameters	156
6.6 Conclusions	158
7 Conclusions	161

Appendices	170
A Cluster analysis classification	171
B Neural network classification	185
Bibliography	199

Resum

Els esclats de raigs gamma (GRBs¹ a partir d'ara) són un dels grans misteris de l'astrofísica actual, i un dels camps de recerca més actius des dels anys 90, amb més de 400 articles científics publicats cada any des de 1996.

Els GRBs són flaixos de raigs gamma que ens arriben provinents de direccions arbitràries de l'espai a un ritme de gairebé 2 esclats per dia. Aquests esdeveniments tindrien una energia de l'ordre de $10^{42} \text{erg s}^{-1}$ si es tractés de fenòmens galàctics i d'entre $10^{50} \text{erg s}^{-1}$ i $10^{52} \text{erg s}^{-1}$ si fossin d'origen extragalàctic, en ambdós casos suposant emissió isòtropa. Estem parlant d'energies superiors a les noves en un cas i a les supernoves en l'altre, i rebent el pic d'emissió en la banda gamma de l'espectre (per sobre de 100 keV), així s'entén que es parli d'ells com les explosions més violentes a l'Univers després del *Big Bang*. Com veiem, és tot un repte explicar i proposar escenaris progenitors per als GRBs, i aquests solen involucrar objectes compactes (forats negres o estrelles de neutrons), fusions entre aquests objectes, hipernoves o *collapsars*, i tots s'ajuden de la col·limació per concentrar l'energia, i de dolls ultrarelativistes dirigits en la línia de visió per córrer l'emissió cap al blau i contrarestar el corriment al vermell cosmològic (*redshift* a partir d'ara).

L'emissió gamma ve seguida per una postluminiscència anomenada *afterglow*. L'*afterglow* és una emissió més duradora i de més baixa energia que s'observa en raigs X, òptic, i ràdio. El posicionament precís dels *afterglows* ha permès mesurar els *redshifts* de més de 60 GRBs, així com identificar les morfologies de les galàxies hoste, i les localitzacions dels GRBs dintre d'elles, confirmant l'origen extragalàctic d'almenys alguns subgrups de GRBs.

¹de l'anglés "gamma-ray bursts".

0.1 Història

El descobriment dels GRBs està íntimament lligat al desenvolupament de la tecnologia de l'astronomia d'altes energies a l'espai. L'any 1963, en plena guerra freda, es va signar a Ginebra un tractat de prohibició de proves nuclears sota l'aigua, a l'atmosfera i a l'espai. Els Estats Units van idear un projecte militar per vigilar que es complís aquest tractat i van néixer els satèl·lits VELA². Aquests satèl·lits portaven detectors de neutrons i raigs X i gamma, i es situaven en parelles en posicions oposades en una òrbita d'uns 4 dies, de manera que la Terra no pogués tapar mai les observacions. Els VELA no van detectar mai cap violació del pacte, però si que van detectar flaixos de raigs gamma. El perfeccionament dels instruments que portaven la cinquena i sisena generació dels VELA, llençats el 1969, amb resolucions temporals de 0.2 s (més petita que el temps de viatge de la llum entre la parella, 1 s aproximadament), va fer possible determinar amb certa precisió l'angle de provinença d'aquesta emissió gamma, i va resultar que no provenia ni de la Terra ni del Sol. Finalment, el 1973 es va anunciar el descobriment dels GRBs en el famós article de Klebesadel, Strong i Olson (1973), "Observations of Gamma-ray bursts of cosmic origin", on informaven sobre 16 esclats detectats entre 1969 i 1972.

A finals dels anys 70, Kevin Hurley va promoure la creació d'una xarxa de satèl·lits detectors equipant missions interplanetàries, com la Pioneer Venus Orbiter i altres satèl·lits com ara els Venera, amb detectors gamma. La idea era obtenir dades de les posicions dels esdeveniments per triangulació i retard en la detecció. Aquesta xarxa, anomenada IPN (Interplanetary Network), ha sigut durant molt temps l'única font d'informació sobre els GRBs, i encara continua essent una de les fonts amb la IPN³, que compta, entre d'altres, amb els satèl·lits INTEGRAL i HETE2. Altres missions exitoses que han format part del IPN són CGRO i BeppoSAX.

Però el veritable punt d'inflexió, i el major impuls en el camp dels GRBs, es va donar l'any 1991 amb el llançament del Compton Gamma-Ray Observatory (CGRO). Aquest observatori de 17 tones portava a bord l'instrument BATSE (Burst and Transient Source Experiment) que va obtenir una estadística deu vegades superior a la que es tenia als anys 80, amb dades de més de 2500 GRBs (posicions,

²del castellà "velar".

³<http://www.ssl.berkeley.edu/ipn3/>

energies i durades), i que ha permès constatar la isotropia i inhomogeneïtat de la distribució d'esclats. Malauradament, el CGRO va ser destruït en una reentrada dirigida a l'atmosfera el maig de l'any 2000, degut a què només disposava ja de 2 giròscops en funcionament.

Abans de BATSE hi havia una gran discussió sobre l'escala de distància dels GRBs, i la idea més popular era que tenien un origen galàctic. Després de BATSE, l'alt grau d'isotropia, la inhomogeneïtat de la distribució espacial, i la falta d'un excés d'esdeveniments en la direcció de M31, combinada amb l'alta sensibilitat de l'instrument, va fer que els astrònoms canviessin d'idea, guanyant suport els que creien en un origen extragalàctic dels GRBs. Per establir una resposta definitiva al problema de l'escala de distàncies, era necessari trobar una contrapartida òptica, o una galàxia hoste, d'un GRB. Desafortunadament, la precisió d'apuntat de BATSE no era prou bona, i dintre de la capsa d'error típica hi podien haver centenars de fonts òptiques. Aquesta limitació es va superar amb el llançament del satèl·lit BeppoSAX. La missió, compartida entre l'agència espacial italiana i la holandesa, observava principalment en la banda X de l'espectre, fet que va permetre millorar la precisió d'apuntat; dels 4° d'error de BATSE es va passar a menys de 1 *arcmin* amb BeppoSAX. El 28 de febrer de 1997, BeppoSAX va detectar el primer *afterglow* en raigs X (Costa et al., 1997), permetent l'observació òptica (van Paradijs et al., 1997). Finalment, el 8 de maig, BeppoSAX va detectar i localitzar amb precisió el GRB970508 (Galama et al., 1997), enviant immediatament la seva posició a astrònoms arreu del món. En poques hores, molts dels telescopis més potents del món apuntaven en la direcció del GRB, trobant allà una font òptica esvaint-se a $z = 0.835$. Des de llavors, s'han mesurat més de 60 *redshifts* de GRBs, confirmant la naturalesa extragalàctica del fenomen.

Els GRBs es van relacionar amb supernoves quan es va detectar la supernova SN1998bw simultàniament al GRB980425 (Galama et al., 1998) i dins de la seva capsa d'error. Indicis d'una corba de llum de supernova subjacent a l'*afterglow* òptic van ser observades a molts GRBs, i finalment es van confirmar pel GRB030329 (Stanek et al., 2003; Hjorth et al., 2003; Gorosabel et al., 2005). Ara, és un fet comument acceptat que els GRBs de llarga durada estan relacionats amb supernoves de col·lapse gravitatori, i que els seus progenitors són estrelles massives.

La revolució actual està essent liderada pel satèl·lit SWIFT, que ha permès

de mesurar més de 20 *redshifts* de GRBs en menys d'un any de funcionament (la meitat de la mostra obtinguda durant 8 anys amb BeppoSAX i HETE2). A més, ha descobert recentment els *afterglows* dels GRBs curts (Castro-Tirado et al., 2005; Piro, 2005; Fox et al., 2005; Gehrels et al., 2005; Villasenor et al., 2005; Hjorth et al., 2005), revelant part del misteri que envolta aquesta classe de GRBs.

0.2 Energies

Les fluències observades es troben en el rang d'entre $10^{-4} \text{erg cm}^{-2}$ a $10^{-7} \text{erg cm}^{-2}$, corresponent a lluminositats d'entre $10^{50} \text{erg s}^{-1}$ i $10^{52} \text{erg s}^{-1}$, considerant emissió isòtropa. Gràcies a la mesura de *redshifts* de GRBs va ser possible calcular l'energia total alliberada en un esdeveniment (suposant una cosmologia determinada). Aparentment, aquesta energia s'estenia sobre 3 ordres de magnitud, de 10^{51}erg a 10^{54}erg , però més tard, gràcies a la mesura dels angles de col·limació, es va comprovar que l'energia total alliberada estava concentrada al voltant dels 10^{51}erg (Frail et al., 2001).

L'espectre continu és no tèrmic, i té el màxim per sobre dels 100 keV . En alguns casos s'han detectat fotons de fins a 20 GeV . L'espectre s'ajusta bé a una llei de potències trencada suavament connectada que anomenem espectre de Band (Band et al., 1993). La figura 1.1 mostra l'espectre de GRB911127 com a exemple.

0.3 Estructura temporal

Els GRBs no tenen una corba de llum típica. Poden haver GRBs amb un sol pols curt, polsos amb pujades i baixades suaus, esdeveniments amb grans intervals entre dos o més polsos, esdeveniments complexos amb molts polsos superposats. Hi ha corbes de llum de tot tipus, simples o caòtiques, suaus o picudes, lentes o ràpides, amb un sol pic o múltiples pics, i totes les combinacions d'aquests tipus; en definitiva una gran varietat difícil de classificar. D'entre totes, destaca l'única classe definida de corba de llum, els FREDs (Fast Rise Exponential Decays⁴), a la qual pertanyen

⁴Ràpida pujada i decaïment exponencial.

aproximadament el 15% dels GRBs. La figura 1.2 mostra aquesta varietat de corbes de llum.

La majoria de GRBs presenten una estructura temporal asimètrica; els polsos individuals tenen temps de pujada més curts que els temps de decaïment. No s'ha trobat cap estructura periòdica mitjançant transformades de Fourier ni anàlisi de *wavelets*. La ràpida variabilitat temporal, en escales de l'ordre de 1 *ms* o inferiors, impliquen unes fonts de mida al voltant dels 100 *km*, és per això que els astrònoms pensen en objectes compactes com a progenitors dels GRBs.

La distribució de durades dels GRBs s'estén cinc ordres de magnitud, des de 10 *ms* fins a 1000 *s*, i mostra un aspecte bimodal, on es poden distingir clarament dos subgrups parcialment superposats. Els GRBs curts tenen una durada mitja de 0.6 *s* mentre que els GRBs llargs duren 50 *s* en mitjana. Els GRBs curts són més durs en mitjana que els GRBs llargs, en el sentit que el màxim del seu espectre es troba a energies majors. En concordança amb aquestes característiques, els GRBs s'han classificat tradicionalment en dos grups diferents: els GRBs curts i els GRBs llargs (Kouveliotou et al., 1993). La figura 1.3 resumeix les característiques dels GRBs curts i llargs. La gràfica de la part superior esquerra mostra la distribució de durades en escala logarítmica. La durada està representada per la variable T_{90} , que és el temps transcorregut fins a que es rep el 90% del flux total. La gràfica mostra l'aspecte bimodal, amb un decreixement separant les dues distribucions a $T_{90} \approx 2$ *s*. Els GRBs curts estan representats per una línia sòlida negra i els llargs per una línia de punts vermella. Les durades mitjanes es mostren com a línies verticals. Típicament s'agafa 2 *s* com el límit entre els GRBs curts ($T_{90} < 2$ *s*) i els llargs ($T_{90} > 2$ *s*). La gràfica inferior esquerra és el diagrama de dispersions de duresa (H_{32}) en front a durada (T_{90}). H_{32} es defineix com la fluència rebuda amb energies entre 100 i 300 *keV* dividida per la fluència rebuda amb energies entre 50 i 100 *keV*. Els GRBs curts, representats per cercles negres, tendeixen a ser més durs que els GRBs llargs, representats per triangles vermells. Les línies verticals i horitzontals mostren les durades i dureses mitjanes respectives per a cada classe de GRB. Finalment, la gràfica inferior dreta mostra la distribució de dureses pels GRBs curts (línia sòlida negra) i pels GRBs llargs (línia de punts vermella). Aquí es pot apreciar més clarament la diferència en duresa de cada classe de GRB. Els GRBs curts tenen $\langle H_{32} \rangle = 6.3 \pm 0.2$, mentre que els llargs tenen $\langle H_{32} \rangle = 3.1 \pm 0.1$.

0.4 Distribució espacial

L'evidència més directa de la distribució espacial dels GRBs prové de l'observació de les distribucions angular i d'intensitats. La distribució angular ens dóna dos de les tres dimensions de la distribució espacial, mentre que la distribució d'intensitats és una convolució de la funció de lluminositat i la distribució radial dels GRBs.

0.4.1 Isotropia

La distribució de GRBs en coordenades galàctiques observada per BATSE (figura 1.4) és consistent amb la isotropia. Els valors dels moments dipolar i quadrupolar galàctics, que mesuren la concentració d'esdeveniments cap el Disc Galàctic i cap el Centre Galàctic, respectivament, confirmen l'alt grau d'isotropia. Aquest fet va suposar un repte per la majoria de models galàctics existents a començaments dels anys 90. No hi havia cap concentració cap el Centre Galàctic, ni cap excés de GRBs cap a la direcció de M31. El grau d'isotropia podia correspondre a una mostra amb distàncies inferiors a l'alçada del Disc Galàctic, o a estrelles de neutrons d'alta velocitat situades a un Halo Galàctic Extens de radi entre 100 i 200 Kpc , molt més gran que la distància de la Terra al Centre Galàctic.

0.4.2 Inhomogeneïtat

Com s'ha comentat, la distribució d'intensitats dels GRBs està relacionada amb la seva distribució de distàncies. La figura 1.5 mostra la distribució d'intensitats pels GRBs llargs ($T_{90} > 2$ s), representada per la distribució acumulativa $\log N - \log P$. Com es pot apreciar, existeix un defecte de GRBs de baix flux respecte a l'esperada línia de pendent $-3/2$ en el cas d'una distribució homogènia en un espai euclidià. La primera pista d'aquest defecte va ser suggerida per una sèrie d'experiments amb globus aerostàtics (Meegan et al., 1985), i va ser finalment confirmada per BATSE (Meegan et al., 1992). Aquest fet va jugar un paper molt important en el Gran Debat (Lamb, 1995; Paczyński, 1995; Rees, 1995) sobre l'escala de distàncies dels GRBs, fent canviar d'opinió a la majoria d'astrònoms per situar els GRBs com esdeveniments d'origen extragalàctic en comptes de galàctics, que era la idea generalitzada

d'aquell temps.

Què ens indica el defecte de GRBs de baix pic de flux?

Considerant P com un estimador de la lluminositat, resulta que els GRBs amb pics de flux més baixos són també els més llunyans. Des del punt de vista d'un origen galàctic, la falta de GRBs llunyans podria significar que el detector ha arribat a detectar el límit de la població, i malgrat tenir prou sensibilitat com per detectar GRBs més llunyans, de fet no s'en produueixen. D'una altra part, també podria voler dir que el nombre de GRBs produïts decreix amb la distància a la Terra. Com que no hi ha cap població coneguda d'objectes distribuïts al voltant de la Terra⁵, aquesta opció implicaria que els GRBs es produueixen a partir d'una població de progenitors distribuïda a distàncies molt més grans que la distància del Sol al centre de la Galàxia. L'alt grau d'isotropia, però, elimina tots els models amb una gran concentració cap el Disc Galàctic. Amb aquestes restriccions, Hartmann et al. (1994) van dissenyar un model molt popular en què els GRBs es produïen en un Halo Galàctic Extens d'estrelles de neutrons d'alta velocitat. El model requeria la formació d'estrelles de neutrons d'alta velocitat en el Disc Galàctic per poblar l'Halo Extens, un retardament en el mecanisme d'explosió per a què els GRBs es produïssin lluny del Disc Galàctic, i una correlació entre la velocitat i la direcció d'emissió dels raigs gamma per incrementar la probabilitat de detecció amb la distància al centre del disc.

D'una altra banda, la desviació del pendent $-3/2$ en la distribució $\log N - \log P$ podria ser interpretada de manera més natural com una desviació de l'espai euclidiana, implicant per tant una origen extragalàctic pels GRBs. A distàncies molt grans, l'efecte de la curvatura de l'Univers fa que l'element de volum comòbil es redueixi, disminuint per tant el nombre d'esdeveniments llunyans. A part d'aquest efecte geomètric, també existeix la possibilitat de barrejar efectes evolutius, com poden ser la variació del ritme d'esclats, o de la seva lluminositat, amb la distància. Els models cosmològics de GRBs van ser postulats per primera vegada per Usov i Chibisov (1975), i per van den Bergh (1983). Distribucions cosmològiques d'esclats han sigut ajustades a la distribució d'intensitats observada per Piran (1992), Mao i Paczyński (1992), i Wickramasinghe et al. (1993) entre d'altres.

⁵Malgrat existir molts models proposats per GRBs produïts en el Sistema Solar, o en el núvol d'Oort (centrat en el Sol), mai han sigut populars dins la comunitat científica.

0.5 La bola de foc

La bola de foc relativista (*fireball* en anglès) és un model genèric (Paczynski, 1986; Goodman, 1986), independent del tipus de progenitor, que intenta reproduir les condicions físiques del medi on es produeix el GRB. El model ha estat molt exitós, arribant a predir l'existència de l'*afterglow* abans de què fos observat.

La rapidíssima variabilitat temporal dels GRBs, de l'ordre de 1 ms, implica una font extremadament compacte de radi $R_s \leq c\delta t \sim 300 \text{ km}$. Aquest fet, combinat amb l'energia de sortida requerida (al voltant de 10^{52} erg en raigs gamma), fa que es creï un plasma d'electró-positrò independentment del tipus de progenitor. Aquesta bola de foc resulta en una gran profunditat òptica que termalitzaria els fotons, produint un espectre de cos negre, mentre que l'espectre observat és clarament no tèrmic. Aquesta paradoxa, coneguda com el problema de compactivitat, es resol amb una expansió relativista.

Amb una expansió relativista, l'energia dels fotons emesos és menor que l'observada en un factor de Lorentz Γ . Com a resultat, la fracció de fotons capaços de produir parelles e^-e^+ és menor en un factor Γ^2 . La distància des de la font a la que la radiació és emesa s'incrementa en un factor Γ , i conseqüentment el volum ho fa en un factor Γ^3 . La combinació d'aquests efectes redueix la densitat d'energia en un factor Γ^6 . Factors de Lorentz $\Gamma > 10^2$ ens donen un medi òpticament prim, ara bé, la bola de foc ha d'estar pràcticament lliure de barions, o d'altra manera l'expansió es veuria frenada abans de què el medi es fes òpticament prim.

La bola de foc està composta de moltes capes de fotons, parelles e^-e^+ , i una petita fracció de barions, que es produeixen per un motor central intermitent. Aquestes capes interaccionen entre elles (xocs interns) fins què finalment són desaccelerades pel medi interestel·lar en un xoc extern.

El model més acceptat per a l'emissió inicial de raigs gamma en un GRB és el model de xocs interns (Sari and Piran, 1997; Daigne and Mochkovitch, 1998; Spada et al., 2000), malgrat que el model de xocs externs (Panaitescu and Mészáros, 1998; Dermer et al., 1999) no es pugui encara descartar. Hi han moltes altres preguntes sense resposta definitiva, com per exemple si la bola de foc està dominada pels camps magnètics (Spruit et al., 2001; Vlahakis and Königl, 2003a; Vlahakis and Königl,

2003b) o per l'energia cinètica (Rees and Mészáros, 1994). El mecanisme de radiació més acceptat és el d'emissió sincrotró (Mészáros and Rees, 1993a), però d'altres, com l'efecte Compton invers (Panaitescu and Mészáros, 2000), també s'estan estudiant.

Dintre del model de bola de foc, l'emissió de l'*afterglow* ve produïda pel xoc extern de la bola de foc mateixa amb el medi interestel·lar.

0.6 L'afterglow

L'*afterglow* d'un GRB és una emissió de banda ampla, que cobreix els raigs X, l'òptic, l'infraroig, i la banda ràdio, i és detectada després de l'emissió inicial de raigs gamma. En cada banda, la corba de llum té típicament un comportament de decaïment en llei de potències. L'emissió d'*afterglow* va ser detectada per primera vegada pel GRB970228. Els *afterglows* solament havien sigut detectats per GRBs de llarga durada fins que recentment se n'han detectat pels GRBs curts, com GRB050509B (Castro-Tirado et al., 2005) i GRB050709 (Villasenor et al., 2005).

L'*afterglow* s'entén com el xoc extern de la bola de foc amb el medi interestel·lar que accelera els electrons produint la radiació sincrotró. L'espectre de l'*afterglow* i la seva evolució s'obtenen de la teoria clàssica de la radiació sincrotró (Sari et al., 1998; Mészáros et al., 1998), suposant una distribució en llei de potències pels factors de Lorentz dels electrons accelerats. La figura 1.6 mostra un espectre teòric, on: ν_a és la freqüència sincrotró d'autoabsorció; ν_m és la freqüència sincrotró característica, corresponent al factor de Lorentz mínim; i finalment, ν_c és la freqüència de refredament: els electrons que radien a freqüències superiors a ν_c només radien mentre el xoc s'està produint. L'evolució en el temps d'aquestes freqüències característiques depèn del medi extern. Per a un medi de densitat constant l'evolució és l'etiquetada com ISM, mentre que per a un medi caracteritzat per un vent estel·lar, amb densitat $\rho \propto r^{-2}$, l'evolució és l'etiquetada com a WIND.

L'*afterglow* en raigs X és el senyal que rebem primer, i el més potent, però és alhora el més curt. S'observa pel 90% dels GRBs ben localitzats. S'han detectat línies d'emissió en bastants *afterglows* de raigs X (Piro et al., 2000; Reeves et al., 2002), i la majoria han estat interpretades com a presència de Fe en l'ambient.

Al voltant del 50% dels *afterglows* ben localitzats tenen *afterglow* en l'òptic i l'infraroig. Els *afterglows* òptics són, típicament, al voltant de magnitud 19-20 un dia després del propi GRB. El senyal decau, inicialment, com una llei de potències en el temps ($\propto t^{-\alpha}$, amb $\alpha \approx 1.2$). Molts *afterglows* mostren un trencament acromàtic cap a un decaïment més pronunciat amb $\alpha \approx 2$. Aquest trencament s'interpreta, comunament, com el trencament del doll, permetent l'estimació de l'angle d'obertura del doll d'emissió (Kulkarni et al., 1999; Harrison et al., 1999).

Els *afterglows* òptics duren típicament de l'ordre de setmanes, malgrat que l'*afterglow* òptic de GRB970228 va ser visible durant més de sis mesos.

En molts casos s'han observat crescudes en la part vermella de l'*afterglow* al voltant d'un mes després del GRB. Aquestes crescudes s'han interpretat com la corba de llum creixent d'una supernova (Bloom et al., 1999; Garnavich et al., 2003). El senyal més clar de supernova es va observar pel GRB030329 (Stanek et al., 2003; Hjorth et al., 2003; Gorosabel et al., 2005). La figura 1.7 mostra la crescuda en l'*afterglow* òptic de GRB011121, així com una modelització de la corba de llum subjacent de la supernova SN1998bw.

Els *afterglows* en ràdio es detecten per a un 50% dels GRBs ben localitzats. Les observacions ràdio es fan típicament a les bandes de 5 i 8.5 GHz , i els fluxos detectats són de l'ordre de 2 mJy . Algunes fonts es poden observar fins i tot anys després de què es produís el GRB.

0.7 Progenitors

Malgrat que existeixen més de 100 models proposats com a progenitors de GRBs (Nemiroff, 1994), la majoria cau en dues classes ben definides: les fusions d'objectes compactes i el col-lapse d'estrelles massives. Altres objectes, més peculiars, inclouen: cordes còsmiques (Babul et al., 1987), estrelles estranyes (Alcock et al., 1986), estrelles de quarks (Dar, 1999), forats blancs (Narlikar and Apparao, 1975), cometes (Harwit and Salpeter, 1973), asteroides (Newman and Cox, 1980), planetes (Hannam, 1992), i galàxies de nucli actiu (AGN) (Prilutskii and Usov, 1975). Nosaltres ens concentrarem bàsicament en les dues principals classes de models.

0.7.1 Col·lapse d'estrelles massives

Existeixen raons observacionals que semblen lligar els GRBs de llarga durada amb el col·lapse d'estrelles massives. Primer, el senyal de supernova subjacent als *afterglows* d'alguns GRBs. Segon, soLEN ocórrer en galàxies amb formació estel·lar, i en particular dintre de les regions de formació estel·lar. A més, la distribució d'esdeveniments dintre de les galàxies hoste és consistent amb la del col·lapse d'estrelles massives. Finalment, el descobriment de línies de *Fe* en els *afterglows* de raigs X impliquen que els GRBs es produueixen en entorns com els que queden després d'una explosió de supernova.

El model més popular per produir GRBs és conegut com a *collapsar* (Woosley, 1993; MacFadyen and Woosley, 1999). El punt de partida és una estrella de tipus Wolf-Rayet. És necessari que l'estrella hagi perdut l'embolcall d'hidrogen per tal què la bola de foc pugui travessar l'estrella col·lapsada. Partint d'estrelles d'entre 25 i $35 M_{\odot}$ a la seqüència principal, acabem amb una estrella d'heli d'entre 10 i $15 M_{\odot}$, amb un nucli de *Fe* d'entre 1.5 i $2.3 M_{\odot}$. Quan aquest nucli col·lapsa, comença a acréixer material de l'embolcall. Si l'expulsió de neutrins és incapaç d'aturar aquest acreixement, la protoestrella de neutrons creix amb ritmes dde l'ordre de $0.5 M_{\odot}s^{-1}$, i en pocs segons es forma un forat negre que continua acretant matèria. Per moments angulars inicials d'entre $j \sim 10^{16} - 10^{17} cm^2 s^{-1}$, uns pocs segons després del col·lapse es té un forat negre de $\sim 3 M_{\odot}$, envoltat per un disc d'acreixement de $\sim 0.5 M_{\odot}$. Neutrins tèrmics són radiats pel disc. L'energia requerida per crear la bola de foc es pot obtenir per aniquilació de neutrins o mitjançant el mecanisme de Blandford-Znajek (Blandford and Znajek, 1977).

Les simulacions de *collapsars* no poden reproduir GRBs amb durades menors de $\sim 5 s$, de manera que aquest model no és adequat per descriure els GRBs curts.

Els temps d'evolució de les estrelles massives, des de la seva formació fins a la seva explosió, són menors que 10 *Myr*. Amb una evolució tan ràpida exploten molt a prop dels seus llocs de naixement, per tant a les regions de formació estel·lar, i no succeeixen a les galàxies el·líptiques. La ràpida evolució també fa que el seu ritme d'esclat en funció del *redshift* sigui aproximadament proporcional a la tasa de formació estel·lar.

0.7.2 Fusions d'objectes compactes

Els primers models extragalàctics proposats com a progenitors de GRBs van ser fusions d'estrelles de neutrons amb estrelles de neutrons (NS-NS) (Paczyński, 1990) i estrelles de neutrons amb forats negres (NS-BH) (Narayan et al., 1992; Mochkovitch et al., 1993). Aquests objectes compleixen perfectament les necessitats de petita mida de la font. També, l'energia de lligam d'una estrella de neutrons, 10^{53}erg , és suficient com per a produir un GRB.

La massa límit per a la creació d'un forat negre es supera durant el procés de fusió de dues estrelles de neutrons. El producte final d'aquesta fusió serà un forat negre que, depenent del tipus d'equació d'estat emprada, estarà al voltant de $2.5 M_{\odot}$. No tota la matèria de les dues estrelles de neutrons va a parar a la creació del forat negre, part d'ella, la que té massa moment angular com per caure sobre el forat negre immediatament, va a parar a un disc d'acreixement d'entre $0.1 - 0.3 M_{\odot}$. L'evolució a partir d'aquest moment depèn de la temperatura del disc d'acreixement. Per a baixes temperatures, el disc no emet neutrins i pot sobreviure durant uns $\sim 10 \text{s}$. Durant aquest temps, qualsevol flux relativista només pot ser produït per mitjà de processos magnetohidrodinàmics, amb camps magnètics requerits de l'ordre de 10^{16}gauss . En el cas d'un disc d'acreixement calent, l'acreixement total del disc dura $\sim 100 \text{ms}$, i la major part de l'energia de lligam del disc és radiada en forma de neutrins. Aproximadament el 1% d'aquests neutrins s'aniquilen al voltant de l'eix de rotació, produint parelles $e^- e^+$, i la subseqüent bola de foc. Les simulacions mostren ritmes d'acreixement al voltant de $1 M_{\odot} \text{s}^{-1}$, lluminositats en neutrins de l'ordre de $10^{53} \text{erg s}^{-1}$, i una deposició d'energia de $5 \cdot 10^{50} \text{erg s}^{-1}$ per aniquilació de neutrins. En resum, l'energia total disponible és $\approx 5 \cdot 10^{49} \text{erg}$, i un cop col·limada arriba a les energies observades dels GRBs.

El cas de fusió de NS-BH és força similar al cas NS-NS, però en aquest, el forat negre està format des del principi. Ara, el disc d'acreixement pot ser de fins $0.5 M_{\odot}$, però amb ritmes d'acreixement superiors al cas NS-NS.

Les simulacions mostren que els GRBs provinents de fusions d'objectes compactes no poden durar més de $\sim 2 \text{s}$, i conseqüentment el model és només útil per a produir GRBs curts.

Abans de la formació del sistema binari compacte s'han de produir dues explosions de supernova que transfereixen al sistema forts impulsos. Com a resultat, aquests sistemes tenen velocitats molt altes ($\sim 450 \text{ km s}^{-1}$ en mitjana, però poden arribar als $\sim 1000 \text{ km s}^{-1}$), excedint en alguns casos les velocitats d'escapament de les galàxies hostes. Aquestes velocitats, combinades amb el llargs temps transcorreguts abans de la fusió ($\sim 0.1 - 1 \text{ Gyr}$), fan que les fusions succeeixin a més grans distàncies dels centres galàctics que en el cas dels *collapsars*. La meitat d'aquestes fusions es produeixen a distàncies superiors a 10 Kpc dels centres galàctics, i el $\sim 25\%$ d'elles a distàncies superiors a 100 Kpc . Una segona conseqüència dels llargs temps transcorreguts abans de les fusions és que el *redshift* mitjà esperat per aquests esdeveniments és entre un 20% i un 50% inferior a l'esperat pels *collapsars* (Fryer et al., 1999a).

0.8 Aquesta tesi

La tesi s'estructura en dues parts diferents. L'objectiu de la primera part de la tesi és obtenir una nova classificació de GRBs. Després d'una introducció sobre l'instrument BATSE i el seu catàleg de GRBs, s'expliquen els algorismes de classificació automàtica: anàlisi de *clusters* i xarxa neuronal. Seguidament, es procedeix a la classificació dels GRBs del darrer catàleg de BATSE. S'obtenen dues classificacions diferents: una en dues classes, com la classificació tradicional presentada en aquesta introducció; i una altra en tres classes diferents. Es donen arguments a favor de la nova classificació en tres classes, així com una interpretació de les possibles diferències físiques de cada classe de GRB amb les altres. Els GRBs corresponents a cada classe i cada classificació es troben tabulats en els apèndixs A i B, per tal que altres autors puguin investigar sobre la naturalesa de la nova classificació.

La segona part de la tesi està dedicada a l'estudi dels paràmetres extragalàctics dels GRBs, com el ritme d'esclats i la funció de lluminositat. Aquests paràmetres s'obtenen ajustant la distribució d'intensitats dels GRBs. Primer, ve una introducció sobre la distribució d'intensitats i una descripció detallada de tots els paràmetres involucrats en el seu càcul. Després de construir les distribucions d'intensitats observades per a cada classe de GRB obtinguda amb la xarxa neuronal, es presenten els resultats dels ajusts. Seguidament, la distribució d'intensitats dels GRBs es fa

servir per mesurar els paràmetres cosmològics Ω_M i Ω_Λ . La segona part conclou amb una sèrie de simulacions que mostren les possibilitats del mètode treballant amb una mostra de GRBs un ordre de magnitud superior a la present.

La tesi es tanca finalment amb les conclusions principals.

0.9 Conclusions

Tradicionalment, els GRBs s'han classificat en dos tipus diferents: els GRBs curts i els GRBs llargs, essent l'espectre dels GRBs curts més dur que el dels GRBs llargs. Aquesta classificació es basa en la distribució bimodal de les durades dels GRBs. La distribució de T_{90} , el temps durant el qual es rep el 90% del flux d'un GRB, en escala logarítmica té un decreixement al voltant de $T_{90} \approx 2$ s. Aquest decreixement separa les dues classes de GRBs amb durades mitjanes de $T_{90} \approx 0.6$ s pels curts, i $T_{90} \approx 50$ s pels llargs. Les dues classes de GRBs estan isòtropament i inhomogèniament distribuïdes, per bé que la distribució de GRBs llargs és més inhomogènia. Aquesta distribució espacial va dur a pensar que els GRBs eren esclats d'origen extragalàctic, de manera que les lluminositats es situaven entre 10^{50} i $10^{52} \text{erg s}^{-1}$, suposant emissió isòtropa. La natura extragalàctica dels GRBs de llarga durada va ser finalment confirmada el 1997, quan el satèl·lit BeppoSAX va detectar el GRB970508. La precisa localització d'aquest GRB va permetre l'observació òptica, que va revelar una font a $z = 0.835$. Des de llavors s'han mesurat més de sis desenes de *redshifts* de GRBs de llarga durada. Per la seva banda, els GRBs curts han resultat ser més difícils de localitzar. BATSE localitzava els GRBs amb una gran incertesa (amb una capsula d'error típica d'uns 4°), fet que impossibilitava trobar la font d'emissió en altres longituds d'ona diferents dels raigs gamma i mesurar el seu *redshift*. BeppoSAX, per la seva part, podia apuntar els GRBs, en la banda X, amb una major precisió (3 arcmin amb la *Wide Field Camera* i $\sim 50 \text{ arcsec}$ amb els *Narrow Field Instruments*). Desafortunadament, BeppoSAX tenia poca sensibilitat als GRBs amb durades menors que 2 s. No ha sigut fins el recent llançament del satèl·lit SWIFT que ha sigut possible mesurar *redshifts* de GRBs curts, comprovant el seu origen extragalàctic. Els *afterglows* dels GRBs llargs tenen un senyal subjacent de supernova. Aquest senyal és més feble que el de l'*afterglow* en si, però a mesura que l'*afterglow* decau, si el GRB és prou proper, la

llum de la supernova emergeix, creant un bony en la corba de llum de l'*afterglow*. Aquest fet, i la distribució de GRBs llargs dins de les seves galàxies hoste, que es donen sempre en regions de formació estel·lar, ha portat als astrònoms a relacionar aquesta classe de GRBs amb les supernoves de collapse gravitatori. En quant als GRBs curts, la detecció de GRB050509B i GRB050709 sembla descartar l'existència d'una supernova subjacent. Si a més comptem amb que GRB050509B va esclatar en una galàxia el·líptica, i GRB050709 a les rodalies de la seva galàxia hoste, la comunitat científica comença a relacionar els GRBs curts amb fusions de sistemes binaris compactes.

El catàleg de GRBs més gran i homogeni és el catàleg BATSE. BATSE era un instrument que va volar en el CGRO (Compton Gamma Ray Observatory), i estava dedicat exclusivament a la detecció de GRBs. Amb una camp de visió de $2.6\pi \text{ sr}$, va detectar 2702 GRBs durant els seus 9 anys de vida. El catàleg BATSE ens dóna fins a 9 magnituds intrínseques a l'esclat (7 relacionades amb l'energia i 2 relacionades amb la durada). Aquestes magnituds són: quatre fluències $F_{Ch\#1} - F_{Ch\#4}$, corresponents respectivament als canals espectrals d'entre 20–50 keV, 50–100 keV, 100–300 keV, and 300 – 2000 keV; tres pics de flux P_{64} , P_{256} , i P_{1024} , mesurats en intervals de 64, 256, i 1024 ms respectivament; i dos mesures de la durada de l'esclat, T_{50} i T_{90} , els temps transcorreguts mentre es detecta el 50% i el 90% del flux. Amb tota aquesta informació disponible, inferir una classificació fent servir només una variable (T_{90}) és altament inefficient. Es necessita l'anàlisi multivariant per tal de treballar amb un gran nombre de variables que presenten relacions complexes entre elles (fins i tot relacions no lineals). Aquest anàlisi aporta una nova classificació dels GRBs, i el descobriment d'una nova classe de GRBs.

Dintre d'aquesta tesi, primer apliquem un anàlisi de components principals (PCA) al catàleg BATSE més recent. El PCA és un mètode estadístic emprat en l'anàlisi multivariant de dades per obtenir noves variables, expressades com a combinacions lineals de les originals, que porten la més gran part de la informació del sistema. Basant-se en correlacions entre les variables originals, algunes de les noves variables poden ser descartades si aporten poca informació al sistema. Aquí obtenim, d'aquesta manera, que només 3 variables aporten el 96% de la informació del sistema. La primera variable és una suma ponderada de totes les variables originals, amb més pes per part de les fluències dels canals d'energia del #1 al #3. La segona variable és aproximadament la diferència entre la suma ponderada dels

tres pics de flux i les dues durades. La darrera variable en importància és la fluència en el canal d'energia #4.

Seguidament, en aquesta tesi, hem presentat una nova classificació de GRBs, basant-nos en dos algorismes de classificació automàtica: l'anàlisi de *clusters* i la xarxa neuronal.

L'anàlisi de *clusters* és una eina d'exploració i anàlisi de dades que té com a objectiu separar objectes en diferents grups de manera que el grau d'associació entre dos objectes sigui màxim si pertanyen al mateix grup, i mínim en cas contrari. En aquesta tesi es fa servir el mètode de Ward. Aquest mètode segueix un procediment d'agrupació aglomeratiu i jeràrquic, que comença amb un espai d'entrada de n punts situats en un espai de 9 dimensions, i els va agrupant fins acabar amb un sol grup. L'algorisme busca grups amb mínima variança entre els objectes que pertanyen al mateix grup, i màxima variança entre grups. El mètode treballa amb el centre de gravetat de cada grup. Això ens dóna grups tant compactes i tant separats com és possible. Obtenim un dendograma que mostra la manera en que s'agrupen els objectes, així com la dissimilitud entre els grups resultants. D'aquesta manera, si detectem un increment en la dissimilitud en el moment d'ajuntar dos grups, això ens indica que estem ajuntant dos grups amb característiques molt diferents. Dels dendogrames obtinguts es conclou que existeixen dues classes de GRBs ben separades, i una tercera emergent. La feblesa més gran del mètode d'anàlisi de *clusters* és que només treballa amb relacions lineals entre les variables. Aquesta feblesa pot ser superada mitjançant una xarxa neuronal, que pot detectar fins i tot complexes relacions no lineals entre les variables.

Les xarxes neuronals són algorismes d'intel·ligència artificial que són útils per realitzar classificacions automàtiques i objectives. Una xarxa neuronal es composa d'un llarg nombre d'elements de processat interconnectats (que anomenem neurones) treballant alhora per resoldre problemes específics. Estan inspirades en la manera com processen la informació els sistemes nerviosos biològics, com el cervell. Per tal de classificar GRBs fem servir un mètode no supervisat com el *self-organizing map* (SOM) ja que no volem començar a partir d'una classificació coneguda prèviament. La dimensió de l'espai de sortida ha de ser especificada a priori, i basant-nos en els resultats dels dendogrames de l'anàlisi de *clusters*, correm la xarxa neuronal dos cops, demanant primer un espai de sortida de dues dimensions, i després un altre

espai de sortida de tres dimensions, agrupant d'aquesta manera dues o tres classes de GRBs.

Amb els dos mètodes, anàlisi de *clusters* i xarxa neuronal, hem obtingut dues classificacions diferents: una en dues classes i una altra en tres classes. La classificació en dues classes correspon a la classificació tradicional, i la classificació en tres classes correspon al suggeriment dels dendogrames d'una possible tercera classe de GRBs.

Amb la classificació en dues classes recuperem la classificació tradicional de GRBs: GRBs curts i durs (aquí anomenats classe 2-I) en front de GRBs llargs i suaus (aquí anomenats classe 2-II), estant aquests darrers més inhomogèniament distribuïts. Podria semblar que aquesta classificació no introduceix cap nou coneixement sobre els GRBs, però de fet contribueix de manera substancial. Primer de tot, la classificació tradicional separa GRBs amb $T_{90} \gtrsim 2\text{ s}$. Això representa una separació molt abrupte. És clar que existeix una distribució bimodal de les durades dels GRBs, però les dues distribucions estan indubtablement superposades. La classificació automàtica presentada en aquesta tesi és capaç d'identificar GRBs individuals i assignar-los a una determinada classe (GRBs curts o llargs), malgrat que la seva durada estigui en la regió de superposició de les dues distribucions de durades. Això és possible gràcies a l'ús de totes les variables disponibles que descriuen un GRB individual, no només la durada com es feia tradicionalment. Només aquest fet ja fa que la classificació valgui la pena per si mateixa. A més, es comprova que els GRBs curts tenen durades de fins a $T_{90} \sim 100\text{ s}$. Aquest fet té conseqüències importants en la modelització de progenitors de GRBs curts, que, d'acord amb recents observacions, provenen de fusions de sistemes binaris compactes. Les simulacions de fusions NS-NS i NS-BH, mostren que no poden produir GRBs amb durades més grans que 2 s. Aquestes simulacions haurien de ser corregides perquè, segons la classificació presentada en aquesta tesi, els GRBs curts tenen durades més llargues que 2 s. Altres tipus de fusions, com ara estrelles d'heli amb forats negres i nanes blanques amb forats negres, es creu que tindrien una distribució més inhomogènia que els GRBs curts, i per tant no són adequades per a llurs progenitors.

En la classificació en tres classes, la nova classe 3-II es composa dels GRBs més llargs i més suaus de la classe 2-I, i pels GRBs més curts de la classe 2-II. Aquesta nova classe de durada intermitja té la mateixa duresa que la classe de

GRBs llargs 3-III. Per contra, té una fluència menor, un menor pic de flux, i està distribuïda de manera més homogènia que la classe 3-III. La separació en tres classes ha rebut suport també d'altres autors citats al llarg d'aquesta tesi. Hem mostrat igualment una possible diferència física entre les classes 3-II i 3-III, que suggereix que la classificació en tres classes té un significat real i no és per cap artifici de la classificació automàtica. Els clàssics GRBs llargs mostren una evolució en duresa, en el sentit que els GRBs més llunyans són més durs que els GRBs més propers. Tenint en compte la correlació duresa-intensitat, l'evolució en duresa suggereix una evolució de la funció de lluminositat, fet que ja ha estat demostrat. Si separam els clàssics GRBs llargs en les classes 3-II i 3-III, aquesta evolució només la manté la classe 3-III, mentre que la classe 3-II la perd totalment. Aquest fet, que no es pot atribuir únicament a una casualitat, és una confirmació important de que la classificació en tres classes té un significat físic. Per donar més suport a l'evolució en lluminositat de la classe de GRBs 3-III, direm que dels 220 GRBs de la mostra de Lloyd, Fryer, i Ramirez Ruiz (2002) que va confirmar l'evolució, 205 GRBs van entrar en la classificació aquí presentada, i 198 d'ells han estat classificats com a classe 3-III per la xarxa neuronal. Els *collapsars*, que provenen del col·lapse gravitatori d'estrelles molt massives, poden mostrar aquesta evolució. És comument acceptat que el límit superior de la funció inicial de masses depèn de la metal·licitat, i que menors metal·licitats permeten que es formin estrelles més massives. Quan detectem GRBs més i més llunyans, estem observant un Univers cada cop més jove, amb metal·licitats menors, i per tant amb més estrelles més massives. Per aquesta raó, si els GRBs provenen d'estrelles molt massives, en l'Univers primitiu aquestes eren més massives encara i tenien més poder per a produir explosions més lluminoses.

Dintre de l'esquema de la classificació en tres classes, la classe 3-III és l'única que es pot pensar que tingui els *collapsars* com a progenitors. En canvi, la classe 3-I és força similar als clàssics GRBs curts, que es creu que provenen de fusions NS-NS o NS-BH. Pel que fa als GRBs de durada intermitja, classe 3-II, la seva natura roman encara desconeguda, malgrat que s'ha suggerit en aquesta tesi que la diferència entre les classes 3-I i 3-II pot ser deguda a què una d'elles sigui produïda per fusions NS-NS, i l'altra per fusions NS-BH. Tantmateix, la identificació dels progenitors de la classe 3-II, així com la confirmació definitiva sobre els progenitors de les classes 3-I i 3-III forma part del treball futur. Altres plans de futur inclouen l'adaptació de la classificació a GRBs detectats per altres instruments diferents de BATSE. Diferents

instruments mesuren diferents magnituds i amb diferents sensibilitats. Aquestes diferències dificulen la classificació de GRBs detectats posteriorment a BATSE. L'interès en classificar GRBs que es detecten de nou no és per confirmar les característiques ja mesurades en aquesta tesi, sinó que radica en la mesura de *redshifts*, morfologies de les galàxies hoste i la localització dins d'elles. Aquestes propietats són clau per descobrir el tipus de progenitor per a cada classe de GRB, i són la raó principal per classificar correctament els nous GRBs.

La segona part de la tesi està dedicada a l'estudi dels paràmetres extragalàctics dels GRBs, com el ritme d'esclats i la funció de lluminositat, així com a l'estudi dels paràmetres cosmològics Ω_M i Ω_Λ , que governen la dinàmica de l'Univers. Hem determinat aquests paràmetres per a cada una de les classes de GRBs obtingudes amb la xarxa neuronal durant la primera part de la tesi. S'han mesurat en dos casos particulars: sense evolució en lluminositat i amb evolució en lluminositat. S'ha fet la mesura d'aquests paràmetres mitjançant l'ajust de la distribució observada d'intensitats dels GRBs amb la distribució teòrica. La representació $\log N - \log P$ de la distribució d'intensitats dels GRBs és una gràfica que mostra el nombre de GRBs N en funció de la intensitat, mesurada com el pic de flux P . El pendent de la distribució acumulativa d'intensitats es desvia del valor $-3/2$ esperat per a una distribució d'esdeveniments homogènia en un espai euclià. Aquest fet va fer que els astrònoms canviessin d'idea respecte a l'escala de distàncies als GRBs, ja que, combinat amb l'alt grau d'isotropia de la mostra, portava a la convicció del seu origen extragalàctic, fins i tot abans que es mesurés cap *redshift*. La distribució d'intensitats ja ha estat emprada per a mesurar ritmes d'esclats, distribucions de *redshifts*, tases de formació estel·lar, i funcions de lluminositat per a GRBs. En aquesta tesi continuem aquests treballs, expandint-los ajustant tots els paràmetres alhora, cadascun amb més llibertat que en treballs anteriors, i estenent l'ajust als paràmetres cosmològics Ω_M i Ω_Λ .

El ritme d'esclats de GRBs és una mesura del nombre d'esdeveniments per unitat de temps i de volum comòbil. Ens dóna un cens del nombre de GRBs formats a *redshifts* determinats, i pot contribuir a distingir entre els diferents tipus de progenitors. Per exemple, s'espera que el ritme de *collapsars* segueixi una evolució molt similar a la de la tasa de formació estel·lar, degut al temps de vida molt curt dels estels progenitors. Per la seva banda, les fusions NS-NS i NS-BH s'espera que succeeixin a *redshifts* mitjans, d'entre un 20% i un 50% inferiors als dels *collapsars*,

degut als seus llargs temps d'evolució. Aquesta classe de progenitors mostraria un retard respecte a la tasa de formació estel·lar. Basant-nos en diverses mesures de la tasa de formació estel·lar i en el ritme de GRBs, aquí hem fet servir una triple llei de potències de $(1 + z)$ com a modelització del ritme de GRBs. El model té 6 paràmetres lliures: tres exponents, dos punts de trencament, i un *redshift* màxim pels GRBs. Els resultats mostren que amb el mètode presentat en aquesta tesi i el nombre de GRBs de durada curta i intermitja (classes 2-I, 3-I, i 3-II), a dia d'avui no és possible determinar el ritme de GRBs amb una mínima precisió. Per la seva part, la precisió obtinguda pel ritme d'esclats dels GRBs de llarga durada (classes 2-II i 3-III) és acceptable, essent el mètode alhora bo per a mesurar indirectament la tasa de formació estel·lar fins a *redshift* molt alt. Per aquests GRBs el ritme d'esclats creix des de $z = 0$ fins a $z \approx 5$ ($z \approx 9$ si tenim en compte l'efecte de l'evolució en lluminositat). Després es manté pràcticament constant fins a $z \approx 10$ ($z \approx 30$ si tenim en compte l'efecte de l'evolució en lluminositat). En ser no negatiu, l'exponent del ritme d'esclats a alt *redshift* ens indica que el suposat decreixement del ritme de GRBs a alts *redshifts* queda modelat aquí pel paràmetre z_{max} , el qual representa una caiguda sobtada en el ritme d'esclats. Aquest fet implica que el ritme d'esclats per a GRBs llargs va començar amb una crescida sobtada, així com ho va fer la tasa de formació estel·lar.

La funció de lluminositat és una mesura del nombre d'objectes per unitat de lluminositat. Tradicionalment, la funció de lluminositat dels GRBs s'ha intentat mesurar amb les distribucions de $\langle V/V_{max} \rangle$ i $\log N - \log P$. La funció de lluminositat típicament triada pels GRBs és una llei de potències doble. La funció de lluminositat dels GRBs de llarga durada s'ha mesurat recentment mitjançant calibradors de lluminositat com la correlació entre variabilitat–lluminositat. Aquests treballs han detectat l'existència d'una evolució en lluminositat, que fa que els GRBs més llunyans siguin també més lluminosos que els propers. Aquesta possibilitat ja s'havia suggerit en la primera part d'aquesta tesi, i en la publicació Balastegui et al. (2001). Amb el nombre actual de GRBs observats, l'ajust de la distribució d'intensitats no pot determinar si realment existeix evolució en lluminositat o no. Per bé que les simulacions mostren que incrementant la mostra en un ordre de magnitud es podria distingir l'efecte de l'evolució perfectament. Els resultats presentats en aquesta tesi suggerixen que, dins de la classificació en tres classes, els GRBs de durada intermitja, classe 3-II, són els més lluminosos. Això afegeix un nou requeriment que

han de complir els progenitors d'aquesta nova classe de GRBs.

Per a cada un dels paràmetres que modelitzen el ritme de GRBs i la seva funció de lluminositat, s'ha inclòs una completa discussió sobre la variació de la distribució d'intensitats en funció de la variació pròpia del paràmetre. Considerem que és una compilació útil d'efectes que modelitzen la distribució d'intensitats.

La part final de la tesi està dedicada a la mesura dels paràmetres cosmològics Ω_M i Ω_Λ . Aquests paràmetres adimensionals representen la relació entre la densitat de cada component de l'Univers (Ω_M de matèria, Ω_Λ de constant cosmològica) i les densitats crítiques, és a dir, les densitats d'un univers pla. Són paràmetres clau per tal de determinar la geometria i la dinàmica de l'Univers. $\Omega_M + \Omega_\Lambda = 1$ implica que la densitat d'energia de l'Univers és igual a la crítica i l'Univers és pla. $\Omega_M + \Omega_\Lambda > 1$ implica que la densitat d'energia de l'Univers és superior a la crítica i l'Univers és tancat. Finalment, $\Omega_M + \Omega_\Lambda < 1$ implica que la densitat d'energia de l'Univers és inferior a la crítica i l'Univers és obert. La comunitat científica ha dedicat un esforç extraordinari a la mesura de Ω_M i Ω_Λ , especialment durant la darrera dècada. El mètode més exitós ha estat l'ajust del diagrama de Hubble de les supernoves de tipus Ia. Aquest mètode va portar al descobriment de l'expansió accelerada de l'Univers, i conseqüentment a la necessitat d'alguna forma d'energia fosca, que primer es va postular com una constant cosmològica. En els càlculs previs en aquesta tesi s'han fet servir els valors $\Omega_M = 0.3$ i $\Omega_\Lambda = 0.7$. Aquest és l'anomenat model de concordància, i són els valors obtinguts mitjançant diferents mètodes (supernoves de tipus Ia, radiació còsmica de fons de microones, i agrupacions de raigs X). Hem suggerit una pregunta: si coneguéssim el ritme d'esclats de GRBs i la seva funció de lluminositat, seria possible fer servir la distribució d'intensitats per a mesurar Ω_M i Ω_Λ ? La resposta és que sí.

El procediment seguit ha estat: prendre els millors valors pel ritme d'esclats de GRBs i la funció de lluminositats derivats ajustant la distribució d'intensitats i considerar-los com a paràmetres fixes. Després, hem procedit a l'ajust de la distribució d'intensitats considerant Ω_M i Ω_Λ com a paràmetres lliures. El resultat és que s'han retrobat els valors originals de $\Omega_M = 0.3$ i $\Omega_\Lambda = 0.7$ amb una precisió similar a l'obtinguda amb supernoves de tipus Ia. Les millors classes de GRBs per mesurar els paràmetres cosmològics han resultat ser les classes 2-II, 3-II, i 3-III. El punt feble del mètode és que es necessiten conèixer d'avançada el ritme d'esclats de

GRBs i la funció de lluminositat, mentre que els mètodes per mesurar-los suposen valors fixes per Ω_M i Ω_Λ . El pla de treball futur, pel que fa a aquesta matèria, inclou l'ajust de la cosmologia alhora que l'ajust del ritme d'esclats de GRBs i la funció de lluminositat. Aquí no s'ha pogut procedir d'aquesta manera degut a l'excessiu temps de computació que es necessita.

La mostra de *redshifts* mesurats s'ha incrementat en 20 GRBs en menys d'un any d'operació del satèl·lit SWIFT. Aviat es doblarà la mostra mesurada en tota una dècada. Un cop disposem d'una gran mostra de *redshifts*, serà possible mesurar el ritme d'esclats de GRBs i la lluminositat de manera directa, simplement comptant GRBs. Llavors serem capaços de comparar aquestes magnituds amb els resultats presentats en aquesta tesi. A més, la detecció de *redshifts*, galàxies hoste, i localitzacions dins d'elles, ens està aportant una informació sense precedents sobre els progenitors dels GRBs. Trobar diferents classes de progenitors confirmaria l'existència de diferents classes de GRBs, confirmant, o bé rebutjant, la nova classificació de GRBs presentada en aquesta tesi.

Chapter 1

Introduction

Gamma-ray bursts (GRBs from now on) are one of the greatest mysteries in nowadays astrophysics. Nevertheless, it has been one of the most active research fields of the 90's, with over 400 scientific papers per year since 1996. Although the mystery is starting to clarify, there are yet lots of open questions.

GRBs are flashes of gamma-rays coming from random directions in space at a rate of about 2 bursts per day. The luminosity of these events ranges from the order of $10^{42} \text{erg s}^{-1}$, in case of their being galactic events, to between $10^{50} \text{erg s}^{-1}$ and $10^{52} \text{erg s}^{-1}$, if their origin is extragalactic, in both cases assuming isotropic emission. We are talking about energies superior to that of a nova in one case, and superior to a supernova in the other, always emitting the energy peak over 100 keV, which is why they are said to be the most violent explosions in the Universe since the Big Bang. It is then a challenge to explain, and to propose, progenitor's scenarios for GRBs, and those existing use to involve compact objects (neutron stars or black holes), mergings between these objects, hypernovae or collapsars, always requiring beaming to concentrate energy, and using ultrarelativistic jets along the line of vision to blueshift the spectrum.

The GRB is followed by an afterglow, a lower energy, long lasting emission in the X-ray, optical, and radio bands. The accurate positioning of the afterglows has allowed to measure the redshifts of more than 60 GRBs, as well as to identify the host galaxy morphology and the positions of the GRBs within them, thus confirming the extragalactic origin of at least some subgroups of GRBs.

1.1 History

The discovery of GRBs is closely related to the development of technology for high energy astrophysics in space. The year 1963, during cold war, a treaty was signed in Geneva, which banned nuclear tests under water, in the atmosphere, and in space. The USA started then a military project to watch out for the fulfilment of this treaty, and so the VELA¹ satellites were born. Those satellites carried neutron, X-ray, and gamma-ray detectors, and were paired on opposite sides of a 4 days orbit, in a way that Earth could never cloak the observations. The VELA satellites never detected any violation of the treaty, but they did detect gamma-ray flashes. The improvement of the instruments in the fifth and sixth generations of VELA, launched in 1969, with temporal resolutions of 0.2 s (faster than the light travel time between a pair, 1 s approximately), allowed to determine, with certain accuracy, the incoming angle of those gamma-ray flashes, resulting in that they did not come neither from Earth nor from the Sun. Finally, in 1973 the discovery of GRBs was announced in the famous paper "Observations of Gamma-ray bursts of cosmic origin", by Klebesadel, Strong, and Olson (1973), where they inform about 16 bursts detected between 1969 and 1972.

By the end of the 70's, Kevin Hurley promoted the creation of a detector's network onboard interplanetary missions, like the Pioneer Venus Orbiter and other satellites with gamma-ray detectors, like the Venera spacecrafts with the KONUS and SIGNE experiments. The idea was to pinpoint the position of GRBs by triangulation, and it was called the Interplanetary Network (IPN). For years, it has been the only source of information about GRBs, and nowadays it is still working in its third generation. IPN² counts now with satellites like HETE2 and INTEGRAL. Other successful missions, now finished, have been CGRO and BeppoSAX.

The real turning point, and the biggest impulse in the GRB field, happened in 1991 with the launch of the Compton Gamma-Ray Observatory (CGRO). It was a 17 tons observatory, carrying onboard the BATSE (Burst And Transient Source Experiment) instrument, which multiplied by ten the sample of previously observed GRBs. Its catalogue contains data on position, energy and duration, for more than

¹from the spanish verb "velar" which means to watch.

²<http://www.ssl.berkeley.edu/ipn3/>

2500 bursts, and has allowed to check the isotropy and inhomogeneity of the bursts distribution. Unfortunately, and after a life longer than expected, the CGRO had to be destroyed in a controlled reentry to the atmosphere on May 2000, due to its having only two gyroscopes left.

Before BATSE, the question about the distance scale to GRBs was a big debate, and the most popular idea was that of their galactic origin. After BATSE, the high degree of isotropy, the inhomogeneity of the spatial distribution, and the lack of an excess of events towards M31, combined with the high sensitivity of the instrument, made astronomers change their minds and the extragalactic origin of GRBs gained support. In order to definitely settle the distance scale problem of GRBs, it was necessary to find an optical counterpart, or the host galaxy of the GRB. Unfortunately, the pointing accuracy of BATSE was not good enough, and within the typical error box of a BATSE GRB there could be hundreds of optical sources. This limitation was eventually overcome with the launch of BeppoSAX. The Italian-Dutch mission worked mainly on the X-ray band, improving the pointing accuracy from 4° to less than 1 arcmin . The 28th of February of 1997, BeppoSAX detected the first X-ray afterglow (Costa et al., 1997), facilitating the optical observation (van Paradijs et al., 1997). Finally, on May the 8th, the orbiting BeppoSAX satellite detected and precisely located GRB970508 (Galama et al., 1997), quickly relaying its position to astronomers. Within hours, many of the world's most powerful telescopes were re-pointed in the direction of the new GRB, finding there an optical fading source at $z = 0.835$. Since then, more than 60 GRB's redshifts have been measured, confirming the cosmological nature of the phenomenon.

GRBs were related to supernovae when detecting simultaneously SN1998bw within the error box of GRB980425 (Galama et al., 1998). Hints of a supernova lightcurve underlying the optical afterglow were observed for several GRBs and finally confirmed for GRB030329 (Stanek et al., 2003; Hjorth et al., 2003; Gorosabel et al., 2005). Now, it is commonly accepted that long-duration GRBs are related to core collapse supernovae, and that their progenitors are very massive stars.

The current revolution is led by the SWIFT satellite. It has allowed to measure over 20 redshifts in less than one year of operation (half of the sample measured during 8 years by BeppoSAX and HETE2). Moreover, it has recently discovered the afterglows of short-duration GRBs (Castro-Tirado et al., 2005; Piro, 2005; Fox

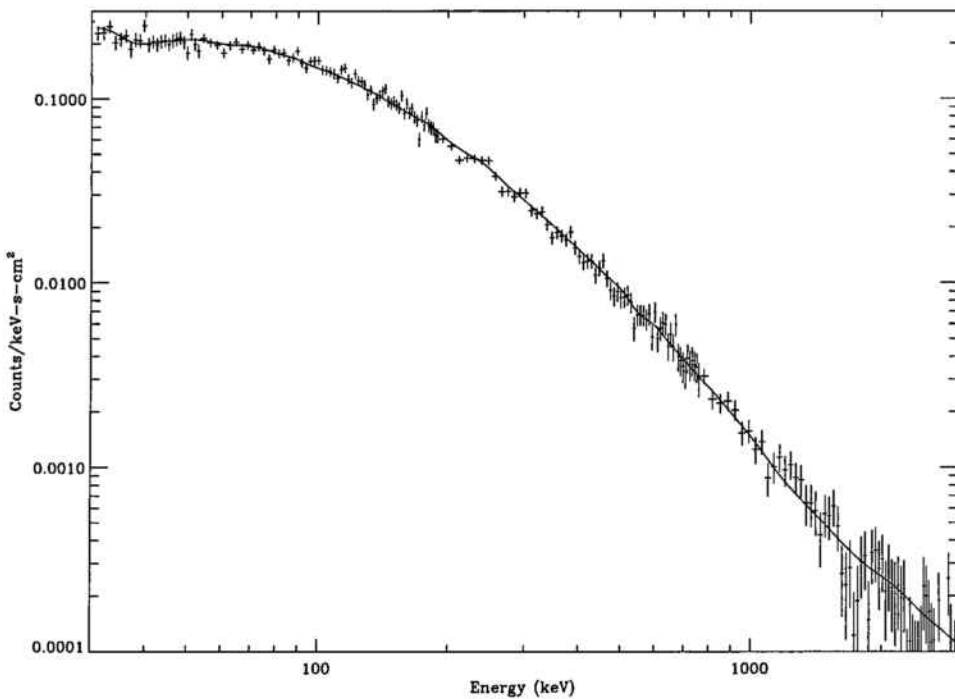


Figure 1.1: Spectrum of GRB910503. Extracted from Band et al. (1999).

et al., 2005; Gehrels et al., 2005; Villasenor et al., 2005; Hjorth et al., 2005), shedding some light over the mystery of this kind of GRBs.

1.2 Energetics

The observed fluences range from $10^{-4} \text{ erg cm}^{-2}$ to $10^{-7} \text{ erg cm}^{-2}$, corresponding to isotropic luminosities between $10^{50} \text{ erg s}^{-1}$ and $10^{52} \text{ erg s}^{-1}$. With the determination of redshifts for GRBs, it was possible to determine the energy released in a single event (assuming a given cosmology). It appeared that this energy was spread over 3 orders of magnitude, from 10^{51} erg to 10^{54} erg . Later on, thanks to the measurement of the beaming angle using the break times of optical and radio afterglows, it was possible to correct the total energy emitted from the beaming effect. The total energy released when one takes into account the beaming is narrowly clustered around 10^{51} erg (Frail et al., 2001).

The continuum spectrum is non-thermal, and peaks over 100 keV . In some cases, photons of up to 20 GeV have been detected. The spectrum is well fitted with

a smoothly joined broken power law, called the Band spectrum (Band et al., 1993) (see section 5.3.6 for more details). Figure 1.1 shows the spectrum of GRB911127 as an example.

1.3 Temporal structure

GRBs do not have a typical lightcurve: there can be bursts with only one short pulse, pulses with smooth rise and decay, events with wide gaps between two or more pulses, complex events with several pulses and peaks superimposed. There are lightcurves of all kinds, simple or chaotic, smooth or rough, slow or fast, single peaked or multipeaked, and all combinations; to sum up, a wide variety, very difficult to classify. Among all these arises the only well-defined lightcurve class, the FREDs (Fast Rise Exponential Decays), to which belong approximately 15% of all GRBs. Figure 1.2 shows the variety of GRB lightcurves: plot A) shows a single-peak event; plot B) shows two well separated episodes of emission; plots C) and D) show very erratic, chaotic, and spiky bursts; plot E) shows a smooth multipeaked event; and finally, plot F) shows a typical FRED lightcurve.

Most GRBs show an asymmetric temporal structure: individual pulses have rise times shorter than decay times. There has not been found any periodic structure neither with Fourier transforms nor with wavelet analysis. The very fast temporal variability, on scales of 1 *ms* or even lower, imply source sizes of about 100 *km*: that is why astronomers think of compact objects as GRBs progenitors.

The duration distribution of GRBs spans five orders of magnitude, ranging from 10 *ms* to 1000 s, and shows a bimodal aspect, clearly distinguishing two groups partially overlapped. Short GRBs have a mean duration of about 0.6 s while long-duration GRBs last about 50 s in mean. Short GRBs are also harder than long GRBs, meaning that their spectrum peaks at higher energies. According to these characteristics, GRBs have been traditionally classified into two different classes: short-duration GRBs and long-duration GRBs (Kouveliotou et al., 1993). Figure 1.3 summarizes the characteristics of short and long-duration GRBs. The top left plot shows the duration distribution in logarithmic scale. The duration is represented by the quantity T_{90} , which is the time within which one receives 90% of the total

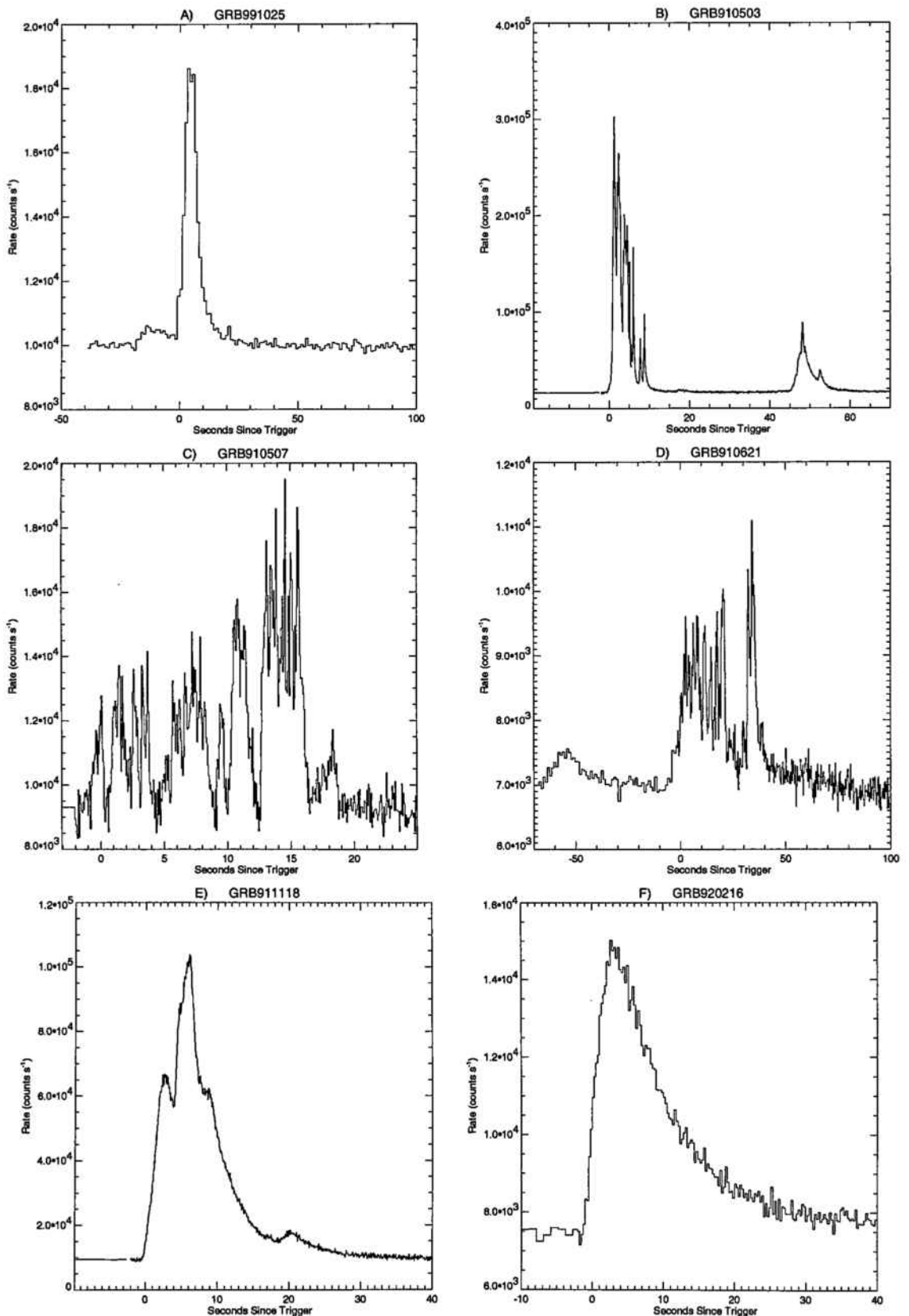


Figure 1.2: Variety of lightcurves of GRBs. A) Single-peak event. B) Two well separated episodes of emission. C) and D) Very erratic, chaotic, and spiky bursts. E) Smooth multipeaked event. F) Typical FRED lightcurve.

received flux. It shows a bimodal aspect, with a dip separating both distributions at $T_{90} \approx 2$ s. Short GRBs are displayed with a black solid line, and long GRBs with a red dotted line. Mean durations are represented by the vertical lines. Typically, 2 s is taken as the limiting value between short ($T_{90} < 2$ s) and long ($T_{90} > 2$ s) GRBs. The bottom left plot is the scatter plot of hardness (H_{32}) *vs* duration (T_{90}). H_{32} is defined here as the fluence received with energies from 100 to 300 keV divided by the fluence received with energies from 50 to 100 keV. Short GRBs, represented by black filled circles, tend to be harder than long-duration GRBs, represented by red filled triangles. Vertical and horizontal lines show mean durations and hardnesses, respectively, for each GRB class. Finally, the bottom right plot shows the hardness distribution for short GRBs (black solid line) and long GRBs (red dotted line). Here, it can be more clearly appreciated the difference in hardness for each class of GRB. Short-duration GRBs have $\langle H_{32} \rangle = 6.3 \pm 0.2$, while long-duration GRBs have $\langle H_{32} \rangle = 3.1 \pm 0.1$.

1.4 Spatial distribution

The most direct evidence of the spatial distribution of GRBs comes from the observed intensity and angular distributions. The angular distribution provides two of the dimensions of the spatial distribution, while the intensity distribution is a convolution of the luminosity function and the radial distribution.

1.4.1 Isotropy

The distribution in galactic coordinates of the GRBs observed with BATSE (Figure 1.4) is consistent with isotropy. The values of the galactic dipole and quadrupole momenta, which measure the concentration towards the Galactic Disc and the Galactic Centre, respectively, confirm the high degree of isotropy. This fact challenged most of the galactic models for GRBs existent at the beginning of the 90's. There was no clustering towards the Galactic Centre, neither there was any excess of GRBs towards the direction of M31. The isotropy degree could either correspond to a sample with distances shorter than the height of the Galactic Disc, or to an Extense Halo of high-velocity neutron stars with a radius of about 100 to 200 Kpc, longer

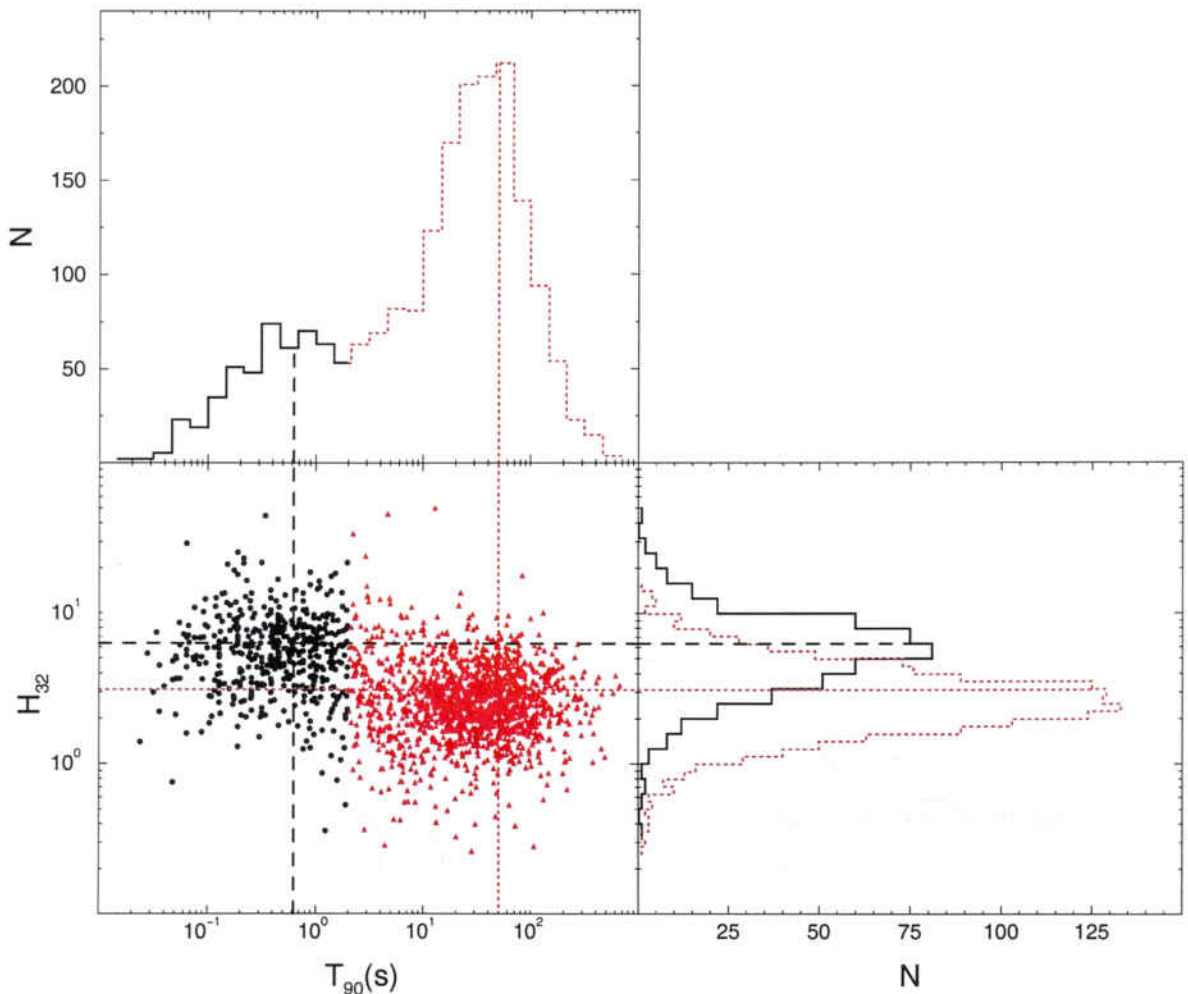


Figure 1.3: Characteristics of short and long-duration GRBs. The top left plot shows the duration distribution in logarithmic scale. The bottom right plot shows the hardness distribution. Short GRBs ($T_{90} < 2$ s), displayed as black solid lines, tend to be harder than long GRBs ($T_{90} > 2$ s), displayed as red dotted lines. The vertical lines show the mean durations, and the horizontal lines the mean hardnesses for each GRB class. The bottom left plot is the scatter plot of hardness *vs.* duration, where short GRBs are represented by black filled circles and long-duration GRBs by red filled triangles.

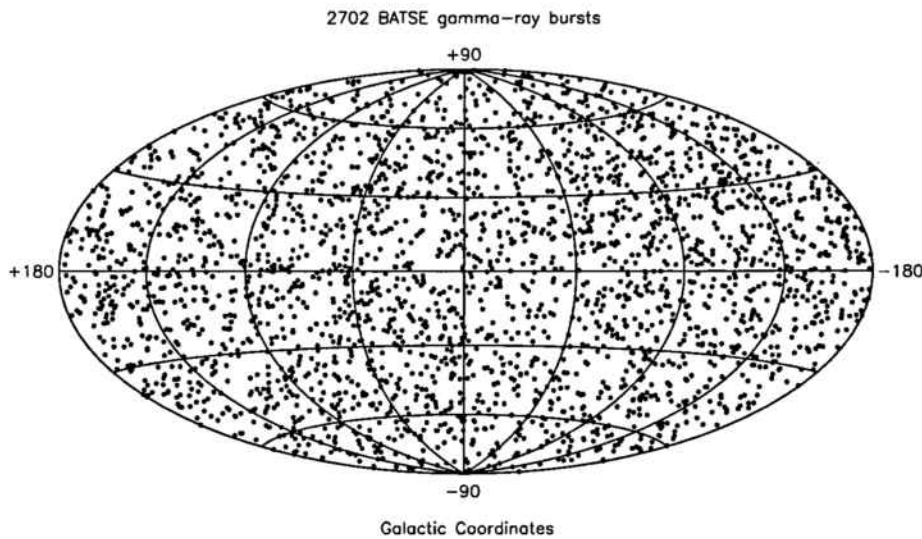


Figure 1.4: Angular distribution of GRBs in galactic coordinates for the 2702 GRBs detected by BATSE. It is not observed any clustering towards the Galactic Centre neither any excess of GRBs towards the direction of M31. Other statistical tests confirm the high degree of isotropy.

than the distance from Earth to the Galactic Centre.

Mészáros et al. (2000), however, found that the angular distribution of a subclass of intermediate duration GRBs is not compatible with isotropy.

1.4.2 Inhomogeneity

As it has been said, the intensity distribution of GRBs is related to their distance distribution. Figure 1.5 shows the intensity distribution for long-duration ($T_{90} > 2$ s) GRBs, represented by the cumulative $\log N - \log P$ distribution. As it can be seen, there is a deficit of low peak flux GRBs with respect to the line of slope $-3/2$, expected in the homogeneous euclidean spatial distribution. The first clue to this defect was given by a series of balloon test experiments (Meegan et al., 1985), and confirmed eventually by BATSE (Meegan et al., 1992). This fact played a very important role in the Great Debate (Lamb, 1995; Paczyński, 1995; Rees, 1995) about the distance scale to GRBs, making most astronomers change their minds and set GRBs as extragalactic events, as opposed to the idea of their galactic origin,

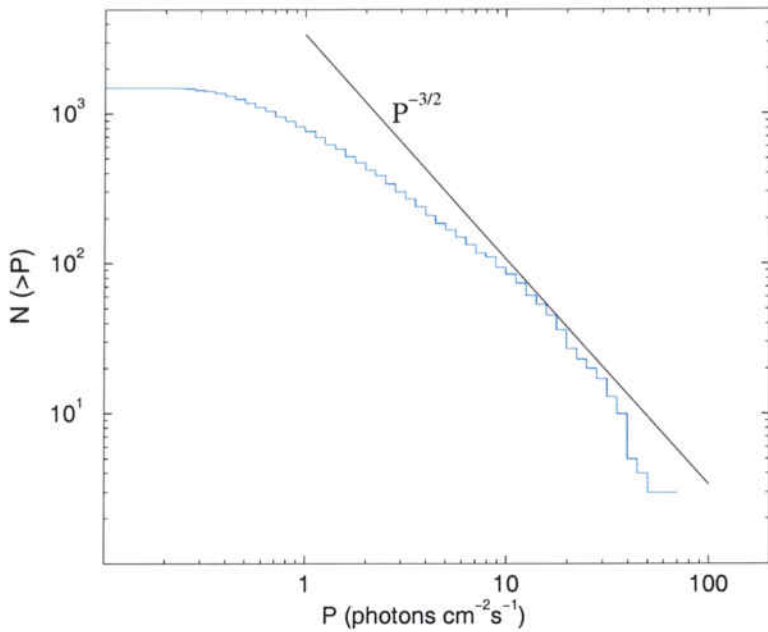


Figure 1.5: Cumulative $\log N - \log P$ distribution for long-duration ($T_{90} > 2$ s) GRBs. The black line has slope $-3/2$, and represents the expected distribution of an homogeneous sample of objects in euclidean space.

which was dominant those days.

What does this deficit of low peak flux GRBs stand for?

Considering P as a luminosity estimator, it follows that the lower peak flux GRBs are the most distant ones. From a point of view of a galactic origin, this lack of distant GRBs could mean that the detector has reached the edge of the population, and although it has enough sensitivity to detect farther GRBs, as a matter of fact, they are not produced. On the other hand, it could also mean that the number of GRBs produced decreases with the distance to Earth. Since no known objects are distributed around Earth³, this option would imply that GRBs are produced from a progenitor population distributed at distances much longer than the distance from the Sun to the centre of the Galaxy. As stated in section 1.4.1, the high degree of isotropy seen by BATSE rules out any model which produces a high concentration of GRBs towards the Galactic Disc. With these constraints, Hartmann et al. (1994)

³Although there are several proposed models for GRBs occurring in the Solar System, or in the Oort cloud, centered on the Sun, they have never been popular within the community. See Maoz (1993) for details.

proposed a popular model which produced GRBs from an Extended Galactic Halo of high-velocity neutron stars. The model required the formation of high-velocity neutron stars in the Galactic Halo in order to populate the Extended Galactic Halo, a delay in the explosion mechanism so that the GRBs explode far from the Galactic Disc, and a correlation between the velocity and the emission direction of gamma-rays to increase the detection probability with the distance to the disc center.

On the other hand, the deviation from the slope $-3/2$ in the $\log N - \log P$ distribution could be interpreted as a deviation from euclidean space, thus implying an extragalactic origin for GRBs. At very long distances, the effect of the curvature of the Universe makes the comoving volume element to shrink, hence diminishing the number of distant events. Aside from this geometric factor, there is also the possibility of evolutionary effects, such as a variation of the explosion rates, or of the luminosity with distance. Of course, all these effects can also happen at the same time. Cosmological models for GRBs were first postulated by Usov and Chibisov (1975) and by van den Bergh (1983). Cosmological distributions have been fit to the observed intensity distribution by Piran (1992), Mao and Paczyński (1992), and Wickramasinghe et al. (1993), among others.

1.5 The fireball

The relativistic fireball is a generic model (Paczyński, 1986; Goodman, 1986), independent from the kind of progenitor, that tries to reproduce the physical properties in the GRB environment. It has been very successful, predicting the afterglow emission even before it was ever observed (Paczyński and Rhoads, 1993; Katz, 1994).

The very fast temporal variability of GRBs, of the order of 1 ms , implies a very compact source with radius $R_s \leq c\delta t \sim 300\text{ km}$. This fact, combined with the output energy required, of about 10^{52} erg in gamma-rays, implies an electron-positron plasma, independently from the progenitor kind. This fireball results in an enormous optical depth that would thermalize the photons, producing a black body spectrum, while the observed spectrum is clearly non-thermal. This paradox, known as the compactness problem, is solved by the relativistic expansion.

With a relativistic expansion, the energy of the emitted photons is lower than

that of the observed photons by the Lorentz factor Γ , resulting in a fraction of photons able to produce e^-e^+ pairs lower by a factor Γ^2 . The distance from the source at which the radiation is emitted increases by a factor Γ , and thus the volume by a factor Γ^3 . The combination of these effects reduces the energy density by a factor Γ^6 . Lorentz factors $\Gamma > 10^2$ result in an optically thin medium, although the fireball has to be almost free of barions or, otherwise, the expansion would be stopped before the medium turns optically thin.

The fireball is made of many shells of photons, e^-e^+ pairs, plus a small amount of baryons, which are produced by an intermittent central engine. These shells interact with each other (internal shocks) until they are eventually decelerated by the interstellar medium in an external shock.

The leading model for the GRB prompt gamma-ray emission is the internal shock model (Sari and Piran, 1997; Daigne and Mochkovitch, 1998; Spada et al., 2000), although the external shock model (Panaiteescu and Mészáros, 1998; Dermer et al., 1999) cannot yet be rejected. Many other questions are not yet definitely settled, for instance whether the fireball is magnetically (Spruit et al., 2001; Vlahakis and Königl, 2003a; Vlahakis and Königl, 2003b) or kinetic energy dominated (Rees and Mészáros, 1994). The leading radiation mechanism is synchrotron emission (Mészáros and Rees, 1993a), but others such as inverse Compton (Panaiteescu and Mészáros, 2000) are also being studied.

Within the fireball model, the afterglow emission would be produced by the external shock of the fireball itself with the interstellar medium.

1.6 The afterglow

The afterglow of a GRB is a broad-band emission, covering X-rays, optical, infrared, and radio bands, that is detected after the prompt gamma-ray emission. In each band, the lightcurve has generally a power-law decay behaviour. The afterglow emission was first detected for GRB970228. Afterglows had only been detected for long-duration GRBs until the very recent detection of the afterglows for the short GRBs GRB050509B (Castro-Tirado et al., 2005) and GRB050709 (Villasenor et al., 2005).

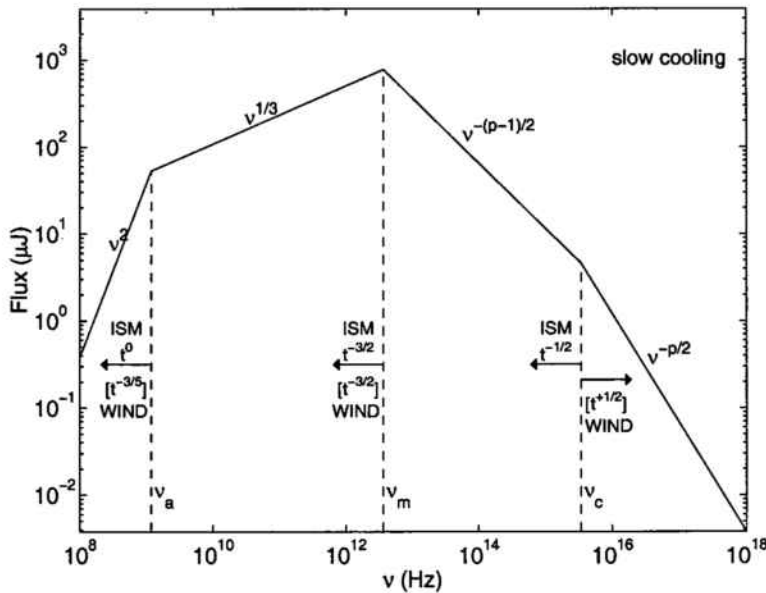


Figure 1.6: Theoretical spectrum of a GRB afterglow. ν_a is the self-absorption synchrotron frequency. ν_m is the characteristic synchrotron frequency, corresponding to the minimum Lorentz factor. ν_c is the cooling frequency. It is shown the evolution of the spectrum int the case of constant density environment (ISM) and $\rho \propto r^{-2}$ (WIND).

The afterglow is understood as the external shock of the fireball with the interstellar medium that accelerates electrons producing synchrotron radiation. The spectrum of the afterglow and its evolution are obtained from classical synchrotron theory (Sari et al., 1998; Mészáros et al., 1998), assuming a power-law distribution of the Lorentz factor of the accelerated electrons. Figure 1.6 shows this theoretical spectrum, where: ν_a is the self-absorption synchrotron frequency; ν_m is the characteristic synchrotron frequency, corresponding to the minimum Lorentz factor; and finally, ν_c is the cooling frequency, electrons radiating at higher frequencies than ν_c can only radiate while the shock is going on. The evolution in time of these characteristic frequencies depend on the external environment. For a constant density environment the evolution is labelled as ISM, while for an environment characterized by a stellar wind, with density $\rho \propto r^{-2}$, the evolution is labelled as WIND.

The X-ray afterglow is the first and strongest signal, but it is also the shortest one. It is observed for 90% of the well localized GRBs. Emission line features have been observed in several X-ray afterglows (Piro et al., 2000; Reeves et al., 2002): most of them have been interpreted as *Fe* lines due to an iron-rich environment.

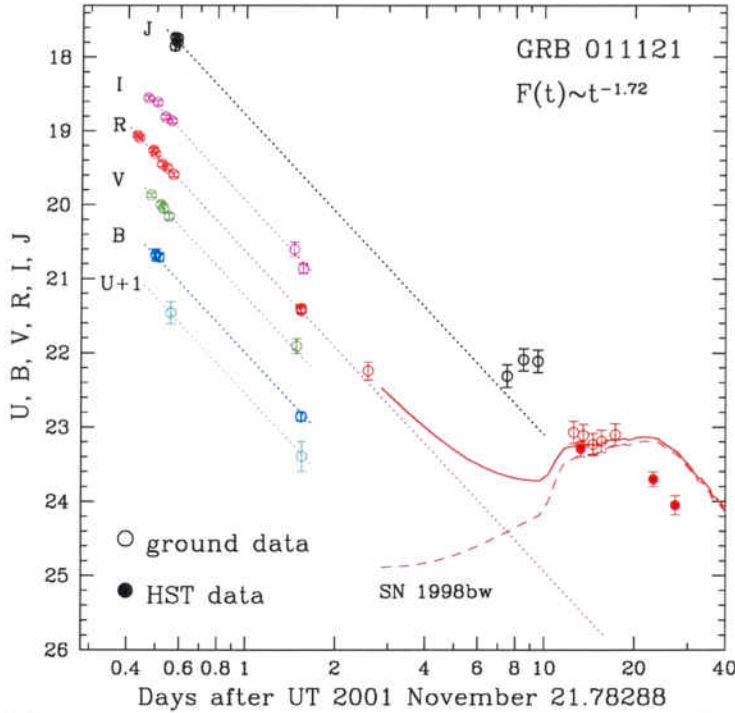


Figure 1.7: Supernova signature in GRB011121. Extracted from Garnavich et al. (2003).

About 50% of well localized GRBs show optical and IR afterglows. The observed optical afterglow is typically around 19-20 magnitude one day after the burst. The signal decays, initially, as a power law in time ($\propto t^{-\alpha}$, with $\alpha \approx 1.2$). Many afterglows show an achromatic break to a steeper decline with $\alpha \approx 2$. This break is commonly interpreted as a jet break that allows the estimate of the jet opening angle (Kulkarni et al., 1999; Harrison et al., 1999).

The optical afterglows typically last of the order of weeks, although the observed optical afterglow of GRB970228 could be seen for more than six months.

In several cases red bumps can happen up to one month after the GRB. These bumps have been usually interpreted as the rising lightcurve of a supernova (Bloom et al., 1999; Garnavich et al., 2003). The most remarkable supernova signature was seen in GRB030329 (Stanek et al., 2003; Hjorth et al., 2003; Gorosabel et al., 2005). This rebrightening of the optical afterglow can be seen for GRB011121 in Figure 1.7, as well as a modelization of the underlying supernova with the lightcurve of SN1998bw.

Radio afterglows are detected in 50% of the well localized GRBs. Radio observations are typically made in the 5 and 8.5 GHz bands, with observed fluxes at the level of 2 mJy . Some sources can be observed on timescales of years.

1.7 Progenitors

Although there have been more than 100 proposed theoretical models as progenitors for GRBs (Nemiroff, 1994), most of them fall into two well-defined classes: collapse of massive stars and merging of compact objects. Other, more peculiar objects involve: cosmic strings (Babul et al., 1987), strange stars (Alcock et al., 1986), quark stars (Dar, 1999), white holes (Narlikar and Apparao, 1975), comets (Harwit and Salpeter, 1973), asteroids (Newman and Cox, 1980), planets (Hanami, 1992), and AGN (Prilutskii and Usov, 1975). Here, we will only focus on the two main model classes.

1.7.1 Collapse of massive stars

Long-duration GRBs appear to be clearly related with the collapse of massive stars, for various observational reasons. First, the supernova signature underlying the afterglows of some GRBs. Second, they happen in star-forming galaxies, and are related to their star-forming regions. Furthermore, the distribution of events within their host galaxies is consistent with that of the collapse of massive stars (Bloom et al., 2002). Finally, the discovery of Fe lines in their X-ray afterglows imply that GRBs are produced in metal-rich environments, such as the one left by a previous supernova explosion.

The most popular model to produce a GRB is known as the collapsar model (Woosley, 1993; MacFadyen and Woosley, 1999). The starting point is a Wolf-Rayet star. It is necessary that the original star has lost his hidrogen envelope for the fireball jet to break through the collapsed star. Starting from stars between 25 to 35 M_{\odot} at the main sequence, they end up as Helium stars between 10 to 15 M_{\odot} , with Fe cores between 1.5 and 2.3 M_{\odot} . When this core collapses, it starts to accrete material from the envelope. If the emission of neutrinos is unable to stop this accretion, the

neutron protostar grows with accretion rates of the order of $0.5 M_{\odot} s^{-1}$, and in a few seconds forms a BH that continues to accrete material. For initial angular momenta of $j \sim 10^{16} - 10^{17} cm^2 s^{-1}$, a few seconds after the collapse there is a BH of $\sim 3 M_{\odot}$ surrounded by an accretion disc of $\sim 0.5 M_{\odot}$. Thermalized neutrinos are radiated from the disc. The energy required for the fireball can be extracted via neutrino annihilation or via the Blandford-Znajek mechanism (Blandford and Znajek, 1977).

Simulations of collapsars cannot produce GRBs with durations less than $\sim 5 s$, so this model is not suitable to describe short GRBs.

The evolution times of massive stars, since their formation to their explosion, are lower than $10 Myr$. With such a fast evolution they explode very near their birth places, so they occur in star-forming regions, that is near the spiral arms, and do not occur in elliptical galaxies. The fast evolution also makes their rate of explosion as a function of the redshift follow very closely the star formation rate (SFR).

1.7.2 Mergings

The first extragalactic models proposed as progenitors of GRBs were NS-NS (Paczynski, 1990) and NS-BH (Narayan et al., 1992; Mochkovitch et al., 1993) mergings. These objects fulfil the requirement of the small size of the source. Also, the binding energy of a NS, $10^{53} erg$, is enough to produce a GRB.

The mass limit for the creation of a BH is exceeded during the merging process of two NS. The final product of the merging will be a BH which, depending on the equation of state, will be of about $2.5 M_{\odot}$. Not all the matter of the two NS goes into the creation of the BH, part of it, which has too much angular momentum as to enter the BH immediately, goes into the creation of an accretion disc of about $0.1 - 0.3 M_{\odot}$. The evolution from this point on depends on the temperature of the accretion disc. For low temperatures, the disc does not emit neutrinos and can survive for as long as $\sim 10 s$. During that time, any relativistic flux can only be produced through a magnetohydrodynamic (Blandford-Znajek mechanism) process, with required magnetic fields of the order of $10^{16} gauss$. In the case of a hot accretion disc, the total accretion time lasts for $\sim 100 ms$, and most of the binding energy of the disc is radiated as neutrinos. Approximately 1% of these neutrinos are anni-

hilated around the rotation axis, producing e^-e^+ pairs and the subsequent fireball. The simulations show accretion rates of about $1 M_\odot s^{-1}$, neutrino luminosities of about $10^{53} erg s^{-1}$, and an energy deposition of $5 \cdot 10^{50} erg s^{-1}$ by neutrino annihilation. In the end, the total energy available is $\approx 5 \cdot 10^{49} erg$, which once collimated reach the observed isotropic energies for GRBs.

The case of the NS-BH merging is very similar to the NS-NS case, but here, the BH is already formed at the beginning. Now, the accretion disc can be up to $0.5 M_\odot$, but with higher accretion rates, resulting in a similar duration GRB.

Simulations show that GRBs coming from compact object mergings cannot last more than $\sim 2 s$, consequently they are only suitable to produce short GRBs.

Before the formation of a compact binary system there has to be two supernova explosions that transfer to the system kick velocities. As a result, these systems have high velocities ($\sim 450 km s^{-1}$ in average, but reaching $\sim 1000 km s^{-1}$), exceeding the escape velocity of the host galaxy in some cases. These velocities, combined with the long lifetime before the merging occurs ($\sim 0.1 - 1 Gyr$), make that the mergings take place at longer distances from the galactic centres than those of the collapsars. Half of the mergings are expected at distances longer than $10 Kpc$ from the galactic centre, and $\sim 25\%$ of them at distances longer than $100 Kpc$. A second consequence of the long lifetime before the merging is that the mean redshift expected for these events is between 20% to 50% lower than that of collapsars (Fryer et al., 1999a).

1.8 This thesis

The thesis is structured in two different parts. The first part aims to the classification of GRBs. After an introduction on the BATSE instrument and its catalogue, the automatic classification algorithms (cluster analysis and neural network) are explained. Next, we proceed to the classification of the GRBs in the last BATSE catalogue. Two classifications are obtained: one with two different classes, like the classical classification presented in this introduction, and another one with three different classes. Arguments in favour of the three-class classification are given, as well as interpretations of the physical differences between these classes of GRB. The GRBs corresponding to each class are tabulated in the appendices A and B, so that

other authors can further investigate their nature.

The second part of the thesis is devoted to the study of extragalactic parameters of GRBs, like the GRB rate and luminosity function. These parameters are obtained by fitting the GRB intensity distribution. First comes an introduction on the intensity distribution and a detailed description of all the parameters involved in its calculation. After building the observed intensity distribution for each class of GRB derived with the neural network, the results of the fits are presented. Next, the intensity distribution of GRBs is used to measure the cosmological parameters Ω_M and Ω_Λ . We conclude this part with a series of simulations that show the potential of the method when using a sample of GRBs one order of magnitude larger than the present one.

The thesis is finally wrapped with the main conclusions.

Part I

Classification of gamma-ray bursts

Chapter 2

The GRB catalogue

BATSE has been the most important instrument dedicated to GRBs. It multiplied by ten the sample of observed GRBs, providing the scientific community with a statistically significant amount of data. The BATSE catalogue is still today the largest and most homogeneous sample of GRBs ever collected. Most of the actual knowledge about lightcurves, spectra, duration and spatial distributions comes from the analysis of the BATSE catalogues. This chapter introduces the BATSE instrument and its catalogues, which are the basis of the studies presented in this thesis.

2.1 The Compton gamma-ray observatory

The BATSE instrument was part of the Compton Gamma-Ray Observatory (CGRO). CGRO is the second of NASA's program named 'Great Observatories', a series of four space-borne observatories designed to conduct astronomical studies over many different wavelengths. These include: the Hubble Space Telescope, the CGRO, the Chandra X-Ray Observatory, and the Spitzer Space Telescope. The Observatory was named in honor of Dr. Arthur Holly Compton, who won the Nobel prize in physics in 1927 for his work on scattering of high-energy photons by electrons. This process is central to the gamma-ray detection techniques of all four instruments on board the observatory.

The development of such a complex mission took about 14 years. Figure

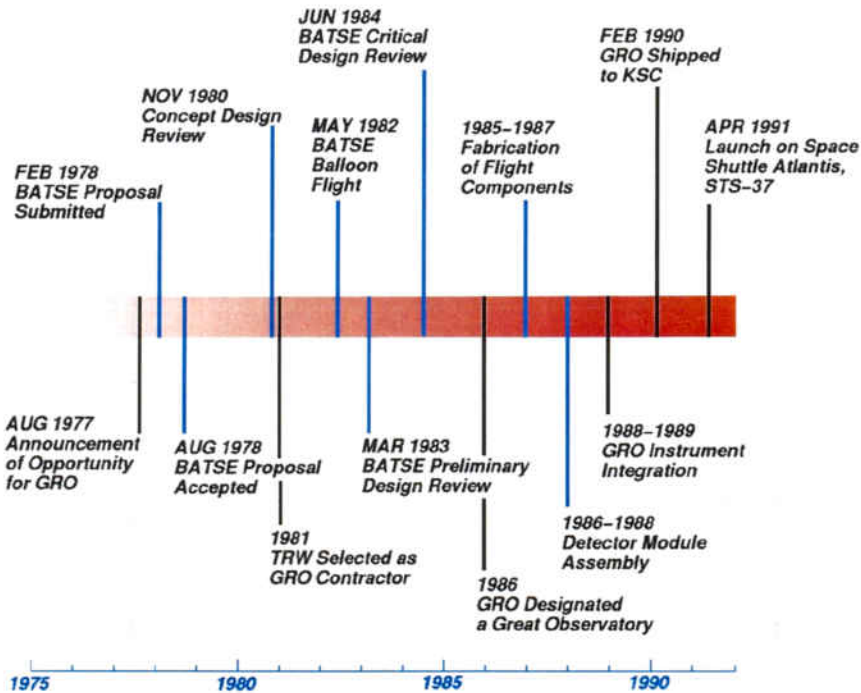


Figure 2.1: Timeline for CGRO. The development of the observatory took 14 years from its design to its launch.

2.1 shows the timeline following the design of CGRO, and particularly BATSE, that started back in 1977. CGRO was launched on April 5, 1991 aboard the space shuttle Atlantis. The orbit of the observatory had a period of about 90 minutes, with an inclination of 28° , and a mean altitude of 470 km . The friction with the atmosphere made the observatory orbit to decay down to 350 km , and it was necessary to thrust it a couple of times to recover altitude. Weighting 17 tons it was the heaviest astrophysical payload ever flown at the time of its launch. After a long and successful mission, CGRO was safely deorbited and re-entered the Earth's atmosphere on June 4, 2000, after 9 years of continuing operation.

Figure 2.2 shows a blueprint of the observatory. It was composed by four instruments covering an unprecedented six decades of the electromagnetic spectrum, from 30 keV to 30 GeV . In order of increasing spectral energy coverage, these instruments were: the Burst And Transient Source Experiment (BATSE), the Oriented Scintillation Spectrometer Experiment (OSSE), the Imaging Compton Telescope (COMPTEL), and the Energetic Gamma Ray Experiment Telescope (EGRET).

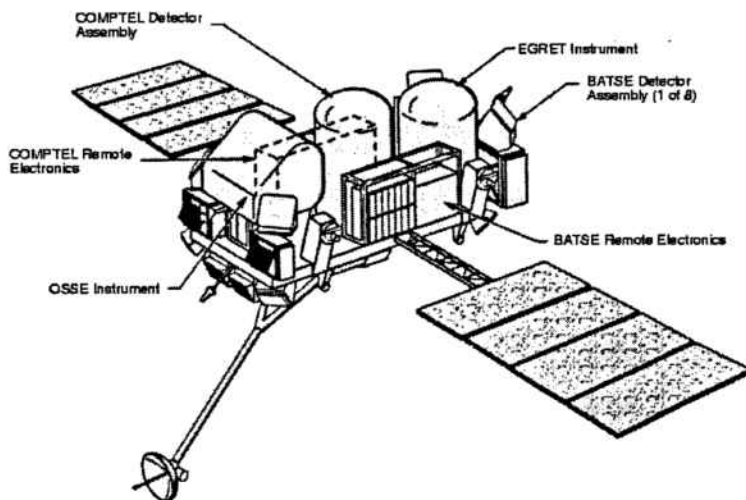


Figure 2.2: Compton Gamma Ray Observatory schematics. It shows the four main instruments: BATSE, OSSE, COMPTEL and EGRET.

For each of the instruments, an improvement in sensitivity of better than a factor of ten was achieved over previous missions. Here it follows a short description of each instrument, and a detailed description of the instrument BATSE.

2.1.1 OSSE

The Oriented Scintillation Spectrometer Experiment (OSSE) consisted of four *NaI* scintillation detectors, sensitive to energies from 50 keV to 10 MeV. Each of these detectors could be individually pointed. This allowed observations of a gamma-ray source to be alternated with observations of nearby background regions, for an accurate subtraction of background contamination.

The OSSE instrument produced observations of the energy spectrum of nuclear lines in solar flares, the radioactive decay of nuclei in supernova remnants, and the signature of matter-antimatter (electron-positron) annihilation in the Galactic Centre region.

2.1.2 COMPTEL

The Imaging Compton Telescope (COMPTEL) used the Compton effect and two layers of gamma-ray detectors to reconstruct an image of a gamma-ray source in the energy range 1 to 30 *MeV*.

COMPTEL's upper layer of detectors were filled with a liquid scintillator which scattered an incoming gamma-ray photon according to the Compton effect. This photon was then absorbed by *NaI* crystals in the lower detectors. The instrument recorded the time, location, and energy of the events in each layer of detectors which made it possible to determine the direction and energy of the original gamma-ray photon and reconstruct an image and energy spectrum of the source.

Gamma rays from active galaxies, radioactive supernovae remnants, and diffuse gamma rays from giant molecular clouds have been studied with this instrument.

2.1.3 EGRET

The Energetic Gamma Ray Experiment Telescope (EGRET) provided the highest energy gamma-ray window for the CGRO. Its energy range was from 20 *MeV* to 30 *GeV*. EGRET was 10 to 20 times larger and more sensitive than previous detectors operating at these high energies.

The EGRET instrument produced images at these energies using high-voltage gas-filled spark chambers. High energy gamma-rays entered the chambers and produced an electron-positron pair of particles which caused sparks. The path of the particles was recorded allowing the determination of the direction of the original gamma-ray. The particle energies were recorded by a *NaI* crystal beneath the spark chambers providing a measure of the original gamma-ray energy.

EGRET made detailed observations of high-energy processes associated with diffuse gamma-ray emission, GRBs, cosmic rays, pulsars, and active galaxies known as blazars.

2.1.4 BATSE

The primary objective of BATSE was the detection, location and study of GRBs. The rate of GRBs observed by BATSE was approximately 0.85 per day. Correcting for Earth blockage, experiment dead-time due to false triggers and for operational reasons (primarily SAA¹ passages), the full-sky burst rate at the BATSE sensitivity is estimated to be about 800 bursts per year.

Aside from GRBs, BATSE triggered on more than 700 solar flares and detected more than 2000². The main criterion for generating the solar flare trigger signal was that the relative count rates be consistent within limits for a burst coming from the direction of the sun. Pulsar analysis was also a secondary BATSE science objective. Time series of pulsed light curves were correlated with pulse shape templates to determine pulse times of arrival. These were used in studies of binary orbits and pulsar rotational dynamics and to create a pulsar source catalogue³. BATSE also monitored known hard X-ray sources, steady or transient. Among them there were the Crab, Cyg X-1, Sco X-1, Geminga, and others.

BATSE consisted of eight identical uncollimated detector modules (Figure 2.3) disposed parallel to the eight faces of a regular octahedron, each one situated on one corner of CGRO. This layout allowed to observe the whole sky simultaneously, although Earth blockage reduced the field of view to approximately $2.6\pi sr$. Each detector module contained two *NaI* scintillation detectors: a Large Area Detector (LAD) optimized for sensitivity and directional response, and a Spectroscopy Detector (SD) optimized for energy coverage and energy resolution.

The LAD detector was a disk of *NaI* scintillation crystal with 2025 cm^2 of area and 1.27 cm thick, mounted on a 1.9 cm layer of quartz. The large diameter-to-thickness ratio of the scintillation crystal produced a detector response similar to that of a *cosine* function at low energies where the crystal was opaque to incident radiation. At energies above 300 keV , the angular response was flatter than a *cosine*. A light collector housing on each detector brought the scintillation light

¹The South Atlantic Anomaly is a dip in the shielding effect of the magnetosphere.

²Interactive access to BATSE solar flare data available at

http://umbra.nascom.nasa.gov/batse/batse_years.html.

³Available for public access at <http://gamma-ray.msfc.nasa.gov/batse/pulsar>.

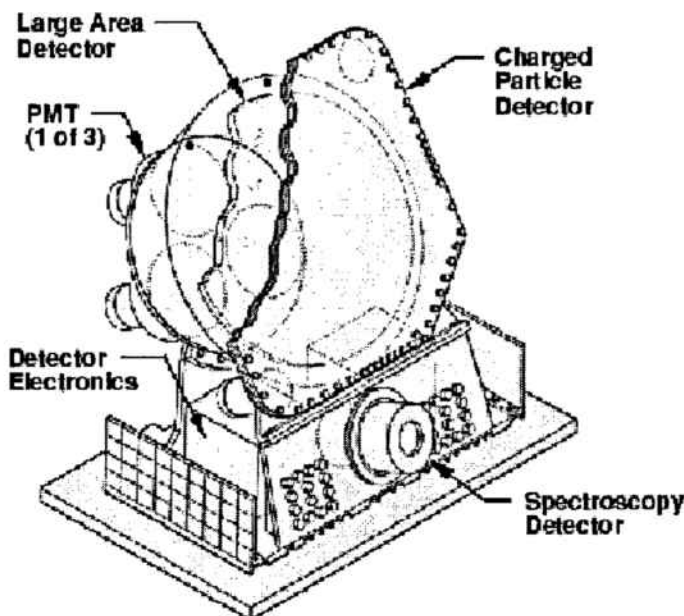


Figure 2.3: One of the eight BATSE modules arranged in the corners of CGRO. It is composed of two detectors: the LAD optimized for sensitivity and directional response, and the SD optimized for energy coverage and energy resolution.

into three 12.7 cm diameter photomultiplier tubes. The signals from the three tubes were summed at the detector. A 0.64 cm plastic scintillation detector in front of the LAD was used as an anticoincidence shield to reduce the background due to charged particles. A thin lead and tin shield inside the light collector housing reduced the amount of background and scattered radiation entering the back side.

The SD was an uncollimated $NaI(Tl)$ scintillation detector 12.7 cm in diameter and 7.62 cm thick. A single 12.7 cm photomultiplier tube was directly coupled to the scintillation detector window. The housing of the photomultiplier tube had a passive lead and tin shield similar to that of the LADs. The crystal housing had a 7.62 cm diameter 50 mm thickness beryllium window on its front face in order to provide high efficiency down to 10 keV.

The LADs were able to measure spectra with 128 channels of resolution, while the SD had 256 channels. There were also four broad band discriminator channels: channel #1 20 – 50 keV, channel #2 50 – 100 keV, channel #3 100 – 300 keV, channel #4 300 – 2000 keV. BATSE's sensitivity covers the range from 20 keV to 2 MeV.

BATSE detected GRBs on-board by examining the count rates of each of the eight LADs for statistically significant increases of photon counts, in channel #2 + channel #3, above background on each of three integration time scales: 64 ms, 256 ms, and 1024 ms. The required increase threshold over the background was set at 5.5σ . The background rate was determined for each detector over a time interval set at 17.4 s. At least two detectors should exceed threshold for a burst trigger to occur. An additional requirement for burst triggering was that the detector with the greatest increase in count rate had to have an increase in the charged particle rate that was less than a specified fraction of the increase in the neutral rate. This was done in order to avoid triggering on charged-particle event encounters, such as those produced by spacecraft containing nuclear reactor power sources.

When a GRB was detected, the Central Electronics Unit entered a fast data acquisition mode and rapidly stored a variety of data types into memory. Over a period of about 45 minutes for weak bursts and 105 minutes for strong bursts the normally scheduled output of pulsar and high resolution spectra was suspended. While the burst memories were being telemetered, the trigger thresholds were temporarily revised to values corresponding to the maximum rates detected during the burst. Thus, a stronger burst would terminate the readout of a weaker burst and overwrite the burst memories.

Whenever a burst trigger occurred, BATSE provided the other Compton instruments a signal that might be used to initiate special burst data processing modes. BATSE also provided a signal to the other Compton instruments if a triggered burst appeared to be a solar flare. This signal could be used by COMPTEL to enter the neutron detection mode and by OSSE to point to the sun or enter a more appropriate observation mode.

BATSE's sky exposure, the fraction of time that a burst is detectable for a specified declination, was not homogeneous. Figure 2.4 shows that the equator is less exposed, due to the Earth blockage, and also the southern hemisphere is less exposed, due to disabling the instrument while in the SAA.

The main weakness of BATSE was the pointing accuracy. LOCBURST, the localization algorithm on board BATSE, pointed GRBs with a mean uncertainty of 4° . However, this error could be as large as 13° for GRBs detected just over

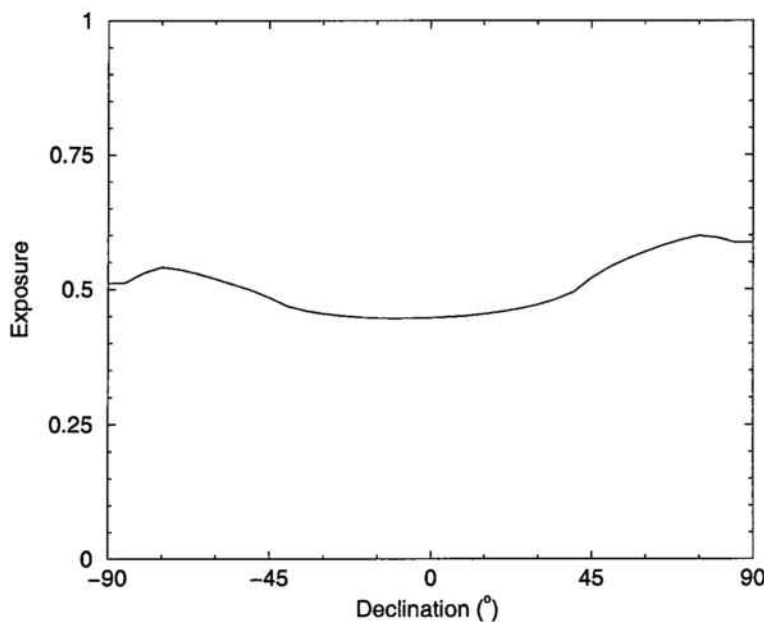


Figure 2.4: BATSE sky exposure as a function of declination. It shows the decrease in sensitivity near the equator due to Earth blockage, and the decrease in sensitivity in the southern hemisphere due to disabling the instrument while in the SAA.

the triggering threshold. Within such a big error box it was very hard to find any optical counterpart for GRBs. In spite of this difficulty, a system to locate this possible optical counterpart was created under the name BACODINE (BATSE COordinates DIstribution NEtwork). BACODINE was able to transmit a GRB position in near real time, with a maximum precision of 4° , to a network of optical and radio observatories. The system did not succeed, but it was the precursor of the GCN (GRB Coordinates Network), which has detected over a hundred radio, optical, and X-ray counterparts of GRBs, thanks to satellites such as BeppoSAX, HETE2, INTEGRAL, and SWIFT.

2.2 BATSE catalogue

The data gathered by BATSE in its 9 years of lifetime is classified in a series of 5 catalogues named 1B, 2B, 3B, 4B, and the yet unpublished 5B catalogue to which we will refer here as the current catalogue. The analysis from these data has been published by the BATSE team in a series of papers (Fishman et al., 1994; Meegan

Catalog Name	End Trigger	Number of Triggers	End Date
1B	1466	263	920306
2B	2230	586	930309
3B	3174	1122	940920
4B	5586	1637	960829
Current	8121	2702	000909

Table 2.1: Summary of the GRBs included in each BATSE catalogue. End Date is in format YYMMDD.

et al., 1996; Paciesas et al., 1999). Table 2.1 is a summary of the GRBs covered in each catalogue.

Each BATSE catalogue is divided into subcatalogues containing different kind of data. Next, we will review each one of these subcatalogues.

2.2.1 The Basic catalogue

The Basic catalogue contains all the information regarding the position of a detected GRB. There are twelve columns in the Basic Table file:

- Column 1. The BATSE trigger number.
- Column 2. The BATSE Catalogue burst name.
- Column 3. The truncated Julian Date (TJD) of the trigger: $TJD = JD - 2440000.5$.
- Column 4. The time in seconds of day (UT) of the trigger.
- Column 5. Right ascension (J2000) in decimal degrees.
- Column 6. Declination (J2000) in decimal degrees.
- Column 7. Galactic longitude in decimal degrees.
- Column 8. Galactic latitude in decimal degrees.
- Column 9. Radius in decimal degrees of positional error box.
- Column 10. Angle in decimal degrees of geocenter (the angle between the burst and the nadir, as measured from the satellite).
- Column 11. Overwrite flag: Y(true) if this burst overwrote an earlier, weaker trigger. N(false) otherwise.

Column 12. Overwritten flag: Y(true) if this burst was overwritten by a later, more intense trigger. N(false) otherwise .

As an example, the first five GRB triggers are shown:

105	4B 910421	8367	33243.7557	270.68	24.76	50.75	21.19	0.53	123.48	N	N
107	4B 910423	8369	71684.7155	193.47	-8.38	303.97	54.49	11.10	143.48	N	N
108	4B 910424	8370	71006.5715	201.31	-45.41	309.13	17.06	13.78	90.87	N	N
109	4B 910425	8371	2265.7075	91.29	-22.77	228.99	-19.94	1.02	88.58	N	N
110	4B 910425B	8371	20253.2915	335.94	25.77	85.83	-26.27	4.79	81.93	N	N

The BATSE trigger number correlates the data in all of the subcatalogues. Observe that the trigger number is not a correlative complete series, that is because it is a running sequence of BATSE triggers which include cosmic bursts, solar flares and other events.

From the data in this catalogue it has been calculated the high degree of isotropy of the spatial distribution of GRBs (see section 1.4.1).

2.2.2 The Flux and Fluence catalogue

This subcatalogue contains the fluences and peak fluxes. The fluence is the energy per unit area received during all the duration of the burst. It is measured separately for each of the BATSE discriminator energy channels #1 to #4. It has units of erg cm^{-2} . The peak flux is the maximum photon flux received in the energy range covered by channels (#2 – #3). Its units are $\text{photon cm}^{-2}\text{s}^{-1}$. The photon flux is measured during time intervals corresponding to each of the three integration timescales. The peak flux is the photon flux corresponding to the time interval, amongst all fluxes measured during the duration of the burst, with greatest flux. Since typical variations of the photon flux occur on timescales lower than 64 ms, the maximum peak flux is always measured for the lower integration timescale.

Due to data gaps during the events, the peak flux and the fluence have not been measured for all GRBs included in the Basic catalogue, but only for 2135 of them.

The format of the Flux/Fluence Table is as follows:

- First row
 - ▷ Column 1. BATSE trigger number.
 - ▷ Column 2. Fluence for channel #1.
 - ▷ Column 3. Error in the fluence for channel #1.
 - ▷ Column 4. Fluence for channel 2.
 - ▷ Column 5. Error in the fluence for channel #2.
- Second row
 - ▷ Column 1. Fluence for channel #3.
 - ▷ Column 2. Error in the fluence for channel #3.
 - ▷ Column 3. Fluence for channel #4.
 - ▷ Column 4. Error in the fluence for channel #4.
- Third row
 - ▷ Column 1. Peak flux on the 64 *ms* timescale.
 - ▷ Column 2. Error in this flux.
 - ▷ Column 3. Time of this flux.
- Fourth row
 - ▷ Column 1. Peak flux on the 256 *ms* timescale.
 - ▷ Column 2. Error in this flux.
 - ▷ Column 3. Time of this flux.
- Fifth row
 - ▷ Column 1. Peak flux on the 1024 *ms* timescale.
 - ▷ Column 2. Error in this flux.
 - ▷ Column 3. Time of this flux.

As an example, we show the data for the first BATSE GRB trigger:

105	$86.850e-08$	$10.887e-09$	$13.209e-07$	$14.368e-09$
	$20.468e-07$	$17.931e-08$	$10.321e-07$	$17.931e-08$
	12.761	0.544	3.840	
	11.857	0.265	3.840	
	9.937	0.123	4.160	

From the fluences and peak fluxes, astronomers were able to measure the inhomogeneity of the distance distribution of GRBs. This fact was key in suggesting an extragalactic origin for GRBs (see section 1.4.2). The fluence gives the energy budget of the phenomena. When the distances to GRBs were unknown, it helped to fix the emitted energy by supposing the phenomena was either galactic or extragalactic. For the GRBs with measured redshift, it gives the emitted energy assuming a cosmology and a beaming angle.

2.2.3 The Duration catalogue

The durations of GRBs are computed with two different quantities, T_{50} and T_{90} . T_{50} is the time interval over which the instrument detects 50% of the counts, this interval starts at the time that 25% of the counts have been detected. T_{90} is the time interval covered between when 5% and 95% of the counts have been detected.

There are seven columns in the Duration Table file:

Column 1. The BATSE trigger number.

Column 2. T_{50} .

Column 3. Uncertainty in T_{50} .

Column 4. The start time of the T_{50} interval, relative to the trigger time. The trigger time can be found in the Basic Table.

Column 5. T_{90} .

Column 6. Uncertainty in T_{90} .

Column 7. The start time of the T_{90} interval, relative to the trigger time. The trigger time can be found in the Basic Table.

Durations are computed for 2041 GRBs. The first 5 BATSE GRB triggers are given here as an example. All times are in seconds.

105	1.792	0.202	2.304	5.184	0.181	0.512
107	68.608	3.238	-168.960	208.576	1.118	-208.896
108	1.280	1.574	-0.960	3.136	0.590	-1.536
109	47.104	0.143	14.912	90.176	0.286	4.224
110	306.368	3.304	-196.096	430.016	1.094	-259.584

Once a good sample of durations of GRBs was measured by BATSE, scientists discovered the bimodality of the duration distribution and the existence of two different classes of GRBs, the short and the long-duration GRBs (see section 1.3).

2.2.4 The CMAX/CMIN catalogue

The BATSE on-board software tests for bursts by comparing the count rates on the eight LADs to threshold levels for three separate time intervals: 64 ms , 256 ms , and 1024 ms . The threshold level, the minimum count rate to consider a positive detection, is set above 5.5σ of the background count rate. A burst trigger occurs if the count rate is above threshold in two or more detectors simultaneously. Since we require that rates be above the thresholds of at least two detectors, the trigger threshold is determined by the threshold of the second most brightly illuminated detector. This catalogue specifies the peak count rate in units of the threshold count rate, and the threshold count rate, on each of the three integration timescales. The name of the catalogue, CMAX/CMIN, states for the fact that it gives the maximum count rate, that is the peak flux, divided by the minimum detectable count rate at the time of detection, that is the minimum peak flux that would trigger a detection.

The format of the file is as follows:

- Column 1. Specifies the BATSE trigger number, which is a key for all of the BATSE Burst Catalog tables.
- Column 2. Maximum counts in the second most brightly illuminated detector divided by the threshold count rate on the 64 ms timescale.
- Column 3. Trigger threshold on the 64 ms timescale. It is the number of counts in 64 ms required to trigger the second most brightly illuminated detector for this particular burst.

- Column 4. Maximum counts in the second most brightly illuminated detector divided by the threshold count rate on the 256 *ms* timescale.
- Column 5. Trigger threshold on the 256 *ms* timescale. It is the number of counts in 256 *ms* required to trigger the second most brightly illuminated detector for this particular burst.
- Column 6. Maximum counts in the second most brightly illuminated detector divided by the threshold count rate on the 1024 *ms* timescale.
- Column 7. Trigger threshold on the 1024 *ms* timescale. It is the number of counts in 1024 *ms* required to trigger the second most brightly illuminated detector for this particular burst.

This catalog contains data on 1318 GRBs, from where the first five detections are shown next:

105	11.929	71	22.213	143	34.143	286
107	-999.000	66	-999.000	132	1.121	264
108	1.033	60	-999.000	121	0.678	242
109	3.987	71	7.447	134	13.122	286
110	0.608	66	1.074	132	1.606	264

The fields filled with -999.000 correspond to non-existent data due to GRBs non-triggered on the given integration timescale.

The quantities in this catalogue are useful to compute the value of $\langle V/V_{max} \rangle$, a parameter that gives a measure of the inhomogeneity of the sample.

Given a GRB with peak flux C_p , it will be detected if $C_p > C_{th}$, being C_{th} the threshold count rate. In a way, C_{th} gives a measure of the maximum distance at which the GRB with peak flux C_p would be detectable. That is, if the GRB occurs at a distance r , the maximum distance r_{max} at which the GRB would be detectable is given by:

$$r_{max}^2 C_{th} = r^2 C_p \quad (2.1)$$

Rearranging equation 2.1 one obtains:

$$\frac{r_{max}}{r} = \left(\frac{C_p}{C_{th}} \right)^{1/2} \quad (2.2)$$

Given that the volume is proportional to r^3 :

$$\frac{V}{V_{max}} = \left(\frac{C_p}{C_{th}} \right)^{-3/2} \quad (2.3)$$

Being C_p/C_{th} precisely tabulated, for each integration timescale, in the even numbered columns of the CMAX/CMIN catalogue.

Why is the mean of V/V_{max} in a sample of GRBs useful?

V is the volume within which a given GRB has been detected. V_{max} is the maximum volume within which the given GRB could have been detected. If the distance distribution of GRBs is homogeneous then one expects $\langle V/V_{max} \rangle \sim 0.5$ in an euclidean space. A homogeneous distance distribution means that GRBs happen with equal probability at all distances. If so, for each detected GRB, although having different V_{max} , the detected V should be uniformly distributed from 0 to V_{max} , thus having a mean of V/V_{max} equal to 0.5. When one computes $\langle V/V_{max} \rangle$ for the BATSE sample it is found that $\langle V/V_{max} \rangle < 0.5$, meaning that GRBs are inhomogeneously distributed in distance. The inhomogeneity of the GRB distance distribution, together with the isotropy, was interpreted as the manifestation of their extragalactic nature.

Chapter 3

Automatic classification algorithms

The knowledge about GRBs extracted from the BATSE catalogue has mostly been based on the study of individual, or at most paired, variables provided by the catalogue itself. However, a deeper knowledge can be extracted from the BATSE catalogue by means of multivariate data analysis, which can handle all of the variables related to the system at once. Some of the methods used for multivariate data analysis are described thoroughly, with applications to astronomy, in Murtagh & Heck (1987).

The principal component analysis (PCA) is useful to derive the variables that best describe the system. By detecting correlations among the original variables, it is also useful to reduce the dimensionality of the problem, eliminating the variables which contribute with less information. PCA was first applied to GRBs by Bagoly et al. (1998) to a sample of 625 GRBs from the BATSE 3B catalogue. Here the sample of GRBs analysed is of 1599 GRBs.

GRBs were classified in two classes (short/hard and long/soft) by Kouveliotou et al. (1993). It is the purpose of this thesis to redefine that classification and suggest a new one. For that, we will be using two automatic classification algorithms: cluster analysis and neural networks.

The term cluster analysis refers to a series of algorithms used to automatically

detect inherent or natural groupings in data. Cluster analysis was first applied to classify GRBs by Mukherjee et al. (1998). For this task they used a sample of 797 GRBs from the BATSE 3B catalogue. Here, cluster analysis will be applied to a sample of 1599 GRBs extracted from the current BATSE catalogue.

Neural networks use artificial intelligence algorithms to objectively classify data. They have been widely used in astronomy; there are more than 400 entries at NASA's ADS¹ with the words 'neural network' in the title. Ball et al. (2004), for instance, used a neural network to morphologically classify galaxies in the Sloan Digital Sky Survey. Neural networks were first used to classify GRBs by Balastegui et al. (2001), in a paper central to the present thesis. Neural networks offer advantage over cluster analysis because they can detect nonlinear relationships between the variables, while cluster analysis deals only with linear relationships.

Let us proceed to describe in detail the mathematical methods that will be used in the next chapter to classify GRBs.

3.1 Principal component analysis

PCA is a statistical method used in multivariate data analysis to obtain new variables, expressed as linear combinations of the original ones, which carry most of the information on the system. Thanks to the correlations between the original variables we can neglect some of the new variables, because they carry very little information. It is a way of identifying patterns in data, and expressing the data in such a way as to highlight their similarities and differences. Since patterns can be hard to find in data of high dimension, where the luxury of graphical representation is not available, PCA is a powerful tool for analysing data in multidimensions. The other main advantage of PCA is that once these patterns have been found, one can compress the data, by reducing the number of dimensions, without much loss of information.

PCA involves a mathematical procedure which rotates the data such that maximum variabilities are projected onto the axes. More formally, it is a linear

¹http://cdsads.u-strasbg.fr/abstract_service.html

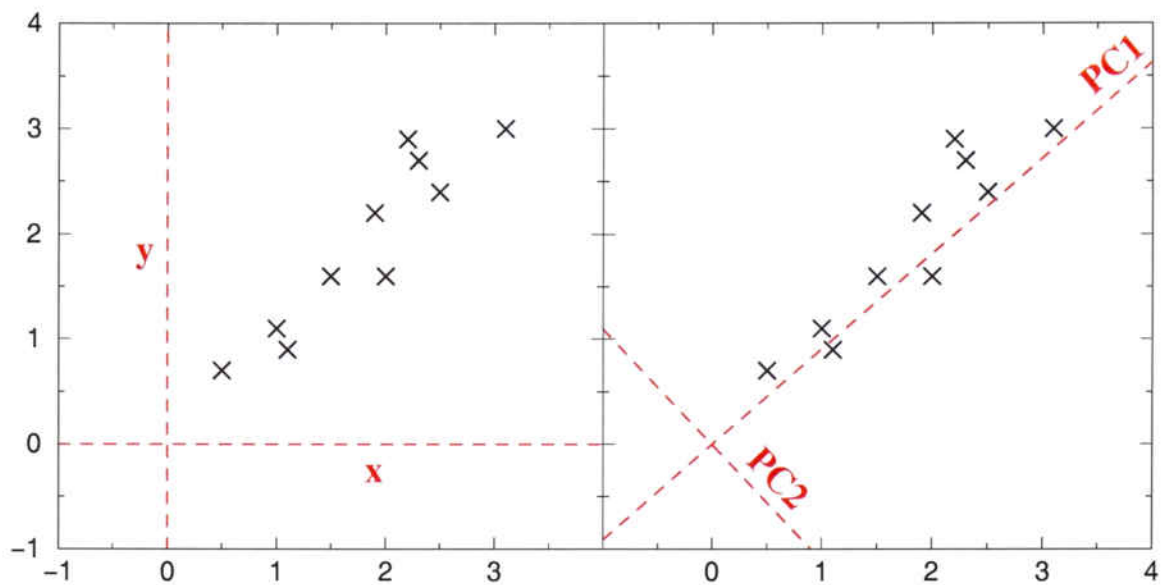


Figure 3.1: Example of application of PCA. On the left plot there is the original data described in terms of the $x - y$ axes. On the right plot, the axes have been rotated so that the data have most of their variance along the axis PC1. If the variance along higher order principal components is negligible, one can describe the data with the desired precision but with less variables.

transformation that chooses a new coordinate system for the data set such that the greatest variance by any projection of the data set comes to lie on the first axis (then called the first principal component), the second greatest variance on the second axis, and so on. Finally, one ends up with a series of axes (equivalently new variables) ordered with decreasing variance. Here, variance is equivalent to information. If the variance around one axis is low, it means that this axis carries no information, since the values of each data point do not much differ. In consequence, one can eliminate the corresponding variable without loosing much information. Figure 3.1 shows an example in two dimensions. In this example, after performing the PCA, the principal component (PC1) could be enough to describe the data. The second component (PC2) only contributes to second order information.

Among the objectives of PCA are:

- Dimensionality reduction.
- Determination of linear combinations of variables.

- The choice of the most useful variables.
- Visualization of multidimensional data.
- Identification of underlying variables.
- Identification of groups of objects or of outliers.

The mathematical description of the PCA is as follows. Consider a set of n objects measured on each of m variables. Let X be the matrix $n \times m$ composed by the n vectors of dimension m describing the data. Let u be a unit vector ($u^T u = 1$). The product Xu gives the projections of the n objects onto the axis u . The variance along u , that is the squared projections of the data points on the axis u , is given by:

$$\sigma_u^2 = (Xu)^T (Xu) = u^T Su \quad (3.1)$$

Where $S = X^T X$. We seek to maximize $u^T Su$, given the constrain $u^T u = 1$. This is achieved by differentiating

$$u^T Su - \lambda(u^T u - 1) \quad (3.2)$$

Where λ is a Lagrange multiplier. Setting the derivative equal to zero one obtains:

$$2Su - 2\lambda u = 0 \quad (3.3)$$

Finally, the optimal value of u is the solution of:

$$Su = \lambda u \quad (3.4)$$

The solution of this equation is well known: u is the eigenvector associated with the eigenvalue λ of the matrix S . Ordering the eigenvectors u_i in decreasing order of eigenvalues λ_i , one obtains the principal components. Therefore, the first principal component is u_1 , and the corresponding largest eigenvalue λ_1 indicates

the amount of variance explained by the axis u_1 . All the principal components are orthogonal unit vectors.

The PCA will be applied in the next chapter to the current BATSE sample of GRBs to investigate the relevant variables in the catalogue and the correlations between them.

3.2 Cluster analysis

A general question facing researchers in many areas is how to organize observed data into meaningful structures, that is, to develop taxonomies. The term cluster analysis encompasses a number of different algorithms and methods for grouping objects of similar kind into respective categories. In other words, cluster analysis is an exploratory data analysis tool which aims at sorting different objects into groups in such a way that the degree of association between two objects is maximal if they belong to the same group and minimal otherwise. The objects to be classified need to have numerical measurements on a set of variables or attributes. Given the above, cluster analysis can be used to discover structures in data without providing any explanation nor interpretation. Cluster analysis simply discovers structures in data without explaining why they do exist.

Cluster analysis may be divisive or agglomerative, depending on whether groups are built by summing up individuals or by separating them. The divisive methods start from the whole set as one class and build new classes by dividing this class in two classes, three classes, and so on, until finishing with as many classes as objects in the sample. The agglomerative methods are just the opposite. Starting with all the objects separately, it joins them until they end up in just one class consisting in the whole set.

Cluster analysis techniques may also be hierarchical or nonhierarchical. In the hierarchical methods, the resulting classification has an increasing number of nested classes. That is, each new class is built by adding or extracting one object from the previous classification. If one classifies first a sample of objects into three classes, and afterwards into two classes, in the case of a hierarchical method the two-class classification is built by the sum of two of the classes obtained from the

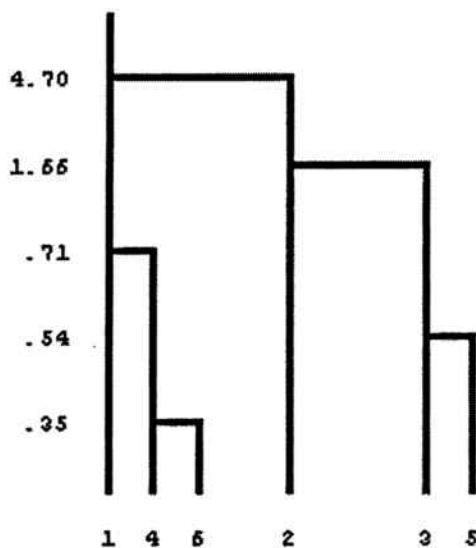


Figure 3.2: An example of a dendrogram showing the last six levels of clustering of an agglomerative hierarchical method. In the vertical axis there is an index of dissimilarity.

three-class classification. In the case of nonhierarchical methods it is not so. In nonhierarchical methods, one must supply the number of clusters into which the data are to be grouped prior to the classification, and one only obtains the final cluster membership for each objects not the history of fusions or fissions.

A hierarchical classification can be represented by a dendrogram. The dendrogram shows the history of fusions or fissions for each cluster. Figure 3.2 shows an example of a dendrogram. This dendrogram represents the last six levels of clustering of an agglomerative hierarchical method. Each group has a numerical label, which is shown in the horizontal axis. In the vertical axis there is an index of dissimilarity. The actual measure of dissimilarity will depend upon the method used; it is usually a simple euclidean distance, averaged and weighted for all the members of a cluster. Note that the clusters are joined at increasing levels of dissimilarity. Group 6 joins group 4 when going from a 6-class classification to a 5-class classification. The dissimilarity index is then 0.35. Group 5 joins group 3 when going from a 5-class classification to a 4-class classification. The dissimilarity index at this point is 0.54. The clustering goes on until one ends up with one last cluster when group 2 joins group 1. The final dissimilarity index is 4.70. The greatest increase in the dissimilarity index has been in this last clustering step, suggesting that two

well-differentiated groups have been joined. One of the biggest problems with cluster analysis is identifying the optimum number of clusters. As the fusion process continues, increasingly dissimilar clusters must be fused, that is, the classification becomes increasingly artificial. Deciding upon the optimum number of clusters is largely subjective, although looking at a graph of the level of dissimilarity at fusion versus number of clusters may help. There will be sudden jumps in the level of dissimilarity as dissimilar groups are fused. Note that in the dendrogram in Figure 3.2, there is a first steep increase of dissimilarity when going from three to two classes. It would be difficult to decide whether a two-class or a three-class classification would be optimal. This decision has to be taken by a supervising human after a thorough study of the properties of each group.

There exist several clustering algorithms with different rules governing between which points distances are measured to determine cluster membership. The criteria used may differ and hence different classifications may be obtained for the same data. This is important since it tells us that although cluster analysis may provide an objective method for the clustering, there can be subjectivity in the choice of method. The four primary algorithms are described next:

- **SINGLE LINKAGE CLUSTERING** (Nearest-Neighbour Method): The dissimilarity between two clusters is the minimum dissimilarity between members of the two clusters. This method produces long chains which form loose, messy clusters. It has been widely used in numerical taxonomy.
- **COMPLETE LINKAGE CLUSTERING** (Furthest-Neighbour Method): The dissimilarity between two clusters is equal to the greatest dissimilarity between members of the two clusters. This method tends to produce very tight clusters of similar cases.
- **AVERAGE LINKAGE CLUSTERING**: The dissimilarity between clusters is calculated using cluster average values. There are many ways to calculate the average (mean, median, centroid; weighted or unweighted), so there are different ways of applying this algorithm.
- **WARD'S METHOD**: Cluster membership is assessed by calculating the total sum of squared deviations from the mean of a cluster. The criterion for fusion

is that it should produce the smallest possible increase in the sum of squares of the errors.

The complete process of any generalized hierarchical clustering can be summarized as follows:

1. Calculate the distance between all initial clusters. In most analyses initial clusters will be made up of individual cases.
2. Fuse the two most similar clusters and recalculate the distances.
3. Repeat step 2 until all cases are in one cluster.

A cluster analysis will be applied to the current BATSE sample of GRBs to try and classify them. The Ward's method (Ward, 1963) is used in this thesis. It is a very robust criterion for cluster analysis and the most commonly used. The algorithm searches for clusters with minimum variance among objects belonging to the same cluster and with maximum variance between clusters, using the centre of gravity of each cluster. The dissimilarity index is a weighted distance between the centers of gravity of each cluster. In the end, one obtains clusters as compact and as detached from each other as possible.

3.3 Neural networks

A neural network is an interconnected group of artificial or biological neurons. In modern usage, the term most often refers to artificial neural networks, especially in computer science and related fields. Although there are electrical and mechanical neural networks, we are interested here strictly on computational simulations or models of artificial neural networks.

The first artificial neuron was produced in 1943 by the neurophysiologist Warren McCulloch and the logician Walter Pits. Their networks were based on simple neurons which were considered to be binary devices with fixed thresholds. The results of their model were simple logic functions such as "a or b" and "a and b".

Following an initial period of enthusiasm, the field survived a period of frustration and discredit. During this period, when funding and professional support were minimal, important advances were made by relatively few researchers. Currently, the neural network field enjoys a resurgence of interest and a corresponding increase in funding.

A neural network is an information processing paradigm that is inspired by the way biological nervous systems, such as the brain, process information. The key element of this paradigm is the novel structure of the information processing system. It is composed of a large number of highly interconnected processing elements (neurons) working in unison to solve specific problems.

Much is still unknown about how the brain trains itself to process information, so theories abound. In the human brain, a typical neuron collects signals from others through a host of fine structures called dendrites. The neuron sends out spikes of electrical activity through a long thin strand known as an axon, which splits into thousands of branches. At the end of each branch, a structure called synapse converts the activity from the axon into electrical effects that inhibit or excite activity in the connected neurons. When a neuron receives an excitatory input that is sufficiently large compared with its inhibitory input, it sends a spike of electrical activity down its axon. Learning occurs by changing the effectiveness of the synapses so that the influence of one neuron on another changes. Figure 3.3 shows the schematics of a biological neuron.

A human brain is made of about 10^{11} neurons, each one connected to 10^4 other neurons. In comparison, an artificial neural network is made by up to 10^6 artificial neurons each one connected up to 10^3 other artificial neurons. Although the human brain operations are exceptionally parallel, while today's computers operate primarily sequentially, this does not represent a fundamental distinction, since any computation that can be performed by a parallel computer can be done by a sequential computer.

The artificial neuron is the basic unit of an artificial neural network, simulating a biological neuron. It receives one or more inputs, sums these, and produces an output after passing the sum through a, usually, nonlinear function known as an activation or transfer function. Figure 3.4 shows the schematics of an artificial

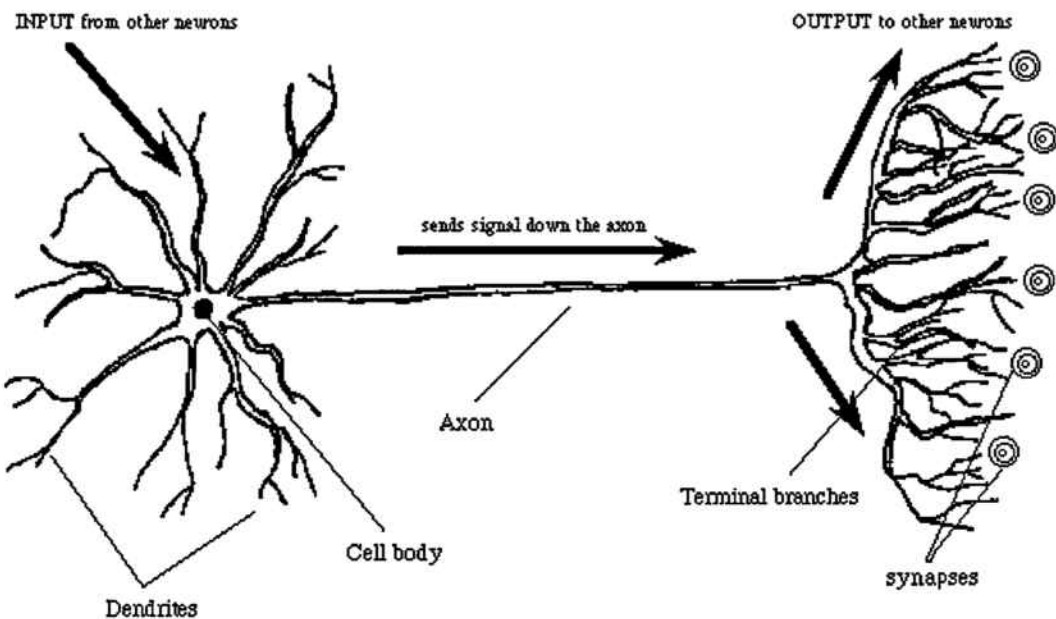


Figure 3.3: A biological neuron schematics. The neuron collects signals from others through the dendrites and sends out spikes of electrical activity through the axon. The synapse sends the signal to other neurons.

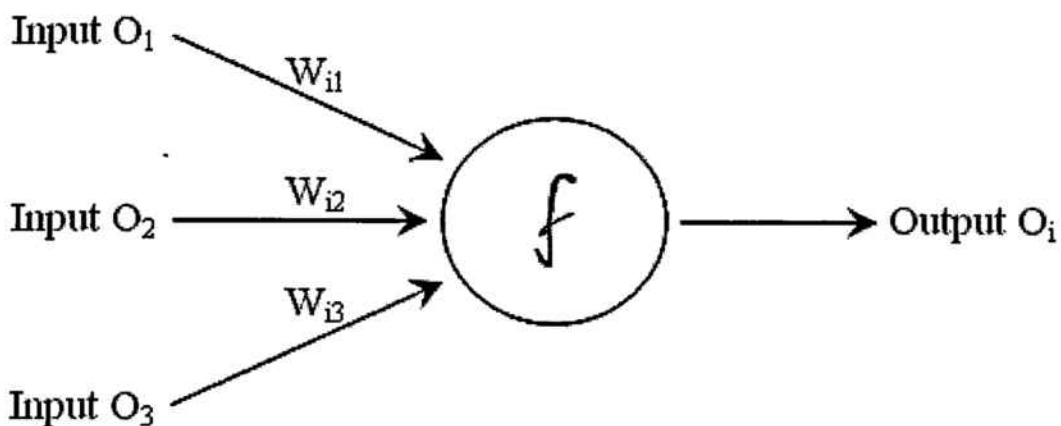


Figure 3.4: An artificial neuron schematics. It receives one or more inputs, sums these, and produces an output after passing the sum through a transfer function.

neuron. For a given artificial neuron labeled i , let there be n inputs with signals O_1 through O_n and weights W_{i1} through W_{in} . The output of the neuron i is:

$$O_i = f\left(\sum_{j=0}^n W_{ij} O_j\right) \quad (3.5)$$

Where f is the activation (or transfer) function. Basically, there exist three different kinds of transfer functions:

- A step function. Where if the input signal is above a certain threshold the output is 1, or the output is 0 otherwise.
- A linear function. Where the output is proportional to the total weighted output.
- A sigmoid function. Where the output is a nonlinear function with an 'S' shape. It is believed that sigmoid transfer functions bear a greater resemblance to real neurons than do linear or step transfer functions.

To summarize the general picture, a neural network is composed of a group or groups of connected neurons. A single neuron can be connected to many other neurons, so that the overall structure of the network can be very complex. The output of each neuron propagates to the next layer (through a weighted synapse) or finally exits the system as part or all of the output.

Neural networks, like people, learn by example. A neural network is configured for a specific application, such as pattern recognition or data classification, through a learning process. Learning in biological systems involves adjustments to the synaptic connections that exist between the neurons. This is true of neural networks as well. The learning process takes place by the modification of the connection weights by the network itself. This process can be supervised or unsupervised, giving rise to two different categories of neural networks. Supervised neural networks incorporate an external teacher, so that each output unit is told what its desired response to input signals ought to be. The most common training algorithm is the backpropagation algorithm. Unsupervised learning uses no external teacher and is based upon only local information. It is also referred to as self-organization, in the sense that it

self-organizes data presented to the network and detects their emergent collective properties. The most used unsupervised algorithm is the Kohonen self-organizing map, based on competitive learning.

Neural networks, with their remarkable ability to derive meaning from complicated or imprecise data, can be used to extract patterns and detect trends that are too complex to be noticed by either humans or other computer techniques. These artificial neural networks are advantageous, especially in pattern recognition and classification tasks. They have found an application in the control of processes in the chemical industry, speech recognition, optical character recognition and adaptive software such as software agents (e.g. in computer and video games) and autonomous robots. The disadvantage is that because the network finds out how to solve the problem by itself, its operation can be unpredictable.

3.3.1 Kohonen self-organizing map

The self-organizing map (SOM) (Kohonen, 1990) is a method for unsupervised learning, based on a grid of artificial neurons whose weights are adapted to match input vectors in a training set. It was first described by the Finnish professor Teuvo Kohonen and is thus sometimes referred to as a Kohonen map.

The SOM algorithm is fed with feature vectors, which can be of any dimension. Output maps can also be made in different dimensions, but most popular are 1D and 2D maps, for SOMs are mainly used for dimensionality reduction rather than expansion.

The algorithm is explained most easily in terms of a set of artificial neurons, each having its own physical location on the output map, which take part in a competitive network where a node with its weight vector closest to the vector of inputs is declared the winner and its weights are adjusted making them closer to the input vector. Each node has a set of neighbours. When this node wins a competition, the neighbours' weights are also changed. The further the neighbour is from the winner, the smaller its weight change. This process is then repeated for each input vector, over and over, for an usually large number of cycles. Different inputs produce different winners.

Mathematically, the algorithm works as follows:

- Assume that the output nodes are connected in an array (usually 1D or 2D).
- Assume that the network is fully connected, so all nodes in the input layer are connected to all nodes in the output layer.
- Use the competitive learning algorithm as follows:
 - ▷ Randomly choose an input vector x .
 - ▷ Determine the winning output node i that fulfills:

$$\|w_i - x\| \leq \|w_k - x\| \quad \forall k \quad (3.6)$$

where w_i is the weight vector connecting the inputs to the output node i .

- ▷ Given the winning node i , the weight is updated by:

$$w_k = w_k + \mu N(i, k)(x - w_k) \quad (3.7)$$

where $N(i, k)$ is called the neighborhood function that has value 1 when $i = k$ and falls off with the distance $\|r_k - r_i\|$ between units i and k in the output array. Thus, units close to the winner, as well as the winner itself, have their weights updated appreciably. Weights associated with far away output nodes do not change significantly. It is here that the topological information is supplied. Nearby units receive similar updates and thus end up responding to nearby input patterns.

Like most artificial neural networks, the SOM has two modes of operation:

1. During the training process a map is built, the neural network organizes itself, using a competitive process. The network must be given a large number of input vectors, as much as possible representing the kind of vectors that are expected during the second phase (if any).

2. During the mapping process a new input vector may quickly be given a location on the map, it is automatically classified or categorized. There will be one single winning neuron: the neuron whose weight vector lies closest to the input vector.

The SOM algorithm will be used in next chapter to classify GRBs.

Chapter 4

Reclassification of gamma-ray bursts

The existence of two different classes of GRBs has been known since 1993 (Kouveliotou et al., 1993). The bimodal distribution of the duration logarithms defined the separation between long ($T_{90} > 2$ s) and short ($T_{90} < 2$ s) GRBs. It was also known that short GRBs have harder spectra than long GRBs. That is the classical separation between short/hard and long/soft GRBs. In 1998 Horváth (1998) made the first step towards a three-class classification of GRBs by fitting the duration distribution with three gaussians. However, these firsts classifications were unable to assign individual bursts to definite classes: they only defined limiting durations, while short and long GRBs durations overlap.

The main objective of this chapter is to obtain automatic classifications of GRBs (Balastegui et al., 2001; Balastegui et al., 2005). We will use here two different methods: a cluster analysis and a neural network. Prior to applying the cluster analysis we will perform a principal component analysis to obtain the variables into which the sample becomes easier to separate. Then we will use these new variables to perform the cluster analysis. After the two classifications have been done, we present a study of the characteristics of each new class of GRB.

4.1 Principal component analysis

PCA was first applied to GRBs by Bagoly et al. (1998) to a sample of 625 GRBs from the BATSE 3B catalogue. Here, PCA is applied to the BATSE current catalogue with a sample of 1599 GRBs, and the results presented resemble those obtained with the BATSE 3B catalogue. The PCA, as well as the cluster analysis, has been performed with the MIDAS¹ statistical package (Warmels, 1991).

The entry parameters for the PCA will be the standardized logarithms of the following nine quantities: four time-integrated fluences $F_{Ch\#1} - F_{Ch\#4}$, respectively corresponding to the $20 - 50 \text{ keV}$, $50 - 100 \text{ keV}$, $100 - 300 \text{ keV}$, and $300 - 2000 \text{ keV}$ spectral channels; three peak fluxes P_{64} , P_{256} , and P_{1024} , measured in 64, 256, and 1024 ms bins, respectively; and two measures of burst duration T_{50} and T_{90} , the times within which 50% and 90% of the flux arrives. The BATSE current catalogue has a sample of 1599 GRBs for which there exists a measure for all nine variables. We use the logarithms because the values of each quantity may span several orders of magnitude. After taking the logarithms we standardize the variables, that is, transform them so that they have zero mean and unit variance. This is done because each quantity has its own scale, which may differ by several orders of magnitude with respect to the others. With the standardized quantities the scale disparity problem is overcome.

Table 4.1 shows the principal components. The first column shows the percentage of the variance carried by each of the new axes, the other columns show the components of each principal axis in the base of the original variables. The first three components account for the 96.2% of the variance. To decide how many variables are important there exists the Jolliffe criterium (Jolliffe, 1986), which states that the minimum percentage of the variance for a variable to be significant is $70/n\%$, n being the total number of variables involved in the PCA. In this case the minimum percentage is $70/9 = 7.8\%$. From Table 4.1 the third principal component, with $\sim 5\%$ of the variance, would not be significant. Nevertheless, a 5% is not a negligible value, and the inclusion of the third principal component should be considered in order to have a better description of the sample. In fact, going from 9 to 3 variables is a good enough reduction of the dimensionality, made possible by the considerable

¹<http://www.eso.org/projects/esomidas/>

%	$\log F_{Ch\#1}$	$\log F_{Ch\#2}$	$\log F_{Ch\#3}$	$\log F_{Ch\#4}$	$\log P_{64}$	$\log P_{256}$	$\log P_{1024}$	$\log T_{50}$	$\log T_{90}$
64.3	-0.39	-0.40	-0.40	-0.33	-0.22	-0.28	-0.36	-0.29	-0.30
27.0	+0.15	+0.12	+0.04	-0.05	-0.53	-0.47	-0.30	+0.44	+0.41
4.9	-0.22	-0.19	+0.06	+0.92	-0.10	-0.13	-0.17	-0.06	-0.08
1.7	+0.48	+0.41	+0.21	+0.03	-0.22	-0.25	-0.13	-0.47	-0.46
0.8	+0.56	-0.05	-0.77	+0.19	+0.16	+0.06	-0.09	-0.01	+0.12
0.6	+0.01	+0.11	+0.19	-0.06	+0.60	-0.03	-0.75	+0.13	-0.00
0.4	-0.02	-0.05	+0.11	-0.02	+0.04	-0.04	-0.07	-0.69	+0.71
0.2	+0.49	-0.78	+0.38	-0.07	-0.04	+0.05	-0.03	+0.04	-0.06
0.1	-0.01	+0.08	+0.01	+0.00	-0.46	+0.78	-0.40	-0.03	+0.01

Table 4.1: Principal Component Analysis for the standardized logarithms of fluences, peak fluxes and durations. There is shown, in each row, the components of each principal axis in the base of our original variables (columns), together with the percentage of the variance carried by each of the new axes (first column). For instance, the first principal component is: $PC1 = -0.39\log F_{Ch\#1} - 0.40\log F_{Ch\#2} - 0.40\log F_{Ch\#3} - 0.33\log F_{Ch\#4} - 0.22\log P_{64} - 0.28\log P_{256} - 0.36\log P_{1024} - 0.29\log T_{50} - 0.30\log T_{90}$.

amount of correlations between the variables.

The first principal component, with 64.3% of the variance, is a linear combination of all the variables, the fluences having more weight, in particular for energy channels from #1 to #3. The second principal component, with 27.0% of the variance, is a linear combination of mainly the peak fluxes and the durations. In this component the fluences have very little weight. The third principal component is mainly the fluence in the energy channel #4. All other principal component carry very little information (3.8% with all of them) and are negligible.

4.2 Cluster analysis classification

The cluster analysis algorithm is applied to the nine new variables obtained with the PCA, because these are the variables into which the problem becomes easier to separate. This result provides the starting point for the cluster analysis, where the Ward's criterion of minimum variance (Ward, 1963) is used. The analysis follows an agglomerative hierarchical clustering procedure, which starts from n points spread

over the 9-dimensional space and groups them until ending up with a single cluster. The algorithm searches for clusters with minimum variance among objects belonging to the same cluster and with maximum variance between clusters, and works with the center of gravity of each cluster. That gives clusters as compact and as detached from each other as possible.

A dendrogram is obtained, that shows the way groups are clustering, as well as the dissimilarity index of the resulting groups. The dissimilarity index is a weighted distance between the centers of gravity of each cluster. This way, detecting a large rise in the dissimilarity when joining two clusters means that two groups with remarkably different characteristics have been merged.

In Figure 4.1 the dendrogram with the last six levels of clustering is shown. It can be seen that the first important increase of the dissimilarity occurs when joining group 3 with group 2, which tells that three groups with somewhat different characteristics have been merged, but the most significant rise in dissimilarity occurs when merging cluster 2 with cluster 1. From that it is concluded that there are two well-separated classes plus an emergent third class.

Figure 4.2 shows what happens when adding, to the nine starting variables, the two extra variables H_{32} and $\langle V/V_{max} \rangle$. In that case the sample is reduced to 757 bursts only (instead of 1599), for which all the eleven quantities are known. It can be seen that the largest increase in the dissimilarity index occurs when merging cluster 3 and 1, so the three-class classification is the most favoured one. The quantity H_{32} , the hardness ratio, is the ratio of the fluences measured in energy channels #2 and #3 ($H_{32} = F_{ch\#3}/F_{ch\#2}$). Remember that the two classical classes, the short/hard and the long/soft GRBs, differ not only in duration but also in hardness. Katz and Canel (1996) also showed that long-duration GRBs have $\langle V/V_{max} \rangle$ significantly lower than short-duration GRBs. Adding these two quantities to the cluster analysis, one should be reinforcing the difference between the two classical classes of GRBs.

As a conclusion, the dendrograms suggest the possibility of a third class of GRBs. The classification is interesting even in the case that there only exist two classes of GRBs, since the algorithm can classify individually each GRB. One can cut the dendrogram at any level, obtaining the correspondent number of classes. In the following, we present the two possible classifications: a two-class and a three-class

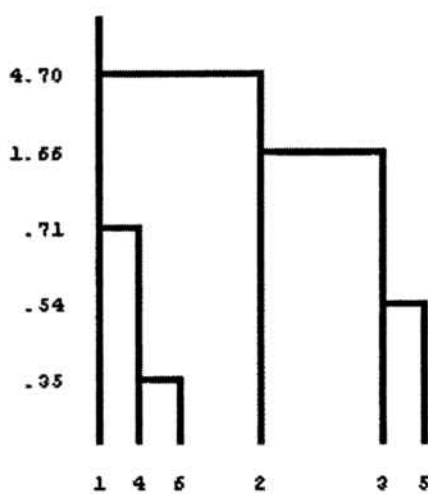


Figure 4.1: Dendrogram of the 9-dimensional analysis. The numbers at the bottom of the diagram are identifiers of the groups, and those at the left are the dissimilarity index. A large increase in the dissimilarity is used to decide the number of classes. The dendrogram suggest two well differentiated classes, with an increase of dissimilarity equal to $4.70 - 1.66 = 3.04$, plus a possible third class, with an increase of dissimilarity equal to $1.66 - 0.71 = 0.95$.

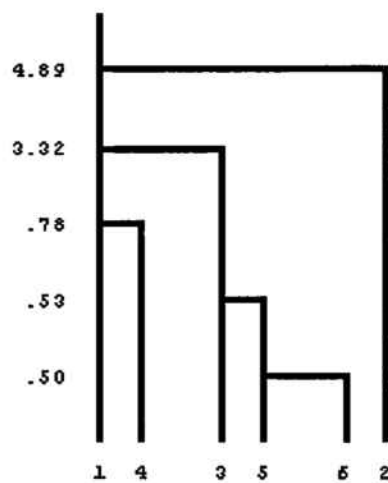


Figure 4.2: Dendrogram of the 11-dimensional analysis. The numbers at the bottom of the diagram are identifiers of the groups, and those at the left are the dissimilarity index. A large increase in the dissimilarity is used to decide the number of classes. In this case the largest increase in the dissimilarity index occurs when merging cluster 3 and 1, thus suggesting a three-class classification.

Class	N	$\langle T_{90} \rangle$	$\langle H_{32} \rangle$	$\langle V/V_{max} \rangle$	$\langle P_{1024} \rangle$	$\langle F_{total} \rangle$
2-I	580	2.65 ± 0.17	5.96 ± 0.20	0.265 ± 0.017	1.29 ± 0.08	1.75 ± 0.13
2-II	1019	59.7 ± 2.1	3.11 ± 0.05	0.184 ± 0.008	3.33 ± 0.20	22.5 ± 1.8
3-I	580	2.65 ± 0.17	5.96 ± 0.20	0.265 ± 0.017	1.29 ± 0.08	1.75 ± 0.13
3-II	570	51.3 ± 2.3	2.85 ± 0.07	0.296 ± 0.012	0.88 ± 0.02	4.58 ± 0.21
3-III	449	70.3 ± 3.8	3.43 ± 0.06	0.051 ± 0.004	6.44 ± 0.41	45.3 ± 3.9

Table 4.2: Characteristics of the classification from the 9-dimensional cluster analysis. T_{90} is in units of s , P_{1024} in $\text{photons cm}^{-2}s^{-1}$, and F_{total} ($F_{total} = F_{Ch\#1} + F_{Ch\#2} + F_{Ch\#3} + F_{Ch\#4}$) in units of $10^{-6}\text{erg cm}^{-2}$.

classification.

In Table 4.2, the main characteristics of each GRB class are shown; 2-I and 2-II corresponding to the two-class classification, and 3-I, 3-II, and 3-III corresponding to the three-class classification. The classes are ordered from short to long durations. The results of the 11-dimensional cluster analysis are not shown here. They are very similar to those of the 9-dimensional one but are less significant because the sample is reduced to one-half. We only comment that since the hardness has been added there, its weight has thus been enforced, and then classes 2-I and 3-I become slightly harder and shorter than when obtained from the 9-dimensional cluster analysis.

With the two-class classification the classical GRB types are recovered: short/hard, which are fainter (taking as brightness the peak flux P_{1024}), and long/soft which are brighter and more non-Euclidean in their space distribution (because they have lower values of $\langle V/V_{max} \rangle$). As seen from Figure 4.3, two classes with an overlapping distribution of durations have been obtained, in contrast with the classical definition of short, $T_{90} < 2 s$, and long, $T_{90} > 2 s$, GRBs. Now, the short class has durations up to $T_{90} \sim 20 s$ while the long-duration class starts at $T_{90} \sim 2 s$. This overlapping of the two classes was obviously supposed to exist, but based on the distribution of durations alone it could not be decided whether, in the overlapping region, a given GRB belonged to either of the two classes. Now, the algorithm handles all the available magnitudes and assigns each GRB to the cluster to whose characteristics it is closer to. The hardness distribution (Figure 4.4) does not differ significantly from that in Kouveliotou et al. (1993).

A first look at the three-class classification reveals that class 3-I is exactly

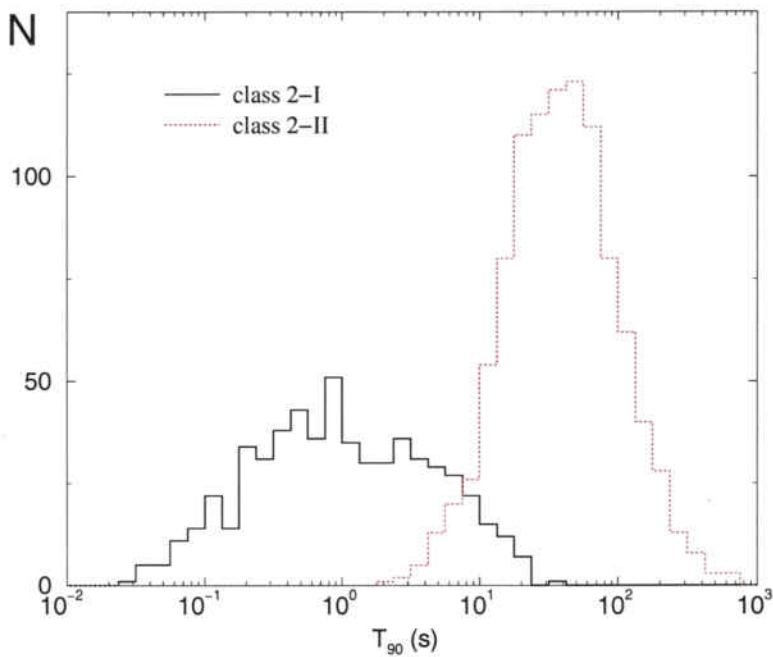


Figure 4.3: Duration distribution of the two-class classification obtained with the cluster analysis. The classical short/long GRB classes are recovered. GRBs can be classified into any class in the overlapping region of the traditional separation in durations ($T_{90} \lesssim 2$ s).

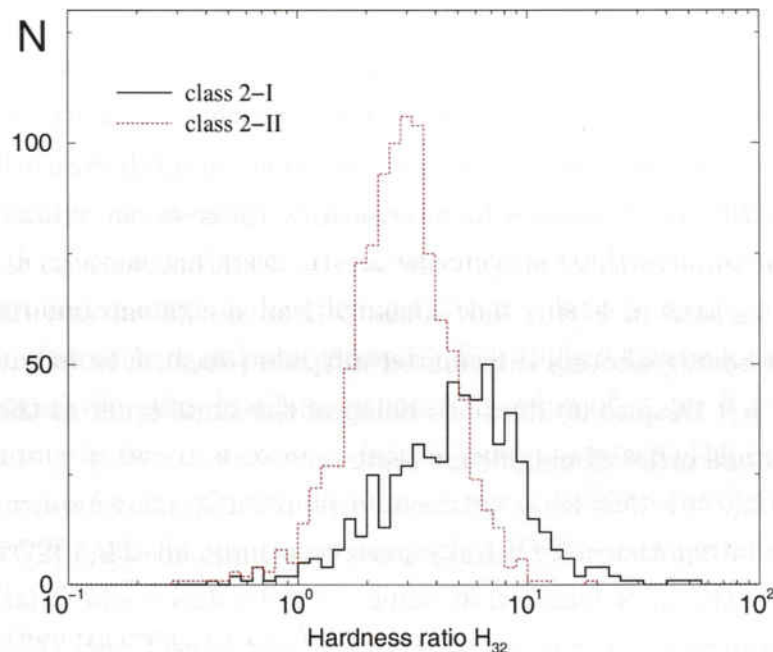


Figure 4.4: Hardness distribution of the two-class classification obtained with the cluster analysis. The traditional classification is recovered: short-duration GRBs (class 2-I) are harder and long-duration GRBs (class 2-II) are softer.

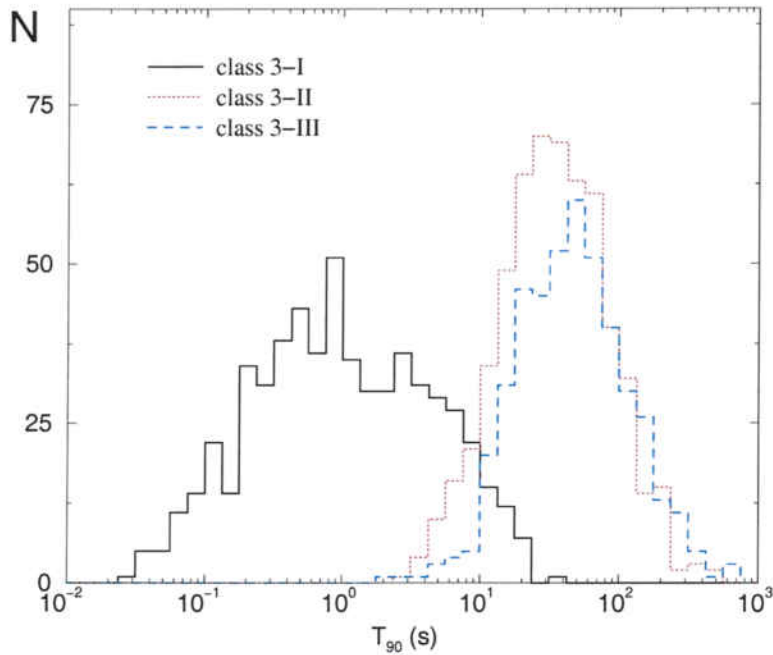


Figure 4.5: Duration distribution of the three-class classification obtained with the cluster analysis. Classical long-duration GRBs (class 2-II) has been splitted into two classes (3-II and 3-III) with similar duration distributions.

the same as in the two-class grouping: this is because the clustering method is agglomerative, which means that new groups are formed by merging former ones, so the passage from three to two classes happens when merging class 3-II and class 3-III GRBs. Class 3-II is not properly an intermediate class: it has intermediate duration, but still of the same order of magnitude as class 3-III, and with an almost coincident distribution, as seen in Figure 4.5. Class 3-II is the softest and faintest class and the one most homogeneously distributed in space (because they have higher values of $\langle V/V_{max} \rangle$). Despite its duration being of the same order as that of class 3-III, the fluence is one order of magnitude lower.

In calculating the $\langle V/V_{max} \rangle$ parameter, not all the 1599 bursts could be used, but only those for which that value could be derived (757 GRBs). With the two-class classification, the result observed by Katz and Canel (1996) is recovered, with the short-duration GRBs having a higher value of $\langle V/V_{max} \rangle$ than long-duration GRBs, which consequently are distributed more inhomogeneously. With the new three-class classification it is obtained that class 3-II GRBs have a higher value of $\langle V/V_{max} \rangle$ than class 3-I, and that GRBs of class 3-III are extremely

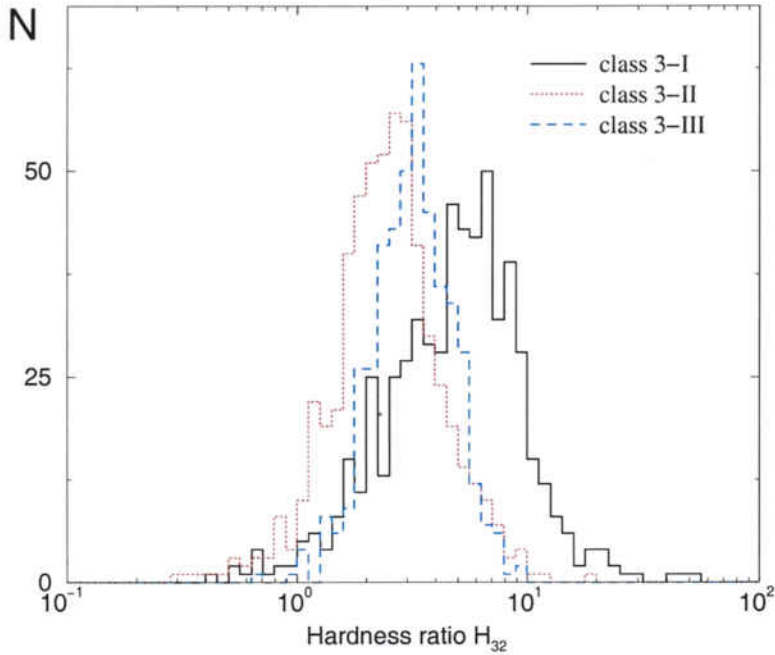


Figure 4.6: Hardness distribution of the three-class classification obtained with the cluster analysis. Classical long-duration GRBs (class 2-II) have been splitted into two classes, 3-II being softer than 3-III.

inhomogeneous, with $\langle V/V_{max} \rangle = 0.051$.

In order to test the isotropy of the GRBs distribution, here we use the values of the galactic dipole momentum $\langle \cos \theta \rangle$, and the galactic quadrupole momentum $\langle \sin^2 b - 1/3 \rangle$. The angle θ is measured between the GRB and the Galactic Center; it can be computed by solving the spherical triangle $\cos \theta = \cos l \cos b$, l being the galactic longitude and b the galactic latitude. The angle θ can be found in the Basic BATSE catalogue. For the dipole momentum, a value of $\langle \cos \theta \rangle$ significantly different from zero indicates a concentration of events towards the Galactic Center. The expected value for the quadrupole momentum of an isotropic distribution is also zero. If $\langle \sin^2 b - 1/3 \rangle$ is negative, that implies a concentration of events towards the galactic plane, whereas if $\langle \sin^2 b - 1/3 \rangle$ is positive, it implies a concentration of events towards the galactic poles. When calculating the dipole and quadrupole moments, the GRBs that were overwritten were not taken into account, as described in Paciesas et al. (1999). Due to the nonhomogeneous sky coverage during the BATSE mission, the values for an isotropic distribution are not equal to zero, but close to it. Adopting the same expected values for isotropy as for the 4B catalogue, that is

Class	$\langle \cos \theta \rangle$	$\langle \sin^2 b - 1/3 \rangle$
2-I	-0.031±0.026	-0.006±0.013
2-II	-0.004±0.019	+0.001±0.010
3-I	-0.031±0.026	-0.006±0.013
3-II	+0.021±0.025	-0.000±0.013
3-III	-0.035±0.030	+0.002±0.015

Table 4.3: Characteristics of the spatial distribution of the classification from the 9-dimensional cluster analysis. Galactic dipoles $\langle \cos \theta \rangle$, and quadrupole momenta $\langle \sin^2 b - 1/3 \rangle$ are shown for each GRB class.

for the Galactic dipole moment $\langle \cos \theta \rangle = -0.009$ and for the quadrupole Galactic moment $\langle \sin^2 b - 1/3 \rangle = -0.004$, it can be seen in Table 4.3 that only one of the corresponding values for classes 3-I and 3-III lies beyond 1σ of the expected value, and that it is the dipole for the 3-II class, which is $+1.2\sigma$ above. Just such value being above 1σ appears not significant and it is concluded that all three classes are isotropically distributed.

Figures 4.7 and 4.8 show the scatter plots of the three-class classification represented by the first, second, and third principal components derived from the PCA. Both figures show that all three classes are well separated in the axis representing the first principal component. Figure 4.7 shows that classes 3-I and 3-III are similarly scattered around the axis representing the second principal component (class 3-III being more skewed towards higher values of PC2), whereas class 3-II is clearly situated in the upper values of the second principal component. Within the two-class classification, the sum of classes 3-II and 3-III correspond to class 2-II. One can see in Figure 4.7 that it is possible to trace a diagonal line separating classes 2-I and 2-II in the scatter plot of the first and second principal components. Finally Figure 4.8 shows that all three classes are very similarly scattered around the axis representing the third principal component. The scatter plot of the second versus third principal component shows the classes well mixed and is not represented here.

Concerning the previous work of Mukherjee et al. (1998), they obtain an intermediate duration class of GRBs with T_{90} ranging from 2 – 20 s, which is completely different from class 3-II, whose durations span the range 2 – 600 s. It must be noted that they choose six variables for their analysis, three of them being the peak

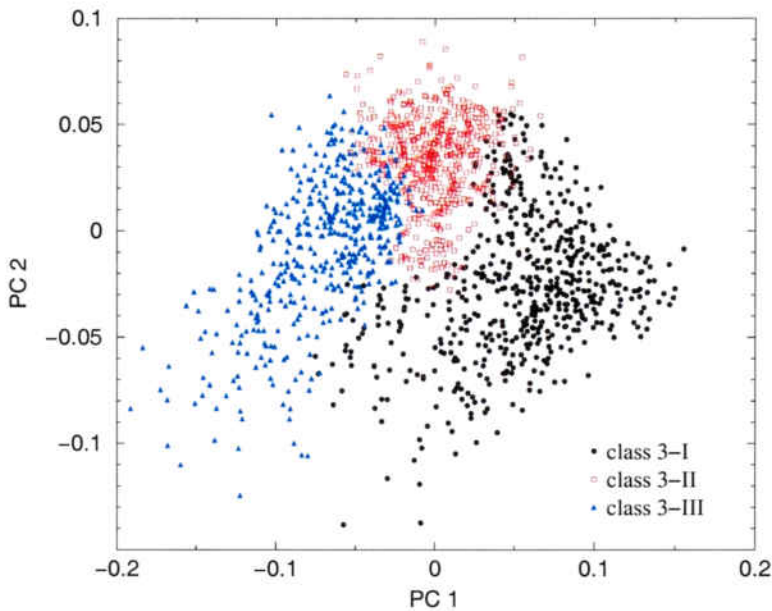


Figure 4.7: Scatter plot of the three class-classification of GRBs. The axes correspond to the first and second principal component derived from the PCA. It represents the axes in which the three classes are best separated.

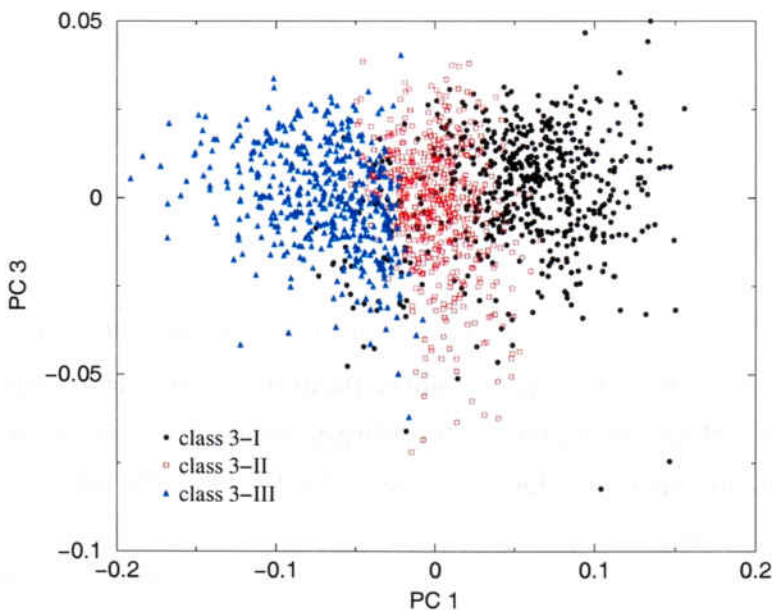


Figure 4.8: Scatter plot of the three class-classification of GRBs. The axes correspond to the first and third principal component derived from the PCA. With this representation the classes are still very well separated.

flux $\log P_{256}$ plus the two durations ($\log T_{50}$ and $\log T_{90}$), the other three being the total fluence $\log F_{total}$ and two hardnesses, $\log H_{321}$ and $\log H_{32}$. It has been learned from the PCA, that three variables are necessary, which together carry more than 95% of the variance, one of them being approximately the logarithm of the fluence in the fourth channel, $\log F_{Ch\#4}$. So it seems that Mukherjee et al. (1998) do lose information by not taking into account the fluence in the fourth channel separately, and also by not considering any peak flux later on. It must equally be noticed, when comparing results, that the GRB sample presented here is twice as large as theirs.

The main weakness of the cluster analysis is that it only deals with linear combinations of the variables. Such a weakness can be overcome by means of a neural network analysis, which also detects nonlinear relationships.

A list of the BATSE trigger numbers and GRB names corresponding to each class of GRB derived from the cluster analysis can be found in appendix A.

4.3 Neural network classification

Neural networks are artificial intelligence algorithms that can be used for an automatic and objective classification. We do not want to start from any prior classification. Therefore, a non-supervised algorithm is used. As we do not wish to introduce any tracer object either, the net is initialized at random. The 'Self-Organizing Map' algorithm (Kohonen, 1990), implemented in the SOM_PAK² package from the Laboratory of Computer and Information Science of the University of Helsinki, is used.

As in the cluster analysis, the entry parameters are the logarithms of the same nine variables. The dimension of the output space must be specified beforehand, and based on the results of the cluster analysis the network is run twice, asking first for a two-dimensional and then for a three-dimensional output space, thus grouping either two or three classes of GRBs. The net is trained in two steps before looking for results. Table 4.4 summarizes the characteristics of the classification with the neural network.

As it would be expected, there are some differences in the composition of

²Available to download at <http://www.cis.hut.fi/research/som.pak/>

Class	N	$\langle T_{90} \rangle$	$\langle H_{32} \rangle$	$\langle V/V_{max} \rangle$	$\langle P_{1024} \rangle$	$\langle F_{total} \rangle$
2-I	685	6.24 ± 0.50	5.50 ± 0.18	0.288 ± 0.015	0.94 ± 0.04	1.44 ± 0.09
2-II	914	63.5 ± 2.3	3.12 ± 0.05	0.159 ± 0.008	3.82 ± 0.22	25.1 ± 2.0
3-I	531	3.05 ± 0.34	6.20 ± 0.22	0.287 ± 0.017	0.81 ± 0.04	1.13 ± 0.07
3-II	341	25.0 ± 1.4	3.05 ± 0.10	0.307 ± 0.019	1.25 ± 0.08	2.82 ± 0.16
3-III	727	71.8 ± 2.8	3.15 ± 0.05	0.123 ± 0.008	4.51 ± 0.28	30.8 ± 2.5

Table 4.4: Characteristics of the classification with the neural network. T_{90} is in units of s , P_{1024} in $\text{photons cm}^{-2}\text{s}^{-1}$, and F_{total} ($F_{total} = F_{Ch\#1} + F_{Ch\#2} + F_{Ch\#3} + F_{Ch\#4}$) in units of $10^{-6}\text{erg cm}^{-2}$.

the classes as compared with those obtained from the clustering method, since the neural network method is not agglomerative. So, for instance, class 2-I is no longer identical, in the two-group classification, to class 3-I in the three-group scheme. Also, the short GRBs which make up this class now have longer average durations than in the cluster analysis.

There is also some change from the results of the cluster analysis in the three-group classification. Classes 3-II and 3-III now become more widely separated in duration, basically due to the decrease in duration of class 3-II. The difference in hardness between class 3-II and class 3-III, in contrast, has decreased. The fraction of GRBs belonging to each class is also different to the one obtained with the cluster analysis. The latter has similar number of GRBs in each class, while the former has clearly more GRBs belonging to class 3-III, and less GRBs belonging to class 3-II.

Class 3-II is now the intermediate class in peak flux. From both methods, cluster analysis and neural network, it is seen that despite the difference by one order of magnitude between durations of class 3-I and class 3-II, their respective total fluences remain of the same order.

The durations of class 2-I GRBs extend up to $\sim 100\text{ s}$ (Figure 4.9), while in the classification with the cluster analysis they only extend up to $\sim 20\text{ s}$. On the contrary, class 2-II GRBs cover the same range of durations in both classification methods. In general, the two-class classification with the neural network recovers the same trends as the classical classification of short/hard and long/soft GRBs, but now we are able to classify individual bursts in the overlapping region of durations.

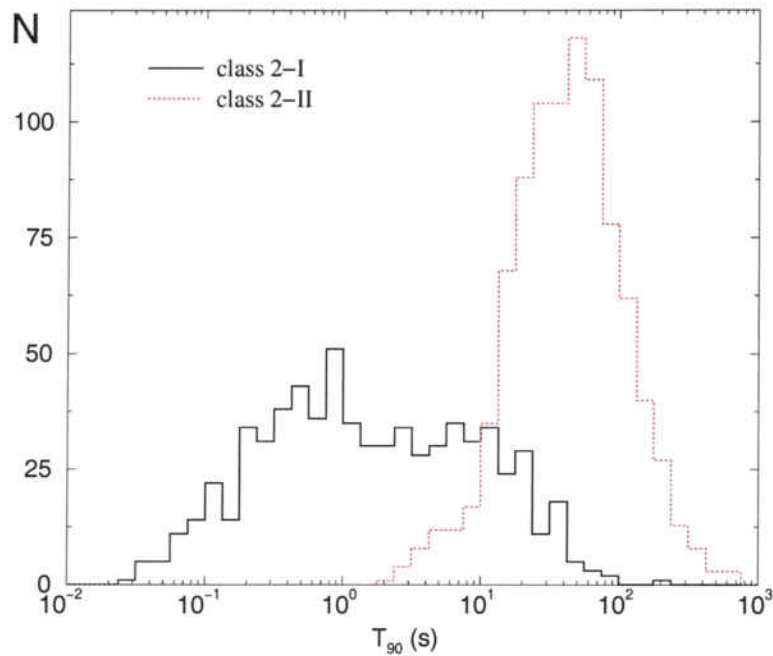


Figure 4.9: Duration distribution of the two-class classification obtained with the neural network. The classical short/long GRB classes are recovered. The durations of short GRBs extend up to ~ 100 s, while long-duration GRBs have durations as short as 2 s.

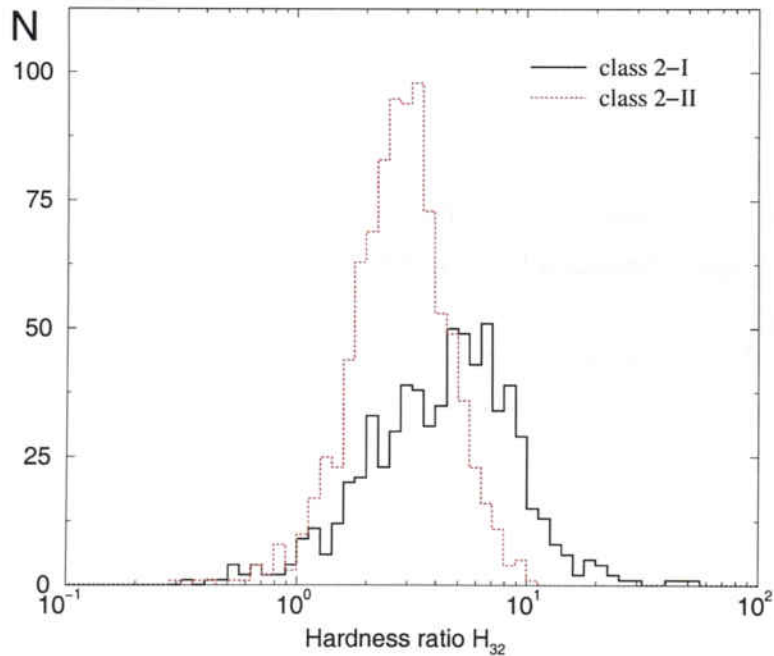


Figure 4.10: Hardness distribution of the two-class classification obtained with the neural network. The traditional classification is recovered: short-duration GRBs (class 2-I) are harder and long-duration GRBs (class 2-II) are softer.

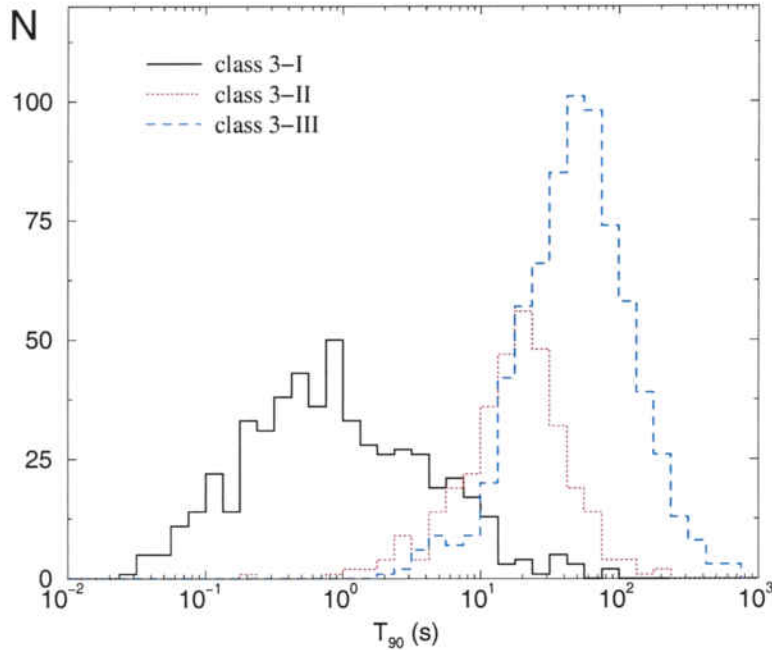


Figure 4.11: Duration distribution of the three-class classification obtained with the neural network. Three classes with different durations are obtained. Short GRBs (class 3-I) durations extend up to ~ 100 s.

Figures 4.11 and 4.12 show the duration and hardness distribution of the three-class classification obtained with the neural network. As a difference with the cluster analysis classification, here the duration distributions of classes 3-II and 3-III are not so similar. In fact, the mean duration of class 3-II GRBs is less than half that of class 3-III GRBs obtained with the neural network, while in the cluster analysis classification the durations are of the same order. The new class 3-II consists of the longer and softer bursts from class 2-I and of the shorter bursts from class 2-II. This new class of intermediate duration has the same hardness as the long-duration class. In contrast, they have different fluences, peak fluxes, and rather different values of $\langle V/V_{max} \rangle$.

As in the cluster analysis, all three classes are highly isotropic, with no value of the momenta above 0.8σ of the values expected for isotropy (see Table 4.5). The fact that all classes of GRBs presented in this thesis are isotropically and inhomogeneously distributed suggests that we are dealing with extragalactic distributions of events.

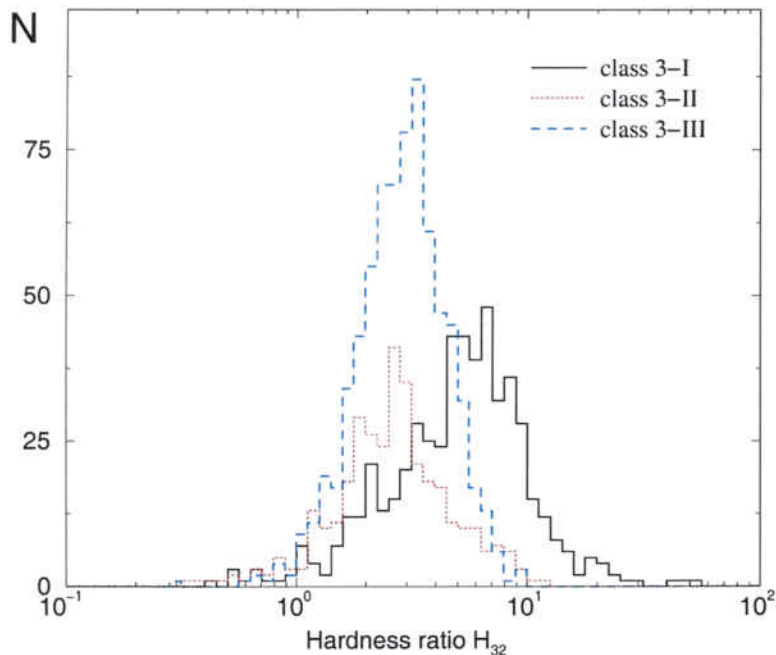


Figure 4.12: Hardness distribution of the three-class classification obtained with the neural network. Short-duration GRBs (class 3-I) are hard, while intermediate (class 3-II) and long (class 3-III) duration GRBs are soft and have similar H_{32} .

Class	$\langle \cos \theta \rangle$	$\langle \sin^2 b - 1/3 \rangle$
2-I	$+0.002 \pm 0.024$	-0.005 ± 0.012
2-II	-0.024 ± 0.021	$+0.001 \pm 0.010$
3-I	-0.003 ± 0.027	-0.014 ± 0.014
3-II	-0.012 ± 0.033	$+0.009 \pm 0.016$
3-III	-0.022 ± 0.023	$+0.003 \pm 0.012$

Table 4.5: Characteristics of the spatial distribution of the classification with the neural network. Galactic dipoles $\langle \cos \theta \rangle$ and quadrupole momenta $\langle \sin^2 b - 1/3 \rangle$ are shown for each GRB class.

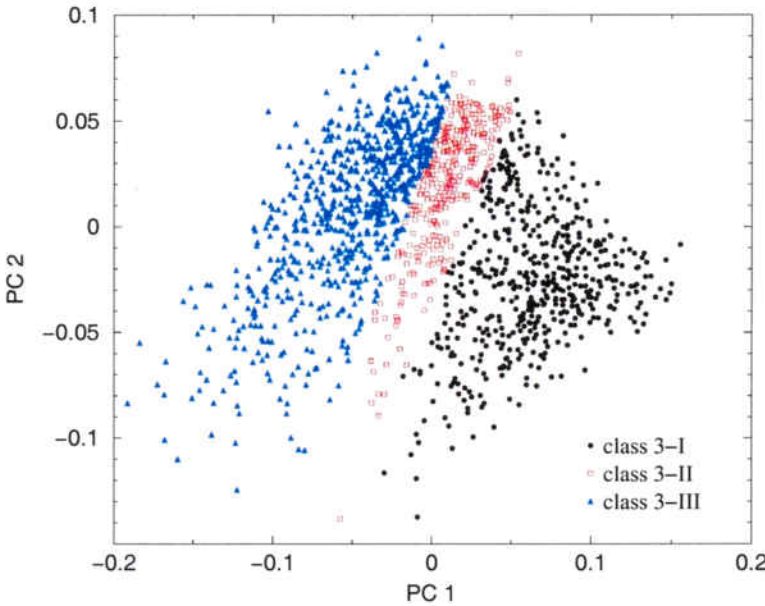


Figure 4.13: Scatter plot of the three class-classification of GRBs. The axes correspond to the first and second principal component derived from the PCA. It represents the axes in which the three classes are best separated.

To finish this section, we show scatter plots of the three classes obtained with the neural network using the principal components obtained from the PCA. Figure 4.13 shows the scatter plot of the first two principal components. One can see the differences of classification, obtaining better separated classes with the neural network classification than with the cluster analysis classification. Figure 4.14 shows class 3-II, the less populated one, mixed in the region between classes 3-I and 3-III.

A list of the BATSE trigger numbers and GRB names corresponding to each class of GRB derived from the cluster analysis can be found in appendix B.

4.4 The maximum redshift

It has been seen in the previous sections that different classes of GRBs have different values of $\langle V/V_{max} \rangle$, and consequently, different distribution in distance of the events. All classes are inhomogeneously distributed ($\langle V/V_{max} \rangle < 0.5$) and isotropically distributed, which suggest an extragalactic origin of GRBs, as has already been obtained from observations of redshifts. With a series of simplifications

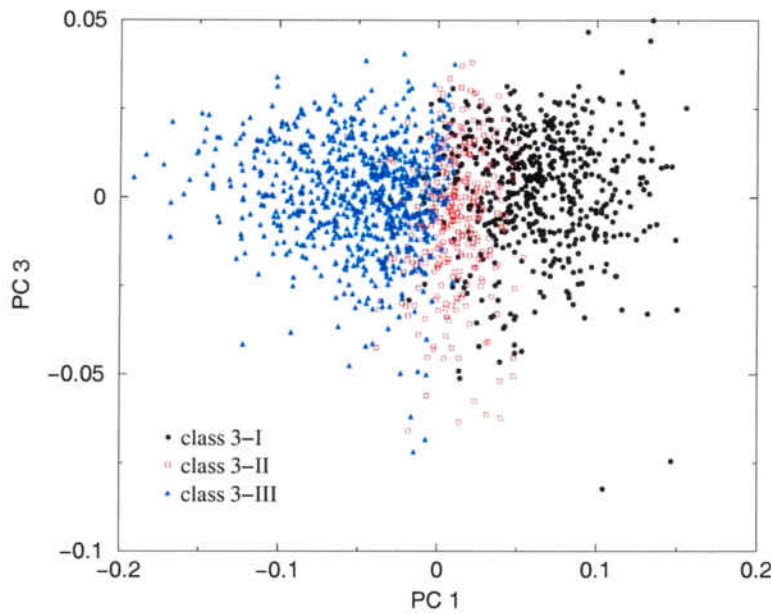


Figure 4.14: Scatter plot of the three class-classification of GRBs. The axes correspond to the first and third principal component derived from the PCA. With this representation the classes are still very well separated.

(Mao and Paczyński, 1992), $\langle V/V_{max} \rangle$ can be used to determine the maximum redshift at which a population of GRBs is visible.

From section 2.2.4, equation 2.3, one can see that:

$$\frac{V}{V_{max}} = \left(\frac{P_{min}}{P} \right)^{3/2} \quad (4.1)$$

The minimum observed peak flux, P_{min} , depends on the maximum redshift of a GRB. One can calculate the theoretical value of $\langle (P_{min}/P)^{3/2} \rangle$ as a function of z_{max} , and by equation 4.1 with the value of $\langle V/V_{max} \rangle$ of a given class of GRBs find the value of z_{max} for that class. In order to do this, one has to make several assumptions. The first one is to use a simple power law for the GRB spectrum:

$$\frac{dI}{d\nu} = C\nu^{-\alpha} \quad (4.2)$$

Where I , the emitted flux, is in units of $\text{photons s}^{-1}\text{Hz}$, ν is the frequency, C is a normalizing constant, and α is the spectral slope. Here, $\alpha = 1$ is taken for all

GRBs (Mallozzi et al., 1996). Using the standard candle hypothesis:

$$I_0 \equiv \int_{\nu_1}^{\nu_2} C\nu^{-\alpha} d\nu \quad (4.3)$$

One can calculate the flux emitted in the detector bandwidth from $\nu_1 - \nu_2$:

$$I(z) = \int_{\nu_1(1+z)}^{\nu_2(1+z)} C\nu^{-\alpha} d\nu = (1+z)^{-\alpha+1} I_0 \quad (4.4)$$

The observed peak flux from a GRB at redshift z is:

$$P(z) = \frac{I(z)}{4\pi d_L^2(z)} = \frac{I_0(1+z)^{-\alpha}}{4\pi D^2(z)} \quad (4.5)$$

Where d_L is the luminosity distance, equal to the comoving distance D multiplied by $(1+z)$. The comoving distance D will be defined in section 5.3.3. The minimum observed peak flux will be the one coming from the farthest detected GRB, that is, the GRB exploded at z_{max} :

$$P_{min} = \frac{I_0}{4\pi} \frac{(1+z_{max})^{-\alpha}}{D^2(z_{max})} \quad (4.6)$$

We can now calculate P_{min}/P as a function of z_{max} . To calculate its mean, one needs the total number of events produced up to a redshift z_{max} :

$$N(z_{max}) = \frac{c}{H_0} \int_0^{z_{max}} \frac{4\pi}{1+z} R_{GRB}(z) \frac{D^2(z)}{\sqrt{\Omega_M(1+z)^3 + \Omega_K(1+z)^2 + \Omega_\Lambda}} dz \quad (4.7)$$

Where H_0 is the Hubble constant, c is the speed of light, R_{GRB} is the comoving rate of explosions, D is the comoving distance, and Ω_M , Ω_K and Ω_Λ are the cosmological parameters. All these parameters will be explained in detail in chapter 5. In the end we obtain:

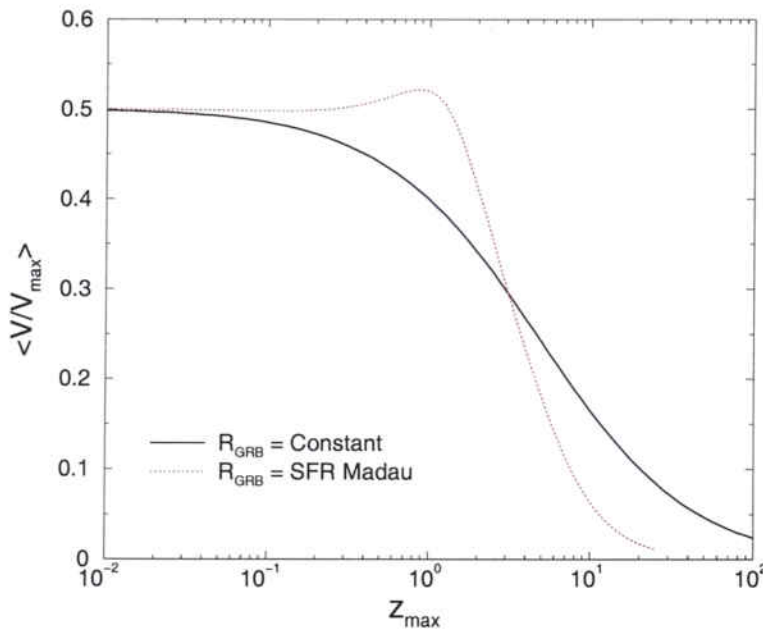


Figure 4.15: $\langle V/V_{max} \rangle$ as a function of the maximum observed redshift z_{max} , for a constant comoving rate of GRBs, and a comoving rate proportional to the SFR of Madau and Pozzetti (2000). Given a GRB class with a certain value of $\langle V/V_{max} \rangle$, one can find the maximum redshift of that population of GRBs from this plot.

$$\langle \left(\frac{P_{min}}{P(z)} \right)^{3/2} \rangle = \frac{1}{N(z_{max})} \frac{c}{H_0} \times$$

$$\int_0^{z_{max}} \left(\frac{P_{min}}{P(z)} \right)^{3/2} \frac{4\pi}{1+z} R_{GRB}(z) \frac{D^2(z)}{\sqrt{\Omega_M(1+z)^3 + \Omega_K(1+z)^2 + \Omega_\Lambda}} dz \quad (4.8)$$

With equation 4.8 and the relationship between $\langle (P_{min}/P)^{3/2} \rangle$ and $\langle V/V_{max} \rangle$ given by equation 4.1, one can plot $\langle V/V_{max} \rangle$ as a function of z_{max} . One can numerically invert the relation and compute the z_{max} for each GRB class using their respective values of $\langle V/V_{max} \rangle$.

Here we use $H_0 = 72 \text{ km s}^{-1} \text{Mpc}^{-1}$, $\Omega_M = 0.3$, and $\Omega_\Lambda = 0.7$. For the comoving rate of explosions R_{GRB} , we use two different assumptions: constant comoving rate, and R_{GRB} proportional to the star formation rate (SFR) derived by Madau and Pozzetti (2000) (see section 5.3.4). Figure 4.15 shows $\langle V/V_{max} \rangle$ as a function

Class	Cluster Analysis		Neural Network	
	$R_{GRB} = Ct$	$R_{GRB} \propto SFR_{Madau}$	$R_{GRB} = Ct$	$R_{GRB} \propto SFR_{Madau}$
2-I	$4.1^{+0.7}_{-0.6}$	$3.5^{+0.3}_{-0.2}$	$3.3^{+0.5}_{-0.4}$	$3.2^{+0.2}_{-0.2}$
2-II	$8.3^{+0.6}_{-0.6}$	$4.9^{+0.2}_{-0.2}$	$10.6^{+0.9}_{-0.8}$	$5.5^{+0.1}_{-0.2}$
3-I	$4.1^{+0.7}_{-0.6}$	$3.5^{+0.3}_{-0.2}$	$3.3^{+0.6}_{-0.5}$	$3.2^{+0.2}_{-0.2}$
3-II	$3.1^{+0.4}_{-0.3}$	$3.1^{+0.2}_{-0.1}$	$2.8^{+0.5}_{-0.5}$	$3.0^{+0.2}_{-0.2}$
3-III	$45.2^{+4.2}_{-3.6}$	$11.3^{+0.6}_{-0.4}$	$15.4^{+1.5}_{-1.3}$	$6.7^{+0.3}_{-0.3}$

Table 4.6: Maximum redshifts observed for each GRB class, for a constant comoving rate of GRBs, and for a comoving rate proportional to the SFR of Madau and Pozzetti (2000).

of the maximum observed redshift z_{max} for the two assumptions: constant comoving rate of GRBs, and a comoving rate proportional to the SFR of Madau and Pozzetti (2000). With this plot and the values of $\langle V/V_{max} \rangle$ for each class of GRB we construct Table 4.6 with the maximum observed redshift of each GRB class obtained from the cluster analysis and the neural network, respectively.

The values for z_{max} in Table 4.6 are not to be taken strictly. There are many assumptions and simplifications, but their relative values are interesting. They show that, in a classical two-class classification, long-duration GRBs happen at longer distances than short-duration GRBs. This is consistent with the progenitor models that are nowadays believed to be responsible for each class of GRB. Short-duration GRBs, coming from mergings of compact objects, occur at shorter distances than long-duration GRBs, coming from collapsars, due to the longer times from birth to explosion. On the other hand, collapsars start to happen almost as soon as the star formation begins in the Universe, because high-mass stars evolve very rapidly. This kind of progenitors follow an explosion rate proportional to the SFR, while mergings do have a delay with respect to the SFR. With a three-class classification, class 3-II GRBs explode at similar distances as class 3-I, both of them being candidates to come from mergings. Class 3-III GRBs happen at longer distances than classes 3-I and 3-II, in particular they are expected to happen at longer distances than those of class 2-II.

4.5 Hardness evolution

As it has been seen, $\langle V/V_{max} \rangle$ gives a measure of the maximum redshift of a sample of GRBs, the lower its value the deepest the population being. Figure 4.16 represents $\langle V/V_{max} \rangle$ as a function of hardness for classical long-duration GRBs ($T_{90} > 2$ s). The value of $\langle V/V_{max} \rangle$ decreases with increasing H_{32} , which means that hard GRBs tend to happen at longer distances than soft GRBs. There is indeed evolution in hardness. The hardness bins are taken so as to include similar numbers of bursts (~ 60) in each of them, in order to have comparable error bars. The value of $\langle V/V_{max} \rangle$ is displayed in the position of the mean of the hardness for each bin, and no error bars for the hardness are shown because the deviation is less than the symbol size, except for the last bin for which it is of about 0.2.

When $\langle V/V_{max} \rangle$ decreases, one is dealing with a more distant sample of GRBs, and then Figure 4.16 tells us that, when sampling to higher distances, GRBs tend to be harder, and taking into account the hardness-intensity correlation (Dezaley et al., 1997) they should also be more luminous. This effect has to be interpreted, in a cosmological scenario, as a source evolution. There is a possible explanation: it is generally admitted that the upper limit of the stellar initial mass function (IMF) depends on metallicity, and that lower metallicity allows more massive stars to form. When sampling GRBs farther away, one looks to a younger Universe, with lower metallicity, and thus with more massive stars. Therefore, if GRBs come from very massive stars, those ancient GRBs had sources with higher power and they were brighter and harder.

In Figure 4.17, it can be appreciated how in the three-class scheme class 3-II no longer shows any trend of $\langle V/V_{max} \rangle$ decreasing with increasing H_{32} . Such a trend in class 2-II was due to the fusion into it of classes 3-II and 3-III, and now it is seen that class 3-III is the only one to uphold the trend. To evaluate numerically the correlation, a Spearman rank test (Press et al., 1986) has been applied, obtaining for class 3-III a Spearman-rank correlation coefficient $r_s = -0.354$, with significance $4 \cdot 10^{-13}$, for the class resulting from the neural network. In contrast, for class 3-II from the neural network $r_s = -0.051$ with a 0.51 significance level, showing no correlation at all. The results are equivalent for the classes derived with the cluster analysis, with $r_s = -0.344$ and a significance level of $2 \cdot 10^{-8}$ for class 3-III, and

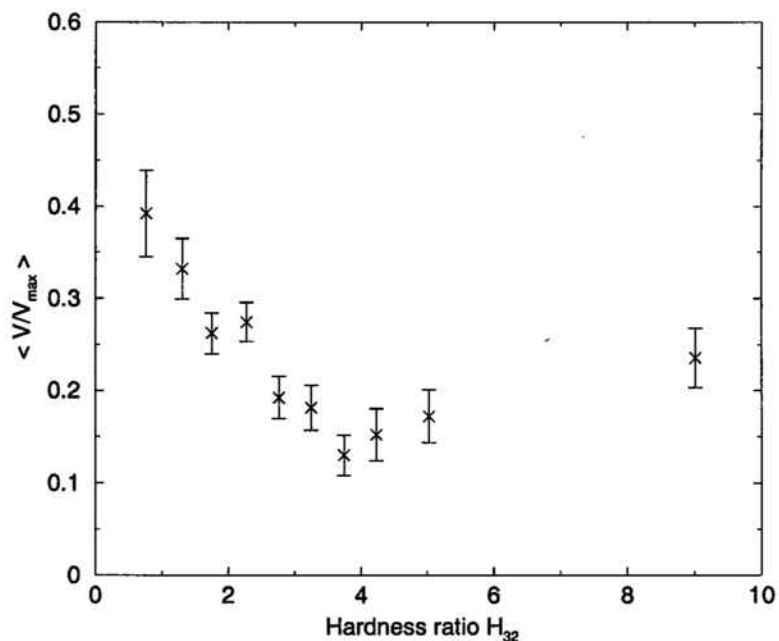


Figure 4.16: $\langle V/V_{max} \rangle$ as a function of hardness for classical long-duration GRBs ($T_{90} > 2$ s). The correlation between these two variables is clearly seen. Hardness bins have been taken so as to include similar numbers of bursts in all of them. Each hardness bin contains ~ 60 GRBs. The error bars are 1σ .

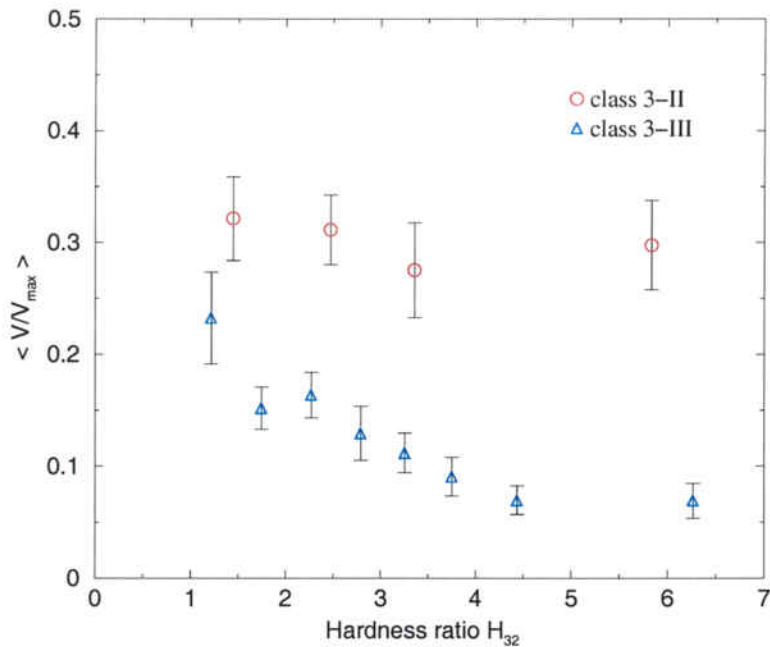


Figure 4.17: $\langle V/V_{max} \rangle$ as a function of hardness for classes 3-II and 3-III obtained with the neural network. With the three-class classification, $\langle V/V_{max} \rangle$ is constant in H_{32} for class 3-II. Only class 3-III keeps the trend of lower $\langle V/V_{max} \rangle$ with higher H_{32} .

$r_s = 0.066$ and a significance level of 0.26 for class 3-II. It is concluded, therefore, that class 3-III really shows clues of cosmological source evolution, which can be due to its being made of GRBs produced by very massive stars, likely through collapsars.

With respect to the new classification, one should be concerned whether the structure of the GRB data may partially reflect instrumental biases. Hakkila et al. (2000) have suggested that the three-class classification obtained by Mukherjee et al. (1998) might arise from a bias in measuring some bursts properties, such as duration and fluence, which would make some bursts in 'classical' class 2-II to take the 'new' class 3-II characteristics (by lowering their duration and fluence). The fluence-duration bias, however, in spite of being qualitatively understood, is not well quantified. Hakkila et al. (2000) based their analysis on Mukherjee et al. (1998) classes: their intermediate duration class has durations T_{90} of between 2 s and 20 s, while the class 3-II deduced here extends up to T_{90} longer than 100 s. Moreover, such bias acts on the farthest bursts, while what we find is that our 'new' class 3-II GRBs are the closest ones. In addition, any bias that would make some bursts in

the 'old' class 2-II appear shorter and with lower fluence could hardly separate at the same time the evolutionary effects that we see in Figure 4.16 into two groups: one with evolution (class 3-III) and the other one without it (class 3-II).

4.6 Conclusions

There are reasons to think that there exists more than one type of possible progenitors for GRBs, and each type may give rise to groups of burst with different properties. We have searched for those groups in the current BATSE catalogue, with the aid of two automated classification algorithms, and confirmed that there exist two clearly separated classes of GRBs corresponding to the 'classical' classification of long/short GRBs. In addition, we have also obtained clear hints that there exists a third class, different from those previously reported. An oversimplified way of looking at this would be to say that the third class arises from splitting the original long class into two groups with high and low peak fluxes respectively, in a similar way that the whole sample of GRBs has been divided, in previous studies, into pairs of groups according to duration (Kouveliotou et al., 1993), hardness (Tavani, 1998), brightness (Nemiroff et al., 1994), or other characteristics (Pendleton et al., 1997). The present work, however, goes beyond that since nine quantities related to the bursts are used for the classification, instead of taking a single parameter and then finding a value separating the bursts into two classes; there are overlapping zones in every original variable. What our procedures do is to trace a surface in the 9-dimensional space, separating classes from the way each variable relates to all others. Two different classes may well have the same duration or show nearly the same distribution for a given variable, but by taking into account the other variables as well, these procedures still detect their existence. In contrast, univariate distributions would overlook them. There have been other authors that have studied the possible existence of three different classes of GRBs (Mukherjee et al., 1998; Horváth, 1998; Hakkila et al., 2000).

Apart from the power of the method, the new grouping of the bursts thus obtained has to be examined for its possible physical meaning and its correspondence with separate classes of GRB progenitors and/or mechanisms. Classes 3-I, 3-II, and 3-III here defined correspond to different observational depths (z_{max}) and may

result from varying geometries of the observer with respect to the emitter, different parameters of the explosion, or from different progenitors having different spatial distributions. Thus, every class has to be compared with several possible models. The physical separation of classes 3-II and 3-III is strongly supported by the fact, which can hardly be due to chance alone, that having both classes together they show evolution of hardness and intensity with the maximum distance sampled, while when separated such evolution only exists in class 3-III.

The current observations of GRBs afterglows, that allow the measurement of redshifts and the identification of host galaxies, have shown evidence that long-duration GRBs are associated with core collapse supernovae (Bloom et al., 2002), which provides strong support for the collapsar model. That would also be consistent with the low $\langle V/V_{max} \rangle$ values found here for class 3-III: collapsars should show evolutionary effects and are expected to happen since the beginning of the star formation in the early Universe. We conclude, therefore, that class 3-III, which likely has collapsars as progenitors, is the one that can be detected up to very large redshifts, and it should thus be the most adequate one to learn about the history of the Universe at high z . The detection of short GRB afterglows has only been possible recently, thanks to the SWIFT and HETE2 missions (Castro-Tirado et al., 2005; Piro, 2005; Fox et al., 2005; Gehrels et al., 2005; Villasenor et al., 2005; Hjorth et al., 2005). The observations of GRB050509B and GRB050709 exclude a supernova association with short-duration GRBs and show smaller energy outputs. These GRBs have been found in an elliptical galaxy and in the outskirts of a star-forming galaxy, respectively. All these evidences point to NS-NS or BH-NS mergings as progenitors of short-duration GRBs. Class 3-I presented here corresponds to short-duration GRBs and has higher values of $\langle V/V_{max} \rangle$, as it is expected for NS-NS or BH-NS mergings (expected at lower redshifts than collapsars, and being, thus, more homogeneously distributed). As for class 3-II GRBs, they have similar durations to class 3-III, and similar inhomogeneity to class 3-I. The latter fact points to them being caused by binary mergings. Helium stars-BH and WD-BH mergers follow closely the SFR and should present similar inhomogeneity as collapsars. This kind of mergers are, consequently, not adequate to describe class 3-II GRBs. Binary mergers like BH-NS or NS-NS mergings show a delay between their formation and their merging with respect to the SFR, and occur at mean redshifts 20%-50% lower than collapsars (Fryer et al., 1999a), having thus similar inhomogeneity as class 3-I

GRBs. The problem is that simulations of this kind of mergings cannot produce GRBs with durations much longer than ~ 2 s (Ruffert and Janka, 1999). However, simulations are not conclusive. In fact, here it has been shown that classical short-duration GRBs, class 2-II, have durations up to ~ 100 s. In this context, we can even speculate whether the difference between class 3-I and class 3-II GRBs might be due to one of them coming from NS-NS mergings, and the other one being produced by BH-NS mergings. Nevertheless, caution is recommended when assigning binary mergers as progenitor for short-duration GRBs, since, for the time being, only two of them have redshift and host galaxy measurements.

Part II

Cosmology with gamma-ray bursts

Chapter 5

The gamma-ray burst intensity distribution

The second part of the thesis is dedicated to the study of extragalactic parameters of GRBs, such as the GRB explosion rate and the GRB luminosity function, and to the study of the cosmological parameters of the Universe itself, Ω_M and Ω_Λ . The measurement of these parameters is made by fitting the observed GRB intensity distribution to the theoretical one, which includes models of the GRB explosion rate and of the GRB luminosity function. A preliminary study of this method can be found in Balastegui et al. (2003).

This chapter introduces the intensity distribution, all the parameters related to it, and the fitting method. The following chapter presents the results.

5.1 Introduction

A common way to study the GRBs intensity distribution is through the $\log N - \log P$ distribution. The $\log N - \log P$ distribution is a plot showing the number of GRBs N with peak fluxes greater than P , that is, a cumulative distribution of the peak fluxes shown in logarithmic scale. Its shape can reveal important properties of the spatial distribution of GRBs. For instance, in the case of an homogeneous distribution in an euclidean space, one would expect the $\log N - \log P$ distribution to be a line with

slope $-3/2$. The latter comes from the fact that the number of photons¹ decreases as the distance squared, r^{-2} , while the number of GRBs is proportional to the volume, that is to r^3 , one obtains as a result that $N(> P) \propto P^{-3/2}$, which is a line in logarithmic scale.

As already mentioned, the distribution of GRB intensities is a way to infer the distribution of GRB distances, but P is not the only quantity useful as an intensity indicator. The fluence², S , has also been used by some authors (Petrosian and Lee, 1996). They argue that the peak flux for transient phenomena is not well established and depends on the observed time scale. One would need an instantaneous measure of the flux in order to obtain the real peak flux. Otherwise, if the instrument integrates for a time longer than the typical variation time scale of the phenomenon, it will cause a reduction of the measured peak flux and subsequently an instrumental bias. Another argument in favour of using S is that it is more likely that the total received energy be a standard candle of the phenomena, rather than P , due to the wide diversity of temporal profiles and durations of GRBs. Here we use the peak flux to construct the intensity distribution, since P is the best indicator as it was shown by Paczyński and Long (1988). The arguments in favour of using P are mainly instrumental. As it has been stated in section 2.2.2, BATSE triggers a detection whenever a detector records an excess in the photon count rate over the background. Since the photon's energy does not matter for triggering the instrument, it is not useful for making inferences about the spatial distribution of sources. In addition, it is virtually impossible to determine the efficiency for detecting bursts as a function of fluence, being easier to join peak fluxes measured with different instruments than to join measures of the fluence.

Once it is known that GRBs have an extragalactic origin, there is a theoretical equation that models the $\log N - \log P$ distribution as a function of a series of parameters related to GRBs, such as: the density of bursts, their spectra, their luminosity function; and of a series of parameters related to the Universe, such as: the cosmological parameters, Ω_M and Ω_Λ , and the Hubble constant H_0 . This chapter is dedicated to search for the best values of these parameters by fitting the observed $\log N - \log P$ distribution to the theoretical one, and to study how the $\log N - \log P$ distribution changes with them. We will carry out the fit for each class of GRBs

¹Remember that the peak flux is in units of $\text{photons cm}^{-2}\text{s}^{-1}$.

²Remember that the fluence is in units of erg cm^{-2} .

found with the neural network classification (section 4.3), even though there is not yet any confirmation of the extragalactic origin for classes 2-I, 3-I and 3-II. First, we will introduce a short review of the use of the $\log N - \log P$ distribution as a method to estimate parameters, both within the field of GRBs and outside this field. Then, we will describe the theory and equations that govern the $\log N - \log P$ distribution. Afterwards, we will comment individually each parameter that goes into the equation for the $\log N - \log P$ distribution, discussing its fixed value or the minimum searching region, in case it is a free parameter. Finally, we will show how to construct the observed $\log N - \log P$ distributions. In the next chapter the best set of parameters is presented, together with a thorough examination of how the $\log N - \log P$ distribution varies with each parameter. Let us start with the historical background of the use of intensity distributions in cosmology.

5.2 Historical review

Intensity distributions have been a fundamental tool in observational cosmology since the very beginnings (Hubble, 1934; Hubble, 1936), when the quality of the data did not allow accurate cosmological parameter determinations. Galaxy number counts, as the test is traditionally known, was included in a classical review (Sandage, 1961) as one of four fundamental tests of observational cosmology possible with the Mount Palomar 200-inch telescope. The fundamentals of this technique are described in depth in Weinberg (1972). Galaxy number counting faces two main difficulties: the first is observational, and it comes from the selection effects inherent to the methods used to detect faint galaxy images, causing sample incompleteness at the faintest magnitudes; the second one comes from the modelization of the luminosity evolution of the galaxies. Since then, not only the instruments have improved, but also the modelizations of the galaxy evolution (Bruzual A. and Kron, 1980; Tinsley, 1980; Yoshii and Takahara, 1988), to the point of being able to suggest the existence of a cosmological constant (Yoshii and Peterson, 1995) even before the suggestion of deriving its value from the study of the Hubble diagram of Type Ia supernovae (Goobar and Perlmutter, 1995). As it is already known, the existence of a cosmological constant (or at least some kind of dark energy) was lately confirmed by Riess et al. (1998) and Perlmutter et al. (1999).

One can also use other sources, different from normal galaxies, to plot their numbers as a function of their intensity. Traditionally, this has been done with non-optical sources such as: radio sources, quasars (Petrosian, 1969), and X-ray sources (Maccacaro et al., 1982).

Within the field of GRBs, the $\log N - \log P$ test has been widely used for several purposes, which mainly involve the measurement of: GRB explosion rates, redshift distributions, star formation rate, GRB luminosities and luminosity function (Horváth et al., 1996; Reichart and Mészáros, 1997; Totani, 1999; Kromers et al., 2000; Schmidt, 1999a). In this thesis we continue this work, expanding it by fitting all the parameters at once, and extend it to the determination of the cosmological parameters.

5.3 The $\log N - \log P$ distribution

The differential $\log N - \log P$ distribution, which comes from equation 5.1, is the one used for the fits because it is numerically faster than the use of the cumulative distribution, since the limits of the luminosity function integral are closer to each other.

$$N(P_1 \leq P < P_2) =$$

$$\frac{c}{H_0} \int_0^{z_{max}} \frac{R_{GRB}(z)}{1+z} \frac{D^2(z)}{\sqrt{\Omega_M(1+z)^3 + \Omega_K(1+z)^2 + \Omega_\Lambda}} dz \int_{L(P_1,z)}^{L(P_2,z)} \phi(L) dL \quad (5.1)$$

The magnitudes in equation 5.1 are: c , the speed of light; H_0 , the Hubble constant; z_{max} , the maximum redshift at which GRBs are produced; $R_{GRB}(z)$, the comoving GRB rate; $D(z)$, the comoving distance; $\phi(L)$, the luminosity function of GRBs; Ω_M , Ω_K and Ω_Λ are the usual cosmological parameters.

Following equation 5.1, the number of GRBs with peak fluxes between P_1 and P_2 is calculated by integrating the number density of GRBs per comoving volume ($R_{GRB}(z)$ with units of $yr^{-1}Mpc^{-3}$), multiplied by the comoving volume element

($\frac{dV}{dz}$; equation 5.2), from $z = 0$ to $z = z_{max}$, and accounting only for those GRBs which, according to the luminosity function, will be detected with peak fluxes between P_1 and P_2 at a distance z .

$$\frac{dV}{dz} = \frac{c}{H_0} \frac{D^2(z)}{\sqrt{\Omega_M(1+z)^3 + \Omega_K(1+z)^2 + \Omega_\Lambda}} \quad (5.2)$$

Let us proceed to introduce the parameters in equation 5.1, starting with the Hubble constant.

5.3.1 The Hubble constant

Edwin Hubble discovered in 1929 a linear relation between the distance, d , and the recession velocity of the galaxies v (Hubble, 1929), it was the Hubble law:

$$v = H_0 d \quad (5.3)$$

It is certainly amazing that he saw a linear relationship from the original plot (Figure 5.1). In fact he was somehow looking for a test that showed that the Universe was not static, as Einstein thought, and he found that the Universe was expanding. The first value he found for the Hubble constant was $H_0 \sim 500 \text{ km s}^{-1} \text{Mpc}^{-1}$. Since then, this value has kept decreasing and decreasing.

The Hubble parameter (equation 5.4) measures the rate of expansion of the Universe at any time, and the Hubble constant is just the value of the Hubble parameter at the present epoch.

It is not the purpose of this work to measure the value of the Hubble constant. Besides, it seems that the long-term historical controversy about the value of H_0 has come to its conclusion. The battle between the two old schools, with Sandage and Tammann defending a value of $H_0 \simeq 50 \text{ km s}^{-1} \text{Mpc}^{-1}$ (Sandage and Tammann, 1982), and van den Bergh and de Vaucouleurs claiming for a value of $H_0 \simeq 100 \text{ km s}^{-1} \text{Mpc}^{-1}$ (van den Bergh, 1992; de Vaucouleurs, 1993), has ended in a draw. The now accepted value for the Hubble constant, $H_0 = 72 \pm 8 \text{ km s}^{-1} \text{Mpc}^{-1}$,

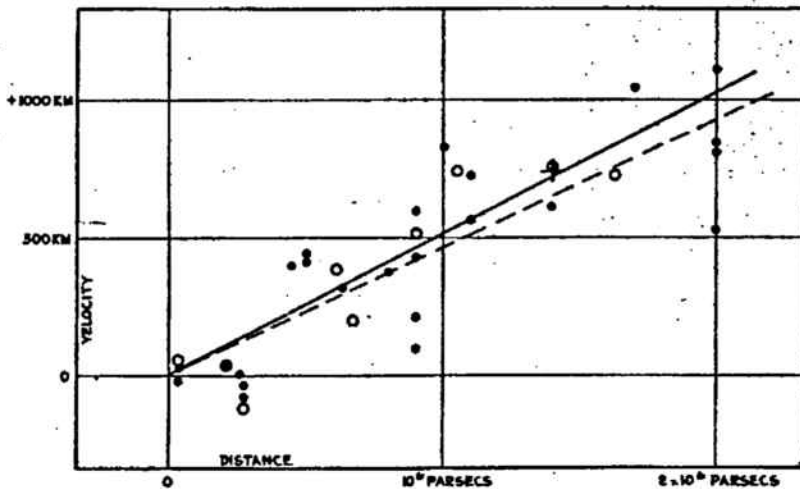


Figure 5.1: Original plot from where Hubble deduced the law of the expansion of the Universe. Figure extracted from Hubble (1929).

was measured by the Hubble Key Project (Freedman et al., 2001). The value for the Hubble constant used throughout this work is $H_0 = 72 \text{ km s}^{-1} \text{Mpc}^{-1}$.

5.3.2 The cosmological parameters Ω_M , Ω_Λ , and Ω_K

The Friedmann equation (5.4) governs the evolution of the scale factor of the Universe, $R(t)$. This equation comes from solving the Einstein field equations, imposing an homogeneous and isotropic universe.

$$H^2 \equiv \left(\frac{\dot{R}}{R} \right)^2 = \frac{8\pi G}{3} \rho_M + \frac{\Lambda}{3} - \frac{k}{R^2} \quad (5.4)$$

The cosmological parameters are defined as:

$$\Omega_M \equiv \frac{8\pi G}{3H_0^2} \rho_M^0, \quad \Omega_\Lambda \equiv \frac{\Lambda}{3H_0^2}, \quad \Omega_K \equiv -\frac{k}{R_0^2 H_0^2}, \quad (5.5)$$

These are dimensionless parameters that represent the ratio between the density of each component of the universe (Ω_M for matter; Ω_Λ for cosmological constant;

Ω_K in analogy to the others) and the critical density, that is, the energy density of a flat universe. The Friedmann equation can be rewritten as equation 5.6 by using the definitions of the cosmological parameters Ω_M , Ω_Λ , and Ω_K .

$$H^2 = H_0^2(\Omega_M(1+z)^3 + \Omega_\Lambda + \Omega_K(1+z)^2) \quad (5.6)$$

Equation 5.6 implies that:

$$\Omega_M + \Omega_\Lambda + \Omega_K = 1 \quad (5.7)$$

Ω_K defines the curvature of the universe. $\Omega_M + \Omega_\Lambda = 1$, means that the energy density of the Universe is equal to the critical value and the Universe is flat ($\Omega_K = 0$). $\Omega_M + \Omega_\Lambda > 1$, means that the energy density of the Universe is higher than the critical one and the Universe is closed ($\Omega_K < 0$). Finally, $\Omega_M + \Omega_\Lambda < 1$, means that the energy density of the Universe is smaller than the critical value and the Universe is open ($\Omega_K > 0$).

The Λ term, the cosmological constant, was originally introduced by Einstein, as a means to obtain a static universe (Einstein, 1917). Although, after the discovery by Hubble that the Universe was not static but it was expanding, Einstein regretted the inclusion of Λ as the biggest blunder of his life³, nowadays, the cosmological constant is again a hot topic of debate in science, due to the recent results based on Type Ia supernovae (Perlmutter et al., 1999; Riess et al., 1998) and the cosmic microwave background (Spergel et al., 2003). These current studies in cosmology suggest the existence of a cosmological constant, and also that we live in a flat ($\Omega_K = 0$) universe. Today, one of the most active research fields in cosmology is centered on the search of dark energy, in any of its variations, such as a cosmological constant (Carroll et al., 1992), running cosmological constant (España-Bonet et al., 2004), quintessence (Peebles and Ratra, 1988), k-essence (Armendariz-Picon et al., 2001), phantom energy (Caldwell, 2002), cardassian models (Freese and Lewis, 2002), etc...

In section 6.4, we will use the $\log N - \log P$ distribution to measure Ω_M and Ω_Λ , comparing this test with other experiments. For the fits of the GRB parameters

³This sentence was attributed to Einstein by Gamow in (Gamow, 1970), but, since Gamow had a reputation of anecdotal inaccuracy, there is no evidence that Einstein ever pronounced it.

we keep Ω_M and Ω_Λ as constants, using the commonly accepted values of $\Omega_M = 0.3$ and $\Omega_\Lambda = 0.7$.

5.3.3 The comoving distance

The comoving distance is calculated by integrating the line element over a null geodesic. The line element in a Robertson-Walker metrics is:

$$ds^2 = c^2 dt^2 - R^2(t) \left[\frac{dr^2}{1 - kr^2} + r^2(d\theta^2 + \sin^2 \theta d\varphi^2) \right] \quad (5.8)$$

The comoving distance as a function of redshift has a different expression depending on whether we live in an open ($\Omega_k > 0$), flat ($\Omega_k = 0$), or closed ($\Omega_k < 0$) universe:

$$D(z) = \begin{cases} \frac{c}{H_0} \frac{1}{\sqrt{\Omega_k}} \sinh \left[\sqrt{\Omega_k} \int_0^z \frac{dz}{\sqrt{\Omega_M(1+z)^3 + \Omega_K(1+z)^2 + \Omega_\Lambda}} \right] & \Omega_k > 0 \\ \frac{c}{H_0} \sqrt{\Omega_k} \int_0^z \frac{dz}{\sqrt{\Omega_M(1+z)^3 + \Omega_K(1+z)^2 + \Omega_\Lambda}} & \Omega_k = 0 \\ \frac{c}{H_0} \frac{1}{\sqrt{|\Omega_k|}} \sin \left[\sqrt{|\Omega_k|} \int_0^z \frac{dz}{\sqrt{\Omega_M(1+z)^3 + \Omega_K(1+z)^2 + \Omega_\Lambda}} \right] & \Omega_k < 0 \end{cases} \quad (5.9)$$

Figure 5.2 shows the comoving distance in *Mpc* as a function of redshift for different cosmologies. It can be appreciated that, the less matter and the more cosmological constant there is in the Universe, the faster the expansion of the Universe is, and so the distance to a certain redshift is larger.

5.3.4 The explosion rate

Let us start now explaining the GRB parameters appearing in the $\log N - \log P$ distribution. The comoving explosion rate, a measure of the number of events per unit comoving volume and time, provides a census of the number of objects formed

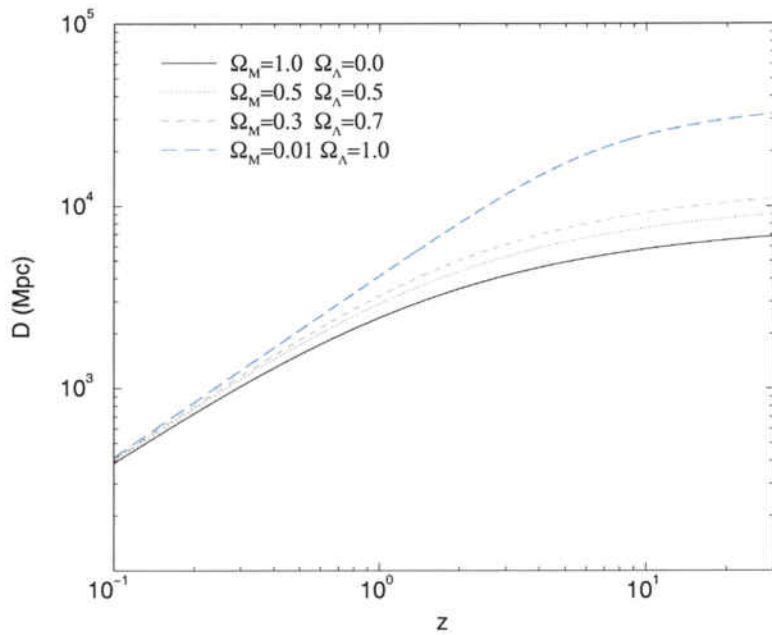


Figure 5.2: Comoving distance as a function of redshift for different cosmologies. The less matter and the more cosmological constant there is in the Universe, the faster the expansion of the Universe is.

at a given redshift and can help to discern among different kinds of progenitors. The main model for the central engine of a long-duration GRB involves the collapse of a massive star to a black hole (MacFadyen et al., 2001). Since the evolution of these massive stars is very fast from their formation to the explosion epoch, the rate of explosion of GRBs should closely follow the history of the star formation rate (SFR from now on).

The GRB rate can be obtained from three different processes. From a theoretical point of view, one can calculate the star formation history (Bromm and Loeb, 2002), and suppose that the GRB rate is proportional to the SFR. These models predict an exponentially growing SFR that peaks at $z \sim 3$, followed by a second rise, peaking at $z \sim 8$, decreasing exponentially from there on. The SFR can be modelled this way up to $z \approx 30$ (see Figure 5.3).

One can also use the observed SFR. The three main models competing on this field (Madau and Pozzetti, 2000; Steidel et al., 1999; Blain et al., 1999) give similar SFRs up to $z \sim 1.5$, but diverge from there on. These studies estimate the SFR by observing the UV luminosity density of galaxies. The difference between these

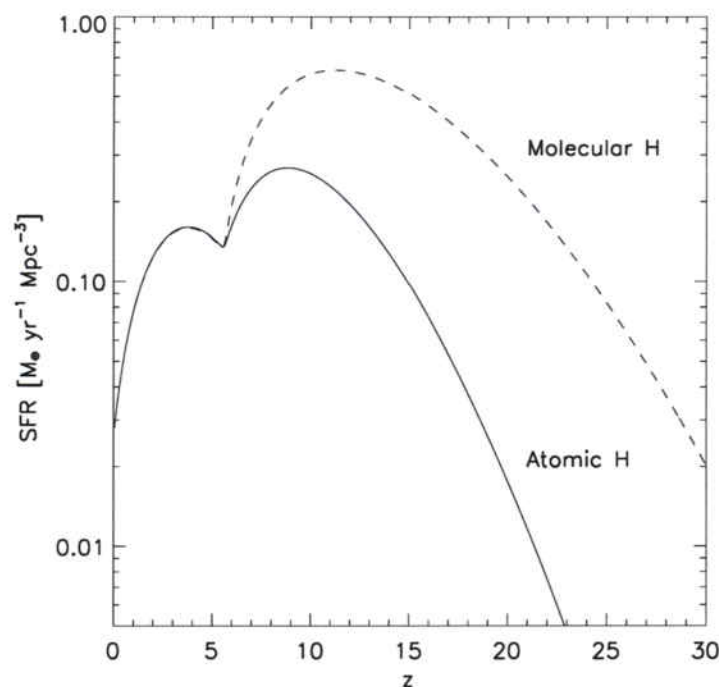


Figure 5.3: History of cosmic comoving star formation rate (SFR) in units of $M_{\odot} \text{yr}^{-1} \text{Mpc}^{-3}$, as a function of redshift. Solid line: Cooling due to atomic hydrogen only; dashed line: added cooling via molecular hydrogen. Figure extracted from Bromm and Loeb (2002).

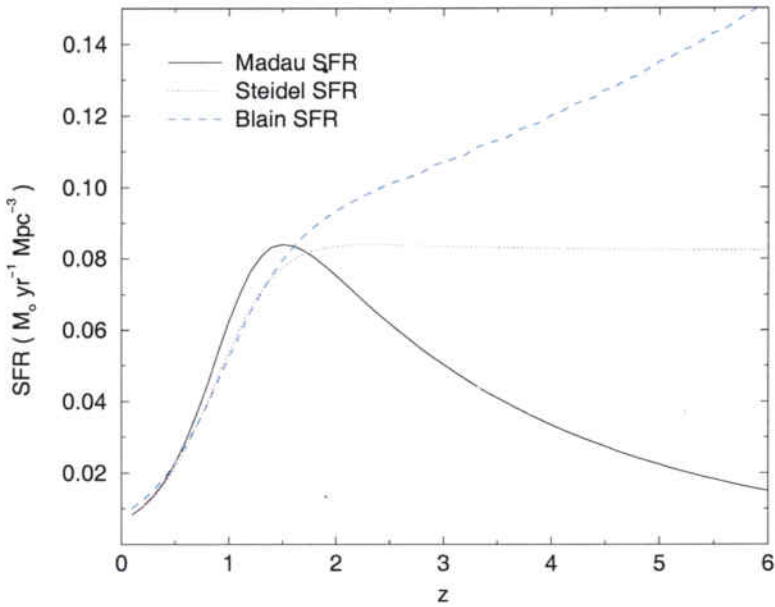


Figure 5.4: The observed star formation rates. From Madau and Pozzetti (2000), Steidel et al. (1999), and Blain et al. (1999).

models (Figure 5.4) comes from the different corrections for sample incompleteness and dust extinction. Equations 5.10, 5.11, and 5.12 are the three models of SFRs considered here. This technique can trace the SFR up to at most $z \approx 4$.

$$SFR_{Madau}(z) \propto \frac{\exp(3.4z)}{\exp(3.8z) + 45} M_\odot \text{yr}^{-1} \text{Mpc}^{-3} \quad (5.10)$$

$$SFR_{Steidel}(z) \propto \frac{\exp(3.4z)}{\exp(3.4z) + 22} M_\odot \text{yr}^{-1} \text{Mpc}^{-3} \quad (5.11)$$

$$SFR_{Blain}(z) \propto \frac{\exp(3.05z - 0.4)}{\exp(2.93z) + 15} M_\odot \text{yr}^{-1} \text{Mpc}^{-3} \quad (5.12)$$

The third option is to use the BATSE data together with empirical calibrations of the luminosity, such as the luminosity–variability correlation (Fenimore and Ramirez-Ruiz, 2000), or the E_p –luminosity relation (Amati et al., 2002; Attiea, 2003). Lloyd-Ronning, Fryer and Ramirez-Ruiz (2002) (LFR from now on) used 220 GRB redshifts and luminosities, derived from the luminosity–variability correlation, to find the comoving rate density of GRBs (equation 5.13). Yonetoku et

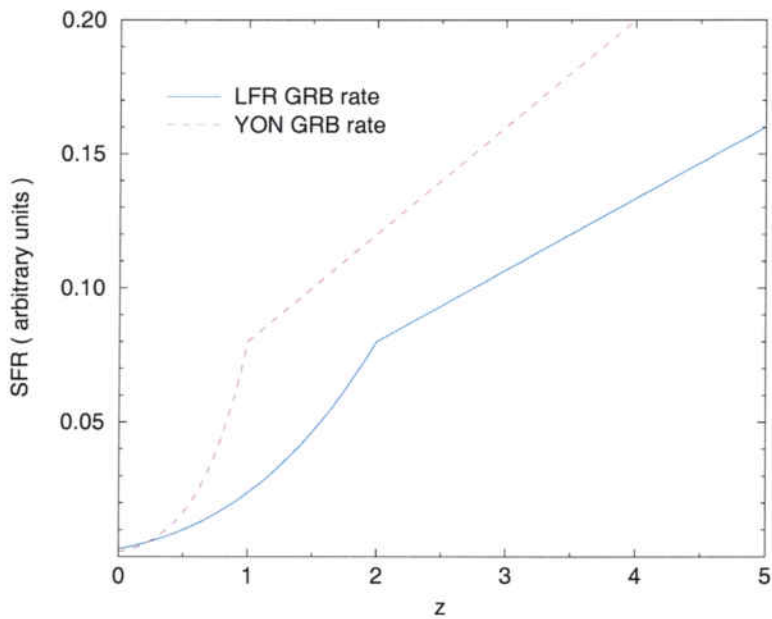


Figure 5.5: GRB explosion rates derived by LFR and YON.

al. (2004) (YON from now on) used the E_p –luminosity relation to estimate the luminosity and redshift for 684 GRBs, deriving the GRB rate shown in equation 5.14. Both groups estimate the GRB rate up to $z \approx 10$. Figure 5.5 shows the GRB rates measured with luminosity calibrations. It is important to remind that the GRB rate and luminosity function obtained by LFR and YON refer only to long-duration GRBs.

$$R_{GRB}^{LFR}(z) \propto \begin{cases} (1+z)^3 & z < 2 \\ (1+z) & z \geq 2 \end{cases} \quad (5.13)$$

$$R_{GRB}^{YON}(z) \propto \begin{cases} (1+z)^{5.5} & z < 1 \\ (1+z) & z \geq 1 \end{cases} \quad (5.14)$$

See that by measuring the GRB rate of long-duration GRBs, one can empirically determine the SFR at very high redshifts (even $z \geq 10$). Since the Universe is almost transparent to γ -rays and X-rays, while there exists significant absorption in the UV, increasing the sample of GRBs with known redshifts (or finding a good redshift calibration for GRBs) is the best method to empirically measure the global SFR of the Universe.

Based on the previous results, we will model the GRB rate as a triple power law of $(1 + z)$ (see equation 5.15 and Figure 5.6). There will be 5 free parameters, which are: two break points (z_1 and z_2), and three exponents (e_1 , e_2 , and e_3). This way we can mimic any of the GRB rates obtained with the previous techniques: a first break, z_1 , around $z \approx 2$, and a second break, z_2 , where the GRB rate starts to decrease, at around $z \approx 10$. This decrease has not yet been observed by LFR and YON, but it happens in the simulations of the star formation history. These break points are joined with power laws of $(1 + z)$, like equations 5.13 and 5.14.

$$R_{GRB}(z) \propto \begin{cases} (1 + z)^{e_1} & z < z_1 \\ (1 + z)^{e_2} & z_1 \leq z \leq z_2 \\ (1 + z)^{e_3} & z > z_2 \end{cases} \quad (5.15)$$

One last parameter can also be thought of as a parameter of the GRB rate, that is z_{max} . The first integral of equation 5.1, has its upper limit in z_{max} . That is because equation 5.15 only becomes zero at $z = \infty$. From a realistic point of view, there exists a maximum redshift at which GRBs are produced, and this is controlled by the parameter z_{max} . Moreover, from a numerical point of view, it is not efficient to integrate up to $z = \infty$, because from a certain z up you will not detect any GRBs due to their low peak fluxes; numerically, the integral over the luminosity in equation 5.15 will be zero. Lamb and Reichart (2000) suggest that GRBs can be produced up to at least $z \approx 15 - 20$.

Both LFR and YON measured the GRB rate for long-duration GRBs, which are thought to come from collapsars, and thus follow closely the SFR. Since almost nothing is known about the spatial distribution, in distance, of short-duration GRBs, we will use the same model for short GRB rates (equation 5.15). Compact object mergings, including here NS-NS (Rosswog and Davies, 2002; Rosswog et al., 2003), NS-BH (Narayan et al., 1992; Mochkovitch et al., 1993), BH-WD (Fryer et al., 1999b), BH-He star (Fryer and Woosley, 1998), are the most popular models for the central engines of short-duration GRBs. The rates of compact object mergings do not follow the SFR. Their evolution times from their birth to their merging span from 10^7 yr to 10^{12} yr, so the merger rate is significantly delayed from the SFR. As a result, the mean redshift expected for these events is between 20% to 50% lower than that of collapsars (Fryer et al., 1999a). In any case, we expect that the shape of

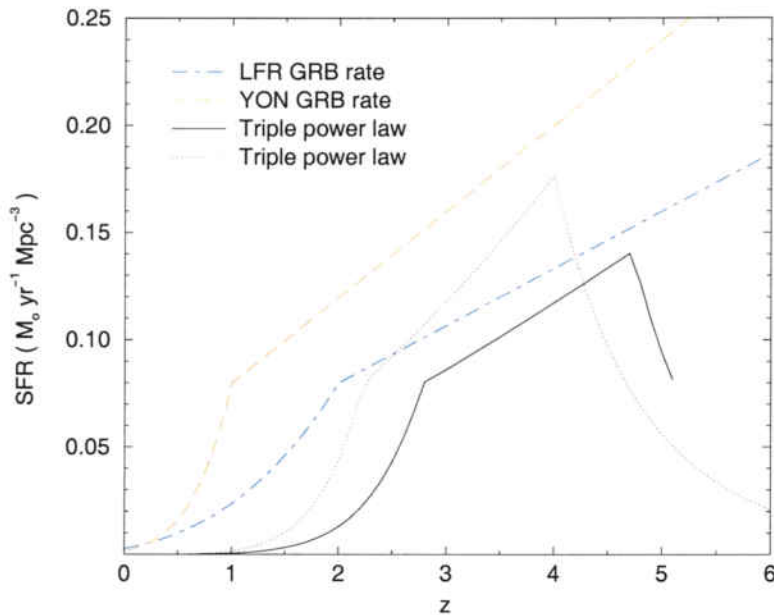


Figure 5.6: Two different triple power law models of the GRB explosion rate, as compared to the LFR and YON GRB rates.

our modelization of GRB rates (equation 5.15) will be general enough so as to fit a population of explosions delayed from the real SFR. As a matter of fact, simulations of merging rates as a function of redshift (Fryer et al., 1999b) have a double power law shape.

5.3.5 The luminosity function

First of all, we define the luminosity of a GRB as L in equation 5.16, where the limits have been chosen so as to reflect the sensitivity of BATSE⁴. $S(E)$ is the spectrum of a GRB (see section 5.3.6).

$$L \equiv \int_{20}^{2000} E S(E) dE \quad (5.16)$$

A luminosity function is a measure of the number of objects per unit luminosity. There are not enough GRBs yet, with known redshifts, as to determine an

⁴Approximately from 20 keV to 2000 keV (see section 2.2.2).

empirical luminosity function, but the observed fluxes from GRBs with reliable redshifts rule out, at least, the classical standard candle hypothesis (Frail et al., 2001). That is, not all GRBs have the same luminosity. In order to measure the luminosity function, one has to use indirect methods that can be divided in two main groups.

The first group (Schmidt, 1999b) assumes a variety of broken power law luminosity functions. From these luminosity functions, they obtain $\langle V/V_{max} \rangle$ and $\log N - \log P$ distributions to compare them with the observational ones.

The second group of tests uses luminosity calibrations to derive the luminosity function. The different luminosity correlations used are: variability–luminosity (Fenimore and Ramirez-Ruiz, 2000; Lloyd-Ronning et al., 2002; Schaefer et al., 2001; Yonetoku et al., 2004), spectral lag–luminosity (Schaefer et al., 2001; Norris, 2002), and spectral hardness–luminosity (Schmidt, 1999a).

All these methods use broken power laws for the luminosity function, spanning 2-3 orders of magnitude. Based on the most modern of these works (Yonetoku et al., 2004), our model of luminosity function is a broken power law, spanning 2.5 orders of magnitude, from $L = L_0/10$ to $L = 50 \times L_0$, L_0 being the break point:

$$\phi(L) = C \times \begin{cases} \left(\frac{L}{L_0}\right)^\kappa & 0.1L_0 \leq L < L_0 \\ \left(\frac{L}{L_0}\right)^\beta & L_0 \leq L \leq 50L_0 \end{cases} \quad (5.17)$$

LFR found $\kappa = -1.5$ and $\beta = -3.3$, while YON found $\kappa = -1.3$ and $\beta = -2.2$ (see Figure 5.7). However, these two groups include a particular feature for their luminosity function, that is, luminosity evolution.

5.3.5.1 Luminosity evolution

Most studies assume the luminosity function of GRBs to be independent of the redshift. However, it has been shown that this assumption is not valid for many astrophysical objects, such as galaxies (Marzke et al., 1994) and quasars (Hewett et al., 1993).

As stated in section 4.5, Balastegui et al. (2001) had already established

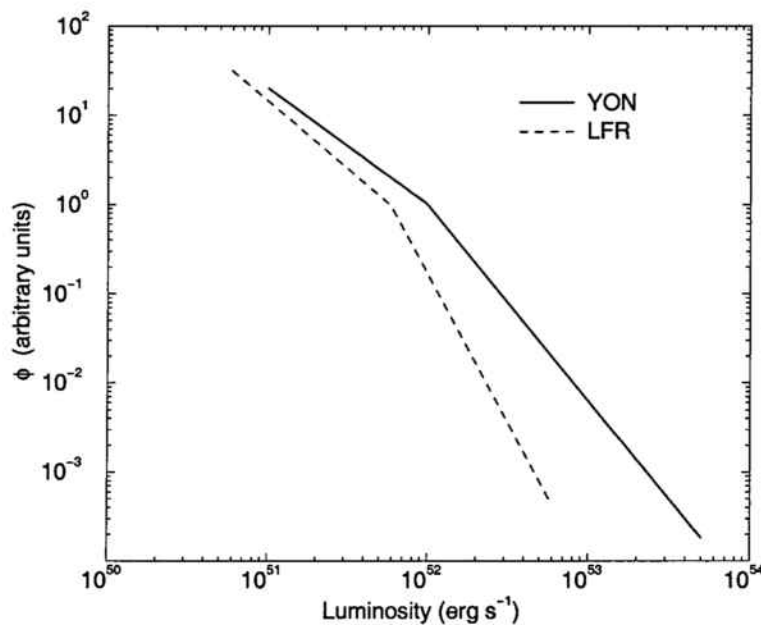


Figure 5.7: Luminosity functions measured by LFR and YON.

the existence of a luminosity evolution effect in GRB classes 2-II and 3-III. That evolution was first quantified by LFR. They assume a general, redshift dependent, luminosity function, like equation 5.18, where $Z = 1 + z$, and they model $\lambda(Z)$ as $\propto (1 + z)^\eta$.

$$\Psi(L, Z) = R_{GRB}(Z) \frac{\phi\left(\frac{L}{\lambda(Z)}\right)}{\lambda(Z)} \quad (5.18)$$

Their luminosity function, ϕ , depends on the redshift through $\lambda(Z)$ (see equation 5.19), which they find to be $\lambda(Z) \propto (1 + z)^{1.4 \pm 0.2}$. YON find a slightly higher value for the evolution, $\lambda(Z) \propto (1 + z)^{1.85 \pm 0.08}$. In equation 5.18, $R_{GRB}(z)$ corresponds to the rate of GRBs, while $\phi\left(\frac{L}{\lambda(Z)}\right)$ is the redshift dependent luminosity function shown in equation 5.19.

$$\phi\left(\frac{L}{\lambda(Z)}\right) = C \times \begin{cases} \left(\frac{L}{L_0 \lambda(Z)}\right)^\kappa & 0.1 L_0 \lambda(Z) \leq L < L_0 \lambda(Z) \\ \left(\frac{L}{L_0 \lambda(Z)}\right)^\beta & L_0 \lambda(Z) \leq L \leq 50 L_0 \lambda(Z) \end{cases} \quad (5.19)$$

With a positive evolution exponent, η , the luminosity function moves as a whole towards higher luminosities as the redshift increases. Taking into account

the effects of the luminosity evolution, the differential intensity distribution can be calculated from:

$$N(P_1 \leq P < P_2) = \frac{c}{H_0} \int_0^{z_{\max}} \frac{R_{GRB}(z)}{1+z} \frac{D^2(z)}{\sqrt{\Omega_M(1+z)^3 + \Omega_K(1+z)^2 + \Omega_\Lambda}} \frac{1}{(1+z)^\eta} dz$$

$$\times \int_{L(P_1,z)}^{L(P_2,z)} \phi\left(\frac{L}{(1+z)^\eta}\right) dL \quad (5.20)$$

The evolution suggests that GRBs are brighter at higher redshifts, implying that GRBs were brighter in the past. This could be the result of a physical variation in the progenitors.

Which is the difference between the Universe at high redshift and now?

Metallicity was lower. During generations, the stars have been enriching the Universe in metals as they eject the processed elements at the end of their lives. As a result, the metallicity of the Universe decreases as the redshift increases. Metallicity has two important effects in the evolution of stars. First on their birth: it makes easier to form very massive stars. More massive stars were formed at higher redshifts than now, that is, the IMF was shifted towards higher masses (Larson, 1998).

Moreover, lower metallicities mean also weaker stellar winds, so in addition to having more massive stars at high redshifts, those stars lose much less mass before they collapse, increasing the overall energy budget of the GRB progenitors.

The luminosity correlation with the redshift does not need to be related only to the progenitor mass, but it could also be due to a jet angle evolution (Donaghy et al., 2004).

In our study of the luminosity evolution, we will include all GRB classes, since various progenitors can give raise to the observed correlation.

5.3.6 The spectrum

In order to calculate the luminosity of a GRB (equation 5.16), one needs to know the spectrum of a gamma-ray burst, $S(E)$. The best modelization of a GRB spectrum is the functional form empirically proposed by Band et al. (1993):

$$S(E) = A \times \begin{cases} \left(\frac{E}{100\text{keV}}\right)^\alpha \exp\left[\frac{E(\beta-\alpha)}{E_{\text{break}}}\right] & E < E_{\text{break}} \\ \left(\frac{E_{\text{break}}}{100\text{keV}}\right)^{\alpha-\beta} \exp(\alpha-\beta) \left(\frac{E}{100\text{keV}}\right)^\beta & E \geq E_{\text{break}} \end{cases} \quad (5.21)$$

$S(E)$ is in units of $\text{photons cm}^{-2}\text{s}^{-1}\text{keV}^{-1}$. The Band spectrum is an asymptotically double broken power law, smoothly joined (see Figure 5.8). A is a normalizing factor. α is the low energy asymptotic exponent, and β is the high energy asymptotic exponent. E_{break} is the equivalent of the energy break in a double broken power law. Preece et al. (2000) found mean values of $\alpha = -1$ and $\beta = -2.25$, from a sample of 156 spectra of BATSE GRBs. The distribution of E_{break} is centered around 250keV . Since we need the value of E_{break} in the rest frame, and the typical redshift of a BATSE GRB is around $z = 1$, we will adopt a value of $E_{\text{break}} = 511\text{keV}$. This value has been typically chosen as a standard value in papers involving the fit of the $\log N - \log P$ distribution, for instance in Porciani and Madau (2001). It seems a reasonable break energy for spectra in an environment where, most probably, there exists a high density of e^-e^+ annihilations, much like the successful fireball model predicts (Rees and Mészáros, 1992; Mészáros and Rees, 1993b).

5.3.7 The peak flux

In the integral of the luminosity in equation 5.1, one needs to know the luminosity as a function of the peak flux, P , and the redshift, z , to establish the limits of the integral. The photon flux (in units of $\text{cm}^{-2} \text{s}^{-1}$) observed at Earth in the energy band covered by BATSE channels #2 and #3 ($50-300\text{keV}$), from a source radiating isotropically at a redshift z , is:

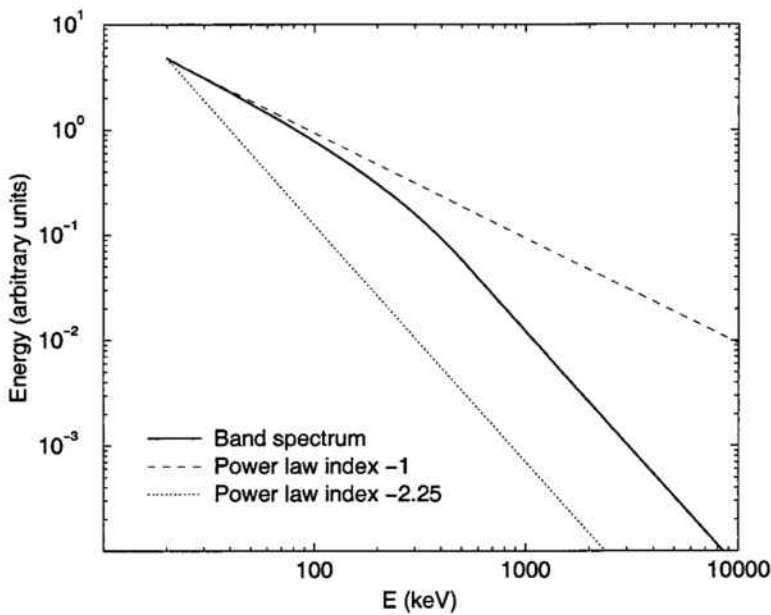


Figure 5.8: An example of a Band spectrum, together with the asymptotic simple power laws.

$$P(z) = \frac{\int_{(1+z)50}^{(1+z)300} S(E)dE}{4\pi D^2(z)(1+z)} \quad (5.22)$$

Multiplying equation 5.22 by the luminosity and dividing it by the definition of luminosity (equation 5.16), one obtains the peak flux as a function of redshift and luminosity.

$$P(L, z) = \frac{\int_{(1+z)50}^{(1+z)300} S(E)dE}{4\pi D^2(z)(1+z)} \frac{L}{\int_{20}^{2000} ES(E)dE} \quad (5.23)$$

Isolating the luminosity in equation 5.23, one obtains the function $L(P, z)$, needed to calculate the limits of the luminosity integral in equation 5.1.

$$L(P, z) = \frac{4\pi D^2(z)(1+z) P \int_{20}^{2000} ES(E)dE}{\int_{(1+z)50}^{(1+z)300} S(E)dE} \quad (5.24)$$

In this equation, the normalization factor of the spectrum, A , vanishes, and therefore it is not needed to compute the luminosity.

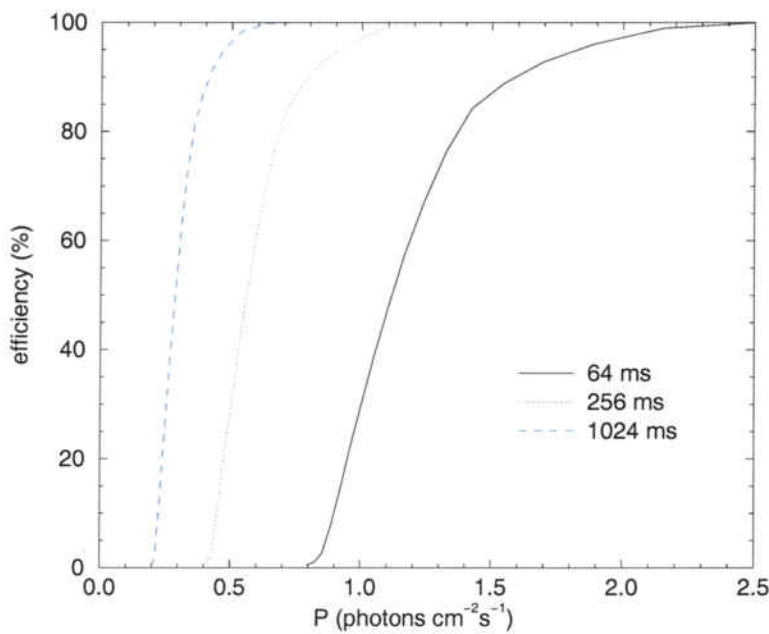


Figure 5.9: GRB detection efficiency, as a function of peak flux, for each of the three integration timescales of BATSE.

5.4 Building the observational intensity distributions

Up to now, all the parameters have been defined, and we have established the numerical relations and equations needed to compute the theoretical differential intensity distribution of GRBs. How to construct the observational intensity distributions from BATSE data will be described in this section.

First, we account for the number of GRBs in bins of peak flux for each GRB class. We use bins of equal widths in logarithmic space, using 20 bins per decade. The number of GRBs per bin has to be corrected for the detection efficiency of BATSE. Figure 5.9 shows the detection efficiency for each of the integration timescales as a function of peak flux. This efficiency gives the detection probability of a GRB with a certain peak flux. Therefore, for each GRB one has to account for 1 divided by the detection probability (probability from 0 to 1).

How to choose the timescale for the peak flux?

As seen in Figure 5.9, the detection efficiency at low peak fluxes increases with longer integration timescales. So, apparently, one should use the peak flux with the longest integration timescale. However, as stated in the introduction of this chapter, using an integration time longer than the variation timescale of the GRB smoothes the lightcurve and causes to measure a peak flux lower than the real one. More explicitly, if the typical variation timescale of the lightcurve of a GRB is 64 ms , and during the peak flux interval of 64 ms it emits $1024\text{ photons cm}^{-2}$, that makes a flux of $1024/0.064 = 16000\text{ photons s}^{-1}\text{cm}^{-2}$. If one measures the flux in 1024 ms intervals, during the peak flux interval we will measure less than 16×1024 , since during the 16 intervals of 64 ms that compose the 1024 ms interval, only in one we receive 1024 photons , while in the other 15 intervals we receive less than 1024 photons . Consequently, one has to reach a compromise between choosing the peak flux with the longer integration timescale, and choosing an integration timescale shorter than the typical variation timescale of the GRB.

The short-duration classes of GRBs, including here classes 2-I and 3-I, contain a fair number of GRBs with duration lower than 1024 ms , and even lower than 256 ms . For these classes of GRBs we take the peak flux in the 64 ms integration timescale. The distribution of T_{90} for the other classes of GRBs (see Figures 4.9 and 4.11) shows very few bursts of duration less than 1 s for class 3-II, while none for classes 2-II and 3-III. Although this fact does not ensure that the typical variation timescale be longer than 1024 ms , we will use this integration timescale for the peak flux in order to benefit from the higher detection efficiency. This is also the timescale chosen by all the studies of the intensity distribution already referred to in this chapter. Figures 5.10 and 5.11 show lightcurves of GRBs of classes 3-II and 3-III, respectively. These figures show typical lightcurves of long-duration GRBs which are of shorter duration than the average of their class. One can say that their variation timescale is longer than 1024 ms , or in the case of Figure 5.10, of the order of 1024 ms . This fact could not be true for all GRBs of these classes, but as it is true in general, we assume that the bias introduced by using this timescale is far smaller than the benefit of the higher detection efficiency.

Table 5.1 gives the detection efficiency represented in Figure 5.9. In order to avoid introducing large corrections for detection efficiency, we will not account for GRBs with peak fluxes with detection efficiencies lower than 50%. For the integration timescale of 64 ms , the first peak flux interval with efficiency greater than

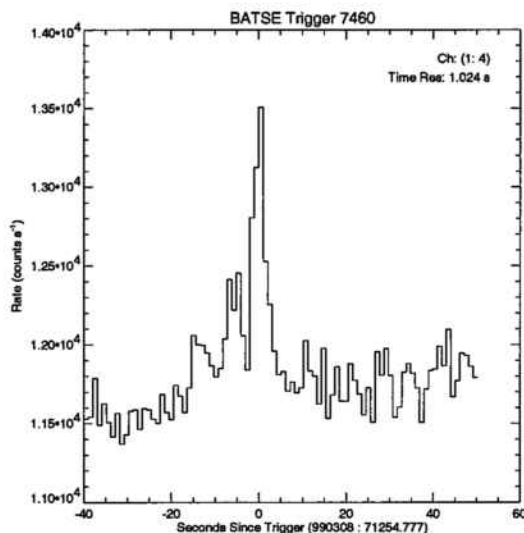


Figure 5.10: Example of a lightcurve of a GRB of class 3-II.

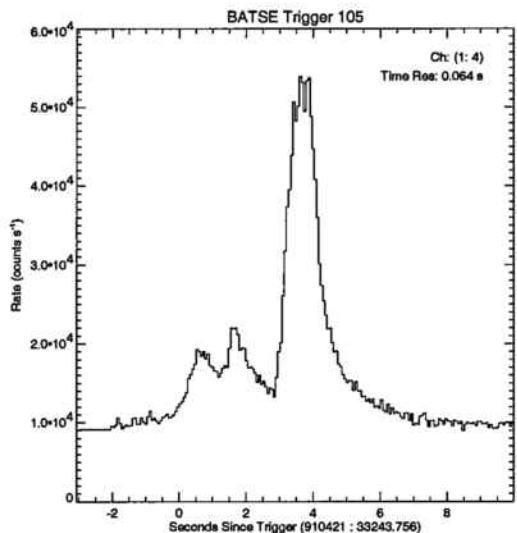


Figure 5.11: Example of a lightcurve of a GRB of class 3-III.

50% is $1.122 - 1.259 \text{ photon cm}^{-2}\text{s}^{-1}$, while for the 1024 ms integration timescale it is $0.3162 - 0.3548 \text{ photon cm}^{-2}\text{s}^{-1}$.

The number of bursts per bin is indeed the number of bursts per bin detected in the whole of BATSE's lifespan. The time interval between two bursts being a random variable, the distribution of the number of bursts in a peak flux interval should be a Poisson distribution, which is characterized by having an error in the number of counts equal to the squared root of that number of counts. As a result, the uncertainties in the number of GRBs per peak flux bin are taken to be $\pm\sqrt{N}$.

Table 5.2 summarizes the observed intensity distributions after accounting for the effects already mentioned. In the end, we obtain 29 bins for class 2-I, 41 bins for class 2-II, 26 bins for class 3-I, 28 bins for class 3-II, and 41 bins for class 3-III.

Figure 5.12 shows the plots of the intensity distributions for all classes of GRBs. For clarity, the number of bursts in each interval is represented as a filled circle in the center of each bin, instead of the classical stair steps of a histogram. The error bars seem asymmetric, although they are not, due to the logarithmic scale of the axis.

64 ms		256 ms		1024 ms	
Peak flux ($\text{photon cm}^{-2}\text{s}^{-1}$)	Efficiency (%)	Peak flux ($\text{photon cm}^{-2}\text{s}^{-1}$)	Efficiency (%)	Peak flux ($\text{photon cm}^{-2}\text{s}^{-1}$)	Efficiency (%)
0.798	0.525	0.399	0.374	0.200	0.345
0.825	1.126	0.412	0.962	0.206	0.874
0.854	2.659	0.427	2.515	0.214	2.282
0.886	7.692	0.443	7.510	0.221	6.864
0.921	14.102	0.461	13.807	0.230	12.464
0.960	22.307	0.480	21.900	0.240	19.757
1.003	30.268	0.502	29.879	0.251	26.950
1.051	39.003	0.526	38.654	0.263	35.085
1.106	48.173	0.553	47.720	0.276	43.495
1.168	57.535	0.584	57.144	0.292	52.898
1.240	67.035	0.620	66.693	0.310	62.781
1.324	76.202	0.662	76.024	0.331	72.333
1.424	84.271	0.712	84.092	0.356	80.937
1.546	88.856	0.773	88.775	0.386	86.426
1.696	92.777	0.848	92.696	0.424	91.100
1.890	96.059	0.945	96.012	0.473	95.123
2.152	98.886	1.076	98.857	0.538	98.281
2.527	99.951	1.263	99.944	0.632	99.696
3.124	99.996	1.562	99.996	0.781	99.988
6.247	100.000	3.124	100.000	1.562	100.000

Table 5.1: Efficiency, in percentage of detection probability, for each of the peak flux integration timescales. As an example of usage, a burst with a peak flux of $0.424 \text{ photon cm}^{-2}\text{s}^{-1}$ in the 1024 ms integration timescale, has a probability of 91.1% of being detected.

Peak flux interval ($\text{photon cm}^{-2}\text{s}^{-1}$)	2-I (N)	2-II (N)	3-I (N)	3-II (N)	3-III (N)
0.3162–0.3548		14.911		16.296	5.436
0.3548–0.3981		18.700		17.676	8.206
0.3981–0.4467		24.108		22.036	10.914
0.4467–0.5012		28.500		23.225	12.631
0.5012–0.5623		21.452		19.471	12.230
0.5623–0.6310		32.273		18.169	20.165
0.6310–0.7079		45.101		26.061	27.060
0.7079–0.7943		33.025		16.010	25.022
0.7943–0.8913		43.005		20.002	31.003
0.8913–1.0000		36.003		20.002	24.002
1.0000–1.1220		43.003		20.002	30.002
1.1220–1.2589	50.752	52.003	38.055	9.001	44.003
1.2589–1.4125	38.822	29.001	27.188	9.000	25.001
1.4125–1.5849	37.974	41.000	31.017	15.000	33.000
1.5849–1.7783	40.179	29.000	33.714	16.000	25.000
1.7783–1.9953	32.344	40.000	27.121	8.000	36.000
1.9953–2.2387	36.639	26.000	32.563	9.000	22.000
2.2387–2.5119	41.200	35.000	36.177	9.000	30.000
2.5119–2.8184	29.012	34.000	23.010	3.000	32.000
2.8184–3.1623	32.005	27.000	27.004	3.000	26.000
3.1623–3.5481	32.001	27.000	27.001	5.000	25.000
3.5481–3.9811	14.000	28.000	12.000	4.000	25.000
3.9811–4.4668	16.000	22.000	11.000	5.000	21.000
4.4668–5.0119	14.000	17.000	11.000	1.000	16.000
5.0119–5.6234	18.000	18.000	17.000	4.000	15.000
5.6234–6.3096	11.000	16.000	10.000	3.000	15.000
6.3096–7.0795	12.000	16.000	11.000	1.000	16.000
7.0795–7.9433	12.000	6.000	10.000	1.000	6.000
7.9433–8.9125	10.000	16.000	9.000		16.000
8.9125–10.0000	3.000	8.000	3.000		7.000
10.0000–11.2202	9.000	11.000	9.000		11.000
11.2202–12.5893	4.000	13.000	2.000		13.000
12.5893–14.1254	8.000	8.000	6.000		8.000
14.1254–15.8489	4.000	6.000	4.000		6.000
15.8489–17.7828	2.000	10.000	1.000		10.000
17.7828–19.9526	3.000	9.000	2.000		9.000
19.9526–22.3872	1.000	4.000	1.000		4.000
22.3872–25.1189	1.000	3.000			3.000
25.1189–28.1838	2.000	3.000			3.000
28.1838–31.6228	2.000	4.000			4.000
31.6228–35.4813		3.000			3.000

Table 5.2: Observed intensity distributions for each class of GRB. In this table it is shown the number of GRBs detected in each peak flux interval. Non-integer numbers are due to the correction for detection efficiency.

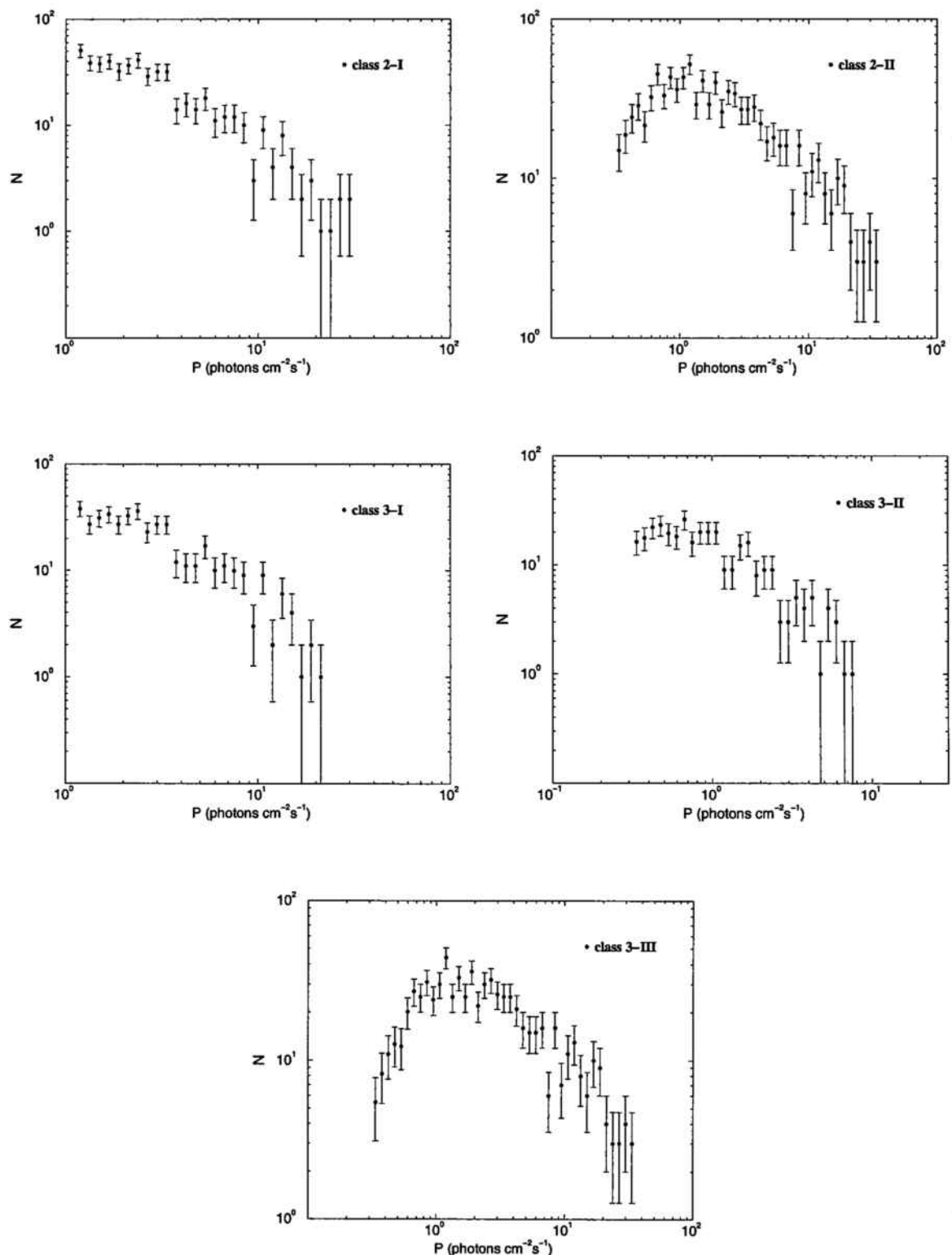


Figure 5.12: Observed intensity distributions for each class of GRB. The error bars are $\pm \sqrt{N}$.

5.5 Fitting the intensity distribution

We want to find the best values for the 9 free parameters of the intensity distribution (10 parameters when we account for luminosity evolution). For this task, we will minimize the χ^2 parameter. In equation 5.25, N_i stands for the observed number of GRBs, n_i stands for the theoretical number of GRBs, and σ_i stands for the uncertainty in the observed number of GRBs, which is $\sqrt{N_i}$.

$$\chi^2 = \sum_i^{nbins} \left(\frac{N_i - n_i}{\sigma_i} \right)^2 \quad (5.25)$$

If the measurement errors are normally distributed, the probability distribution of the quantity χ^2 is the chi-squared distribution with a number of degrees of freedom equal to the number of bins minus the number of free parameters and minus one. We subtract one degree of freedom due to the fact that we normalize the total number of GRBs observed. That is, all the proportionality constants included in the GRB rate and in the luminosity function are taken so as to obtain the total number of GRBs observed during BATSE's lifespan.

In order to test the gaussianity of the errors, we applied a Kolmogorov-Smirnov test (Press et al., 1986) to the errors. The results are summarized in Table 5.3. As with all statistical tests of this kind, one can never prove that a given distribution is equal to another one besides admitting that, given the similarity one cannot reject, with enough confidence, that they be the same. The significance level, p , obtained with this test, gives the probability of being wrong when one assumes that both distributions are different. If p is high, it means that you cannot reject their being the same distribution. A typical value to reject the equivalence is if $p < 0.05$, and this is only true for GRBs of class 3-II. For the other classes one can assume the gaussianity of the errors.

The nongaussianity of the errors does not by itself invalidate our minimization. We have defined our figure-of-merit for the minimization as equation 5.25, and taken this value, χ^2 , as a measure of dissimilarity between the observed and theoretical intensity distributions. We will give the best value for every free parameter as the one that minimizes χ^2 . The problem arises when one wants to give a confidence

GRB Class	2-I	2-II	3-I	3-II	3-III
p	> 0.15	> 0.15	0.12	0.03	0.12

Table 5.3: Significance levels for each class of GRB, when errors are tested against normality with a Kolmogorov-Smirnov test.

level, or a confidence interval, for the obtained parameters. In this case, if the errors are not normally distributed, then one does not know the probability distribution of the quantity χ^2 , making it impossible to give a confidence level, or a confidence interval on the basis of a chi-squared distribution. In this case, one would need to run Monte Carlo simulations of synthetic data sets in order to give a confidence level, or a confidence interval. As it will be explained in the next section, the minimization demands a great deal of computing time, lasting about 24 hours. As a result, it is impractical the use of Monte Carlo simulations to compute a confidence interval, due to the fact that one needs at least of the order of one thousand minimizations.

Assuming the gaussianity of the errors, we will compute the confidence intervals for each parameter as it follows. If one perturbs the parameters away from their values at χ^2_{min} , then χ^2 increases. The region within which χ^2 increases by no more than a set amount, $\Delta\chi^2$, defines some n-dimensional confidence region around the parameter's values at χ^2_{min} . The 1σ confidence interval is normally used, which has 68.3% probability of including the real value of the parameter. The 1σ confidence interval for an individual parameter is characterized by having a $\Delta\chi^2 = 1$ with respect to χ^2_{min} . So, to compute the confidence interval for an individual parameter, say p_1 , we perturb its value around the minimum, and then we minimize χ^2 with respect to the rest of the parameters. Then we model the function $\chi^2(p_1)$ as a parabola, defining the limits of the 1σ confidence interval as those points in the parabola with values equal to $\chi^2_{min} + 1$. Figure 5.13 shows an example of the confidence interval calculation for the z_2 parameter for class 3-II GRBs. The black circles are the χ^2 values found from the minimization of the other parameters at fixed values of z_2 . The blue line is the fitted second order polynomial. The green triangles show the key points: the χ^2_{min} and the $\chi^2_{min} + 1$ over the parabola, which are the limits of the 1σ confidence interval. In this case, the real value of z_2 is between 4.23 and 5.75 with 68.3% of probability.

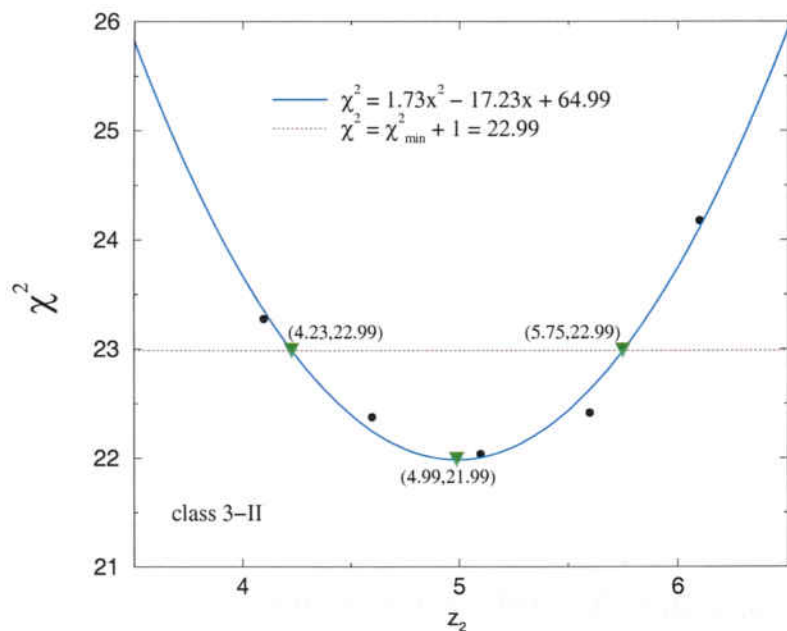


Figure 5.13: Confidence interval calculation for the parameter z_2 of class 3-II GRBs. The black circles are the χ^2 values found from the minimization of the other parameters at fixed values of z_2 . The blue line is the fitted second order polynomial. The green triangles show the key points: the χ^2_{\min} and the $\chi^2_{\min} + 1$ over the parabola.

5.5.1 The minimization

Finding a local minimum is a trivial problem for numerical techniques, but finding the global minimum is indeed a very difficult problem, sometimes even impossible. In order to be sure that a minimum is the global minimum you would need to explore the whole space. One can imagine that in a nine- or ten-dimensional problem this is not feasible with the current computation power. A pentium 4@3GHz takes almost 1 s to compute the intensity distribution for a set of given parameters. If one had to construct a very sparse grid with 100 nodes per parameter, one would need 100^9 s of processor time, that is $\sim 32Gyr$, more than twice the age of the Universe. To finish the calculation in one thesis mean lifetime, one would need ten thousand million processors, definitely out of any science department budget.

Following the Powell's method for minimization in multidimensions (Press et al., 1986) we will search for 100 minimums, choosing random starting points. The lower of these minima will be interpreted as the global minimum. As it has already been explained, it is virtually impossible to find the real global minimum, and it is impossible to ensure that a minimum is the global minimum.

As we have seen, each of the ten free parameters have been already measured with different techniques. Therefore, to speed up the computation, and search in a range somewhat compatible with the current measures, we will limit the minimum search to the following region:

- Gamma-ray burst rate:

- ▷ $1 \leq z_1 \leq 4$
- ▷ $4 \leq z_2 \leq 15$
- ▷ $1 \leq e_1 \leq 8$
- ▷ $-5 \leq e_2 \leq 5$
- ▷ $-10 \leq e_3 \leq 5$
- ▷ $5 \leq z_{max} \leq 30$

- Luminosity function:

- ▷ $10^{51} \text{ erg s}^{-1} \leq L_0 \leq 5 \cdot 10^{53} \text{ erg s}^{-1}$
- ▷ $-5 \leq \kappa \leq 5$
- ▷ $-5 \leq \beta \leq 5$
- ▷ $0 \leq \eta \leq 5$

The results, when not degenerate, are always well within the limited region established. So this a priori limitation does not prevent finding the best values of the parameters presented here. These results will be discussed in the following chapter.

Chapter 6

The $\log N - \log P$ fits

Here are presented the results of the analysis described in the previous chapter. First, it is shown a best set of parameters obtained for each class of GRB, giving also an estimate of their uncertainties and the χ^2 values of the best fits. After discussing some general trends, it comes a thorough study of the GRB rate and luminosity function in terms of each of the individual parameters involved. Later on, it is introduced the issue of fitting cosmological parameters. Finally, a set of future simulations is presented, followed by the conclusions.

6.1 The best fits

Tables 6.1 and 6.2 summarize the values of χ^2 for the best fits of each GRB class. The reduced χ^2 , $\hat{\chi}^2$, is the value of χ^2 divided by the number of degrees of freedom. The probability value, p , is the probability of obtaining a larger value for χ^2 , that is, a worst χ^2 . A typical value for p below which one can reject the fact of the theoretical intensity distribution being representative of the observed one is 0.05. Since all p values obtained for any of the GRB classes are greater than 0.05, one can accept that they are constituted by a cosmological population characterized by the set of parameters shown in Tables 6.3 and 6.4. It is convenient to remind that this test can never prove the real nature of the population, that is, it does not prove the extragalactic origin of each class, but rather implies that it is compatible with

GRB class	χ^2	bins	<i>d.o.f.</i>	$\hat{\chi}^2 = \frac{\chi^2}{d.o.f.}$	<i>p</i>
2-I	23.3	29	19	1.22	0.23
2-II	37.6	41	31	1.21	0.19
3-I	25.0	26	16	1.56	0.07
3-II	22.1	28	18	1.23	0.23
3-III	31.5	41	31	1.02	0.44

Table 6.1: χ^2 values of the best fits without luminosity evolution. Nine parameters are fitted at the same time. The number of degrees of freedom is then the number of bins, minus nine, from the fitted parameters, minus one, from the normalization of the total number of GRBs observed.

a cosmological distribution. Only when the determination of several distances for GRBs show an extragalactic origin for the phenomenon, as it has been measured for long-duration GRBs, then one can say that the differential intensity distribution can be calculated from equation 5.1 (or 5.20 if there is luminosity evolution), and therefore the parameters of that class of GRBs can be determined by the procedure of fitting the intensity distribution.

The higher $\hat{\chi}^2$ values found are those for the fits of class 3-I. The *p* values for these fits are, in fact, in the limit of what is usually acceptable for a fit, that is *p* = 0.05. This fact cannot be attributed to the high dispersion in the observed intensity distribution, since class 3-I has a sample of 531 GRBs, much more than the number of GRBs of class 3-II, equal to 341. Its intensity distribution has also less bins than that of class 3-II, having thus more events per bin and consequently lower error and dispersion. The bad fit is then significative. If there really exists three different classes of GRBs, those represented here as class 3-I, the shortest ones, would be the main suspects for being of galactic origin, but we already know that very short GRBs are of extragalactic origin (Castro-Tirado et al., 2005; Villasenor et al., 2005). The measurement of several distances to short, and intermediate-duration GRBs, could settle the existence, or not, of three different classes of GRBs, either if it is concluded or not that they have different distance scales, or different energy budgets.

Obviously, as one adds more parameters to a model much better has to become the χ^2 obtained from the fit, because this new parameter could always adopt the value it had before being a free parameter, so that χ^2 would be the same as

6.1. The best fits

GRB class	χ^2	bins	d.o.f.	$\hat{\chi}^2 = \frac{\chi^2}{d.o.f.}$	p
2-I	22.4	29	18	1.24	0.21
2-II	37.6	41	30	1.25	0.16
3-I	24.8	26	15	1.65	0.05
3-II	22.0	28	17	1.29	0.18
3-III	30.6	41	30	1.02	0.44

Table 6.2: χ^2 values of the best fits with luminosity evolution. Ten parameters are fitted at the same time. The number of degrees of freedom is then the number of bins, minus ten, from the fitted parameters, minus one, from the normalization of the total number of GRBs observed.

before. However, at the same time the inclusion of a new parameter reduces the number of degrees of freedom and, as a result, a lower χ^2 does not necessarily imply higher probability value. This is what happens in the case of luminosity evolution for all classes of GRBs, all p values with evolution are lower than those obtained without luminosity evolution, except for class 3-III GRBs that is equal in both cases. Moreover, for class 2-II GRBs, the minimum value for χ^2 is the same as the one with no evolution. It can be said that the smooth theoretical distribution cannot fit better the observed one, due to the dispersion of the latter, arising from the small number of GRBs per peak flux interval. The minimum χ^2 is saturated. One needs then a much larger number of observed events, that will reduce the dispersion of the observed distribution, in order to discriminate the existence of luminosity evolution or the lack of it. This will be clearly seen in section 6.5, where with a simulated set of 10000 GRBs a much better fit is obtained when including the luminosity evolution parameter.

Tables 6.3 and 6.4 show the set of parameters which minimizes χ^2 for each class of GRBs, both without and with luminosity evolution respectively. The uncertainties of each parameter, computed as described in section 5.5, are also included. The symbol † indicates that a parameter is absolutely degenerate, meaning that it cannot be measured because it has an uncertainty larger than twice the region originally explored by the minimization algorithm (see section 5.5.1). This fact has two possible causes:

- The combined variation of the intensity distribution as a function of the rest

	2-I	2-II	3-I	3-II	3-III
z_1	2.1^{\dagger}	$3.3^{+0.8}_{-0.5}$	$4.0^{+3.6}_{-2.2}$	$2.9^{+1.7}_{-1.1}$	$3.4^{+1.1}_{-0.6}$
z_2	—	$5.2^{+0.1}_{-1.7}$	—	$5.1^{+0.7}_{-0.9}$	$4.6^{+0.3}_{-0.7}$
e_1	8.0^{\dagger}	$2.4^{+0.5}_{-0.9}$	8.0^{\dagger}	7.5^{\dagger}	$2.1^{+0.6}_{-0.7}$
e_2	$3.9^{+1.2}_{-1.9}$	$3.4^{+2.0}_{-0.3}$	$3.8^{+0.8}_{-1.2}$	$3.3^{+1.9}_{-1.8}$	$4.1^{+3.0}_{-1.4}$
e_3	—	$0.0^{+1.0}_{-0.2}$	—	-3.1^{\dagger}	$0.1^{+0.6}_{-0.5}$
z_{max}	$6.8^{+1.4}_{-1.6}$	$9.8^{+1.5}_{-1.6}$	$9.4^{+0.6}_{-1.1}$	$13.5^{+\dagger}_{-8.5}$	$9.3^{+1.3}_{-0.5}$
L_0 ($erg\ s^{-1}$)	$8.1^{+4.5}_{-4.6}\ 10^{51}$	$5.4^{+2.1}_{-1.4}\ 10^{51}$	$1.7^{+2.6}_{-1.1}\ 10^{52}$	$3.0^{+2.3}_{-2.9}\ 10^{53}$	$4.8^{+2.1}_{-0.7}\ 10^{51}$
κ	$-5.0^{+1.6}_{-1.6}$	-1.1^{\dagger}	-5.0^{\dagger}	$-3.5^{+1.5}_{-1.6}$	-0.2^{\dagger}
β	$-1.0^{+3.4}_{-0.5}$	$0.1^{+1.8}_{-0.4}$	$-1.0^{+7.2}_{-1.2}$	$-0.6^{+4.7}_{-5.8}$	$1.0^{+0.8}_{-0.4}$

Table 6.3: Best parameters for each class of GRBs without luminosity evolution. The symbol \dagger indicates that a parameter is degenerate. For classes 2-I and 3-I, z_2 is higher than z_{max} ; therefore, neither z_2 nor e_3 do have any sense for their explosion rates.

of the parameters mimics the variation of the intensity distribution due to the degenerate parameter.

- The variation of the parameter itself does not produce any significant variation of the intensity distribution.

Although a value is given for a degenerate parameter, that value being the one obtained from the minimization algorithm, it actually has no meaning, since any other value would give the same χ^2 , always with different values for the other parameters, but also always within their uncertainty interval. It is also important to remind at this point that the errors in the intensity distribution of class 3-II GRBs cannot be considered as being normally distributed. Consequently, the confidence intervals given here are to be interpreted as lower limits, meaning that the interval containing the real value with 68.3% probability is always larger than the one given here, and can only be delimited by means of a series of Monte Carlo simulations.

As it can be seen, classes 2-I and 3-I without luminosity evolution do not have a second break in the GRB rate. That is because the minimum of χ^2 is obtained for values of z_2 greater than those of z_{max} . A thorough discussion of the best parameters, their uncertainties, degeneracy, and implications, comes in the next sections.

	2-I	2-II	3-I	3-II	3-III
z_1	1.0 [†]	$2.7^{+1.3}_{-0.9}$	$3.2^{+8.4}_{\dagger}$	$2.9^{+2.0}_{-1.5}$	$5.0^{+1.0}_{-1.0}$
z_2	$15.0^{+11.2}_{-11.2}$	$9.6^{+4.2}_{-3.7}$	15.0 [†]	$5.5^{+2.8}_{-1.3}$	$8.0^{+2.1}_{-2.8}$
e_1	4.4 [†]	7.9 [†]	$2.8^{+7.2}_{-6.4}$	$7.4^{+5.9}_{-3.8}$	$1.3^{+0.3}_{-0.5}$
e_2	$2.1^{+2.1}_{-1.4}$	$2.1^{+1.5}_{-1.3}$	$2.2^{+8.4}_{-4.8}$	$2.9^{+2.5}_{-2.4}$	$2.9^{+1.5}_{-0.4}$
e_3	-0.8 [†]	$0.1^{+1.0}_{-1.4}$	1.3 [†]	-2.3 [†]	$0.7^{+0.2}_{-0.5}$
z_{max}	18.7 [†]	$30.0^{+26.7}_{-6.3}$	$16.0^{+5.0}_{-8.0}$	27.9 [†]	$29.9^{+17.1}_{-6.8}$
L_0 ($erg\ s^{-1}$)	$1.0^{+0.7}_{-0.7}\ 10^{51}$	$8.2^{+5.7}_{-3.2}\ 10^{52}$	$1.0^{+3.6}_{-0.5}\ 10^{52}$	$2.0^{+1.1}_{-1.9}\ 10^{53}$	$1.6^{+2.6}_{-0.4}\ 10^{51}$
κ	$-5.0^{+3.8}_{-8.7}$	$-2.0^{+2.9}_{-2.0}$	$-5.0^{+1.5}_{-3.5}$	$-3.6^{+3.7}_{-1.5}$	-4.5 [†]
β	$-1.0^{+1.7}_{-1.0}$	$-1.8^{+1.9}_{-2.2}$	$-0.8^{+3.2}_{-1.3}$	$-0.3^{+0.3}_{\dagger}$	$1.2^{+1.3}_{-0.3}$
η	$1.5^{+0.9}_{-1.1}$	$1.4^{+0.3}_{-1.2}$	$1.5^{+0.4}_{-1.1}$	$0.3^{+1.2}_{-1.4}$	$1.2^{+0.1}_{-0.3}$

Table 6.4: Best parameters for each class of GRBs with luminosity evolution. The symbol \dagger indicates that a parameter is degenerate.

A quick look at Tables 6.3 and 6.4 reveals that with class 2-I GRBs almost nothing can be said about the GRB rates, since most of their parameters are degenerate. As for the luminosity function, its low energy power law index, κ , is either totally degenerate or it has a high uncertainty for nearly every class. In general, classes 2-II and 3-III appear to be the ones most suitable to measure the GRB's parameters presented in this work. Certainly, this was expected due to the fact that these classes are populated in a number significantly higher than the other ones. Moreover, their differential intensity distribution also carries more information, since it covers a wider range of peak fluxes. In addition to this, the shape of the distribution is more complex, with various turns that change position and angle as the parameters vary.

Figures 6.1 and 6.2 show the best fits of the differential intensity distributions for each class of GRB, without and with luminosity evolution, respectively. Bear in mind that we are comparing distributions, number of GRBs per peak flux intervals, which are commonly plotted as stair steps plots. Here, in order not to get confused with overplotted lines, we have chosen to show the middle points of the intervals of the observed distribution with their error bars, and a continuous line joining the corresponding central points of the theoretical distribution.

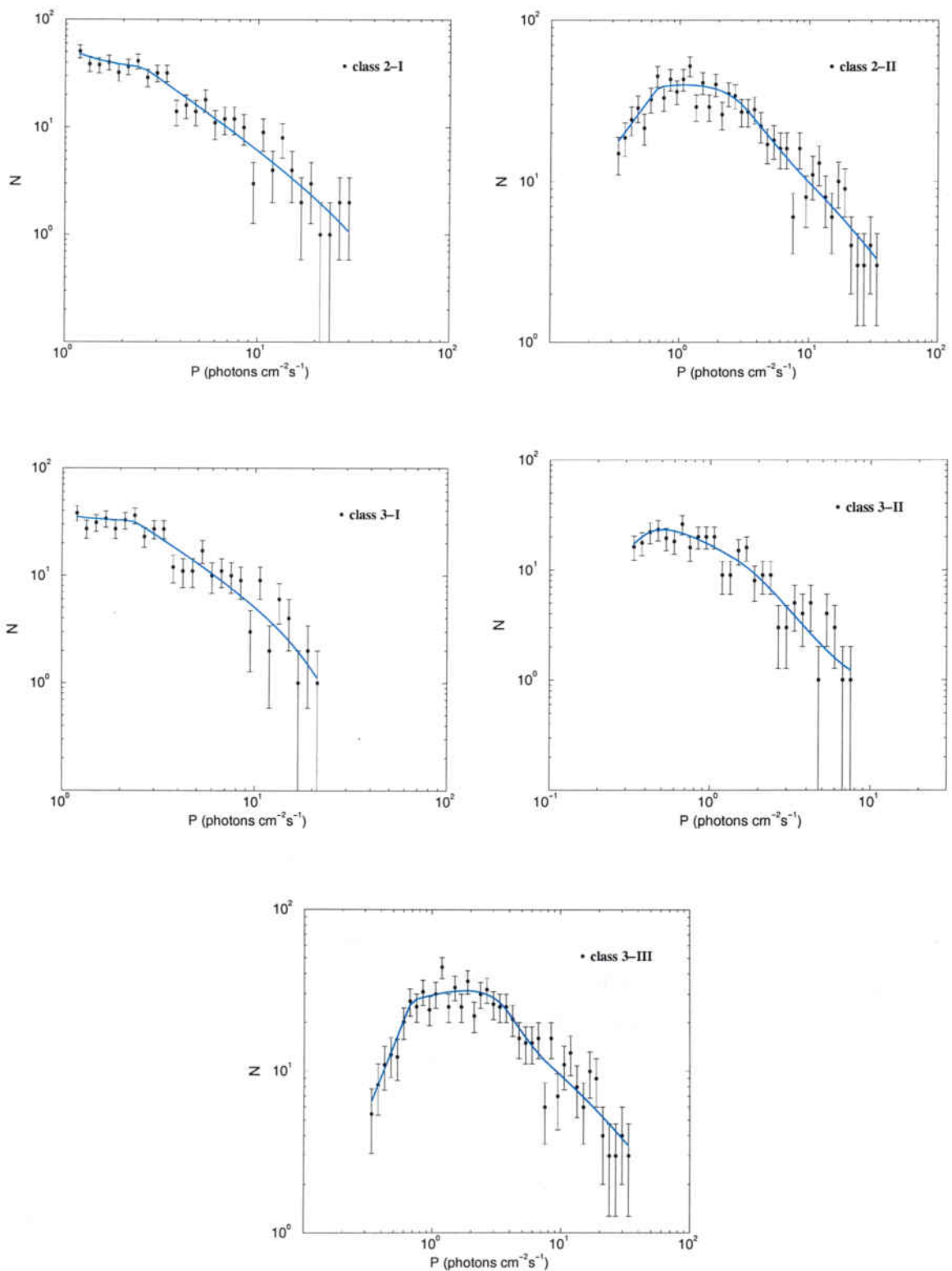


Figure 6.1: Best fits of the intensity distributions for each class of GRB without luminosity evolution. The black filled circles with error bars correspond to the observed differential intensity distribution. The thick blue line is the theoretical best fit.

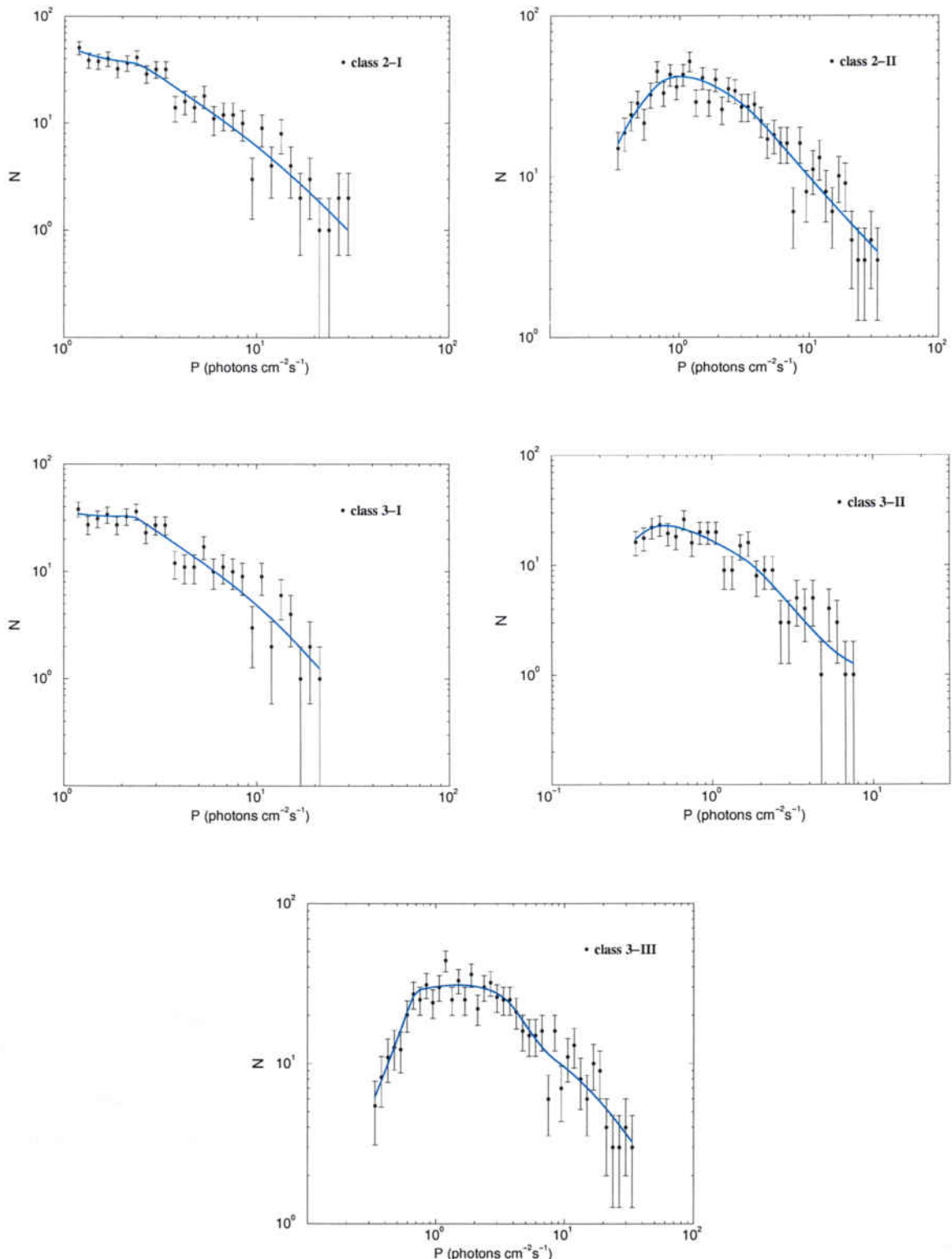


Figure 6.2: Best fits of the intensity distributions for each class of GRB with luminosity evolution. The black filled circles with error bars correspond to the observed differential intensity distribution. The thick blue line is the theoretical best fit.

The intensity distributions of classes 2-I and 3-I are quite similar, so there are the parameters derived from them, both with and without luminosity evolution. The main difference between these two classes is that 2-I extends two bins more towards high peak fluxes than 3-I, and the latter decreases faster from $P = 10 \text{ photons cm}^{-2}\text{s}^{-1}$ upwards. As far as long-duration GRBs are concerned, the differential intensity distributions of classes 2-II and 3-III cover the same range of peak fluxes, but class 3-III has a smaller fraction of GRBs at low peak fluxes. As for class 3-II, its intensity distribution cannot be compared with any other, and it represents the transition between the shape of the intensity distributions of short to long-duration GRBs.

6.2 The gamma-ray burst explosion rate

Figure 6.3 shows the GRB rate for classes 2-I and 2-II without luminosity evolution. As it can be seen from Table 6.3, the parameters z_1 and e_1 for class 2-I are degenerate, so nothing can be said with certainty about the GRB rate of this class. On the contrary, the GRB rate for class 2-II is one of the best determined parameters, together with the GRB rate for class 3-III. For class 2-II, the GRB rate increases from $z = 0$ to $z \sim 5$ with a power law of exponent ~ 3 , and then it keeps constant up to a maximum redshift $z_{\max} \sim 10$.

Figure 6.4 shows the GRB rate for classes 2-I and 2-II with luminosity evolution. Here again, the parameters of the explosion rate for class 2-I GRBs are degenerate. As a conclusion, the differential intensity distribution for classical short-duration GRBs is not sensitive to the explosion rate, at least for the number of GRBs observed as of today. As for the class 2-II GRB rate, it is similar to that obtained without the luminosity evolution. Although e_1 is degenerate, it can be said that the GRB rate increases up to $z_2 \sim 10$, and from there it keeps almost constant until at least $z_{\max} \sim 25$, but this parameter still has a large uncertainty. The cause of the degeneracy of e_1 is that, as Figure 6.20 shows, the fraction of GRBs detected below $z \sim 2$ is extremely low, so the shape of the GRB rate below $z_1 = 2.7$ does not affect the overall shape of the differential intensity distribution.

The GRB rates for the three-class classification, without and with luminosity

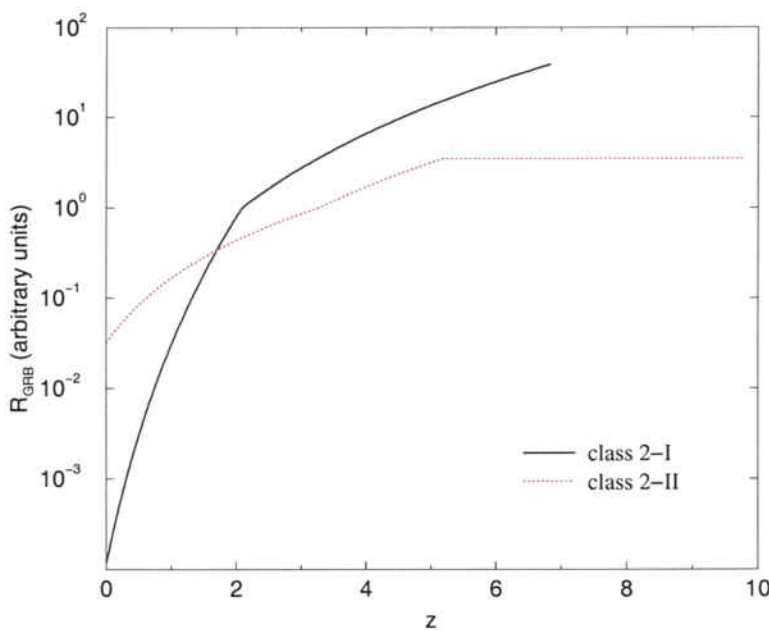


Figure 6.3: GRB comoving explosion rates as a function of redshift for the two-class classification of GRBs without luminosity evolution.

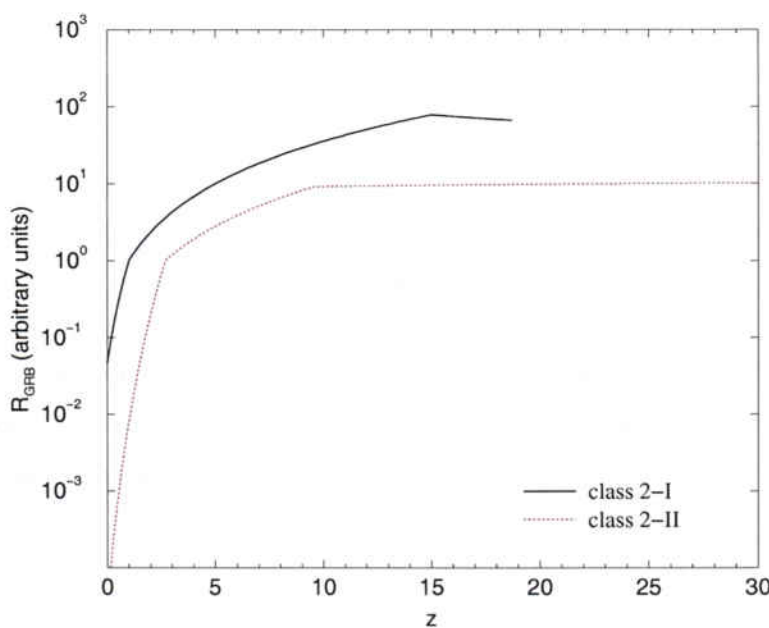


Figure 6.4: GRB comoving explosion rates as a function of redshift for the two-class classification of GRBs with luminosity evolution.

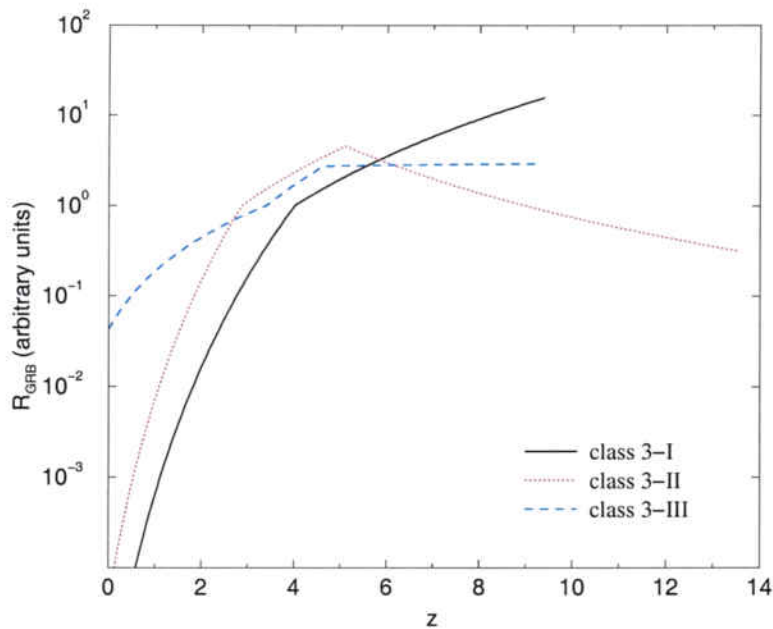


Figure 6.5: GRB comoving explosion rates as a function of redshift for the three-class classification of GRBs without luminosity evolution.

evolution, are shown in Figures 6.5 and 6.6 respectively. Once more, the GRB rate for short-duration GRBs, class 3-I, is very inaccurately determined in both cases, with and without luminosity evolution. For class 3-II without evolution, e_1 and e_3 are degenerate, although e_2 and the break points, z_1 and z_2 , are not so badly determined. As puzzling as it may sound, that has a simple explanation. Figure 6.21 shows that this combination of parameters imply that most of the observed GRBs lie in the interval $z \sim 3 - 6$, meaning that a slight variation of the GRB rate in this interval would involve most of the observed GRBs, severely affecting, henceforth, the intensity distribution. Adding the luminosity evolution to class 3-II GRBs does not improve the determination of its explosion rate. The GRB rate for class 3-III GRBs with evolution is measured with good accuracy, except for the value of z_{max} , that, as well as in the case of class 2-II, has a large uncertainty, mostly in its upper limit.

Most of GRB classes presented here have GRB rates that increase until redshifts higher than the power law breaks of the Madau, Steidel, and Blain SFRs, represented by equations 5.10, 5.11, and 5.12. The GRB rates derived here are like equation 5.12, but at very high redshifts they have a second break, from where the rate keeps almost constant. In comparison to the GRB rates derived by LFR and

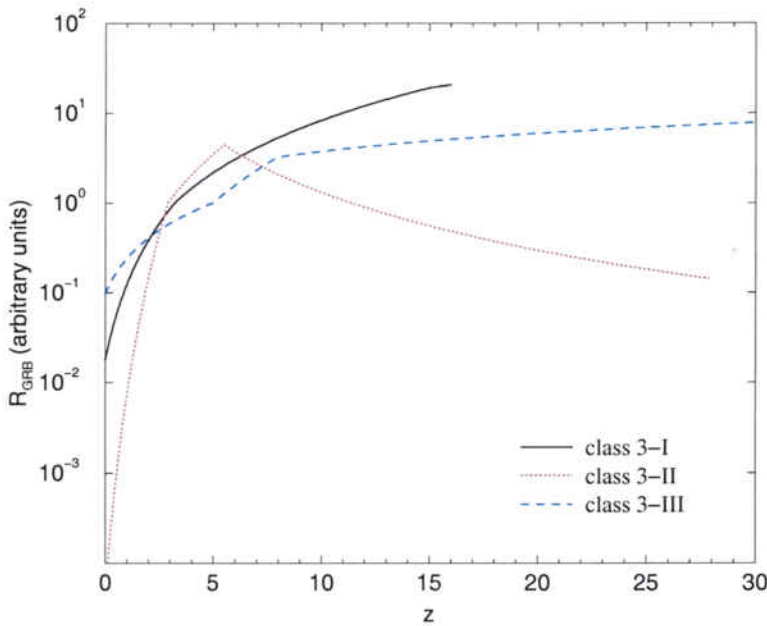


Figure 6.6: GRB comoving explosion rates as a function of redshift for the three-class classification of GRBs with luminosity evolution.

YON, for long-duration GRBs (classes 2-II and 3-III) with luminosity evolution, we obtain:

- Higher values of z_1 . For class 2-II $z_1 = 2.7$ in front of $z_1 = 2$ (LFR) and $z_1 = 1$ (YON). For class 3-III $z_1 = 5.0$ in front of $z_1 = 2$ (LFR) and $z_1 = 1$ (YON).
- e_1 with large uncertainty for class 2-II ($e_1 = 7.9^\dagger$). Lower value for class 3-III GRBs, $e_1 = 1.3$ in front of $e_1 = 3$ (LFR) and $e_1 = 5.5$ (YON).
- Compatible values for e_2 of class 2-II; $e_2 = 2.1_{-1.3}^{+1.5}$ in front of $e_2 = 1$ for both LFR and YON. For class 3-III $e_2 = 2.9_{-0.4}^{+1.5}$ in front of $e_2 = 1$ for both LFR and YON.

Our measurement extends beyond the maximum redshift of YON and LFR, showing how the GRB rate flattens out until at redshift of at least $z \sim 25$, and then decays very fast.

Firmani et al. (2004) tried to constrain the GRB rate and their luminosity function, taking also into account the effect of evolution. Although their results

cannot be compared with ours, because they used a different definition for the luminosity (bandpass $30 - 10000\text{ keV}$) and different parameterization of the GRB rate, they obtain that the GRB rate increases up to very high redshifts ($z > 10$), much like the Blain SFR (equation 5.12).

The GRB explosion rate at high redshifts is expected to decay as the SFR decays. If one obtains non-negative values for e_3 , that means that the value of z_{max} substitutes the smooth decay, simulated by a negative e_3 , for a sudden cut in the explosion rate. The fact that e_3 is usually close to zero, instead of being negative as it should be expected, indicates that the decay of the explosion rates of GRBs at high redshifts occurs suddenly, with a very steep decrease, and it goes to zero within a short range of redshift. This implies that the history of the SFR started with an outburst at redshift around z_{max} , in fact some time before due to the evolution time from birth to explosion of the GRB progenitor.

Figures from 6.7 to 6.18 show the variation of the differential intensity distribution with the parameters belonging to the GRB rate modelization without luminosity evolution. For each parameter it is shown a plot of class 3-III GRBs, representing a long-duration GRB class, and a plot of each of the classes corresponding to intermediate or short-duration GRBs.

The interpretation of the variation of the differential intensity distribution with the parameter z_{max} , and as we will see, also that related to the luminosity function (L_0 , κ , β , and η) is straightforward, because it depends only on their own values. In the case of the parameters z_1 , z_2 , e_1 , e_2 , and e_3 , it is far more complex, because the variation of the intensity distribution not only depends on the variation of the parameter itself, but also on the actual values of the other parameters and their ratios. For instance, in Figures 6.7 and 6.8, the effect of the variation of z_1 is different for each class. Class 3-III GRBs have $e_1 < e_2$, so if z_1 decreases, the number of GRBs at high distances increases, and consequently, the number of GRBs with low peak fluxes increases (see Figure 6.7). After normalization to the total number of GRBs, the effect on the high peak flux tail of the $\log N - \log P$ distribution is opposite to that of the low peak flux tail. On the other hand, for class 3-II GRBs $e_1 > e_2$, meaning that decreasing the value of z_1 decreases the number of GRBs at high distances, and so does the number of GRBs with low peak fluxes (see Figure 6.8). Increasing z_1 one obtains the reverse effect.

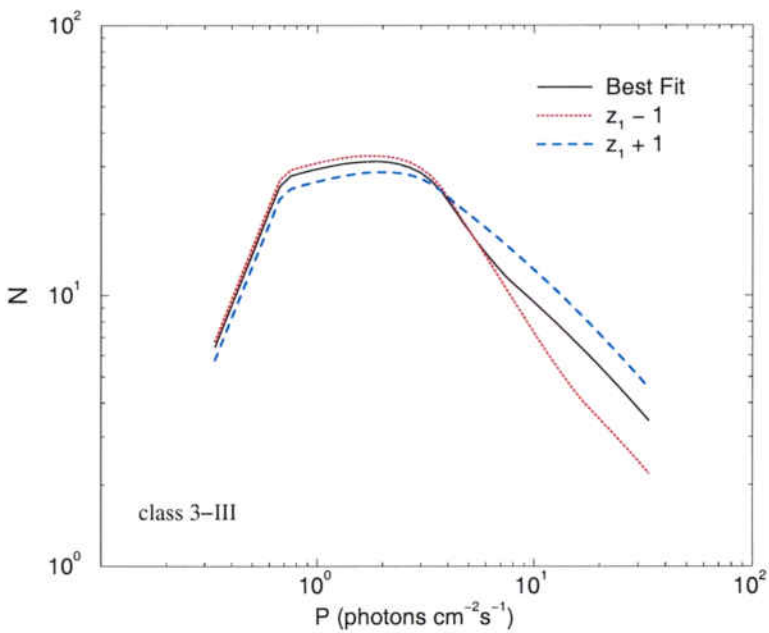


Figure 6.7: Variation of the GRB intensity distribution for class 3-III GRBs as a function of z_1 .

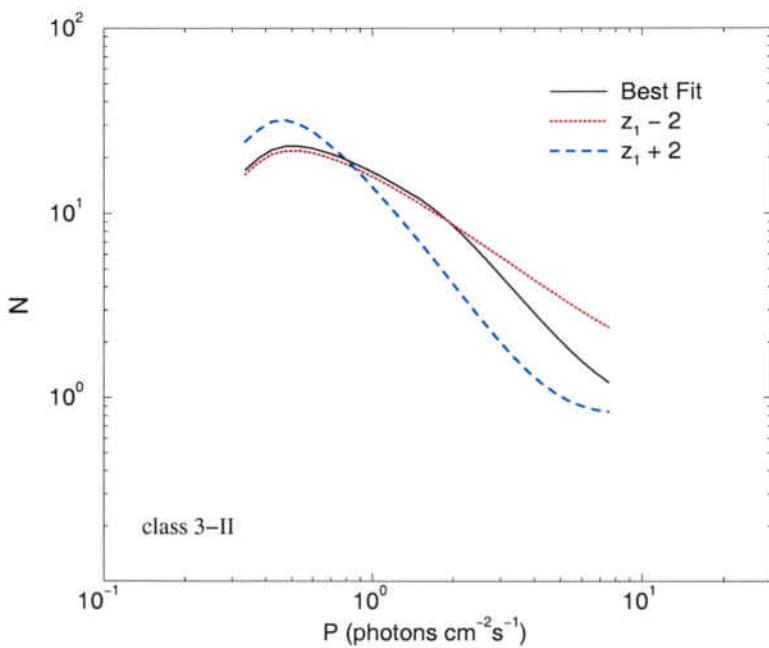


Figure 6.8: Variation of the GRB intensity distribution for class 3-II GRBs as a function of z_1 .

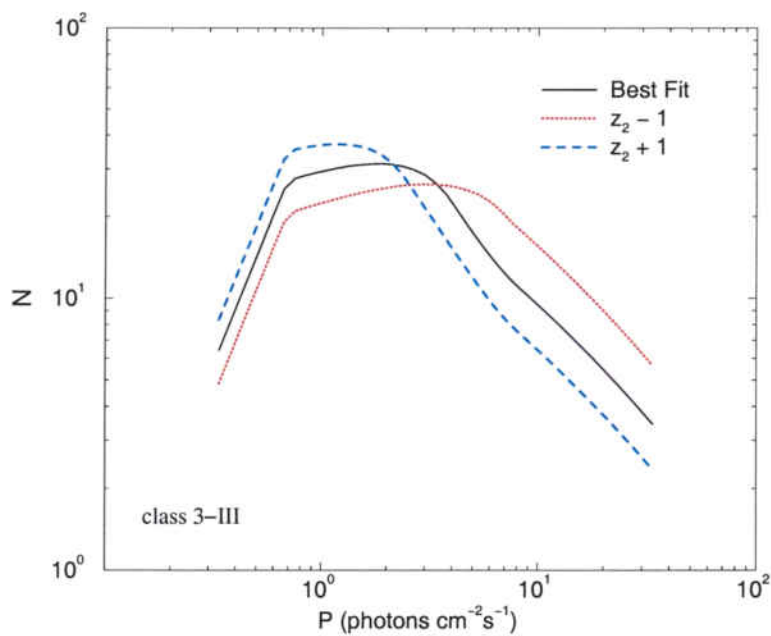


Figure 6.9: Variation of the GRB intensity distribution for class 3-III GRBs as a function of z_2 .

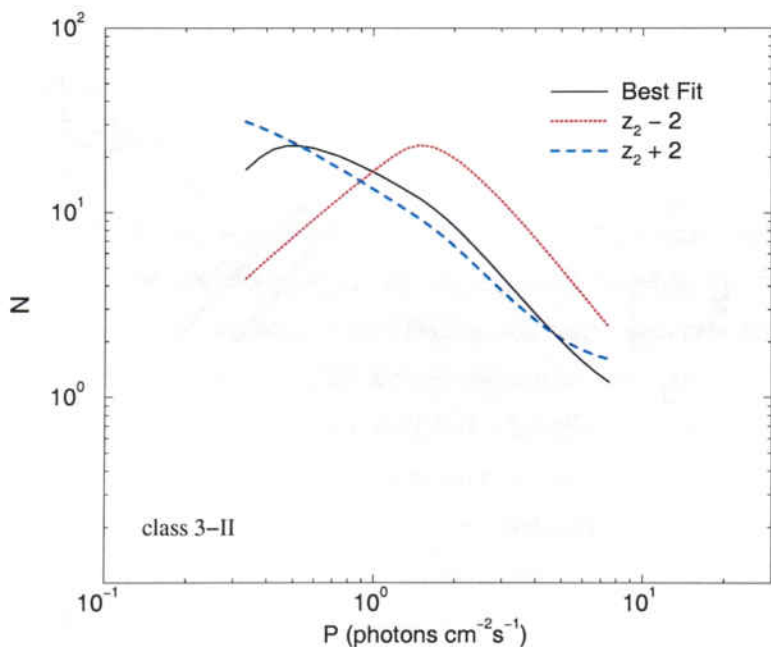


Figure 6.10: Variation of the GRB intensity distribution for class 3-II GRBs as a function of z_2 .

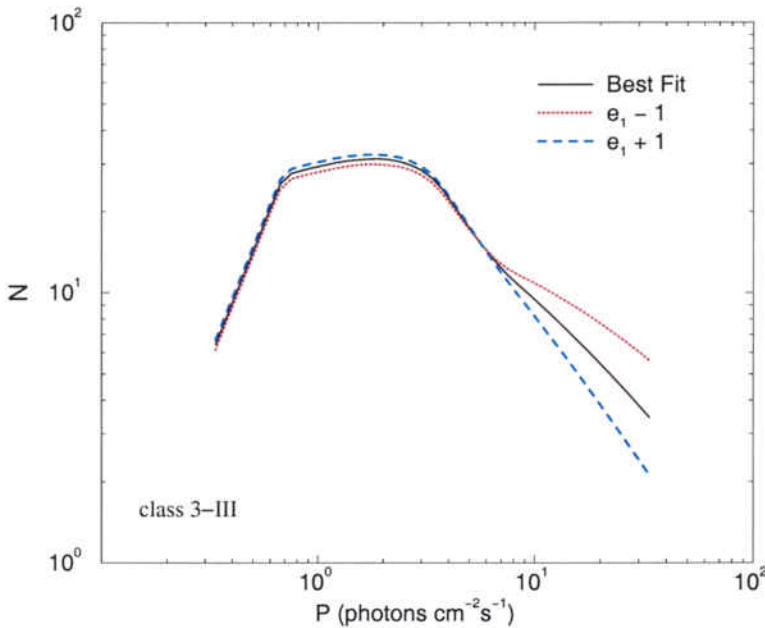


Figure 6.11: Variation of the GRB intensity distribution for class 3-III GRBs as a function of e_1 .

A similar argument can be given for the second break of the GRB rate. For all GRB classes we have that $e_2 > e_3$. In this case, a decrease of z_2 produces a decrease of GRBs at high redshifts (above z_2), which causes a decrease of GRBs with low peak fluxes. Figures 6.9 and 6.10 show this effect for classes 3-III and 3-II. Now, an increase in z_2 increases the number of GRBs above z_2 , which causes an increase of the number of GRBs with low peak fluxes. Figure 6.10 shows as well an increment of GRBs in the tail of high peak fluxes when z_2 increases; that might be the result of the increase of GRBs around $z = z_2$.

Having presented the variations of the intensity distribution due to the break points of the GRB explosion rate, z_1 and z_2 , let us move to comment the variations due to the exponents e_1 , e_2 , and e_3 .

The variation of e_1 modifies the number of GRBs at all distances and, depending on the values of the break points and exponents, it increases differently the ratio of closer to farther GRBs. Since the interval from $z = 0$ to $z = z_1$ is usually smaller than the interval from $z = z_1$ to $z = z_{max}$, the increase in the number of GRBs at high redshift is proportionally larger than the increase of GRBs at low redshifts. As a result, an increase in e_1 implies a decrease of GRBs of high peak

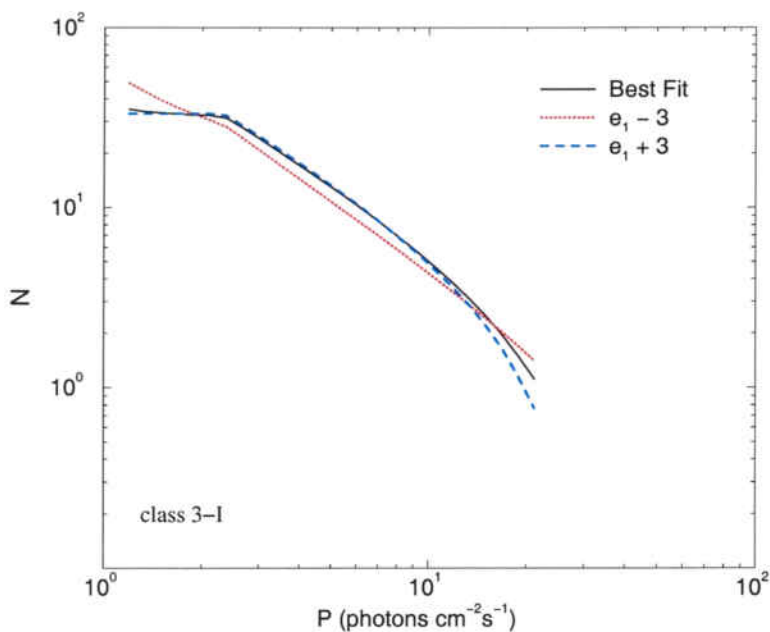


Figure 6.12: Variation of the GRB intensity distribution for class 3-I GRBs as a function of e_1 .

flux, and viceversa, a decrease in e_1 implies an increase of GRBs of high peak flux (see Figure 6.11). For class 3-I GRBs, the increase of the number of GRBs at short and long distances is balanced, resulting in a small variation of the intensity distribution. That variation being in the same direction, either increase or decrease, for both sides, low and high peak flux, of the distribution (see Figure 6.12).

The variation of the parameter e_2 , does not affect the number of nearby GRBs (those with $z < z_1$). An increase in e_2 implies then an increase in the number of GRBs at $z > z_1$, and viceversa, a decrease in e_2 implies a decrease in the number of GRBs at $z > z_1$. Figures 6.13 and 6.14 show that an increase in e_2 increases the number of GRBs with low peak fluxes and decreases the number of GRBs with high peak fluxes.

In much the same way as e_1 and e_2 acts e_3 (see Figures 6.15 and 6.16). From the variation of the differential intensity distribution of class 3-III GRBs with the exponents that model the GRB rate (Figures 6.11, 6.13 and 6.15, as well as the corresponding one with luminosity evolution 6.34), one can see that from e_1 to e_3 the shape of the intensity distribution varies from the high peak flux tail (for e_1), to the low peak flux tail (for e_3), depending on whether each parameter affects the

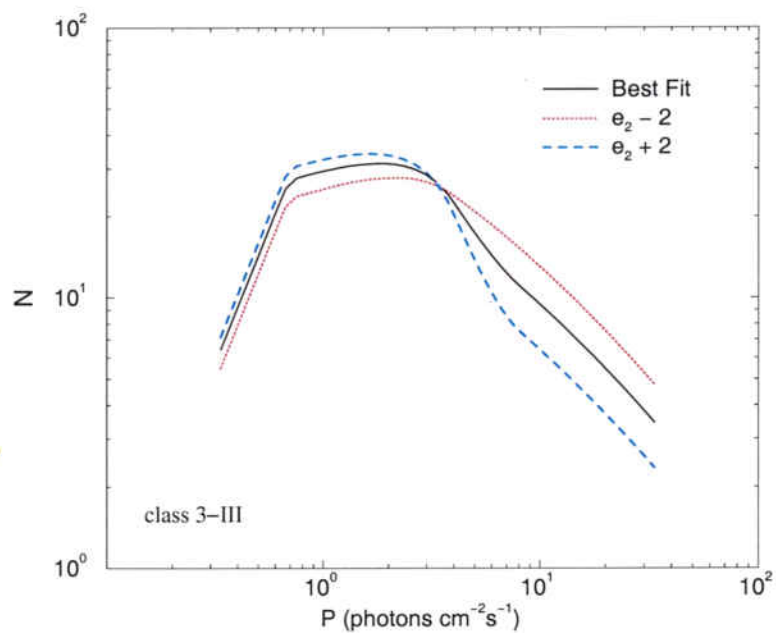


Figure 6.13: Variation of the GRB intensity distribution for class 3-III GRBs as a function of e_2 .

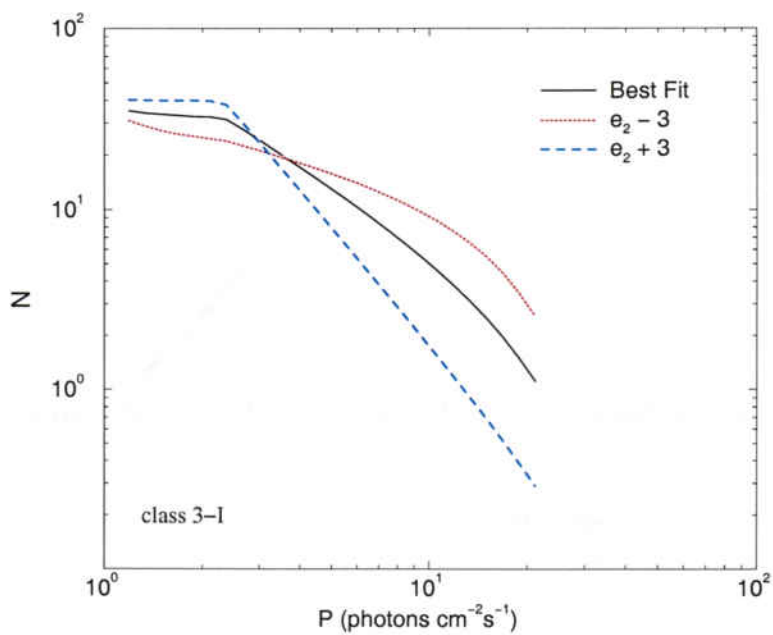


Figure 6.14: Variation of the GRB intensity distribution for class 3-I GRBs as a function of e_2 .

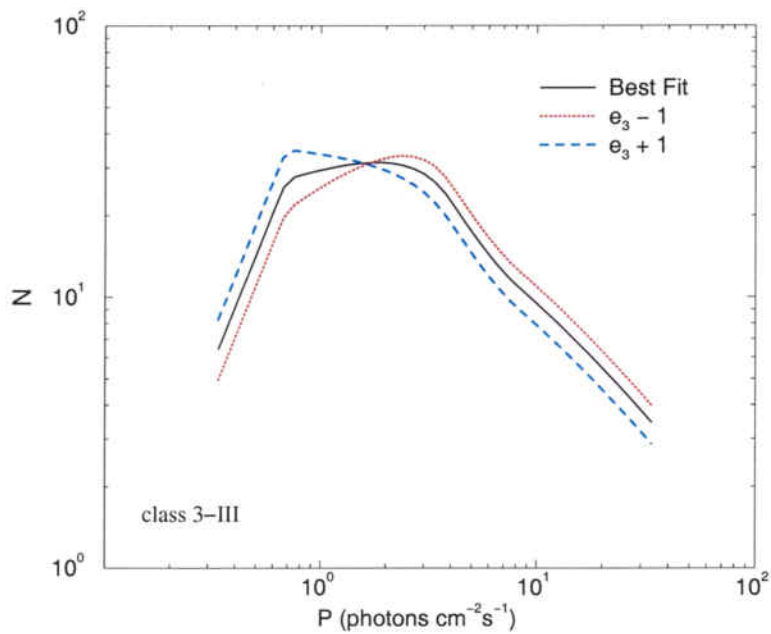


Figure 6.15: Variation of the GRB intensity distribution for class 3-III GRBs as a function of e_3 .

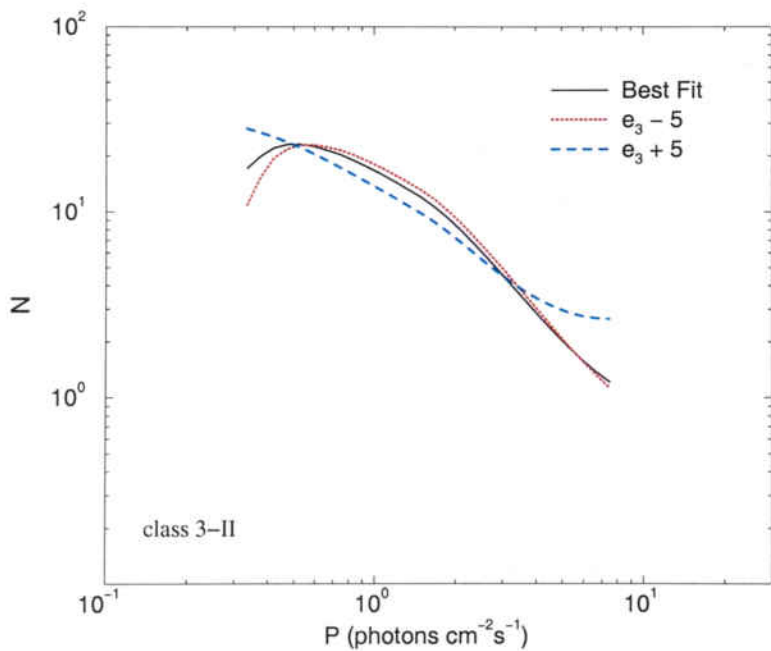


Figure 6.16: Variation of the GRB intensity distribution for class 3-II GRBs as a function of e_3 .

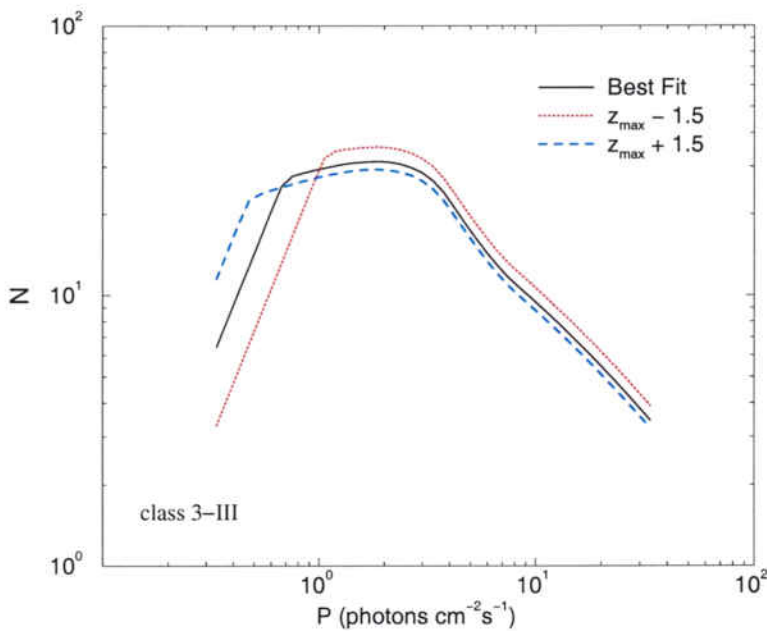


Figure 6.17: Variation of the GRB intensity distribution for class 3-III GRBs as a function of z_{max} .

whole GRB rate, e_1 , or just the high redshift part of the GRB rate, e_3 .

What happens with z_{max} is that as it increases, so does the number of GRBs produced at higher distances, growing correspondingly the number of GRBs with low peak fluxes. This fact is shown in Figures 6.17 and 6.18. As a difference with the other parameters involving the GRB rate, the variation of z_{max} moves the intensity distribution, as a whole, towards lower or higher peak fluxes, instead of modifying its shape, as it can be seen in the previous plots.

6.2.1 The gamma-ray burst redshift distribution

The observed redshift distribution of GRBs is different from the comoving explosion rate of GRBs. The observed redshift distribution of GRBs (equation 6.1) depends not only on the comoving explosion rate of GRBs, $R_{GRB}(z)$, but also on the luminosity function, $\phi(L)$. In fact, it is the convolution of both terms, and depends on the instrument via the minimum peak flux detectable, P_{min} . In this case, the luminosity function is integrated from the minimum luminosity observable by the instrument at a given z , $L(P_{min}, z)$, to the maximum value of the luminosity function, L_{max} .

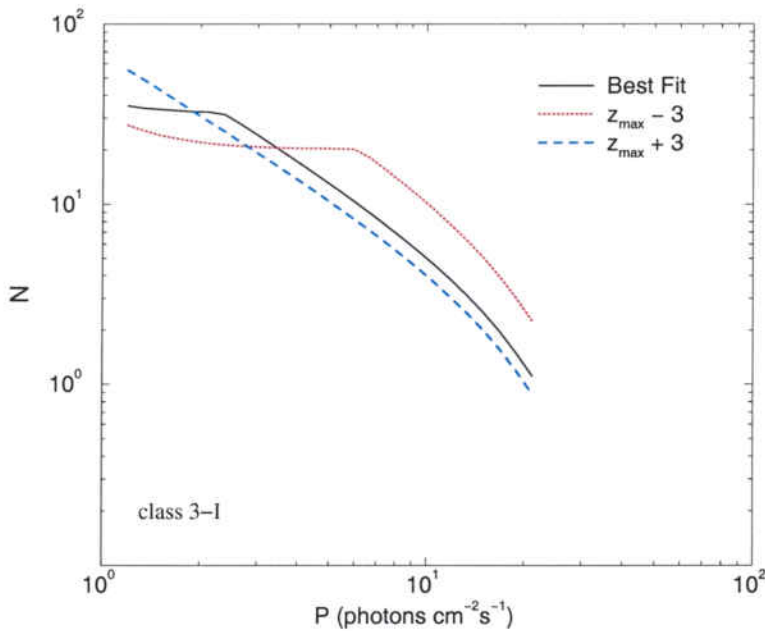


Figure 6.18: Variation of the GRB intensity distribution for class 3-I GRBs as a function of z_{max} .

$$N(z_1 \leq z < z_2) =$$

$$\frac{c}{H_0} \int_{z_1}^{z_2} \frac{R_{\text{GRB}}(z)}{1+z} \frac{D^2(z)}{\sqrt{\Omega_M(1+z)^3 + \Omega_K(1+z)^2 + \Omega_\Lambda}} dz \int_{L(P_{min},z)}^{L_{max}} \phi(L) dL \quad (6.1)$$

Figures from 6.19 to 6.22 plot the observed redshift distribution for all classes of GRBs, without and with luminosity evolution.

The two-class classification shows that short-duration GRBs, class 2-I, are closer than long-duration GRBs. Without luminosity evolution, 50% of class 2-I GRB are detected at $z < 4$, whereas for class 2-II GRBs, 50% of them are detected at $z < 5$. The difference in distance increases when one takes into account the luminosity evolution. In this case, 50% of class 2-I GRB are detected at $z < 6.5$, while for class 2-II GRBs, 50% of them are detected at $z < 9.5$. The difference in distance scale for class 2-I and 2-II GRBs without luminosity evolution comes, mainly, from the peak of class 2-I GRBs detected at $z \sim 0.5$. This peak, that happens in all short GRB classes, is produced to a large extent by the shape of

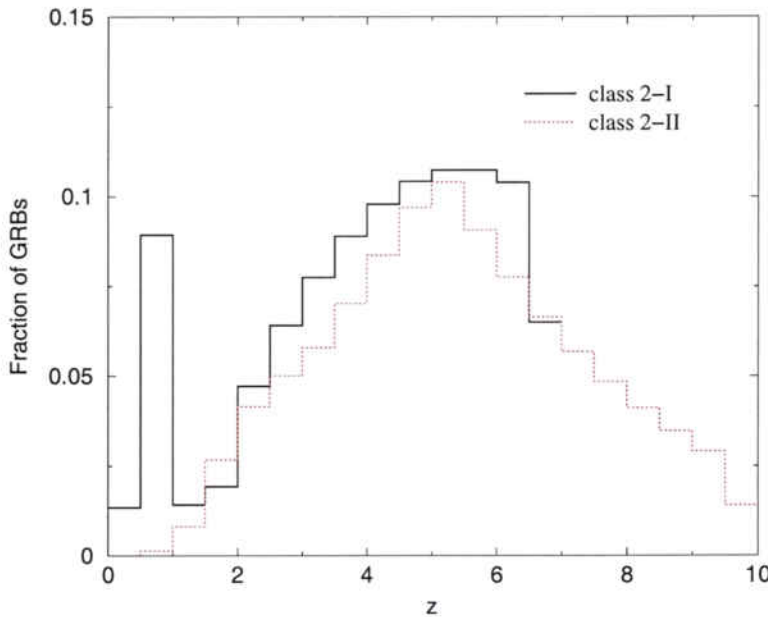


Figure 6.19: Detected GRB redshift distribution for the two-class classification of GRBs without luminosity evolution.

the luminosity function. In all these cases, the low energy part of the luminosity function is very steep (see in Figure 6.23 that in a range of luminosities of one order of magnitude, $\phi(L)$ decreases five orders of magnitude), producing lots of GRBs with low energy. These GRBs are only detected at low redshift. For example, if we use the luminosity function of class 2-II GRBs to compute the detected redshift distribution of class 2-I GRBs, the peak at $z \sim 0.5$ is completely wiped out.

In the case of the three-class classification without luminosity evolution, the farther GRB population is that of class 3-I. When one takes into account luminosity evolution, 50% of the detected GRBs are below $z < 7$, $z < 4.5$, $z < 10$, for classes 3-I, 3-II, and 3-III respectively. In this case, class 3-I GRBs are not yet the closest GRB population.

These results seem to be in contradiction with the distance scales obtained in section 4.4, that gave short-duration GRBs as the closest population. However, it has been said that the observed redshift distribution is the convolution of the comoving GRB rate with the luminosity function. In every GRB class, there is at least one degenerate parameter concerning any of these two terms. As a result, one has a large uncertainty on the redshift distribution, especially on that of short-duration

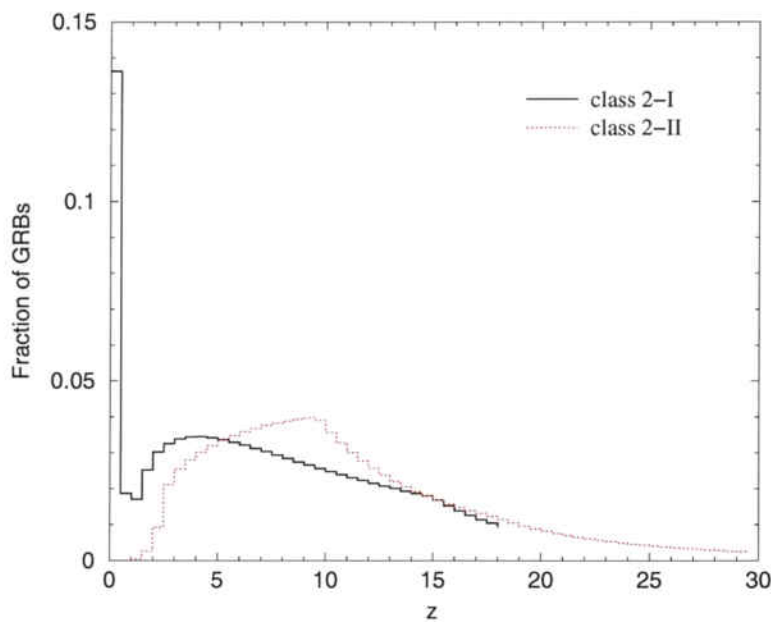


Figure 6.20: Detected GRB redshift distribution for the two-class classification of GRBs with luminosity evolution.

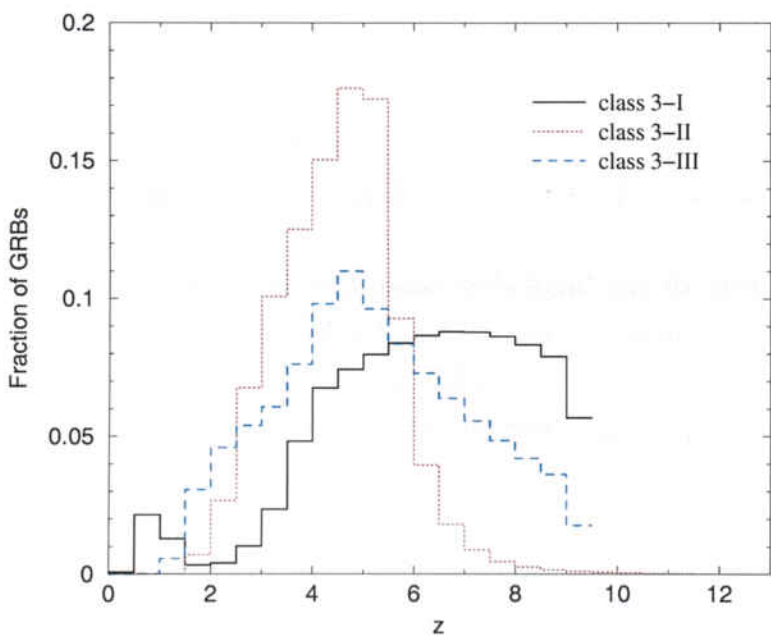


Figure 6.21: Detected GRB redshift distribution for the three-class classification of GRBs without luminosity evolution.

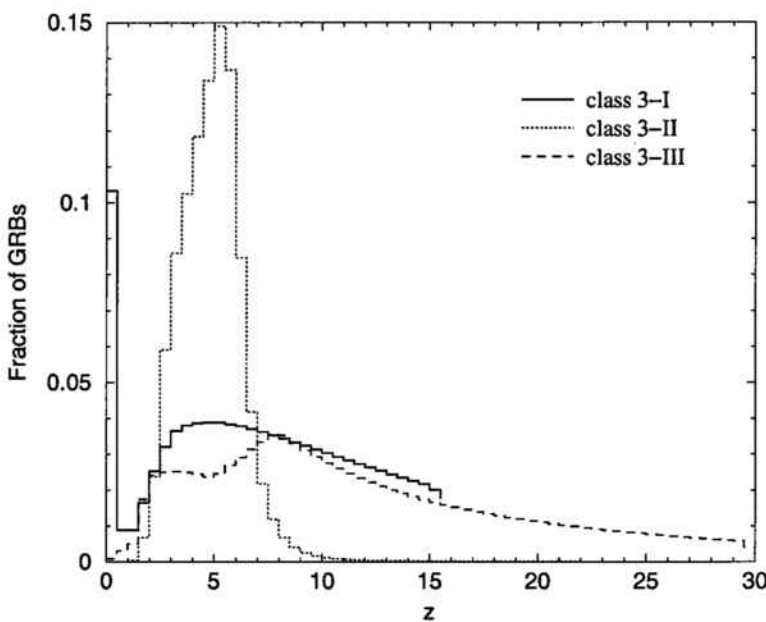


Figure 6.22: Detected GRB redshift distribution for the three-class classification of GRBs with luminosity evolution.

GRBs.

6.3 The gamma-ray burst luminosity function

The GRB luminosity functions for all GRB classes without evolution are shown in Figures 6.23 and 6.24. Although there have been very recent attempts to measure the luminosity function for long (Guetta et al., 2005) and short (Guetta and Piran, 2005) duration GRBs, following the method developed by Schmidt (1999b), their results cannot be compared with those presented here since they used a different bandpass to calculate the luminosity ($50 - 300 \text{ keV}$). Schaefer et al. (2001) report $L_0 = 2 \cdot 10^{52} \text{ erg s}^{-1}$, $\kappa = -1.7$, and $\beta = -2.8$, for long-duration GRBs, without taking into account luminosity evolution. Our results show that L_0 should be one fourth of their value, and $\beta > 0$, showing a moderate increase of GRBs towards high luminosities. On the other hand, there does not exist any measure of the luminosity function of short-duration GRBs with which compare our results. The luminosity function of short-duration GRBs (classes 2-I and 3-I) shows a steeper decrease of GRBs below L_0 than above it.

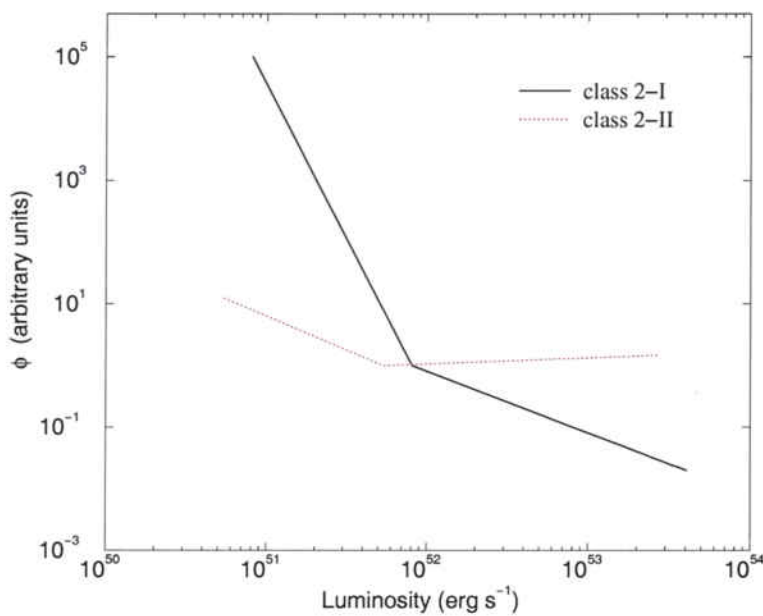


Figure 6.23: Luminosity functions for the two-class classification of GRBs without luminosity evolution.

Keep in mind that with the results presented here nothing can be said about κ for GRB classes 2-II, 3-I, and 3-III. Also β is very uncertain for classes 3-I and 3-II.

Let us study the variation of the intensity distribution with the parameters related to the luminosity function. Figure 6.25 shows the variation of the GRB intensity distribution for class 3-III GRBs as a function of L_0 . Obviously, if the luminosity function moves towards higher luminosities, that is, if L_0 increases, then one detects more GRBs with higher peak fluxes. On the contrary, if L_0 decreases, one detects more GRBs with lower peak fluxes. The same happens for all GRB classes. As an example, Figure 6.26 shows the variation of the GRB intensity distribution for class 2-I GRBs as a function of L_0 .

The parameter κ represents the slope of the luminosity function at low luminosities. If κ decreases, it means that there are more GRBs produced with lower luminosities than if κ increases. The variation of the GRB intensity distribution as a function of κ for classes 3-III and 2-I is shown in Figures 6.27 and 6.28, respectively. As expected, if κ decreases one detects more GRBs at lower peak fluxes than with the best fit, and viceversa, if κ increases, one detects less GRBs at lower

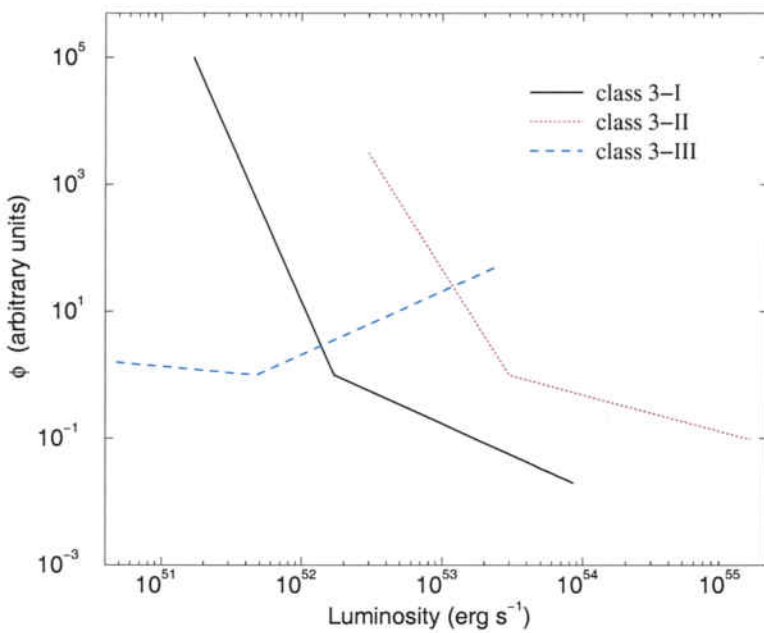


Figure 6.24: Luminosity functions for the three-class classification of GRBs without luminosity evolution.

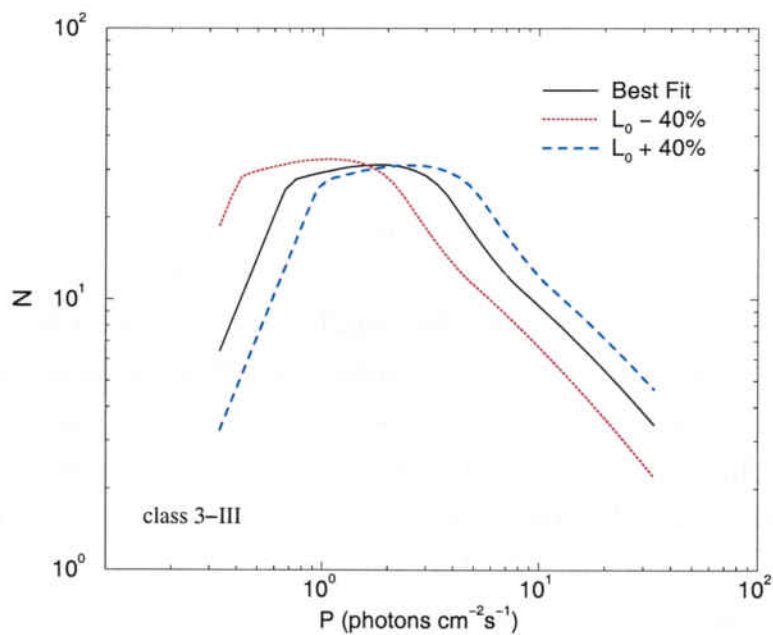


Figure 6.25: Variation of the GRB intensity distribution for class 3-III GRBs as a function of L_0 .

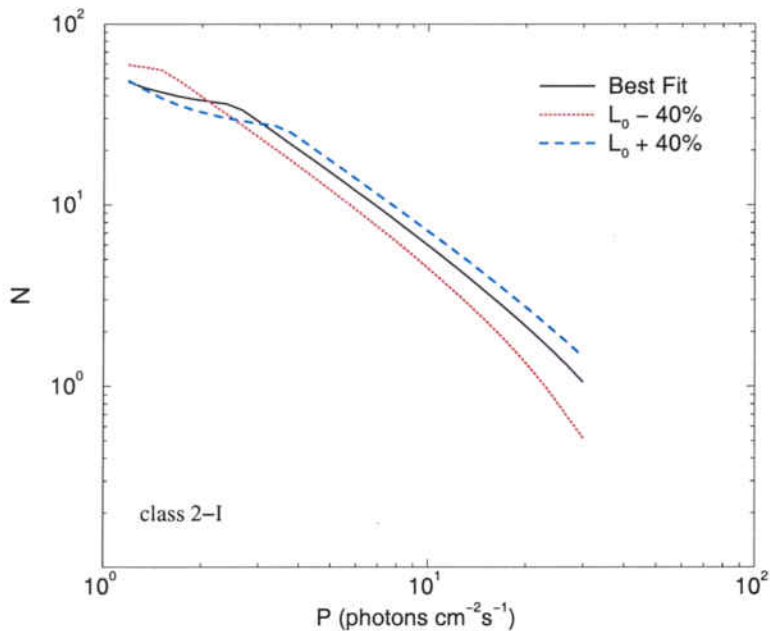


Figure 6.26: Variation of the GRB intensity distribution for class 2-I GRBs as a function of L_0 .

peak fluxes. The variation of the intensity distribution with κ is quite small for class 3-III GRBs, to the extent that, if κ increases the difference is insignificant. In consequence, κ cannot be determined accurately by fitting the intensity distribution and it appears in Table 6.3 as a degenerate parameter. It is also interesting to note that, unlike the case of the variation of L_0 , where the intensity distribution seemed to shift as a whole towards lower or higher peak fluxes without changing its shape, the variation of κ changes only the slope of the intensity distribution in its lower peak flux component, thus varying the overall shape of the distribution. As a result, it changes the number of GRBs in the higher peak flux component of the intensity distribution, due to the normalization to the total observed number of GRBs. The intensity distribution of class 3-III GRBs is so insensitive to κ because either most of the GRBs produced at low luminosities are undetected, or the distribution is dominated by the higher number of GRBs with high luminosities (see Figure 6.24). In any case, κ is usually worse determined than β because it represents the number of GRBs in an interval 5 times smaller than the one covered by β ; therefore, the latter affects a larger fraction of the GRBs produced. This is not always true, depending strictly on the values of κ and β . For example, low values of κ combined with low values of β could lead to a luminosity function dominated by the value of κ .

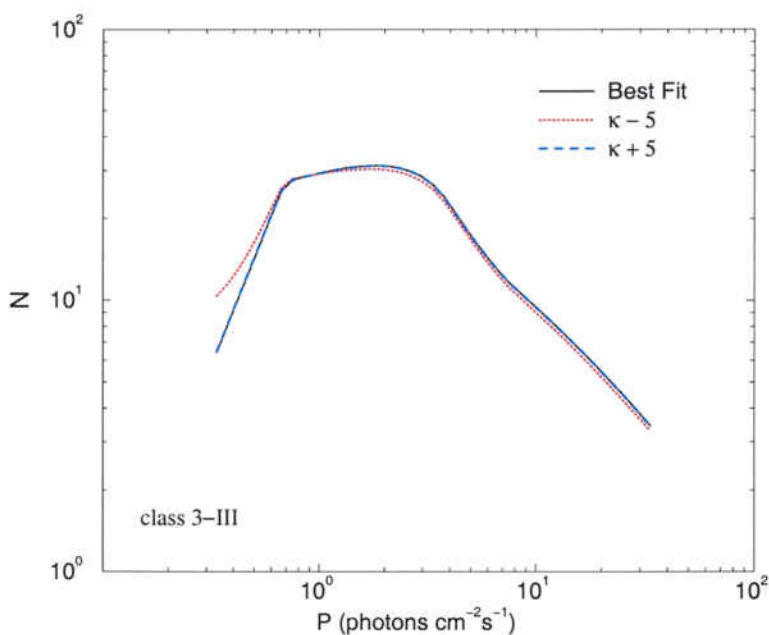


Figure 6.27: Variation of the GRB intensity distribution for class 3-III GRBs as a function of κ .

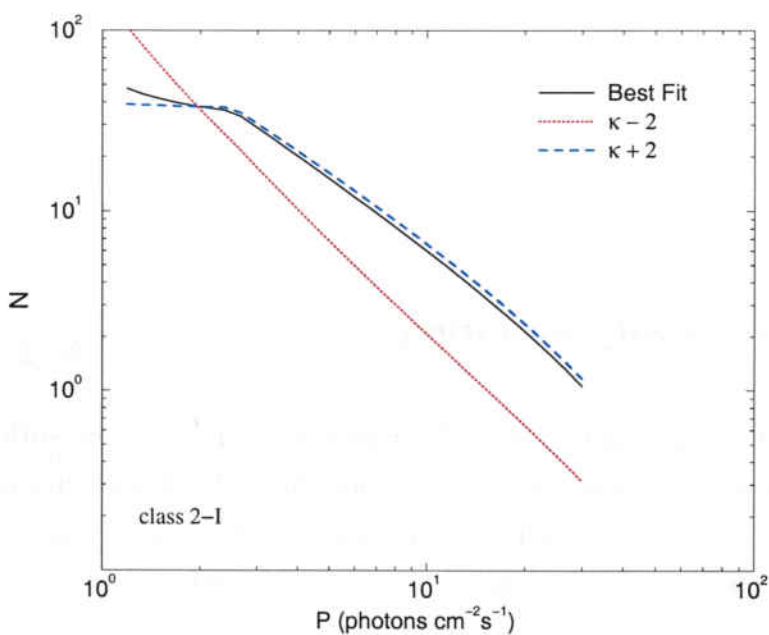


Figure 6.28: Variation of the GRB intensity distribution for class 2-I GRBs as a function of κ .

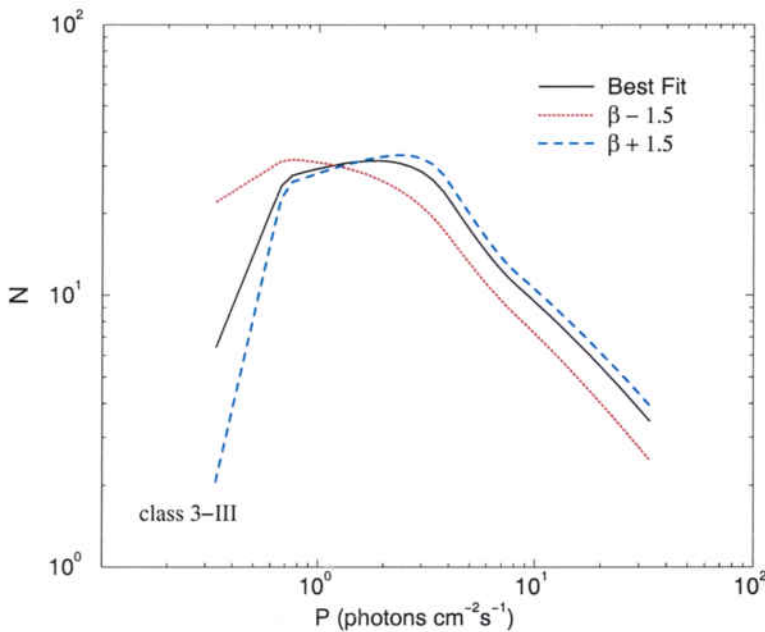


Figure 6.29: Variation of the GRB intensity distribution for class 3-III GRBs as a function of β .

The slope β has the same effect as κ on the intensity distribution, although the magnitude of this effect is larger, as it has already been said. Figures 6.29 and 6.30 show the change of slope of the low peak flux tail of the distribution as the value of β changes. Lower values of β imply a rise in the number of GRBs with low peak flux, while higher values of β imply a decrease in the number of GRBs with low peak flux.

6.3.1 Luminosity evolution

The luminosity function of class 2-I GRBs with luminosity evolution (Figure 6.31) has the same shape as that without evolution, but shifted towards lower luminosities, although the values of κ and β have large uncertainties. As for the luminosity function of class 2-II GRBs, notice that when the effect of evolution is taken into account, the parameter κ is not degenerate.

In the case of the three-class classification, all the values of the luminosity function parameters with evolution, L_0 , κ , and β , are compatible with the ones without evolution within the confidence intervals. There are main differences: now

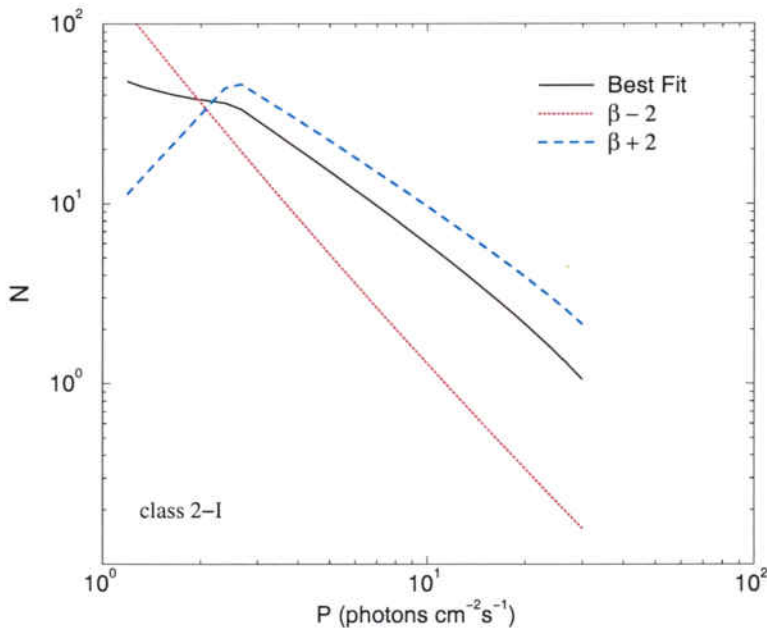


Figure 6.30: Variation of the GRB intensity distribution for class 2-I GRBs as a function of β .

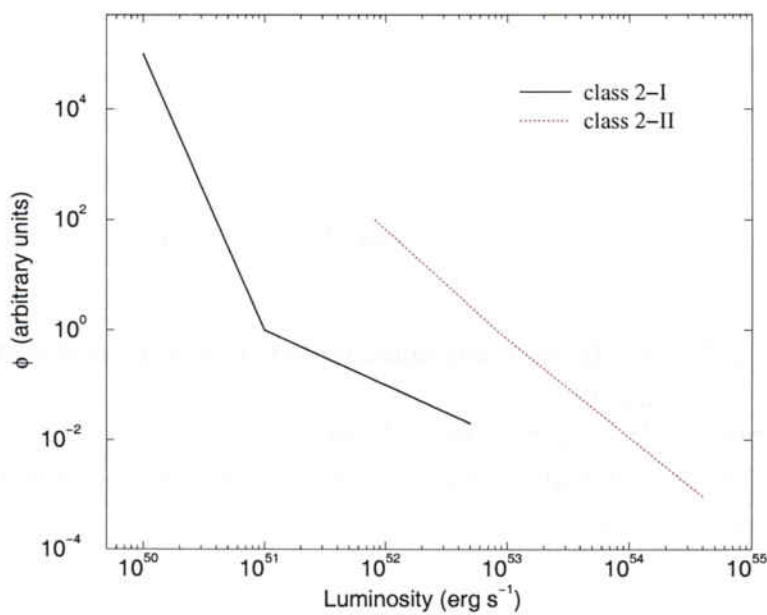


Figure 6.31: Luminosity functions for the two-class classification of GRBs with luminosity evolution.

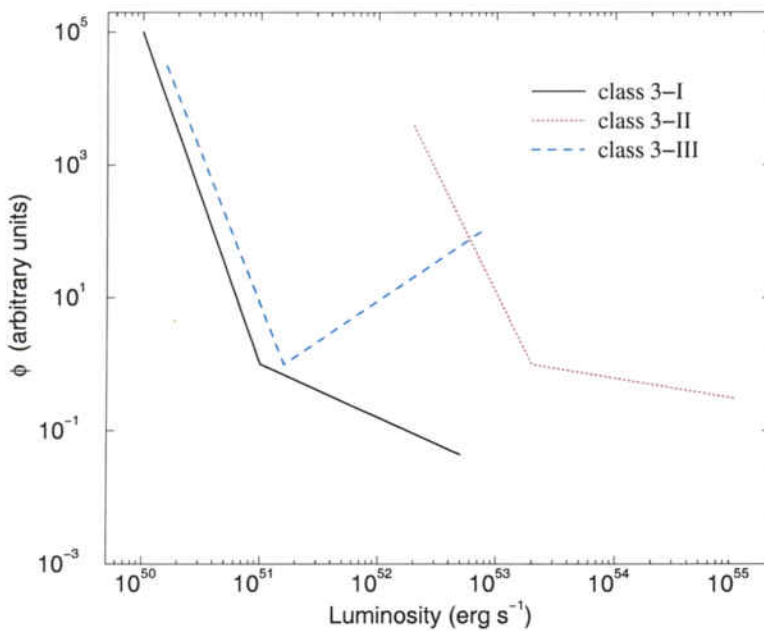


Figure 6.32: Luminosity functions for the three-class classification of GRBs with luminosity evolution.

κ is not degenerate for class 3-I GRBs, and β is degenerate in its lower limit for class 3-II GRBs. The peculiar behaviour of the luminosity function for class 3-III GRBs, where there is first a steep decrease ($\kappa < 0$) of GRBs towards still higher luminosities, followed by a steep increase ($\beta > 0$) of GRBs towards higher luminosities, might not be real, since κ is degenerate, and its real value could be any. All these features are shown in Figure 6.32, as well as in Table 6.4.

In comparison to YON and LFR (see Tables 6.4 and 6.6), here it is found that:

- Class 2-II GRBs: L_0 is significantly higher, but κ , β , and η are compatible.
- Class 3-III GRBs: L_0 is lower; nothing can be said about κ because is degenerate; β is positive and incompatible with both; and η is compatible with LFR but lower than that of YON.

The effect of the luminosity evolution exponent, η , over the intensity distribution is shown in Figure 6.33. Clearly, for a given set of parameters, if η increases, the GRB differential intensity distribution moves towards higher peak fluxes, meaning that one detects a larger number of GRBs with higher peak fluxes than before.

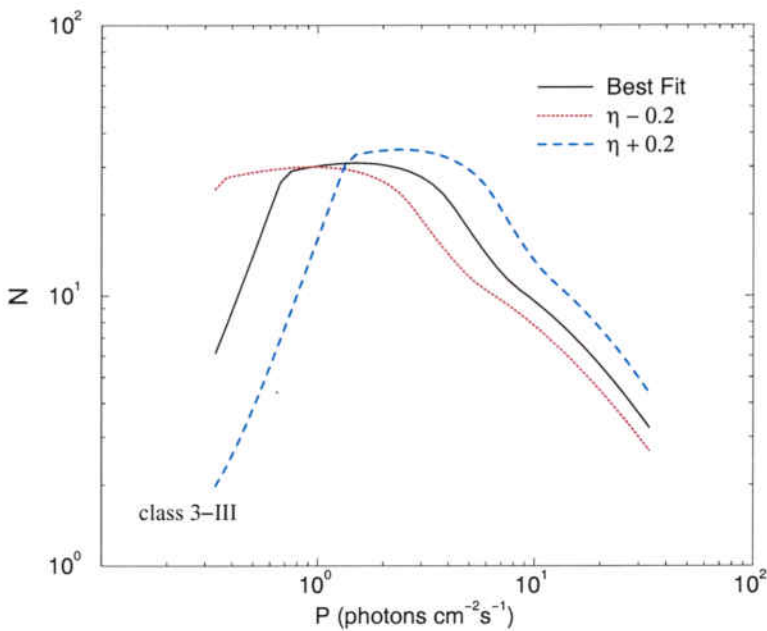


Figure 6.33: Variation of the GRB intensity distribution for class 3-III GRBs as a function of η .

While if η decreases, one detects more GRBs of lower peak fluxes, and less of higher peak fluxes than before.

Figure 6.34 shows the variation of the differential intensity distribution with the parameters regarding the GRB rate for class 2-II GRBs. The variations, to a larger or lesser extent, are the same as those explained in section 6.2.

Figure 6.35 shows the variation of the differential intensity distribution with the parameters regarding the luminosity function for class 2-II GRBs. A couple of interesting features arise for the κ and β parameters in the case of luminosity evolution. First, the variation of the intensity distribution with κ is now more severe. While in Figure 6.27 the difference introduced as κ varies was only for the low peak flux part of the distribution, Figure 6.35 shows that now the difference occurs in the whole range of peak fluxes. The evolution factor strengthens the effect of the variation of κ . As the redshift increases, so does the luminosity limits represented by κ ; therefore, the effect of its variation spreads through a wide range of peak flux values. Second, regarding β , it produces now a change in the shape of the distribution, concerning only the high peak flux part. Again, the evolution exponent moves all the effects of the variation of parameters towards the high peak

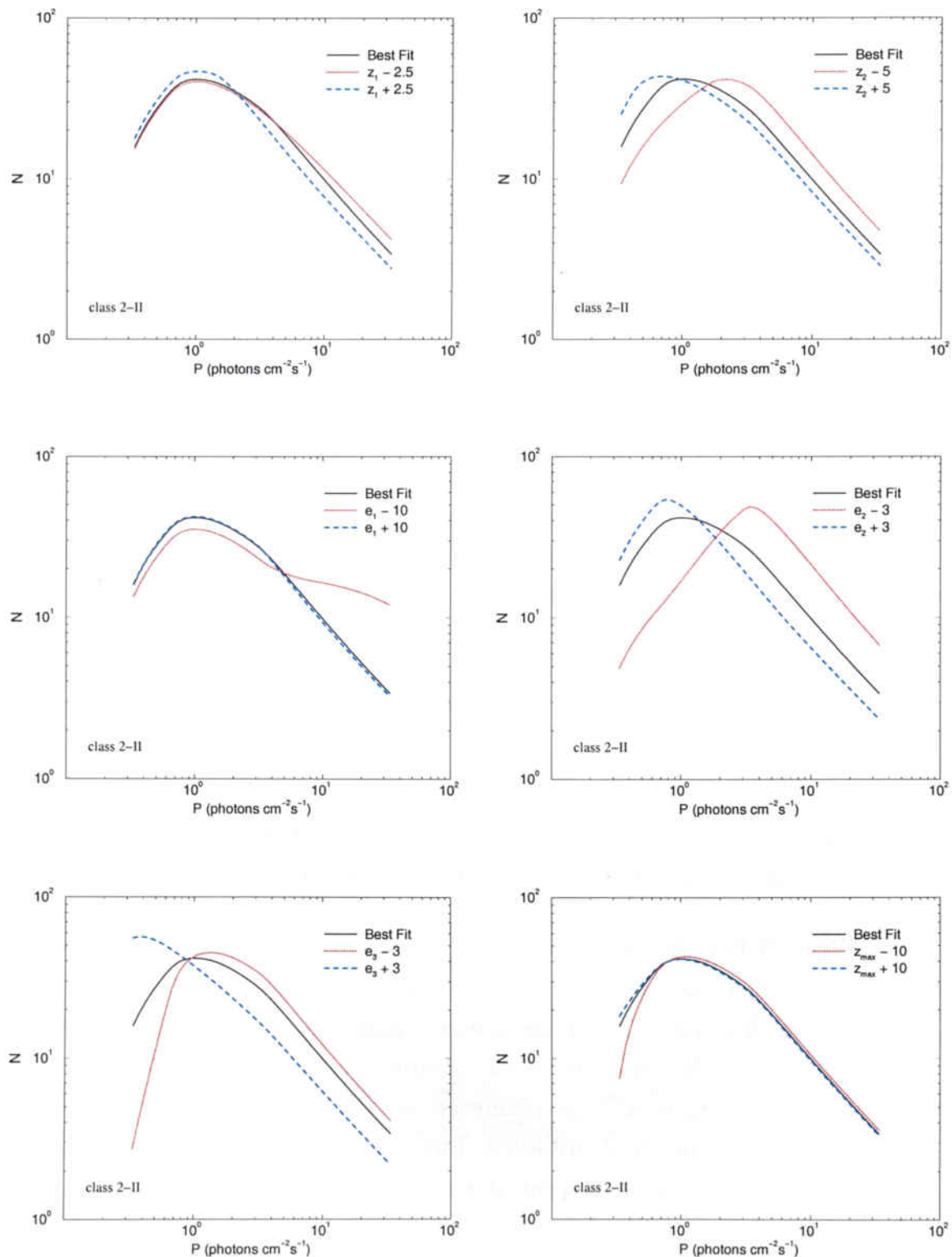


Figure 6.34: Variation of the GRB intensity distribution as a function the GRB rate parameters for class 2-II GRBs with luminosity evolution.

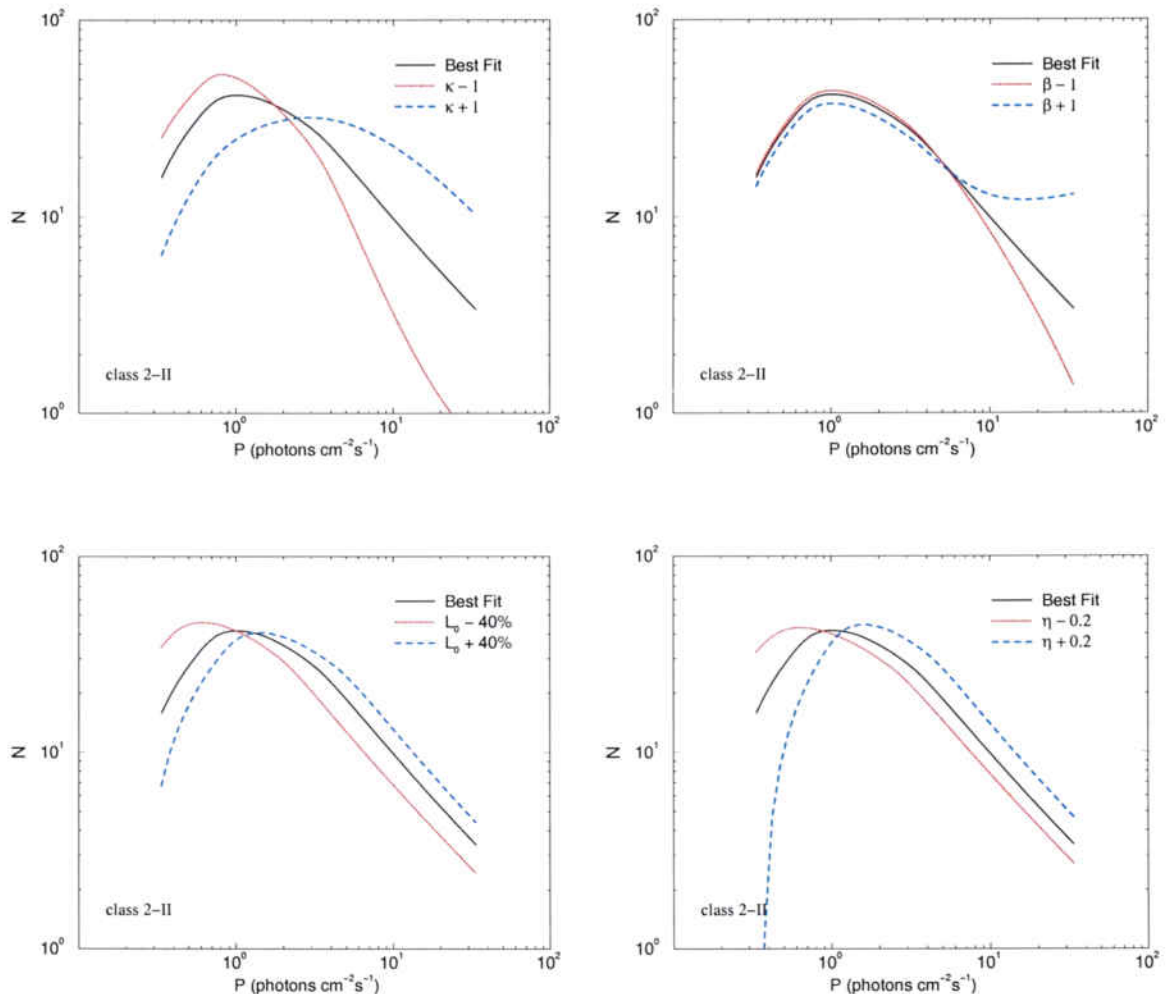


Figure 6.35: Variation of the GRB intensity distribution as a function the luminosity function parameters for class 2-II GRBs with luminosity evolution.

flux part of the intensity distribution.

6.4 Measuring the cosmological parameters

The cosmological parameters Ω_M and Ω_Λ can be constrained by fitting the Hubble diagrams of standard (or standardized) candles, method which has been used with remarkable success since the mid-nineties (Perlmutter et al., 1999; Riess et al., 1998). Recent studies have pointed out that GRBs may be considered as standard cosmological candles. Amati et al. (2002) discovered a relationship between the

peak energy E_{peak} of the burst spectrum νF_ν and the isotropic-equivalent energy E_{iso} . Even more recently, Ghirlanda et al. (2004) provided further information on this relationship and discovered an even tighter relationship between E_{peak} and E_γ . E_γ stands here for the beamed energy, that is, not considering an isotropic 4π sr emission, but a beamed emission instead. The existence of the $E_\gamma - E_{peak}$ correlation allows the knowledge of the intrinsic emission of GRBs, making them standardized candles similar to Type Ia supernovae and Cepheid variables. By using this, several authors (Takahashi et al., 2003; Di Girolamo et al., 2005; Dai et al., 2004) have tried to constrain Ω_M , Ω_Λ , and even the equation of state of dark energy. This correlation is obtained from high redshift GRBs with the consequence that it depends on the cosmological parameters which one is trying to find. Firmani et al. (2005) pointed out that the latter authors fell into a circular problem: if a cosmology is used to fix the $E_\gamma - E_{peak}$ correlation, then the $E_\gamma - E_{peak}$ correlation cannot be used to find a cosmology. They, instead, fitted the cosmology and the $E_\gamma - E_{peak}$ correlation in the same procedure, that giving large uncertainties for Ω_M and Ω_Λ unless they include Type Ia supernovae in the fit. Other authors, such as Friedman and Bloom (2005), show more concern in giving too much credit to this fit, due to the many assumptions introduced when one measures the opening angle θ_{jet} used to transform E_{iso} into E_γ , as well as to the still small sample of GRBs in which the $E_\gamma - E_{peak}$ correlation is based, and also to the circular argument of using cosmology to measure the $E_\gamma - E_{peak}$ correlation. The circular argument is not close to find a solution due to the large sample of very close GRBs ($z < 0.1$) needed, and to their very low rate of detection at such close distances.

Here, a completely different approach is used to measure the cosmological parameters Ω_M and Ω_Λ . We will use, again, the fit of the differential intensity distribution of GRBs. Now the parameters that model the GRB rate and their luminosity function will be fixed, while we will vary the cosmology. Let us have a look, first, at how the differential intensity distribution of GRBs varies with Ω_M and Ω_Λ .

The variation of the differential intensity distribution of GRBs with the cosmological parameters depends on the complex equilibrium between the comoving distance and the comoving volume. If Ω_M increases, the comoving distance to a given redshift, D , decreases. If D decreases, then the peak flux of the GRBs at this given redshift increases, moving the intensity distribution towards higher peak

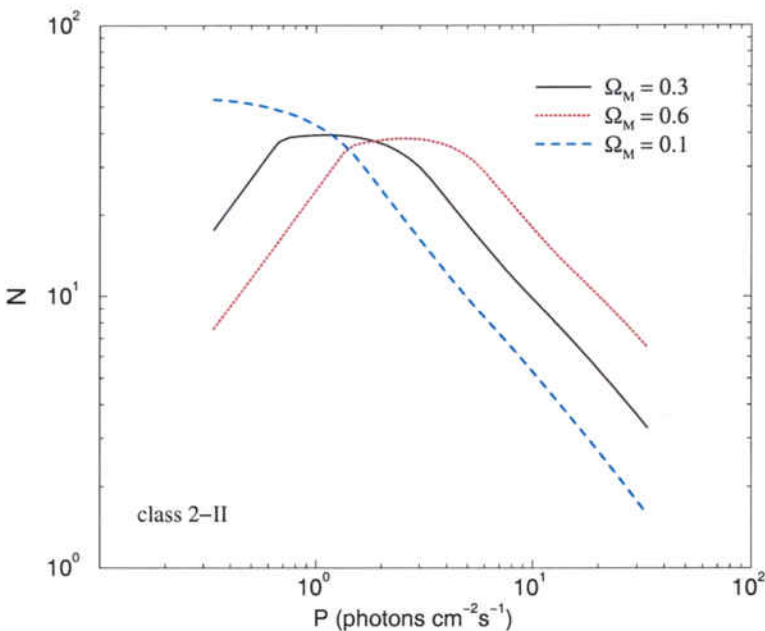


Figure 6.36: Variation of the GRB intensity distribution for class 2-II GRBs as a function of Ω_M .

fluxes. However, if Ω_M increases, not only D_L decreases, but also the differential comoving volume, dV , decreases. Now, although having GRBs with higher peak fluxes at a given redshift, they are produced in smaller amounts, since the rate per unit volume is the same but the unit volume is smaller. This latter effect tends to counteract the former one. The contrary happens when Ω_Λ increases, that is, both D_L and dV increase. In addition, the magnitude of these variations depends on the redshift, as well as on the relative values of Ω_M and Ω_Λ . As a result, the differential intensity distribution varies according to the equilibrium of these two effects and to the redshift distribution of the GRBs. As an example, the variation of the intensity distribution for class 2-II GRBs with Ω_M and Ω_Λ is shown in Figures 6.36 and 6.37, respectively.

With the best sets of parameters derived from the χ^2 minimization, we explore the $\Omega_M - \Omega_\Lambda$ plane, plotting the lines with equal value of χ^2 which comprise the 1σ , 2σ , and 3σ confidence regions, that is, those regions with $\Delta\chi^2$ with respect to the minimum χ^2 equal to 2.30, 6.17, and 11.80 respectively. Figures 6.38 and 6.39 show these regions (from darker to lighter blue) for all classes of GRBs, both without and with luminosity evolution respectively. These figures include a shaded area corresponding to the values of Ω_M and Ω_Λ for which a universe has no Big

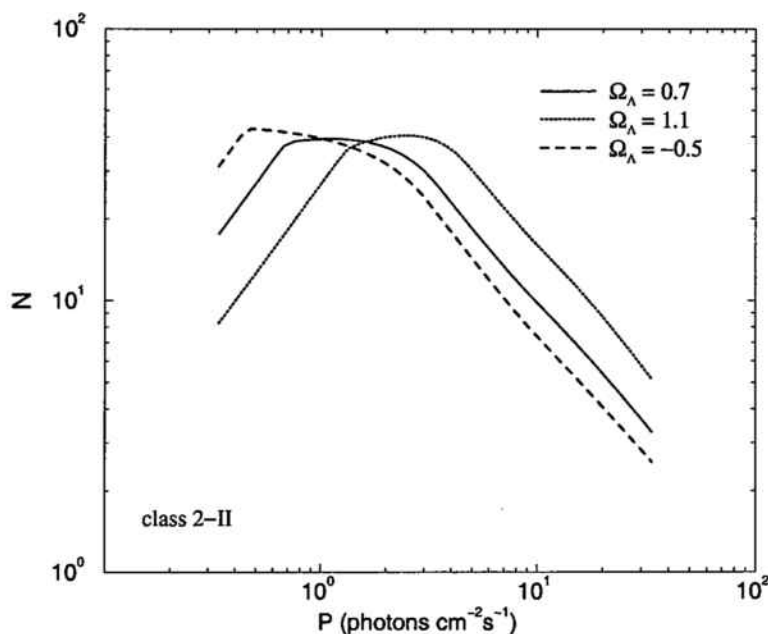


Figure 6.37: Variation of the GRB intensity distribution for class 2-II GRBs as a function of Ω_Λ .

Bang, but a turning point in its past, that is, it collapsed from infinite size to a finite radius and is now reexpanding. This occurs when:

$$\Omega_\Lambda \geq 4\Omega_M \begin{cases} \left[\cosh \left(\frac{1}{3} \cosh^{-1} \left(\frac{1-\Omega_M}{\Omega_M} \right) \right) \right]^3 & \Omega_M < \frac{1}{2} \\ \left[\cos \left(\frac{1}{3} \cos^{-1} \left(\frac{1-\Omega_M}{\Omega_M} \right) \right) \right]^3 & \Omega_M > \frac{1}{2} \end{cases} \quad (6.2)$$

The figures also show the line for a flat universe, $\Omega_K = 0$, and the GRB class. Observing the regions, it is clear that Ω_M and Ω_Λ are better constrained when one takes into account the luminosity evolution. The GRB classes that worst constrain Ω_M and Ω_Λ are the short-duration ones, 2-I and especially 3-I. As it has been said before, long-duration GRBs, classes 2-II and 3-III, have differential intensity distributions that cover a wider range of peak fluxes. Specifically, the intensity distribution of class 3-III GRBs is the one which has a more complex structure, and consequently it is the best class to measure the cosmological parameters Ω_M and Ω_Λ .

The confidence regions, almost perpendicular to the one obtained from super-

GRB class	No evolution		Evolution	
	Ω_M	Ω_Λ	Ω_M	Ω_Λ
2-I	$0.29^{+0.13}_{-0.10}$	$0.72^{+0.30}_{-0.79}$	$0.31^{+0.15}_{-0.10}$	$0.67^{+0.23}_{-0.52}$
2-II	$0.33^{+0.12}_{-0.09}$	$0.58^{+0.32}_{-0.87}$	$0.31^{+0.08}_{-0.06}$	$0.67^{+0.17}_{-0.26}$
3-I	$0.29^{+0.18}_{-0.19}$	$0.73^{+0.28}_{-1.08}$	$0.31^{+0.14}_{-0.09}$	$0.67^{+0.23}_{-0.55}$
3-II	$0.30^{+0.06}_{-0.06}$	$0.72^{+0.26}_{-0.79}$	$0.30^{+0.06}_{-0.05}$	$0.70^{+0.23}_{-0.47}$
3-III	$0.30^{+0.09}_{-0.06}$	$0.69^{+0.21}_{-0.48}$	$0.28^{+0.10}_{-0.05}$	$0.75^{+0.10}_{-0.26}$

Table 6.5: Values of Ω_M , Ω_Λ , and 1σ confidence intervals obtained from each class of GRBs.

novae (Knop et al., 2003), have an inclination intermediate between the one obtained with the cosmic microwave background radiation (CMB) (Spergel et al., 2003), and the one obtained with X-ray clusters (Allen et al., 2002). The line of flat universe crosses the confidence regions near the χ^2 minimum. The best values for Ω_M and Ω_Λ are close to 0.3 and 0.7 respectively, since these were the values of the cosmological parameters adopted when deriving the best parameters for all GRB populations.

Table 6.5 summarizes the best values for Ω_M and Ω_Λ , and their confidence intervals, derived from each class of GRB, both without and with luminosity evolution. The confidence intervals are calculated as the interval for which $\Delta\chi^2 = 1$, since here we are interested in the confidence interval of a single parameter. As it has been said, all values are very close to the cosmology used to determine the parameters related to GRBs, which was $\Omega_M = 0.3$ and $\Omega_\Lambda = 0.7$. Whenever it will be possible to measure the parameters related to GRBs in a way independent from the cosmology, the determination of the cosmological parameters Ω_M and Ω_Λ by fitting the differential intensity distribution will be as precise as any other method used nowadays.

Actually, YON and LFR determined the GRB rate and the luminosity function with different methods, differing at the same time from the one used in the present work. Their best parameters, displayed in Table 6.6, were:

- The value of z_2 is taken from the maximum redshift of their measurements.

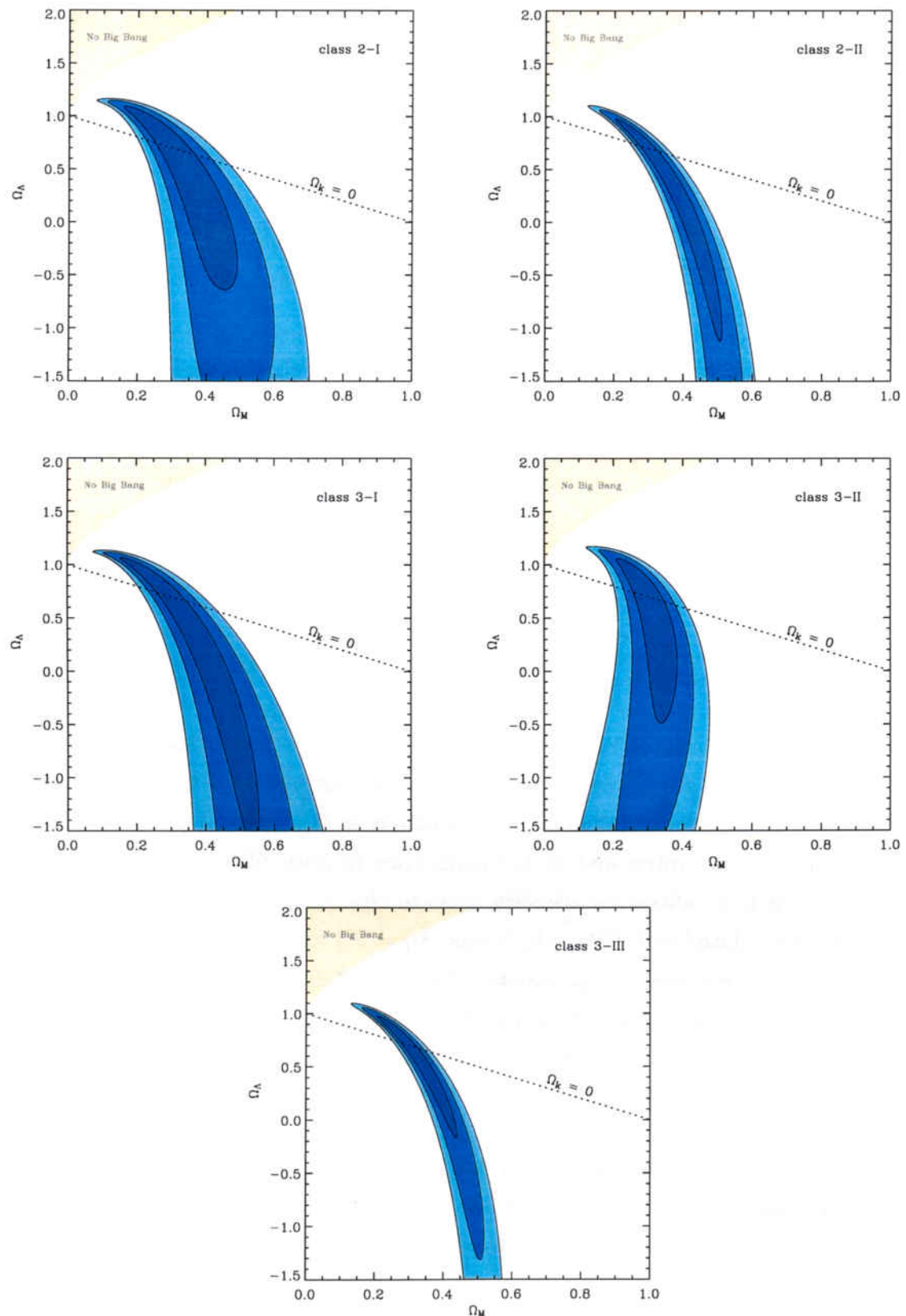


Figure 6.38: Confidence intervals for the cosmological parameters, Ω_M and Ω_Λ , for each class of GRB, without luminosity evolution.

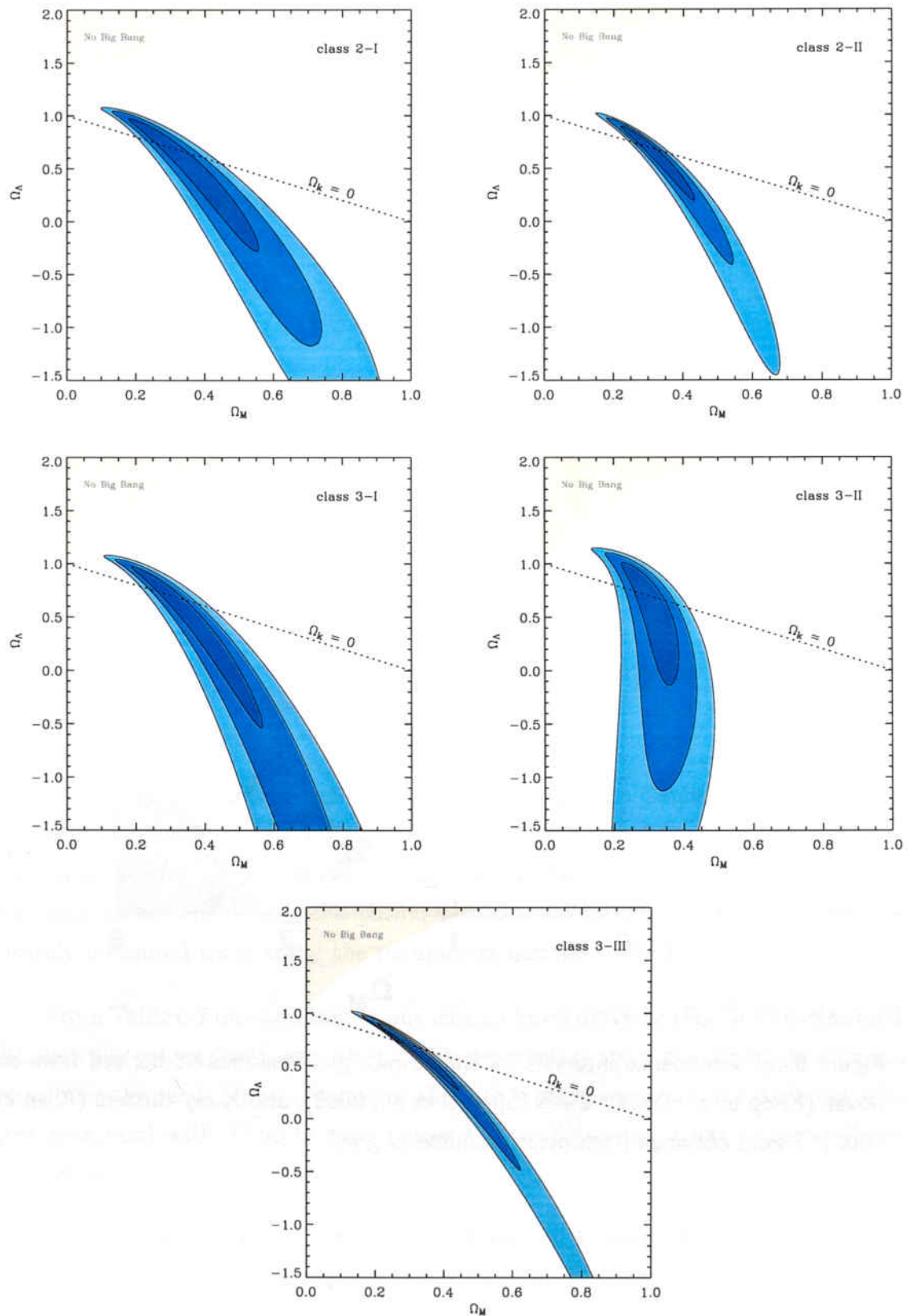


Figure 6.39: Confidence intervals for the cosmological parameters, Ω_M and Ω_Λ , for each class of GRB, with luminosity evolution.

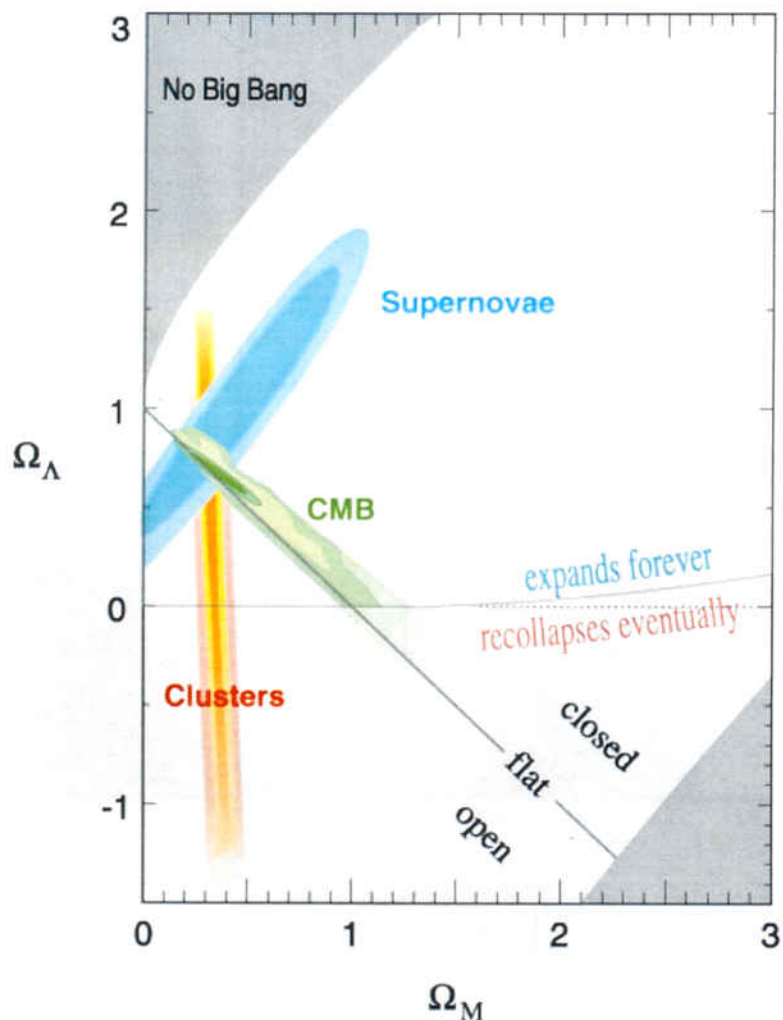


Figure 6.40: Confidence intervals for the cosmological parameters derived from supernovae (Knop et al., 2003), CMB (Spergel et al., 2003), and X-ray clusters (Allen et al., 2002). Figure obtained from <http://panisse.lbl.gov/>.

	YON	LFR
z_1	1.0	2.0
z_2	12.0	12.0
e_1	5.5	3.0
e_2	1.0	1.0
e_3	-8.0	-8.0
z_{max}	20.0	20.0
L_0 ($erg\ s^{-1}$)	$1.0\ 10^{52}$	$5.9\ 10^{51}$
κ	-1.3	-1.5
β	-2.2	-3.3
η	1.8	1.4

Table 6.6: Parameters derived by YON and LFR.

- A value of $z_{max} = 20$ is assumed. There is not a significant difference in using any value from 20 to 30.
- It is also assumed $e_3 = -8$, in order to simulate the very fast decay deduced from the values of e_3 also obtained with our method.

Since these parameters were derived for long-duration GRBs, here we use them to measure Ω_M and Ω_Λ with classes 2-II and 3-III. The confidence regions obtained with these parameters are shown in Figures 6.41 and 6.42. Ω_M and Ω_Λ are very well constrained when using the parameters derived by YON, while they are not precisely measured when using the parameters derived by LFR.

From Table 6.7 one sees that in any case a closed universe ($\Omega_K > 0$) is obtained. Although the values obtained with the LFR parameters are not compatible with any known measurement, those obtained with YON's parameters are in agreement with those measured with Type Ia supernovae without imposing a flat universe (Riess et al., 2004).

In any case, the results derived from Figures 6.41 and 6.42 and Table 6.7 are not significant for class 2-II, and hardly significant for class 3-III. This is because the p value of the comparison of the observed differential intensity distribution with the best theoretical one is either 0.05, for class 3-III, or definitely lower for class 2-II,

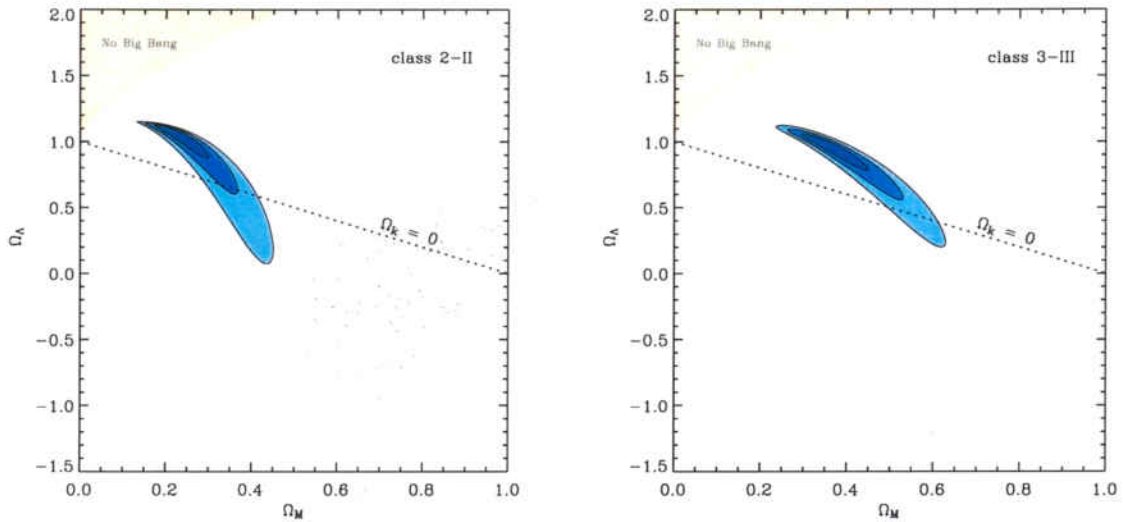


Figure 6.41: Confidence intervals for the cosmological parameters, Ω_M and Ω_Λ , for long-duration GRBs, with the parameters derived by YON.

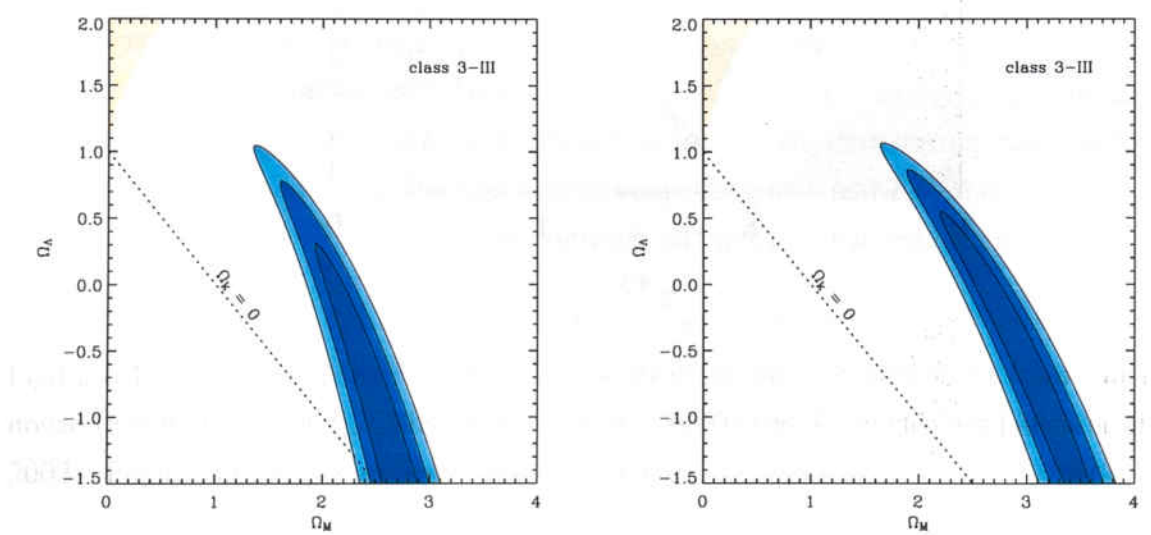


Figure 6.42: Confidence intervals for the cosmological parameters, Ω_M and Ω_Λ , for long-duration GRBs, with the parameters derived by LFR.

GRB class	YON		LFR	
	Ω_M	Ω_Λ	Ω_M	Ω_Λ
2-II	$0.22^{+0.05}_{-0.03}$	$1.06^{+0.05}_{-0.10}$	$2.66^{+0.62}_{-0.54}$	$-1.33^{+1.25}_{-2.13}$
3-III	$0.36^{+0.05}_{-0.05}$	$0.96^{+0.08}_{-0.10}$	$2.86^{+0.59}_{-0.47}$	$-0.36^{+0.66}_{-1.05}$

Table 6.7: Values of Ω_M , Ω_Λ , and 1σ confidence intervals obtained for class 2-II and 3-III GRBs, using the parameters derived by YON and LFR.

GRB class	bins	<i>d.o.f.</i>	YON			LFR		
			χ^2	$\hat{\chi}^2$	<i>p</i>	χ^2	$\hat{\chi}^2$	<i>p</i>
2-II	41	30	45.9	1.53	0.03	48.9	1.63	0.02
3-III	41	30	43.6	1.45	0.05	44.0	1.47	0.05

Table 6.8: χ^2 values for the comparisons of the theoretical and observed differential intensity distributions of GRBs of classes 2-II and 3-III. The parameters for the theoretical distribution come from Tables 6.6 and 6.7.

meaning that it is highly probable that the values for the GRB parameters shown in Table 6.7 are not valid for these GRB classes.

6.5 Simulations

At this point, it is important to evaluate the efficiency of the technique presented here for a nearby future, given that, with the current number of detected GRBs, the parameters that fit the GRB rate and the luminosity function are not accurately determined. In this section, a couple of GRB populations will be simulated, one with a set of parameters without luminosity evolution and another one with evolution. Each population will contain 10000 GRBs, that is about one order of magnitude larger than the actual population of class 2-II GRBs. For example, the SWIFT mission (Gehrels et al., 2004), launched in 2004, is expected to detect at a rate of about 100 GRBs per year, for a lifespan of at least two years and a maximum of eight years. On the other hand, GLAST (von Kienlin et al., 2004), scheduled for launch in 2007, will detect about 200 GRBs per year. SWIFT is enhanced

for the measurement of GRB redshifts, while GLAST is enhanced to detect the very high energy emission, up to 300 GeV. There also exists a proposed mission by Lamb et al. (2005), which expects to detect about 800 GRBs in a 2-year mission. The combination of all these missions would, at most, triple the number of GRBs detected by BATSE, so to detect about 10000 GRBs will require a new generation of dedicated satellites enhanced for high detection efficiency, a concept like BATSE but with today's technology.

6.5.1 The best fits

It has been stated that finding the global minimum is an impossible task. However, we are interested in answering one question: how precisely can we recover a simulated set of parameters?

A Monte Carlo simulation of a differential intensity distribution has been run with the parameters obtained from the bests fits of class 2-II GRBs (see Tables 6.3 and 6.4) without and with luminosity evolution. The sample is of 10000 GRBs, and the number of bins has been doubled, so in average there are 5 times more bursts per bin, which divides by $\sqrt{5}$ the relative uncertainty. The results are summarized in Table 6.9.

The simulated set with evolution is recovered, always within the uncertainty limits. The parameter z_{max} is within the 2σ interval, and L_0 is within the 3σ interval. All as expected.

Table 6.10 shows the χ^2 values, where one sees that in either case the p value has improved. With the current population, it was not possible to distinguish whether there were luminosity evolution or not because the χ^2 and p values were similar in both cases. It was impossible to improve the fit even by adding one more parameter, because the low number of GRBs made the differential intensity distribution very noisy. Now, the fit accounting for luminosity evolution gives a much better fit than the one without evolution, because this noise has been considerably reduced. An important conclusion is that whenever one would dispose of a sample of 10000 GRBs, the fit of the differential intensity distribution will enable to discriminate the luminosity evolution.

	No evolution		Evolution	
	Simulated Set	Best fit	Simulated Set	Best fit
z_1	3.3	$3.0^{+0.3}_{-0.3}$	2.7	$3.3^{+0.4}_{-0.6}$
z_2	5.2	$5.3^{+0.2}_{-2.3}$	9.6	$10.3^{+1.1}_{-1.2}$
e_1	2.4	$1.9^{+0.2}_{-0.3}$	7.9	$8.0^{+18.1}_{-0.6}$
e_2	3.4	$3.4^{+0.3}_{-0.3}$	2.1	$2.3^{+0.6}_{-0.2}$
e_3	0.0	$-0.4^{+0.2}_{-0.4}$	0.1	$0.0^{+0.3}_{-1.1}$
z_{max}	9.8	$9.5^{+0.1}_{-0.6}$	30.0	$26.2^{+2.3}_{-1.3}$
L_0 ($erg\ s^{-1}$)	$5.4\ 10^{51}$	$1.9^{+1.0}_{-1.0}\ 10^{51}$	$0.8\ 10^{53}$	$1.9^{+0.6}_{-0.3}\ 10^{53}$
κ	-1.1	$-3.7^{+1.9}_{-0.2}$	-2.0	$-2.1^{+0.2}_{-0.1}$
β	0.1	$0.3^{+0.6}_{-0.3}$	-1.8	$-1.7^{+0.3}_{-0.2}$
η	-	-	1.4	$1.2^{+0.2}_{-0.4}$

Table 6.9: Simulated parameters and best fit parameters for two sets of simulations: without, and with luminosity evolution.

Simulated set	χ^2	bins	<i>d.o.f.</i>	$\hat{\chi}^2$	<i>p</i>
No evolution	75.7	82	72	1.05	0.36
Evolution	59.3	82	72	0.82	0.86

Table 6.10: χ^2 values for the best fits of the simulated sets without and with luminosity evolution.

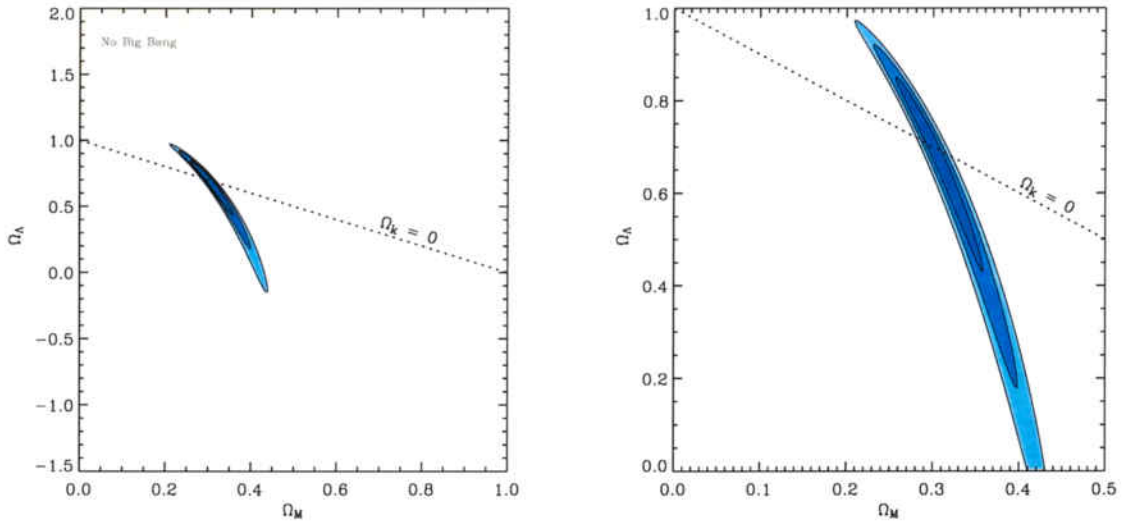


Figure 6.43: Confidence intervals for the cosmological parameters for the simulated set of GRBs, without luminosity evolution. The right plot is a zoom in the left plot.

6.5.2 The cosmological parameters

Figures 6.43 and 6.44 show the confidence regions for the cosmological parameters, Ω_M and Ω_Λ , computed with the simulated samples of 10000 GRBs, without and with luminosity evolution, respectively. The plots are shown in two scales: the first is equal to that used for the current population of GRBs, and is shown for comparison purposes; the second is a closer zoom to reveal the structure which was not appreciable before.

Confidence regions are now much smaller than with the current sample of GRBs of class 2-II, and still centered around the values $\Omega_M = 0.3$ and $\Omega_\Lambda = 0.7$.

Table 6.11 shows the best values for Ω_M and Ω_Λ . We recover, now, almost the exact value used for the minimization, and the uncertainty has been reduced by about a factor of 3. This accuracy is actually only achieved with Type Ia supernovae assuming a flat universe as a prior (Riess et al., 2004). With the latter assumption our uncertainty would be 10 times smaller.

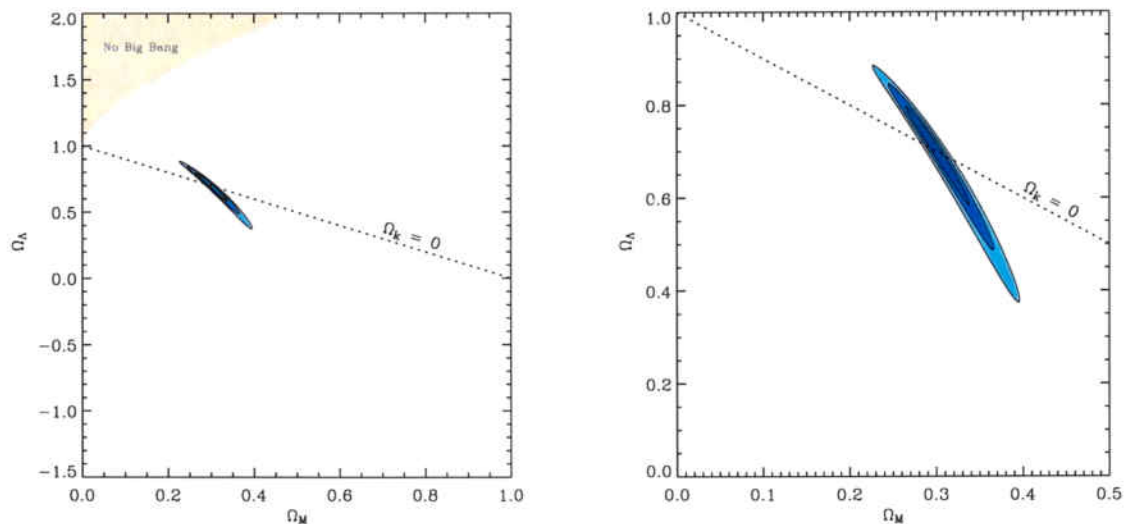


Figure 6.44: Confidence intervals for the cosmological parameters for the simulated set of GRBs, with luminosity evolution. The right plot is a zoom in the left plot.

	No evolution		Evolution	
	Ω_M	Ω_Λ	Ω_M	Ω_Λ
	$0.30^{+0.04}_{-0.03}$	$0.69^{+0.12}_{-0.16}$	$0.30^{+0.03}_{-0.03}$	$0.71^{+0.06}_{-0.08}$

Table 6.11: Values of Ω_M , Ω_Λ , and 1σ confidence intervals obtained for the two sets of simulated GRBs: without, and with luminosity evolution.

6.6 Conclusions

The fit of the differential intensity distribution of GRBs is used here as a tool to measure at the same time the GRB rate and the luminosity function of GRBs. Previous fittings included only a parameterization of the luminosity function and a few discrete options for the GRB rate (Porciani and Madau, 2001). Here, a new parameterization is presented, chosen on basis to the results coming from different methods, which include a continuous set of possible GRB rates modelled by equation 5.15. Moreover, the luminosity evolution predicted by Balastegui et al. (2001), and measured by LFR and YON, is included. It can be concluded that, with the current sample of GRBs, the accuracy in each parameter can be as good as 10 – 30% for long-duration GRBs, classes 2-II and 3-III. On the other hand, the uncertainty in each parameter for the rest of the classes of GRBs is quite large, some of them being impossible to determine with the current technique. This problem would be solved using a larger population. The simulations show that, with a sample of 10000 GRBs, the fit of the differential intensity distribution can constrain the GRB rate and the luminosity function of GRBs with high accuracy, and can even discern whether there exists any luminosity evolution. An important conclusion from the present data is that the history of the SFR started with an outburst, a sudden and massive beginning of the star formation. From long-duration GRBs (classes 2-II and 3-III), which are the ones expected to closely follow the SFR, it is obtained that the formation of stars began at $z > 25$ or $z \sim 10$, depending on whether GRBs have luminosity evolution or not, respectively.

For measuring the cosmological parameters, Ω_M and Ω_Λ , the present number of GRBs is enough to measure them with an accuracy similar to that of some current experiments (Knop et al., 2003; Spergel et al., 2003; Allen et al., 2002), provided that one could determine the GRB rate and the luminosity function independently from cosmology. If one had to adjust any of these parameters simultaneously with the cosmology, the confidence regions would be wider, and the measurement of Ω_M and Ω_Λ would not be so accurate. This possibility has not been studied in the present work. With a possible sample of 10000 GRBs and luminosity evolution, the measurement of Ω_M and Ω_Λ would become so accurate¹ that, within the calculation

¹The uncertainty would be the same as the latest value found with Type Ia supernovae (Riess et al., 2004), but they suppose a flat universe, whereas here is not necessary.

of the χ^2 of the comparison of the differential intensity distribution of GRBs in each point of the $\Omega_M - \Omega_\Lambda$ plane, one could try to introduce, for instance, the method used by YON to determine the GRB rate and the luminosity function of GRBs for the corresponding cosmology. With these procedure one avoids the circular problem of using cosmology to measure the parameters, and later on using these parameters to measure the cosmology. In order to achieve a sample of GRBs ten times larger than the present one, a detector like BATSE equipped with technology of the new generation is required. This fact is not expected to happen within the next five years.

Chapter 7

Conclusions

Traditionally, GRBs have been classified into two different classes: short-duration and long-duration GRBs, the spectra of short GRBs being harder than that of long GRBs. This classification is based on the bimodal distribution of GRB durations. The logarithmic distribution of T_{90} , the time within which one receives 90% of the GRB fluence, has a dip at approximately $T_{90} \approx 2\text{ s}$. This dip separates two subsets with mean T_{90} of approximately 0.6 s and 50 s, respectively (Kouveliotou et al., 1993). Both GRB classes are isotropically and inhomogeneously distributed, although long-duration GRBs are found to be more inhomogeneously distributed. The spatial distribution of GRBs led to the common belief of their extragalactic origin, setting the required source luminosity between 10^{50} and 10^{52}erg s^{-1} , assuming isotropic emission. The extragalactic nature of long-duration GRBs was finally revealed in 1997 when the satellite BeppoSAX detected GRB970508. The very precise location of this GRB allowed optical observations which showed a fading source at $z = 0.835$. Since then, more than six tens of GRBs' redshifts have been measured for long-duration GRBs. On the other hand, short-duration GRBs have proved to be more elusive. BATSE localized GRBs with high uncertainty (an average 4° box error), making it impossible to find the source at wavelengths other than gamma-rays and to measure its redshift. BeppoSAX, on the other hand, could point GRBs, in the X-ray band, with higher precision (3 arcmin with its Wide Field Camera and $\sim 50\text{ arcsec}$ with the Narrow Field Instruments). Unfortunately, BeppoSAX had low sensitivity to GRBs with durations shorter than 2 s. It has not been until the recent launch of the SWIFT satellite that it has been possible to

measure redshifts for short-duration GRBs (Castro-Tirado et al., 2005; Piro, 2005; Fox et al., 2005; Gehrels et al., 2005; Villasenor et al., 2005; Hjorth et al., 2005), proving their extragalactic origin. The afterglows of long-duration GRBs have been found to have the underlying signal of a supernova. The signal coming from the supernova is weaker than that of the afterglow, but as the latter fades, if the GRB is close enough, the light from the supernova emerges, creating a bump in the afterglow lightcurve. This fact and the distribution of long GRBs inside their host galaxies, most of them tracing intensive star-forming regions, have led astronomers to relate long-duration GRBs to core-collapse supernovae. The progenitors of this kind of GRBs are the so-called collapsars. As far as short GRBs are concerned, the detection of GRB050509B and GRB050709 seem to discard the existence of any underlying supernova. Adding to this the fact that GRB050509B exploded in an elliptical galaxy, and GRB050709 exploded in the outskirts of its host galaxy, the GRB community relates short-duration GRBs to binary mergers.

The largest and most homogenous catalogue of GRBs is the BATSE catalogue. BATSE was an instrument that flew on the CGRO, and it was devoted to the detection of GRBs. With a field of view of $2.6\pi \text{ sr}$, it detected 2702 GRBs during its 9-year lifetime. The BATSE catalogue provides up to nine magnitudes intrinsic to the burst (7 related to energy and 2 related to duration). These magnitudes are: four time-integrated fluences $F_{Ch\#1} - F_{Ch\#4}$, respectively corresponding to the $20 - 50 \text{ keV}$, $50 - 100 \text{ keV}$, $100 - 300 \text{ keV}$, and $300 - 2000 \text{ keV}$ spectral channels; three peak fluxes P_{64} , P_{256} , and P_{1024} , measured in 64, 256, and 1024 ms bins, respectively; and two measures of burst duration T_{50} and T_{90} , the times within which 50% and 90% of the flux arrives. With all this information available, inferring a classification of GRBs using only one magnitude (T_{90}) is highly inefficient. Multivariate analysis is needed in order to deal with a large number of variables with complex relationships (including nonlinear ones) being likely present. This analysis leads to a new classification of GRBs, and to the discovery of a new class of GRBs.

Within this thesis, first, a PCA is applied to the most recent BATSE catalogue. The PCA is a statistical method used in multivariate data analysis to obtain new variables, expressed as linear combinations of the original ones, which carry most of the information on the system. Based on the correlations among the original variables, some of the new variables can be disregarded if they carry very little information. It is obtained that only three variables account for 96% of the system

information. The first variable is a weighted sum of all the original variables, the fluences in energy channels #1 to #3 being most important. The second variable is approximately the difference between the weighted sum of the three peak fluxes and the two durations. The last variable in importance is the fluence in energy channel #4.

Secondly, in this thesis a new classification of GRBs has been presented, based on two automatic classification algorithms: cluster analysis and a neural network classification.

Cluster analysis is an exploratory data analysis tool which aims at sorting different objects into groups in such a way that the degree of association between two objects is maximal if they belong to the same group and minimal otherwise. In this thesis the Ward's method is used. The method follows an agglomerative hierarchical clustering procedure, which starts from n points spread over the 9-dimensional input space and groups them until ending up with a single cluster. The algorithm searches for clusters with minimum variance among objects belonging to the same cluster and with maximum variance between clusters, and works with the centre of gravity of each cluster. That gives clusters as compact and as detached from each other as possible. A dendrogram is obtained, that shows the way groups are clustering, as well as the dissimilarity of the resulting groups. Thus, detecting a large rise in the dissimilarity by the union of two clusters means that two groups with remarkably different characteristics have been merged. From the dendograms obtained, it is concluded that there are two well-separated classes plus an emergent third class. The main weakness of the cluster analysis is that it only deals with linear combinations of the variables. Such a weakness can be overcome by means of a neural network, which also detects nonlinear relationships.

Neural networks are artificial intelligence algorithms that can be used for an automatic and objective classification. A neural network is composed of a large number of highly interconnected processing elements (neurons), working in unison to solve specific problems. They are inspired by the way biological nervous systems, such as the brain, process information. In order to classify GRBs, an unsupervised method, the self-organizing map (SOM), has been used, since we do not want to start from any prior classification. The dimension of the output space must be specified beforehand, and based on the results of the cluster analysis dendograms

the network is run two times, asking first for a two and then for a three-dimensional output space, thus producing either two or three classes of GRBs.

With both methods, the cluster analysis and the neural network, two classifications have been obtained: a two-class and a three-class classification. The two-class classification corresponding to the classical classification, and the three-class classification corresponding to the suggestion of the dendrograms of a possible third class of GRBs.

With the two-class classification the classical classes of GRBs are recovered: short-duration, hard GRBs (here called class 2-I) versus long-duration, soft GRBs (here called class 2-II), the latter being more inhomogeneously distributed. It could seem that this classification does not bring any new knowledge about GRBs, but, as a matter of fact, it contributes substantial implications. First of all, classical classification separates GRBs with $T_{90} \gtrsim 2$ s. This is an abrupt separation. Indeed, there seems to be a bimodal distribution of GRBs durations, but these two distributions undoubtedly overlap. The automatic classifications presented in this thesis are able to identify individual GRBs, assigning them to a given class (short or long GRBs), even though they have durations corresponding to the overlapping region of the distributions. This is possible thanks to the use of all the known variables that describe a single burst, not only the duration. This mere fact makes the new classification worthy by itself. In addition to this, it is seen that short GRBs have durations up to $T_{90} \sim 100$ s. This fact has strong consequences for the modelization of short-duration progenitors, which according to recent observations may come from binary mergers. Simulations of NS-NS and BH-NS mergings show that they cannot produce GRBs with durations longer than 2 s. These simulations should be modified in some way since, from the classification presented in this thesis, short GRBs do have durations much longer than 2 s. Other kinds of binary mergers, like Helium stars-BH and WD-BH mergings, are supposed to be more inhomogeneous than short-duration GRBs, hence they are not suitable as their progenitors.

In the three-class classification, the new class 3-II is composed by the longer and softer bursts from class 2-I, and by the shorter bursts from class 2-II. This new class of intermediate duration has the same hardness as the long-duration class 3-III. In contrast, it has lower fluence, lower peak flux, and is more homogeneously distributed than class 3-III. The separation of GRBs into three different classes has

been supported also by several other authors cited throughout this thesis. Here, a possible physical difference between class 3-II and 3-III GRBs has been also found, which suggests that the three-class classification has a real meaning and is not an artifact of the automatic classification. Classical long-duration GRBs are found to have a hardness evolution, in the sense of farther GRBs being spectrally harder than closer GRBs. When one takes into account the hardness-intensity correlation, the hardness evolution suggests an evolution of the luminosity function, a fact that has already been confirmed (Lloyd-Ronning et al., 2002; Yonetoku et al., 2004). When one separates classical long-duration GRBs into classes 3-II and 3-III, that evolution remains for class 3-III but it is absolutely lost for class 3-II GRBs. This fact, which cannot be due to chance alone, is an important confirmation that the three-class classification has a physical meaning. One fact supporting the luminosity evolution of class 3-III GRBs is that from the 220 GRBs in the sample of LFR that confirmed the luminosity evolution, 205 entered into the neural network classification, and 198 were classified as class 3-III GRBs. Collapsars, coming from the collapse of very massive stars, can show this luminosity evolution. It is generally admitted that the upper limit of the stellar initial mass function depends on metallicity, and that lower metallicity allows more massive stars to form. When sampling GRBs farther away, one looks to a younger Universe, with lower metallicity, and thus with more massive stars. Therefore, if GRBs come from very massive stars, those ancient GRBs had sources with higher power and they were brighter and harder.

Within the scheme of the three-class classification, class 3-III GRBs are the ones who are thought to have collapsars as progenitors. In turn, class 3-I GRBs are very similar to classical short-duration GRBs, which are thought to come from NS-NS or NS-BH mergings. Concerning the intermediate duration GRBs, class 3-II, their nature is still unknown, although it has been suggested here that the difference between class 3-I and class 3-II GRBs might be due to one of them coming from NS-NS mergings, and the other one being produced by BH-NS mergings. Nevertheless, the identification of the progenitors for class 3-II GRBs, as well as further confirmation of the progenitors of class 3-I and 3-III GRBs, are part of the future work. Other plans for future work include to adapt the classification to non-BATSE GRBs. The present classification is based on magnitudes measured with BATSE. Other instruments measure other magnitudes and have different sensitivities. These differences difficult the classification of GRBs detected after BATSE. The interest in

classifying newly detected GRBs does not come from confirming the characteristics already measured in this thesis for each GRB class, but rather from the discovery of redshifts, host galaxies morphologies, and identification of positions within host galaxies. These properties are key to discover the type of progenitor of each GRB class, and that is why it is important to classify correctly newly detected GRBs.

The second part of the thesis is dedicated to the study of extragalactic parameters of GRBs, such as the GRB explosion rate and the GRB luminosity function, and to the study of the cosmological parameters of the Universe itself, Ω_M and Ω_Λ . Those parameters are determined for each class of GRBs derived from the neural network in the first part of this thesis, and they are measured both taking into account the effect of luminosity evolution and without it. The measure of these parameters is made by fitting the observed GRB intensity distribution with the theoretical one. The $\log N - \log P$ or intensity distribution is a plot showing the number of GRBs N as a function of the intensity of the GRB, here measured as the peak flux P . The slope of the cumulative intensity distribution of GRBs deviates from the $-3/2$ value expected for an euclidean homogeneous distribution of events. This fact made astronomers change their minds about the distance scale to GRBs, since, combined with the high isotropy of the sample, convinced of their extragalactic origin, even before any GRB redshift was measured. The intensity distribution has already been used to measure GRB explosion rates, redshift distributions, star formation rate, GRB luminosities and luminosity function. Here, in this thesis, we continue this work and expand it by fitting all the parameters at once, each one with higher freedom than in previous works, and extend it to the determination of the cosmological parameters.

The GRB explosion rate is a measure of the number of events per unit comoving volume and time. It provides a census of the number of objects formed at a given redshift and can help to discern among different kinds of progenitors. For instance, the rate of collapsars is expected to follow closely the SFR due to their very fast evolution from their formation to the explosion epoch. On the other hand, NS-NS and BH-NS mergings are expected to happen at mean redshifts between 20% to 50% of that of collapsars, due to their long evolution times from formation to merging. These kinds of progenitors show an explosion rate delayed with respect to the SFR. Based on measures of the SFR, and on the GRB rate with luminosity and redshift calibrations, a triple power law of $(1 + z)$ is used here as a modelization of

the GRB rate. The modelization has 6 free parameters: three exponents, two break points, and a maximum redshift for the GRBs. The results show that with this method and from the number of observed GRBs of short and intermediate duration (classes 2-I, 3-I, and 3-II) it is not possible, as of today, to determine the GRB rate with a minimum of accuracy. On the other hand, the accuracy achieved with long-duration GRBs (classes 2-II and 3-III) is acceptable, being at the same time a good method to measure indirectly the SFR up to very high redshift. For these GRBs the explosion rate increases from $z = 0$ to $z \approx 5$ ($z \approx 9$ when luminosity evolution is taken into account), and then it remains almost constant up to $z \approx 10$ ($z \approx 30$ when luminosity evolution is taken into account). The exponent of the GRB rate at high redshift being nonnegative means that the supposed decay of the GRB explosion rate at high redshifts is modelled here by the parameter z_{max} , which represents a sudden cut. This fact implies that the GRB explosion rate for long-duration GRBs started with an outburst, and consequently so also did the SFR.

A luminosity function is a measure of the number of objects per unit luminosity. Traditionally, the luminosity function of GRBs has been tried to be measured with the $\langle V/V_{max} \rangle$ and $\log N - \log P$ distributions. The typical luminosity function used for GRBs is a double power law. The luminosity function of long-duration GRBs has been measured recently by means of luminosity calibrators such as the variability–luminosity correlation (Lloyd-Ronning et al., 2002; Yonetoku et al., 2004). These works have concluded that there exists a luminosity evolution, with farther GRBs being more luminous than closer GRBs. This possibility was already suggested in the first part of this thesis (see section 4.5) and published in Balastegui et al. (2001). With the current number of observed GRBs, the fit of the intensity distribution cannot determine whether there exists luminosity evolution or not, although simulations show that increasing the sample by one order of magnitude would settle the discussion. The results presented in this thesis suggest that within the three-class classification, intermediate duration GRBs, class 3-II, are the most luminous ones. That makes another requirement that has to be fulfilled by the progenitors of this new class of GRBs.

For each of the free parameters of the modelizations of the GRB rate and the luminosity function, a discussion about the variation of the intensity distribution as a function of the variation of the corresponding parameter has been included. We consider it a useful compilation of effects that shape the intensity distribution.

The final part of the thesis is devoted to the measurement of the cosmological parameters Ω_M and Ω_Λ . These are dimensionless parameters that represent the ratio between the density of each component of the universe (Ω_M for matter, Ω_Λ for cosmological constant) and the critical density, that is, the energy density of a flat universe. They are key parameters to determine the dynamics and geometry of the Universe. $\Omega_M + \Omega_\Lambda = 1$, means that the energy density of the Universe is equal to the critical one and the Universe is flat. $\Omega_M + \Omega_\Lambda > 1$, means that the energy density of the Universe is larger than critical and the Universe is closed. Finally, $\Omega_M + \Omega_\Lambda < 1$, means that the energy density of the Universe is smaller than the critical value and the Universe is open. The scientific community has devoted an extraordinary amount of work to the measurement of Ω_M and Ω_Λ , especially during the last decade. The most successful method has been the fit of the Hubble diagram of Type Ia supernovae. This method led to the discovery of the acceleration of the expansion of the Universe, and consequently to the need of some kind of dark energy, that was first assumed to be in the form of a cosmological constant. In the previous calculations of this thesis, $\Omega_M = 0.3$ and $\Omega_\Lambda = 0.7$ has been used. This is the so-called concordance model, the values derived by using different methods (Type Ia supernovae, CMB, X-ray clusters). Here, a question has been posed: if one knew the explosion rate and the luminosity function of GRBs, would it be possible to use the fit of the intensity distribution to measure Ω_M and Ω_Λ ? The answer is yes.

What has been done is to take the best values for the GRB rate and luminosity function derived by fitting the intensity distribution, and to consider them as fixed parameters. After that, we have proceeded to fit the intensity distribution with Ω_M and Ω_Λ as free parameters. The result is that the values $\Omega_M = 0.3$ and $\Omega_\Lambda = 0.7$ are recovered with an accuracy similar to that obtained with Type Ia supernovae. The best classes to measure the cosmological parameters have been class 2-II, 3-II, and 3-III. The weakness of the method is that one needs to know the GRB rate and luminosity function beforehand, and the methods used to measure these magnitudes assumes fixed values for Ω_M and Ω_Λ . The future work planned on this subject includes the fit of the cosmology simultaneously with the GRB rate and the luminosity function, which has not been done here due to the excessive computation time required.

The sample of measured redshifts of GRBs has increased by about 20 bursts in less than one year of operation of SWIFT. Soon it will double the sample measured

within the previous decade. Once a large sample of redshifts is collected, it will be possible to measure the GRB rate and luminosity function in a direct way, just by counting them. By then, we will be able to compare these magnitudes with the results presented in this thesis. Moreover, the detection of redshifts, host galaxies, and the positioning of the GRBs within them, is bringing unprecedented information on the progenitors of GRBs. Finding different classes of progenitors would confirm the existence of different classes of GRBs, either proving or disproving the new classification of GRBs presented in this work.

Appendix A

Cluster analysis classification

This appendix contains tables with the BATSE trigger numbers and GRB names for each GRB class derived with the cluster analysis.

Table A.1: GRBs corresponding to the cluster analysis class 2-I.

trigger	GRB								
105	910421	108	910424	138	910502B	207	910518	218	910521
229	910526	254	910602C	289	910607	297	910608	298	910609
373	910616	401	910620B	432	910625	444	910626	474	910702
480	910703	491	910705	526	910713	537	910714	543	910717
547	910717B	549	910718C	551	910718	555	910719	568	910722
575	910725	603	910802	677	910814B	690	910817	729	910827
734	910828	741	910829	755	910904	788	910912	809	910919
829	910927	830	910928	836	910929	845	911001	856	911002
867	911004	878	911007	906	911016B	909	911019	936	911025
942	911027	974	911031B	999	911104	1025	911109	1051	911113
1073	911117B	1076	911117	1088	911119	1097	911120B	1102	911120
1112	911123B	1120	911125	1129	911129	1154	911209B	1159	911210
1204	911223	1211	911224	1223	911226	1289	920110C	1306	920120
1346	920203	1359	920205	1382	920209B	1404	920216B	1416	920218B
1439	920226B	1443	920227	1452	920229B	1453	920229	1461	920303B
1492	920318	1518	920325B	1553	920414	1566	920423	1588	920508
1634	920605	1635	920606	1636	920607	1637	920608	1657	920619B
1659	920620B	1662	920622D	1665	920622C	1679	920628	1683	920701
1694	920711B	1704	920717B	1709	920718	1719	920722	1741	920804
1747	920806	1760	920808	1851	920818	1953	920924	1968	921001B
1974	921003	2003	921023B	2035	921031	2041	921102	2043	921108
2044	921109	2049	921111B	2053	921112	2056	921115	2068	921123B
2095	921214	2099	921216	2103	921219	2114	930102	2115	930103
2125	930110	2126	930110B	2145	930124	2146	930125	2155	930201B
2161	930203B	2163	930204	2167	930206	2187	930212	2201	930219

Continued on next page

Table A.1: GRBs corresponding to the cluster analysis class 2-I.

trigger	GRB								
2205	930219E	2206	930220	2217	930304	2220	930305B	2265	930324
2273	930329	2288	930405C	2291	930406C	2312	930421	2317	930425
2320	930428	2321	930430	2326	930503D	2327	930503C	2330	930506B
2332	930510	2347	930519	2352	930524B	2353	930526	2357	930528
2360	930530B	2365	930601	2368	930602B	2377	930606	2382	930608
2384	930609B	2393	930614	2395	930614C	2401	930619	2424	930701B
2437	930709B	2448	930719	2449	930719B	2454	930721C	2463	930725
2487	930811	2502	930824	2512	930903	2513	930903C	2514	930905
2523	930911	2529	930913	2536	930922B	2564	931005	2583	931013
2597	931021B	2599	931022	2614	931101	2615	931101B	2628	931112
2632	931113	2641	931118	2649	931120	2677	931204B	2679	931205
2680	931206B	2690	931211	2693	931215B	2715	931229	2725	940101C
2728	940101	2736	940103	2757	940114	2760	940115	2788	940128B
2793	940129	2795	940201B	2799	940206B	2800	940207	2810	940209
2814	940211B	2828	940216	2834	940219	2846	940224	2860	940305
2861	940305B	2873	940310	2894	940328	2896	940329	2910	940404
2918	940410B	2933	940415	2945	940424	2952	940428	2966	940507
2973	940512C	2975	940512B	2977	940515B	2978	940515	2986	940521C
2988	940524B	2995	940527B	3027	940613	3037	940621C	3038	940621B
3039	940622	3066	940708C	3073	940712	3078	940714C	3087	940717
3088	940717C	3094	940724	3113	940808	3118	940811	3121	940812C
3138	940826	3144	940830B	3146	940831	3152	940902	3164	940910B
3173	940918	3215	941003	3218	941005B	3266	941031B	3278	941110B
3280	941111	3282	941113	3284	941115	3294	941123	3297	941126C
3308	941203	3333	941229B	3335	941230B	3340	950102	3342	950103
3349	950108	3359	950115B	3374	950123	3378	950129	3379	950129B
3410	950210	3412	950211	3437	950221B	3441	950225B	3477	950321
3487	950328	3494	950405B	3502	950410	3510	950416B	3530	950502
3545	950505	3569	950510	3598	950524	3606	950529	3611	950531
3640	950611	3642	950612	3644	950620	3665	950714	3668	950716
3722	950801	3728	950802	3733	950803	3735	950804B	3736	950805
3737	950805B	3742	950806B	3751	950810	3770	950830	3782	950908B
3791	950911B	3807	950919B	3810	950920	3814	950922B	3840	951001
3866	951014B	3867	951014	3868	951015B	3870	951016	3888	951030C
3889	951101	3894	951104B	3895	951104C	3902	951110	3904	951112B
3910	951117B	3919	951124B	3921	951125	3926	951128	3936	951208B
3939	951209	3940	951211	4312	960111	4327	960112	4660	960130
4744	960205B	4776	960207	4807	960209	4814	960210	4871	960214
4955	960220	5079	960229b	5206	960311	5212	960312	5277	960319
5339	960325	5439	960420	5448	960426	5453	960507	5461	960515
5467	960521B	5469	960523B	5471	960524C	5483	960601	5485	960604
5488	960607B	5498	960615B	5499	960615C	5500	960616B	5502	960616
5513	960623D	5527	960703	5528	960704	5529	960705	5530	960707
5533	960708	5537	960713B	5546	960722B	5547	960722C	5559	960802
5561	960803	5562	960804B	5563	960804	5564	960805	5571	960812
5573	960813B	5576	960816	5594	960907	5599	960909	5605	960916
5607	960919	5619	960929B	5620	961001	5638	961020	5647	961027B
5650	961030	5664	961110	5697	961126	5718	961218B	5724	961224B
5730	961228B	5733	961230	5740	970103	5770	970110	5867	970119
6096	970219	6105	970227B	6113	970304	6117	970308	6119	970312

Continued on next page

Table A.1: GRBs corresponding to the cluster analysis class 2-I.

trigger	GRB								
6120	970313	6123	970315	6131	970321	6135	970324	6136	970326
6137	970326B	6145	970329B	6153	970403	6178	970414	6180	970414B
6182	970415	6188	970417	6204	970423	6205	970424	6215	970430
6219	970503	6223	970507	6230	970514	6233	970516	6251	970603B
6265	970612	6269	970613B	6275	970617	6281	970627C	6292	970701
6293	970704	6298	970708	6299	970708B	6301	970709C	6307	970714B
6314	970720	6330	970809	6331	970809B	6341	970820	6342	970821
6343	970824	6347	970826	6361	970904	6368	970907	6372	970908B
6376	970910B	6385	970918	6386	970918B	6395	970924	6398	970926
6401	970928	6408	971002	6411	971004	6412	971004B	6422	971009B
6425	971011	6427	971012	6436	971015B	6439	971016	6443	971021
6445	971023	6451	971027	6452	971028	6462	971104	6486	971118
6488	971120	6497	971124	6527	971209	6534	971216	6535	971218
6536	971218B	6540	971220B	6542	971221	6547	971228	6573	980116
6579	980124C	6580	980125	6591	980207B	6600	980214	6606	980218B
6631	980308	6635	980310B	6638	980312	6641	980315	6643	980315C
6645	980315D	6659	980326	6662	980327	6668	980330	6671	980331B
6679	980404B	6682	980407	6689	980416	6693	980419	6697	980421B
6700	980423	6710	980427	6715	980430	6753	980511	6757	980513
6787	980527	6788	980527B	6800	980530B	6824	980614	6853	980619
6870	980626	6916	980711	6931	980718B	7009	980820	7060	980903
7063	980904	7078	980910B	7102	980918	7106	980920	7133	980929
7142	981005	7148	981009B	7159	981016	7173	981022B	7187	981103
7227	981124	7240	981130	7281	981226	7283	981227	7287	981229
7290	981231	7292	981231B	7294	990102B	7297	990103	7305	990105
7329	990117B	7344	990123B	7353	990126B	7366	990202	7367	990202B
7375	990206B	7378	990208B	7381	990210B	7427	990225	7430	990226B
7440	990302	7446	990304	7447	990304B	7449	990305B	7453	990306B
7455	990307	7456	990308	7472	990315B	7495	990330	7508	990404
7526	990423	7529	990424C	7530	990425	7533	990426	7547	990504
7554	990508	7563	990513	7581	990523C	7584	990527	7587	990527B
7595	990603B	7599	990605	7601	990610	7602	990610B	7626	990701B
7663	990720	7706	990810	7710	990814B	7745	990829B	7749	990902
7753	990905	7754	990906	7770	990918	7775	990925B	7781	991001
7784	991002	7789	991005	7793	991007	7800	991012	7805	991015
7813	991020	7827	991028	7901	991211	7912	991219	7922	991228
7939	000108	7943	000111	7963	000122	7970	000126B	7979	000202
7980	000203	7987	000212	7988	000213	7995	000222	7999	000226B
8018	000306	8027	000310B	8035	000313B	8041	000319	8047	000321
8072	000410	8076	000415B	8079	000418	8082	000420B	8085	000424
8089	000502	8097	000508	8099	000508C	8104	000513	8120	000525

Table A.2: GRBs corresponding to the cluster analysis class 2-II.

trigger	GRB	trigger	GRB	trigger	GRB	trigger	GRB	trigger	GRB
107	910423	109	910425	110	910425B	121	910429	130	910430

Continued on next page

Table A.2: GRBs corresponding to the cluster analysis class 2-II.

trigger	GRB								
133	910501	143	910503	148	910505	160	910507	171	910509
179	910511	204	910517B	219	910522	222	910523	226	910525
228	910526B	235	910528	237	910529	249	910601	257	910602
288	910607B	332	910612	351	910614B	394	910619	398	910620
404	910621B	408	910621	414	910622	451	910627	467	910629
469	910630	473	910702B	503	910709	516	910712	548	910718B
559	910721B	563	910721	577	910725B	591	910730B	594	910730
606	910802B	647	910807	658	910809C	659	910809B	660	910809
673	910813	676	910814C	678	910814	680	910815	685	910816B
686	910816	692	910818	704	910821	717	910823	752	910902
761	910905	773	910908	795	910914	803	910918	815	910923
820	910926	825	910927B	840	910930B	841	910930	869	911005
907	911016	914	911022	927	911024	946	911027B	973	911031
1009	911106B	1046	911111B	1085	911118	1087	911119B	1114	911123
1122	911127	1123	911127C	1126	911128	1141	911202	1145	911204
1148	911205	1150	911207	1152	911208	1156	911209C	1157	911209
1190	911217	1192	911217B	1196	911219B	1197	911219	1200	911221
1213	911224C	1218	911225	1221	911225B	1235	911227	1244	911228
1279	920105	1288	920110	1291	920110B	1303	920116	1384	920210C
1385	920210	1390	920212	1396	920214	1406	920216	1419	920218
1425	920221	1440	920226	1446	920227C	1447	920227B	1449	920228
1456	920301	1458	920302B	1467	920307	1468	920308	1472	920310
1515	920323	1533	920331	1541	920406	1546	920408	1551	920413
1552	920414B	1558	920419B	1559	920419	1567	920423B	1574	920430
1578	920502	1579	920502C	1580	920503	1586	920505	1601	920511
1604	920511B	1606	920513	1609	920517	1614	920520	1623	920524
1625	920525	1626	920525C	1628	920526	1642	920609	1651	920617B
1652	920617	1653	920617C	1655	920618	1660	920620	1661	920620C
1663	920622	1676	920627	1700	920714B	1711	920720	1712	920720B
1714	920721D	1717	920721	1730	920730B	1731	920730	1733	920801
1740	920803	1742	920804C	1806	920812B	1815	920814	1819	920814B
1830	920816	1883	920830	1886	920902	1922	920912	1924	920913
1956	920925	1982	921008	1989	921015	1993	921021	1997	921022
2019	921029	2037	921101	2047	921110	2061	921118	2067	921123
2074	921203	2079	921206B	2080	921206	2081	921207B	2083	921207
2087	921208	2090	921209	2093	921211	2101	921217	2102	921218
2106	921227	2110	921230	2111	921230B	2112	921230C	2122	930106B
2123	930108	2138	930120	2143	930123	2149	930127	2151	930131
2156	930201	2181	930210	2188	930213	2189	930213B	2190	930214
2191	930214C	2193	930214B	2197	930217	2202	930219D	2203	930219B
2204	930219C	2211	930301	2213	930302	2228	930309	2232	930310
2233	930311	2253	930317	2254	930318B	2267	930326B	2276	930331
2277	930331B	2287	930405	2298	930410	2304	930415	2306	930416
2309	930418B	2310	930420B	2311	930420	2315	930424	2316	930425B
2324	930503	2328	930506C	2329	930506	2340	930514B	2344	930517B
2345	930517	2346	930518	2367	930602	2371	930603	2373	930605
2375	930606B	2380	930607	2383	930609	2387	930612	2391	930612D
2392	930613	2394	930614B	2405	930621B	2419	930627	2423	930701
2428	930704	2429	930705	2430	930705B	2431	930706	2432	930706B
2435	930708	2436	930709	2441	930711C	2443	930711	2446	930714

Continued on next page

Table A.2: GRBs corresponding to the cluster analysis class 2-II.

trigger	GRB								
2447	930715	2450	930720	2452	930721B	2458	930724	2472	930730
2476	930731	2482	930805	2495	930819	2500	930822	2508	930901
2510	930902B	2519	930909	2522	930910	2530	930914	2533	930916
2537	930922	2541	930926	2560	931003	2569	931008C	2570	931008B
2581	931013B	2586	931014	2589	931016B	2593	931019	2603	931024
2606	931026	2610	931030B	2611	931031	2619	931106	2623	931110
2634	931114	2640	931117	2662	931127	2664	931128C	2665	931128
2688	931209	2691	931212	2695	931217	2696	931218	2697	931219
2700	931221	2703	931222	2706	931223	2709	931225	2711	931226
2719	931230	2727	940101D	2749	940110	2751	940111	2753	940112B
2770	940119B	2774	940120	2775	940120B	2780	940126	2790	940128
2797	940203	2798	940206	2812	940210	2815	940211	2831	940217
2843	940222	2852	940228	2853	940228B	2855	940301	2862	940305C
2863	940306	2864	940307	2889	940319	2890	940321	2891	940323
2898	940330B	2900	940331B	2913	940406	2916	940407	2919	940410
2922	940412	2924	940413C	2925	940413	2929	940414	2931	940414B
2944	940423	2948	940425C	2953	940429	2958	940503	2961	940504
2984	940520	2992	940526C	2993	940526B	2994	940526	2996	940527
2998	940529D	3001	940529B	3003	940529C	3005	940530	3011	940602B
3015	940604	3017	940606	3026	940611	3029	940616B	3032	940616
3035	940619	3040	940623B	3042	940623	3056	940702	3057	940703
3067	940708	3070	940710B	3071	940710	3072	940711	3075	940714
3076	940714B	3080	940715B	3084	940716	3085	940716B	3091	940720
3101	940728B	3102	940730	3105	940803B	3110	940806	3115	940810
3119	940812B	3120	940812	3127	940816	3128	940817	3131	940821
3134	940823B	3142	940829	3143	940830	3153	940902B	3155	940904
3156	940905	3168	940915	3171	940917	3174	940919	3177	940921B
3178	940921	3193	940925	3212	941003B	3217	941005	3220	941006
3227	941008	3229	941009	3237	941011	3238	941012	3241	941014
3242	941014B	3245	941017	3246	941017B	3247	941018	3248	941018B
3255	941023	3257	941026	3259	941026B	3267	941031C	3269	941031
3276	941109	3283	941114	3287	941119	3290	941121	3292	941122
3301	941126B	3306	941128	3307	941202	3319	941214	3320	941215
3321	941215B	3322	941217	3330	941228	3336	941230	3339	950102B
3345	950104	3347	950105	3350	950110	3351	950111	3352	950111B
3356	950114	3358	950115	3364	950118	3370	950120	3405	950206
3407	950207	3408	950208	3415	950211B	3416	950211C	3436	950221
3439	950223	3448	950301	3458	950305	3465	950311	3471	950317C
3472	950317	3480	950325B	3481	950325	3488	950401	3489	950401B
3491	950403B	3493	950405	3503	950412	3505	950413	3509	950416
3512	950418	3514	950419	3515	950420	3516	950421	3523	950425
3527	950430	3552	950506	3567	950509	3593	950522	3608	950530
3618	950602	3634	950608	3637	950610	3648	950624	3649	950625
3654	950629	3655	950630	3658	950701B	3662	950706	3663	950711
3671	950718	3745	950808	3765	950818	3766	950819	3771	950830B
3773	950901	3776	950904	3779	950907	3788	950909	3801	950916
3805	950918	3811	950921	3815	950922	3843	951002	3853	951007
3860	951011	3864	951013	3869	951015	3871	951016B	3875	951019
3879	951020	3886	951030B	3890	951102C	3891	951102	3892	951102B
3893	951104	3899	951107C	3901	951107B	3903	951111	3905	951112

Continued on next page

Table A.2: GRBs corresponding to the cluster analysis class 2-II.

trigger	GRB								
3906	951113	3908	951116	3909	951117	3912	951119	3913	951119B
3914	951120B	3916	951121	3917	951123	3918	951124	3924	951127
3929	951202	3930	951203	3935	951207	3954	951213	4039	951219
4048	951220	4146	951227	4157	951228	4216	960102	4350	960113
4368	960114	4388	960115	4556	960124	4569	960124B	4701	960201
4710	960202	4745	960205	4939	960219	4959	960221	5080	960229
5304	960322	5305	960322B	5379	960330	5387	960331B	5389	960331
5407	960403B	5409	960403	5411	960405B	5412	960405	5415	960409C
5416	960409B	5417	960409	5419	960411	5420	960412	5421	960414
5423	960415C	5429	960417	5433	960418B	5434	960418C	5450	960428
5451	960430	5454	960508	5456	960508B	5463	960516B	5464	960516
5466	960521	5470	960523	5472	960524B	5473	960524	5474	960525
5475	960527	5476	960528	5477	960529	5478	960530	5479	960531
5482	960601B	5484	960602	5486	960605	5489	960607	5492	960610
5493	960612	5494	960613B	5495	960613	5497	960615	5504	960617B
5512	960623	5515	960623B	5516	960624B	5517	960624	5518	960625
5523	960628	5526	960703B	5531	960707C	5538	960713	5540	960715B
5541	960715C	5542	960716	5545	960720	5548	960722	5554	960730
5566	960806	5567	960807	5568	960808	5569	960810B	5572	960813
5574	960814	5575	960815	5585	960824	5591	960831B	5593	960906B
5597	960908	5601	960912	5603	960913	5604	960913B	5606	960917
5608	960921	5612	960923B	5614	960924	5617	960927	5618	960929
5621	961001B	5624	961006	5626	961008	5628	961009B	5632	961015
5635	961017C	5637	961019	5640	961022	5644	961026	5645	961026B
5646	961027	5654	961102	5667	961111B	5704	961202	5706	961206
5711	961212	5713	961214	5719	961220	5721	961223	5723	961224
5725	961225	5726	961226	5729	961228	5731	961228C	5736	970101
5773	970111	5983	970131	5989	970201	5995	970202	6004	970203
6082	970211	6083	970211B	6090	970214	6098	970221	6100	970223
6101	970224	6102	970226	6103	970226B	6104	970227	6111	970302B
6115	970306	6124	970315B	6127	970317	6139	970327	6141	970328
6147	970330	6151	970402	6152	970402B	6158	970404C	6159	970405
6165	970408	6167	970409	6168	970411	6186	970416	6189	970417B
6190	970417C	6194	970419	6198	970420	6216	970501	6222	970505
6225	970508	6226	970509	6228	970510B	6234	970517	6235	970517B
6241	970525	6242	970526	6243	970529	6244	970530	6249	970603
6266	970612B	6267	970612C	6271	970614	6272	970614B	6273	970616
6274	970616B	6279	970627	6280	970627B	6288	970629	6295	970707
6300	970709	6303	970713	6306	970714	6309	970716	6315	970723
6317	970725	6319	970725B	6320	970731	6321	970801	6322	970802
6323	970802B	6329	970807B	6334	970814	6335	970815	6336	970816
6337	970817	6339	970818	6344	970824B	6346	970825	6349	970827
6351	970829	6353	970831	6355	970902B	6369	970907B	6370	970907C
6375	970910	6380	970912B	6388	970919	6390	970919B	6396	970925
6397	970925B	6399	970926B	6400	970926C	6404	970930	6405	970930B
6413	971005	6414	971006	6435	971015	6440	971020	6446	971023B
6450	971024B	6453	971029	6454	971029B	6472	971110	6489	971121
6498	971125	6504	971127	6519	971204	6521	971206B	6522	971207
6525	971207B	6528	971210	6531	971212	6533	971214	6538	971219
6539	971220	6544	971223	6546	971227	6560	980105	6564	980109

Continued on next page

Table A.2: GRBs corresponding to the cluster analysis class 2-II.

trigger	GRB								
6566	980110	6576	980124	6577	980124B	6582	980126	6583	980129
6585	980202	6587	980203B	6590	980207	6592	980208	6593	980208B
6598	980213	6601	980214B	6602	980215	6605	980218	6611	980222B
6615	980225	6616	980226	6619	980301	6621	980301B	6622	980301C
6629	980306	6630	980306B	6642	980315B	6648	980319	6655	980322
6657	980325	6665	980329	6666	980329B	6670	980331	6672	980401
6674	980401B	6676	980402	6683	980409	6694	980420	6695	980421
6698	980421C	6702	980424	6707	980425	6708	980426	6762	980518
6763	980518B	6764	980519	6767	980520	6774	980523	6782	980525
6802	980601	6814	980609B	6816	980611	6831	980617C	6877	980626B
6880	980627	6882	980627B	6891	980703	6892	980703B	6903	980706
6904	980706B	6917	980712	6930	980718	6935	980720	6938	980722
6963	980803	6987	980813	7012	980821	7028	980828	7030	980829
7064	980904B	7087	980913	7108	980921	7110	980922	7113	980923
7116	980924	7147	981009	7170	981021B	7172	981022	7178	981027
7183	981030	7191	981105	7206	981110	7207	981111	7209	981111B
7213	981117	7219	981121	7228	981125	7230	981125B	7247	981203
7250	981205	7255	981211	7263	981215	7285	981228	7293	990102
7295	990102C	7298	990104	7301	990104B	7310	990108	7318	990111
7319	990111B	7322	990112	7323	990113	7328	990117	7335	990120
7343	990123	7357	990128	7358	990128B	7360	990129B	7369	990204
7371	990205	7374	990206	7377	990208	7379	990210	7386	990213
7387	990213B	7390	990216	7403	990220	7429	990226	7433	990228
7451	990306	7457	990308B	7460	990308C	7464	990311	7475	990316
7477	990316B	7485	990320	7486	990320B	7488	990322	7491	990323B
7493	990328	7494	990329	7497	990330B	7502	990403	7503	990403B
7504	990403C	7515	990411	7518	990413	7520	990415	7523	990420B
7527	990424	7528	990424B	7532	990425B	7548	990505	7549	990506
7550	990506B	7551	990507	7560	990510B	7566	990515	7568	990516B
7573	990518	7575	990518B	7576	990519	7579	990523	7580	990523B
7588	990528	7597	990604	7598	990604B	7605	990611C	7606	990614
7607	990615	7614	990620	7615	990620B	7617	990622B	7619	990625
7630	990703	7635	990706B	7638	990707B	7642	990709B	7648	990712B
7654	990715B	7656	990716	7657	990716B	7660	990718	7662	990719
7674	990725	7677	990726	7678	990728	7683	990730	7684	990730B
7688	990802	7695	990803	7701	990806	7703	990807	7705	990809
7707	990810B	7711	990816	7727	990822	7729	990822B	7744	990829
7752	990904B	7762	990912	7766	990915	7769	990917	7780	990930
7786	991004	7788	991004B	7794	991009	7802	991013	7803	991014
7810	991018	7818	991023	7822	991025	7831	991030	7838	991103
7840	991104	7841	991105	7843	991107	7845	991108	7858	991115
7862	991117	7868	991121	7872	991122	7884	991127	7885	991129
7886	991129B	7900	991210C	7902	991211B	7903	991213	7906	991216
7918	991226	7923	991228B	7924	991229	7929	000101	7932	000103
7936	000107	7938	000107B	7942	000110	7948	000113	7954	000115
7969	000126	7973	000130	7976	000201	7984	000205	7989	000217
7994	000221	7997	000225	8001	000227	8004	000229	8008	000302
8009	000302B	8012	000303	8019	000306B	8022	000307	8026	000310
8030	000312	8045	000320	8049	000323	8054	000326B	8059	000331
8061	000331B	8062	000401	8063	000402	8064	000403	8066	000407

Continued on next page

Table A.2: GRBs corresponding to the cluster analysis class 2-II.

trigger	GRB	trigger	GRB	trigger	GRB	trigger	GRB	trigger	GRB
8073	000412	8075	000415	8084	000421	8086	000424B	8087	000429
8098	000508B	8101	000511	8102	000511B	8105	000513B	8110	000518
8111	000519	8112	000520	8116	000524	8121	000526		

Table A.3: GRBs corresponding to the cluster analysis class 3-I.

trigger	GRB								
105	910421	108	910424	138	910502B	207	910518	218	910521
229	910526	254	910602C	289	910607	297	910608	298	910609
373	910616	401	910620B	432	910625	444	910626	474	910702
480	910703	491	910705	526	910713	537	910714	543	910717
547	910717B	549	910718C	551	910718	555	910719	568	910722
575	910725	603	910802	677	910814B	690	910817	729	910827
734	910828	741	910829	755	910904	788	910912	809	910919
829	910927	830	910928	836	910929	845	911001	856	911002
867	911004	878	911007	906	911016B	909	911019	936	911025
942	911027	974	911031B	999	911104	1025	911109	1051	911113
1073	911117B	1076	911117	1088	911119	1097	911120B	1102	911120
1112	911123B	1120	911125	1129	911129	1154	911209B	1159	911210
1204	911223	1211	911224	1223	911226	1289	920110C	1306	920120
1346	920203	1359	920205	1382	920209B	1404	920216B	1416	920218B
1439	920226B	1443	920227	1452	920229B	1453	920229	1461	920303B
1492	920318	1518	920325B	1553	920414	1566	920423	1588	920508
1634	920605	1635	920606	1636	920607	1637	920608	1657	920619B
1659	920620B	1662	920622D	1665	920622C	1679	920628	1683	920701
1694	920711B	1704	920717B	1709	920718	1719	920722	1741	920804
1747	920806	1760	920808	1851	920818	1953	920924	1968	921001B
1974	921003	2003	921023B	2035	921031	2041.	921102	2043	921108
2044	921109	2049	921111B	2053	921112	2056	921115	2068	921123B
2095	921214	2099	921216	2103	921219	2114	930102	2115	930103
2125	930110	2126	930110B	2145	930124	2146	930125	2155	930201B
2161	930203B	2163	930204	2167	930206	2187	930212	2201	930219
2205	930219E	2206	930220	2217	930304	2220	930305B	2265	930324
2273	930329	2288	930405C	2291	930406C	2312	930421	2317	930425
2320	930428	2321	930430	2326	930503D	2327	930503C	2330	930506B
2332	930510	2347	930519	2352	930524B	2353	930526	2357	930528
2360	930530B	2365	930601	2368	930602B	2377	930606	2382	930608
2384	930609B	2393	930614	2395	930614C	2401	930619	2424	930701B
2437	930709B	2448	930719	2449	930719B	2454	930721C	2463	930725
2487	930811	2502	930824	2512	930903	2513	930903C	2514	930905
2523	930911	2529	930913	2536	930922B	2564	931005	2583	931013
2597	931021B	2599	931022	2614	931101	2615	931101B	2628	931112
2632	931113	2641	931118	2649	931120	2677	931204B	2679	931205
2680	931206B	2690	931211	2693	931215B	2715	931229	2725	940101C
2728	940101	2736	940103	2757	940114	2760	940115	2788	940128B
2793	940129	2795	940201B	2799	940206B	2800	940207	2810	940209

Continued on next page

Table A.3: GRBs corresponding to the cluster analysis class 3-I.

trigger	GRB								
2814	940211B	2828	940216	2834	940219	2846	940224	2860	940305
2861	940305B	2873	940310	2894	940328	2896	940329	2910	940404
2918	940410B	2933	940415	2945	940424	2952	940428	2966	940507
2973	940512C	2975	940512B	2977	940515B	2978	940515	2986	940521C
2988	940524B	2995	940527B	3027	940613	3037	940621C	3038	940621B
3039	940622	3066	940708C	3073	940712	3078	940714C	3087	940717
3088	940717C	3094	940724	3113	940808	3118	940811	3121	940812C
3138	940826	3144	940830B	3146	940831	3152	940902	3164	940910B
3173	940918	3215	941003	3218	941005B	3266	941031B	3278	941110B
3280	941111	3282	941113	3284	941115	3294	941123	3297	941126C
3308	941203	3333	941229B	3335	941230B	3340	950102	3342	950103
3349	950108	3359	950115B	3374	950123	3378	950129	3379	950129B
3410	950210	3412	950211	3437	950221B	3441	950225B	3477	950321
3487	950328	3494	950405B	3502	950410	3510	950416B	3530	950502
3545	950505	3569	950510	3598	950524	3606	950529	3611	950531
3640	950611	3642	950612	3644	950620	3665	950714	3668	950716
3722	950801	3728	950802	3733	950803	3735	950804B	3736	950805
3737	950805B	3742	950806B	3751	950810	3770	950830	3782	950908B
3791	950911B	3807	950919B	3810	950920	3814	950922B	3840	951001
3866	951014B	3867	951014	3868	951015B	3870	951016	3888	951030C
3889	951101	3894	951104B	3895	951104C	3902	951110	3904	951112B
3910	951117B	3919	951124B	3921	951125	3926	951128	3936	951208B
3939	951209	3940	951211	4312	960111	4327	960112	4660	960130
4744	960205B	4776	960207	4807	960209	4814	960210	4871	960214
4955	960220	5079	960229B	5206	960311	5212	960312	5277	960319
5339	960325	5439	960420	5448	960426	5453	960507	5461	960515
5467	960521B	5469	960523B	5471	960524C	5483	960601	5485	960604
5488	960607B	5498	960615B	5499	960615C	5500	960616B	5502	960616
5513	960623D	5527	960703	5528	960704	5529	960705	5530	960707
5533	960708	5537	960713B	5546	960722B	5547	960722C	5559	960802
5561	960803	5562	960804B	5563	960804	5564	960805	5571	960812
5573	960813B	5576	960816	5594	960907	5599	960909	5605	960916
5607	960919	5619	960929B	5620	961001	5638	961020	5647	961027B
5650	961030	5664	961110	5697	961126	5718	961218B	5724	961224B
5730	961228B	5733	961230	5740	970103	5770	970110	5867	970119
6096	970219	6105	970227B	6113	970304	6117	970308	6119	970312
6120	970313	6123	970315	6131	970321	6135	970324	6136	970326
6137	970326B	6145	970329B	6153	970403	6178	970414	6180	970414B
6182	970415	6188	970417	6204	970423	6205	970424	6215	970430
6219	970503	6223	970507	6230	970514	6233	970516	6251	970603B
6265	970612	6269	970613B	6275	970617	6281	970627C	6292	970701
6293	970704	6298	970708	6299	970708B	6301	970709C	6307	970714B
6314	970720	6330	970809	6331	970809B	6341	970820	6342	970821
6343	970824	6347	970826	6361	970904	6368	970907	6372	970908B
6376	970910B	6385	970918	6386	970918B	6395	970924	6398	970926
6401	970928	6408	971002	6411	971004	6412	971004B	6422	971009B
6425	971011	6427	971012	6436	971015B	6439	971016	6443	971021
6445	971023	6451	971027	6452	971028	6462	971104	6486	971118
6488	971120	6497	971124	6527	971209	6534	971216	6535	971218
6536	971218B	6540	971220B	6542	971221	6547	971228	6573	980116

Continued on next page

Table A.3: GRBs corresponding to the cluster analysis class 3-I.

trigger	GRB								
6579	980124C	6580	980125	6591	980207B	6600	980214	6606	980218B
6631	980308	6635	980310B	6638	980312	6641	980315	6643	980315C
6645	980315D	6659	980326	6662	980327	6668	980330	6671	980331B
6679	980404B	6682	980407	6689	980416	6693	980419	6697	980421B
6700	980423	6710	980427	6715	980430	6753	980511	6757	980513
6787	980527	6788	980527B	6800	980530B	6824	980614	6853	980619
6870	980626	6916	980711	6931	980718B	7009	980820	7060	980903
7063	980904	7078	980910B	7102	980918	7106	980920	7133	980929
7142	981005	7148	981009B	7159	981016	7173	981022B	7187	981103
7227	981124	7240	981130	7281	981226	7283	981227	7287	981229
7290	981231	7292	981231B	7294	990102B	7297	990103	7305	990105
7329	990117B	7344	990123B	7353	990126B	7366	990202	7367	990202B
7375	990206B	7378	990208B	7381	990210B	7427	990225	7430	990226B
7440	990302	7446	990304	7447	990304B	7449	990305B	7453	990306B
7455	990307	7456	990308	7472	990315B	7495	990330	7508	990404
7526	990423	7529	990424C	7530	990425	7533	990426	7547	990504
7554	990508	7563	990513	7581	990523C	7584	990527	7587	990527B
7595	990603B	7599	990605	7601	990610	7602	990610B	7626	990701B
7663	990720	7706	990810	7710	990814B	7745	990829B	7749	990902
7753	990905	7754	990906	7770	990918	7775	990925B	7781	991001
7784	991002	7789	991005	7793	991007	7800	991012	7805	991015
7813	991020	7827	991028	7901	991211	7912	991219	7922	991228
7939	000108	7943	000111	7963	000122	7970	000126B	7979	000202
7980	000203	7987	000212	7988	000213	7995	000222	7999	000226B
8018	000306	8027	000310B	8035	000313B	8041	000319	8047	000321
8072	000410	8076	000415B	8079	000418	8082	000420B	8085	000424
8089	000502	8097	000508	8099	000508C	8104	000513	8120	000525

Table A.4: GRBs corresponding to the cluster analysis class 3-II.

trigger	GRB								
107	910423	110	910425B	121	910429	133	910501	148	910505
171	910509	179	910511	204	910517B	228	910526B	235	910528
237	910529	288	910607B	332	910612	404	910621B	408	910621
414	910622	473	910702B	503	910709	516	910712	559	910721B
577	910725B	591	910730B	594	910730	606	910802B	658	910809C
673	910813	680	910815	685	910816B	686	910816	704	910821
717	910823	752	910902	773	910908	795	910914	803	910918
815	910923	820	910926	825	910927B	840	910930B	914	911022
927	911024	946	911027B	1009	911106B	1046	911111B	1087	911119B
1114	911123	1123	911127C	1126	911128	1145	911204	1148	911205
1152	911208	1156	911209C	1190	911217	1192	911217B	1196	911219B
1197	911219	1200	911221	1213	911224C	1218	911225	1221	911225B
1244	911228	1279	920105	1291	920110B	1303	920116	1384	920210C
1390	920212	1396	920214	1446	920227C	1449	920228	1456	920301
1458	920302B	1472	920310	1515	920323	1546	920408	1551	920413

Continued on next page

Table A.4: GRBs corresponding to the cluster analysis class 3-II.

trigger	GRB								
1552	920414B	1558	920419B	1559	920419	1567	920423B	1574	920430
1580	920503	1586	920505	1604	920511B	1614	920520	1626	920525C
1642	920609	1651	920617B	1653	920617C	1655	920618	1661	920620C
1700	920714B	1714	920721D	1730	920730B	1740	920803	1742	920804C
1806	920812B	1819	920814B	1830	920816	1922	920912	1924	920913
1993	921021	2047	921110	2074	921203	2079	921206B	2081	921207B
2087	921208	2093	921211	2101	921217	2102	921218	2111	921230B
2112	921230C	2143	930123	2181	930210	2188	930213	2189	930213B
2190	930214	2191	930214C	2197	930217	2202	930219D	2203	930219B
2204	930219C	2211	930301	2233	930311	2254	930318B	2267	930326B
2276	930331	2277	930331B	2298	930410	2304	930415	2306	930416
2309	930418B	2310	930420B	2311	930420	2324	930503	2340	930514B
2344	930517B	2367	930602	2373	930605	2375	930606B	2380	930607
2391	930612D	2392	930613	2394	930614B	2405	930621B	2419	930627
2423	930701	2429	930705	2430	930705B	2432	930706B	2441	930711C
2447	930715	2452	930721B	2458	930724	2472	930730	2482	930805
2495	930819	2500	930822	2508	930901	2510	930902B	2519	930909
2541	930926	2560	931003	2569	931008C	2581	931013B	2589	931016B
2593	931019	2610	931030B	2619	931106	2623	931110	2634	931114
2640	931117	2662	931127	2664	931128C	2688	931209	2691	931212
2695	931217	2697	931219	2711	931226	2719	931230	2727	940101D
2749	940110	2751	940111	2753	940112B	2770	940119B	2774	940120
2775	940120B	2780	940126	2815	940211	2843	940222	2853	940228B
2862	940305C	2864	940307	2898	940330B	2900	940331B	2916	940407
2924	940413C	2925	940413	2931	940414B	2944	940423	2948	940425C
2961	940504	2992	940526C	2996	940527	2998	940529D	3005	940530
3011	940602B	3017	940606	3026	940611	3029	940616B	3032	940616
3040	940623B	3070	940710B	3072	940711	3076	940714B	3080	940715B
3084	940716	3085	940716B	3091	940720	3102	940730	3119	940812B
3120	940812	3127	940816	3134	940823B	3142	940829	3143	940830
3153	940902B	3155	940904	3156	940905	3168	940915	3171	940917
3174	940919	3177	940921B	3193	940925	3217	941005	3220	941006
3229	941009	3238	941012	3242	941014B	3246	941017B	3248	941018B
3267	941031C	3276	941109	3283	941114	3292	941122	3307	941202
3319	941214	3320	941215	3321	941215B	3322	941217	3339	950102B
3347	950105	3350	950110	3356	950114	3358	950115	3364	950118
3370	950120	3407	950207	3416	950211C	3465	950311	3471	950317C
3472	950317	3493	950405	3503	950412	3505	950413	3509	950416
3514	950419	3515	950420	3527	950430	3552	950506	3608	950530
3655	950630	3671	950718	3766	950819	3771	950830B	3773	950901
3779	950907	3801	950916	3805	950918	3811	950921	3815	950922
3864	951013	3869	951015	3871	951016B	3875	951019	3879	951020
3886	951030B	3890	951102C	3892	951102B	3899	951107C	3901	951107B
3903	951111	3908	951116	3909	951117	3913	951119B	3914	951120B
3916	951121	3917	951123	3924	951127	3935	951207	4146	951227
4216	960102	4388	960115	4569	960124B	4710	960202	4939	960219
4959	960221	5080	960229	5305	960322B	5379	960330	5387	960331B
5407	960403B	5409	960403	5411	960405B	5412	960405	5415	960409C
5416	960409B	5420	960412	5423	960415C	5434	960418C	5454	960508
5456	960508B	5463	960516B	5466	960521	5474	960525	5492	960610

Continued on next page

Table A.4: GRBs corresponding to the cluster analysis class 3-II.

trigger	GRB								
5493	960612	5494	960613B	5495	960613	5497	960615	5504	960617B
5515	960623B	5516	960624B	5517	960624	5538	960713	5540	960715B
5541	960715C	5542	960716	5545	960720	5554	960730	5566	960806
5569	960810B	5572	960813	5574	960814	5603	960913	5608	960921
5612	960923B	5618	960929	5626	961008	5632	961015	5635	961017C
5637	961019	5640	961022	5645	961026B	5646	961027	5667	961111B
5706	961206	5713	961214	5719	961220	5723	961224	5736	970101
5983	970131	6082	970211	6083	970211B	6098	970221	6101	970224
6102	970226	6104	970227	6111	970302B	6127	970317	6139	970327
6141	970328	6147	970330	6151	970402	6152	970402B	6158	970404C
6165	970408	6186	970416	6189	970417B	6190	970417C	6216	970501
6222	970505	6225	970508	6228	970510B	6234	970517	6241	970525
6243	970529	6244	970530	6249	970603	6267	970612C	6271	970614
6273	970616	6279	970627	6280	970627B	6288	970629	6300	970709
6306	970714	6309	970716	6317	970725	6319	970725B	6320	970731
6322	970802	6323	970802B	6334	970814	6337	970817	6339	970818
6344	970824B	6346	970825	6351	970829	6355	970902B	6369	970907B
6370	970907C	6375	970910	6388	970919	6396	970925	6399	970926B
6400	970926C	6405	970930B	6413	971005	6435	971015	6440	971020
6446	971023B	6450	971024B	6498	971125	6519	971204	6522	971207
6531	971212	6538	971219	6544	971223	6546	971227	6564	980109
6566	980110	6577	980124B	6582	980126	6583	980129	6585	980202
6590	980207	6592	980208	6598	980213	6602	980215	6611	980222B
6616	980226	6619	980301	6622	980301C	6648	980319	6655	980322
6657	980325	6666	980329B	6670	980331	6674	980401B	6676	980402
6695	980421	6698	980421C	6707	980425	6708	980426	6762	980518
6767	980520	6774	980523	6782	980525	6802	980601	6831	980617C
6880	980627	6882	980627B	6903	980706	6917	980712	6935	980720
6938	980722	6987	980813	7064	980904B	7087	980913	7108	980921
7110	980922	7116	980924	7147	981009	7178	981027	7183	981030
7191	981105	7206	981110	7209	981111B	7213	981117	7219	981121
7263	981215	7298	990104	7322	990112	7323	990113	7335	990120
7357	990128	7358	990128B	7369	990204	7371	990205	7377	990208
7379	990210	7386	990213	7387	990213B	7403	990220	7433	990228
7451	990306	7460	990308C	7485	990320	7486	990320B	7493	990328
7494	990329	7502	990403	7523	990420B	7528	990424B	7532	990425B
7550	990506B	7551	990507	7566	990515	7568	990516B	7573	990518
7576	990519	7579	990523	7580	990523B	7597	990604	7606	990614
7614	990620	7615	990620B	7617	990622B	7619	990625	7630	990703
7635	990706B	7642	990709B	7654	990715B	7656	990716	7662	990719
7674	990725	7677	990726	7683	990730	7684	990730B	7701	990806
7705	990809	7707	990810B	7729	990822B	7752	990904B	7762	990912
7780	990930	7802	991013	7803	991014	7831	991030	7838	991103
7862	991117	7872	991122	7885	991129	7886	991129B	7900	991210C
7902	991211B	7903	991213	7918	991226	7923	991228B	7924	991229
7936	000107	7942	000110	7948	000113	7973	000130	7997	000225
8001	000227	8009	000302B	8012	000303	8045	000320	8054	000326B
8059	000331	8061	000331B	8062	000401	8064	000403	8066	000407
8073	000412	8102	000511B	8105	000513B	8110	000518	8112	000520

Table A.5: GRBs corresponding to the cluster analysis class 3-III.

trigger	GRB								
109	910425	130	910430	143	910503	160	910507	219	910522
222	910523	226	910525	249	910601	257	910602	351	910614B
394	910619	398	910620	451	910627	467	910629	469	910630
548	910718B	563	910721	647	910807	659	910809B	660	910809
676	910814C	678	910814	692	910818	761	910905	841	910930
869	911005	907	911016	973	911031	1085	911118	1122	911127
1141	911202	1150	911207	1157	911209	1235	911227	1288	920110
1385	920210	1406	920216	1419	920218	1425	920221	1440	920226
1447	920227B	1467	920307	1468	920308	1533	920331	1541	920406
1578	920502	1579	920502C	1601	920511	1606	920513	1609	920517
1623	920524	1625	920525	1628	920526	1652	920617	1660	920620
1663	920622	1676	920627	1711	920720	1712	920720B	1717	920721
1731	920730	1733	920801	1815	920814	1883	920830	1886	920902
1956	920925	1982	921008	1989	921015	1997	921022	2019	921029
2037	921101	2061	921118	2067	921123	2080	921206	2083	921207
2090	921209	2106	921227	2110	921230	2122	930106B	2123	930108
2138	930120	2149	930127	2151	930131	2156	930201	2193	930214B
2213	930302	2228	930309	2232	930310	2253	930317	2287	930405
2315	930424	2316	930425B	2328	930506C	2329	930506	2345	930517
2346	930518	2371	930603	2383	930609	2387	930612	2428	930704
2431	930706	2435	930708	2436	930709	2443	930711	2446	930714
2450	930720	2476	930731	2522	930910	2530	930914	2533	930916
2537	930922	2570	931008B	2586	931014	2603	931024	2606	931026
2611	931031	2665	931128	2696	931218	2700	931221	2703	931222
2706	931223	2709	931225	2790	940128	2797	940203	2798	940206
2812	940210	2831	940217	2852	940228	2855	940301	2863	940306
2889	940319	2890	940321	2891	940323	2913	940406	2919	940410
2922	940412	2929	940414	2953	940429	2958	940503	2984	940520
2993	940526B	2994	940526	3001	940529B	3003	940529C	3015	940604
3035	940619	3042	940623	3056	940702	3057	940703	3067	940708
3071	940710	3075	940714	3101	940728B	3105	940803B	3110	940806
3115	940810	3128	940817	3131	940821	3178	940921	3212	941003B
3227	941008	3237	941011	3241	941014	3245	941017	3247	941018
3255	941023	3257	941026	3259	941026B	3269	941031	3287	941119
3290	941121	3301	941126B	3306	941128	3330	941228	3336	941230
3345	950104	3351	950111	3352	950111B	3405	950206	3408	950208
3415	950211B	3436	950221	3439	950223	3448	950301	3458	950305
3480	950325B	3481	950325	3488	950401	3489	950401B	3491	950403B
3512	950418	3516	950421	3523	950425	3567	950509	3593	950522
3618	950602	3634	950608	3637	950610	3648	950624	3649	950625
3654	950629	3658	950701B	3662	950706	3663	950711	3745	950808
3765	950818	3776	950904	3788	950909	3843	951002	3853	951007
3860	951011	3891	951102	3893	951104	3905	951112	3906	951113
3912	951119	3918	951124	3929	951202	3930	951203	3954	951213
4039	951219	4048	951220	4157	951228	4350	960113	4368	960114
4556	960124	4701	960201	4745	960205	5304	960322	5389	960331
5417	960409	5419	960411	5421	960414	5429	960417	5433	960418B

Continued on next page

Table A.5: GRBs corresponding to the cluster analysis class 3-III.

trigger	GRB								
5450	960428	5451	960430	5464	960516	5470	960523	5472	960524B
5473	960524	5475	960527	5476	960528	5477	960529	5478	960530
5479	960531	5482	960601B	5484	960602	5486	960605	5489	960607
5512	960623	5518	960625	5523	960628	5526	960703B	5531	960707C
5548	960722	5567	960807	5568	960808	5575	960815	5585	960824
5591	960831B	5593	960906B	5597	960908	5601	960912	5604	960913B
5606	960917	5614	960924	5617	960927	5621	961001B	5624	961006
5628	961009B	5644	961026	5654	961102	5704	961202	5711	961212
5721	961223	5725	961225	5726	961226	5729	961228	5731	961228C
5773	970111	5989	970201	5995	970202	6004	970203	6090	970214
6100	970223	6103	970226B	6115	970306	6124	970315B	6159	970405
6167	970409	6168	970411	6194	970419	6198	970420	6226	970509
6235	970517B	6242	970526	6266	970612B	6272	970614B	6274	970616B
6295	970707	6303	970713	6315	970723	6321	970801	6329	970807B
6335	970815	6336	970816	6349	970827	6353	970831	6380	970912B
6390	970919B	6397	970925B	6404	970930	6414	971006	6453	971029
6454	971029B	6472	971110	6489	971121	6504	971127	6521	971206B
6525	971207B	6528	971210	6533	971214	6539	971220	6560	980105
6576	980124	6587	980203B	6593	980208B	6601	980214B	6605	980218
6615	980225	6621	980301B	6629	980306	6630	980306B	6642	980315B
6665	980329	6672	980401	6683	980409	6694	980420	6702	980424
6763	980518B	6764	980519	6814	980609B	6816	980611	6877	980626B
6891	980703	6892	980703B	6904	980706B	6930	980718	6963	980803
7012	980821	7028	980828	7030	980829	7113	980923	7170	981021B
7172	981022	7207	981111	7228	981125	7230	981125B	7247	981203
7250	981205	7255	981211	7285	981228	7293	990102	7295	990102C
7301	990104B	7310	990108	7318	990111	7319	990111B	7328	990117
7343	990123	7360	990129B	7374	990206	7390	990216	7429	990226
7457	990308B	7464	990311	7475	990316	7477	990316B	7488	990322
7491	990323B	7497	990330B	7503	990403B	7504	990403C	7515	990411
7518	990413	7520	990415	7527	990424	7548	990505	7549	990506
7560	990510B	7575	990518B	7588	990528	7598	990604B	7605	990611C
7607	990615	7638	990707B	7648	990712B	7657	990716B	7660	990718
7678	990728	7688	990802	7695	990803	7703	990807	7711	990816
7727	990822	7744	990829	7766	990915	7769	990917	7786	991004
7788	991004B	7794	991009	7810	991018	7818	991023	7822	991025
7840	991104	7841	991105	7843	991107	7845	991108	7858	991115
7868	991121	7884	991127	7906	991216	7929	000101	7932	000103
7938	000107B	7954	000115	7969	000126	7976	000201	7984	000205
7989	000217	7994	000221	8004	000229	8008	000302	8019	000306B
8022	000307	8026	000310	8030	000312	8049	000323	8063	000402
8075	000415	8084	000421	8086	000424B	8087	000429	8098	000508B
8101	000511	8111	000519	8116	000524	8121	000526		

Appendix B

Neural network classification

This appendix contains tables with the BATSE trigger numbers and GRB names for each GRB class derived with the neural network.

Table B.1: GRBs corresponding to the neural network class 2-I.

trigger	GRB								
107	910423	108	910424	138	910502B	179	910511	204	910517B
207	910518	218	910521	228	910526B	229	910526	237	910529
254	910602C	289	910607	297	910608	298	910609	373	910616
401	910620B	414	910622	432	910625	444	910626	473	910702B
474	910702	480	910703	491	910705	516	910712	526	910713
537	910714	547	910717B	549	910718C	551	910718	555	910719
568	910722	575	910725	603	910802	673	910813	677	910814B
680	910815	686	910816	690	910817	717	910823	729	910827
734	910828	741	910829	752	910902	755	910904	788	910912
803	910918	809	910919	830	910928	836	910929	845	911001
856	911002	867	911004	878	911007	906	911016B	909	911019
914	911022	927	911024	936	911025	942	911027	974	911031B
1051	911113	1073	911117B	1076	911117	1088	911119	1097	911120B
1102	911120	1112	911123B	1114	911123	1120	911125	1123	911127C
1129	911129	1145	911204	1154	911209B	1159	911210	1190	911217
1204	911223	1211	911224	1213	911224C	1218	911225	1221	911225B
1223	911226	1289	920110C	1306	920120	1346	920203	1359	920205
1382	920209B	1384	920210C	1390	920212	1404	920216B	1416	920218B
1439	920226B	1443	920227	1452	920229B	1453	920229	1461	920303B
1492	920318	1518	920325B	1546	920408	1553	920414	1558	920419B
1566	920423	1588	920508	1634	920605	1635	920606	1636	920607
1637	920608	1657	920619B	1659	920620B	1662	920622D	1665	920622C
1679	920628	1694	920711B	1704	920717B	1719	920722	1741	920804
1747	920806	1760	920808	1851	920818	1953	920924	1968	921001B
2003	921023B	2035	921031	2041	921102	2043	921108	2044	921109
2049	921111B	2053	921112	2056	921115	2068	921123B	2095	921214

Continued on next page

Table B.1: GRBs corresponding to the neural network class 2-I.

trigger	GRB								
2099	921216	2103	921219	2114	930102	2115	930103	2125	930110
2126	930110B	2145	930124	2146	930125	2155	930201B	2161	930203B
2163	930204	2167	930206	2187	930212	2201	930219	2202	930219D
2204	930219C	2205	930219E	2206	930220	2217	930304	2220	930305B
2233	930311	2254	930318B	2265	930324	2273	930329	2288	930405C
2291	930406C	2306	930416	2312	930421	2317	930425	2320	930428
2326	930503D	2327	930503C	2330	930506B	2332	930510	2347	930519
2352	930524B	2353	930526	2357	930528	2360	930530B	2365	930601
2367	930602	2368	930602B	2377	930606	2382	930608	2384	930609B
2391	930612D	2392	930613	2395	930614C	2401	930619	2423	930701
2424	930701B	2437	930709B	2448	930719	2449	930719B	2454	930721C
2458	930724	2463	930725	2487	930811	2502	930824	2512	930903
2513	930903C	2514	930905	2523	930911	2529	930913	2536	930922B
2564	931005	2583	931013	2597	931021B	2599	931022	2614	931101
2615	931101B	2623	931110	2632	931113	2641	931118	2649	931120
2677	931204B	2679	931205	2680	931206B	2690	931211	2693	931215B
2715	931229	2719	931230	2725	940101C	2728	940101	2749	940110
2751	940111	2757	940114	2760	940115	2788	940128B	2795	940201B
2800	940207	2810	940209	2814	940211B	2828	940216	2834	940219
2846	940224	2860	940305	2861	940305B	2862	940305C	2873	940310
2896	940329	2900	940331B	2910	940404	2918	940410B	2933	940415
2944	940423	2945	940424	2952	940428	2966	940507	2973	940512C
2975	940512B	2977	940515B	2978	940515	2986	940521C	2988	940524B
2992	940526C	2995	940527B	3027	940613	3037	940621C	3038	940621B
3066	940708C	3072	940711	3073	940712	3078	940714C	3087	940717
3088	940717C	3094	940724	3113	940808	3118	940811	3121	940812C
3144	940830B	3146	940831	3152	940902	3155	940904	3164	940910B
3173	940918	3215	941003	3218	941005B	3229	941009	3248	941018B
3266	941031B	3278	941110B	3280	941111	3282	941113	3284	941115
3294	941123	3297	941126C	3308	941203	3321	941215B	3322	941217
3333	941229B	3335	941230B	3340	950102	3342	950103	3349	950108
3356	950114	3359	950115B	3370	950120	3374	950123	3378	950129
3379	950129B	3410	950210	3412	950211	3437	950221B	3441	950225B
3465	950311	3471	950317C	3477	950321	3487	950328	3494	950405B
3502	950410	3503	950412	3510	950416B	3515	950420	3530	950502
3545	950505	3598	950524	3606	950529	3611	950531	3640	950611
3642	950612	3644	950620	3665	950714	3668	950716	3722	950801
3728	950802	3733	950803	3735	950804B	3736	950805	3737	950805B
3742	950806B	3751	950810	3770	950830	3779	950907	3782	950908B
3791	950911B	3807	950919B	3810	950920	3814	950922B	3815	950922
3840	951001	3864	951013	3866	951014B	3867	951014	3868	951015B
3869	951015	3875	951019	3888	951030C	3889	951101	3890	951102C
3892	951102B	3894	951104B	3895	951104C	3902	951110	3904	951112B
3908	951116	3910	951117B	3914	951120B	3919	951124B	3921	951125
3924	951127	3926	951128	3936	951208B	3939	951209	3940	951211
4327	960112	4569	960124B	4660	960130	4744	960205B	4776	960207
4807	960209	4814	960210	4871	960214	4955	960220	5079	960229b
5206	960311	5212	960312	5277	960319	5339	960325	5423	960415C
5439	960420	5448	960426	5453	960507	5456	960508B	5461	960515
5467	960521B	5469	960523B	5471	960524C	5483	960601	5485	960604

Continued on next page

Table B.1: GRBs corresponding to the neural network class 2-I.

trigger	GRB								
5488	960607B	5494	960613B	5498	960615B	5499	960615C	5500	960616B
5502	960616	5504	960617B	5513	960623D	5516	960624B	5517	960624
5527	960703	5528	960704	5529	960705	5533	960708	5537	960713B
5545	960720	5546	960722B	5547	960722C	5559	960802	5561	960803
5562	960804B	5564	960805	5571	960812	5572	960813	5573	960813B
5576	960816	5594	960907	5599	960909	5605	960916	5607	960919
5608	960921	5618	960929	5619	960929B	5620	961001	5626	961008
5638	961020	5640	961022	5647	961027B	5650	961030	5664	961110
5718	961218B	5719	961220	5724	961224B	5730	961228B	5733	961230
5740	970103	5770	970110	5983	970131	6082	970211	6096	970219
6098	970221	6104	970227	6105	970227B	6117	970308	6119	970312
6120	970313	6123	970315	6131	970321	6135	970324	6136	970326
6137	970326B	6145	970329B	6151	970402	6153	970403	6158	970404C
6178	970414	6180	970414B	6182	970415	6186	970416	6188	970417
6189	970417B	6204	970423	6205	970424	6215	970430	6216	970501
6219	970503	6223	970507	6228	970510B	6230	970514	6233	970516
6241	970525	6251	970603B	6265	970612	6267	970612C	6269	970613B
6275	970617	6281	970627C	6292	970701	6293	970704	6298	970708
6299	970708B	6300	970709	6301	970709C	6307	970714B	6314	970720
6317	970725	6322	970802	6323	970802B	6330	970809	6331	970809B
6334	970814	6341	970820	6342	970821	6343	970824	6347	970826
6361	970904	6368	970907	6370	970907C	6372	970908B	6376	970910B
6385	970918	6386	970918B	6395	970924	6398	970926	6401	970928
6408	971002	6411	971004	6412	971004B	6425	971011	6427	971012
6435	971015	6436	971015B	6439	971016	6443	971021	6445	971023
6452	971028	6462	971104	6486	971118	6488	971120	6497	971124
6527	971209	6534	971216	6535	971218	6536	971218B	6540	971220B
6542	971221	6546	971227	6547	971228	6573	980116	6579	980124C
6580	980125	6582	980126	6591	980207B	6600	980214	6606	980218B
6611	980222B	6616	980226	6631	980308	6635	980310B	6638	980312
6641	980315	6643	980315C	6645	980315D	6659	980326	6662	980327
6666	980329B	6668	980330	6671	980331B	6676	980402	6679	980404B
6682	980407	6689	980416	6693	980419	6695	980421	6697	980421B
6700	980423	6708	980426	6710	980427	6715	980430	6753	980511
6757	980513	6762	980518	6774	980523	6782	980525	6787	980527
6788	980527B	6800	980530B	6824	980614	6831	980617C	6853	980619
6870	980626	6880	980627	6916	980711	6917	980712	6931	980718B
6987	980813	7009	980820	7060	980903	7063	980904	7078	980910B
7102	980918	7106	980920	7116	980924	7133	980929	7142	981005
7148	981009B	7159	981016	7173	981022B	7183	981030	7187	981103
7191	981105	7227	981124	7281	981226	7283	981227	7287	981229
7290	981231	7292	981231B	7294	990102B	7297	990103	7305	990105
7329	990117B	7344	990123B	7353	990126B	7366	990202	7367	990202B
7375	990206B	7378	990208B	7381	990210B	7386	990213	7427	990225
7430	990226B	7440	990302	7447	990304B	7449	990305B	7453	990306B
7455	990307	7456	990308	7472	990315B	7485	990320	7486	990320B
7494	990329	7495	990330	7508	990404	7526	990423	7530	990425
7533	990426	7547	990504	7554	990508	7563	990513	7568	990516B
7579	990523	7581	990523C	7584	990527	7587	990527B	7595	990603B
7599	990605	7601	990610	7602	990610B	7615	990620B	7619	990625

Continued on next page

Table B.1: GRBs corresponding to the neural network class 2-I.

trigger	GRB								
7626	990701B	7662	990719	7663	990720	7674	990725	7705	990809
7706	990810	7710	990814B	7745	990829B	7749	990902	7753	990905
7754	990906	7775	990925B	7784	991002	7789	991005	7793	991007
7800	991012	7803	991014	7805	991015	7813	991020	7827	991028
7862	991117	7901	991211	7912	991219	7922	991228	7924	991229
7936	000107	7939	000108	7943	000111	7963	000122	7970	000126B
7979	000202	7980	000203	7988	000213	7995	000222	7999	000226B
8009	000302B	8018	000306	8027	000310B	8035	000313B	8041	000319
8047	000321	8054	000326B	8072	000410	8073	000412	8076	000415B
8079	000418	8082	000420B	8085	000424	8089	000502	8097	000508
8102	000511B	8104	000513	8105	000513B	8112	000520	8120	000525

Table B.2: GRBs corresponding to the neural network class 2-II.

trigger	GRB								
105	910421	109	910425	110	910425B	121	910429	130	910430
133	910501	143	910503	148	910505	160	910507	171	910509
219	910522	222	910523	226	910525	235	910528	249	910601
257	910602	288	910607B	332	910612	351	910614B	394	910619
398	910620	404	910621B	408	910621	451	910627	467	910629
469	910630	503	910709	543	910717	548	910718B	559	910721B
563	910721	577	910725B	591	910730B	594	910730	606	910802B
647	910807	658	910809C	659	910809B	660	910809	676	910814C
678	910814	685	910816B	692	910818	704	910821	761	910905
773	910908	795	910914	815	910923	820	910926	825	910927B
829	910927	840	910930B	841	910930	869	911005	907	911016
946	911027B	973	911031	999	911104	1009	911106B	1025	911109
1046	911111B	1085	911118	1087	911119B	1122	911127	1126	911128
1141	911202	1148	911205	1150	911207	1152	911208	1156	911209C
1157	911209	1192	911217B	1196	911219B	1197	911219	1200	911221
1235	911227	1244	911228	1279	920105	1288	920110	1291	920110B
1303	920116	1385	920210	1396	920214	1406	920216	1419	920218
1425	920221	1440	920226	1446	920227C	1447	920227B	1449	920228
1456	920301	1458	920302B	1467	920307	1468	920308	1472	920310
1515	920323	1533	920331	1541	920406	1551	920413	1552	920414B
1559	920419	1567	920423B	1574	920430	1578	920502	1579	920502C
1580	920503	1586	920505	1601	920511	1604	920511B	1606	920513
1609	920517	1614	920520	1623	920524	1625	920525	1626	920525C
1628	920526	1642	920609	1651	920617B	1652	920617	1653	920617C
1655	920618	1660	920620	1661	920620C	1663	920622	1676	920627
1683	920701	1700	920714B	1709	920718	1711	920720	1712	920720B
1714	920721D	1717	920721	1730	920730B	1731	920730	1733	920801
1740	920803	1742	920804C	1806	920812B	1815	920814	1819	920814B
1830	920816	1883	920830	1886	920902	1922	920912	1924	920913
1956	920925	1974	921003	1982	921008	1989	921015	1993	921021
1997	921022	2019	921029	2037	921101	2047	921110	2061	921118

Continued on next page

Table B.2: GRBs corresponding to the neural network class 2-II.

trigger	GRB								
2067	921123	2074	921203	2079	921206B	2080	921206	2081	921207B
2083	921207	2087	921208	2090	921209	2093	921211	2101	921217
2102	921218	2106	921227	2110	921230	2111	921230B	2112	921230C
2122	930106B	2123	930108	2138	930120	2143	930123	2149	930127
2151	930131	2156	930201	2181	930210	2188	930213	2189	930213B
2190	930214	2191	930214C	2193	930214B	2197	930217	2203	930219B
2211	930301	2213	930302	2228	930309	2232	930310	2253	930317
2267	930326B	2276	930331	2277	930331B	2287	930405	2298	930410
2304	930415	2309	930418B	2310	930420B	2311	930420	2315	930424
2316	930425B	2321	930430	2324	930503	2328	930506C	2329	930506
2340	930514B	2344	930517B	2345	930517	2346	930518	2371	930603
2373	930605	2375	930606B	2380	930607	2383	930609	2387	930612
2393	930614	2394	930614B	2405	930621B	2419	930627	2428	930704
2429	930705	2430	930705B	2431	930706	2432	930706B	2435	930708
2436	930709	2441	930711C	2443	930711	2446	930714	2447	930715
2450	930720	2452	930721B	2472	930730	2476	930731	2482	930805
2495	930819	2500	930822	2508	930901	2510	930902B	2519	930909
2522	930910	2530	930914	2533	930916	2537	930922	2541	930926
2560	931003	2569	931008C	2570	931008B	2581	931013B	2586	931014
2589	931016B	2593	931019	2603	931024	2606	931026	2610	931030B
2611	931031	2619	931106	2628	931112	2634	931114	2640	931117
2662	931127	2664	931128C	2665	931128	2688	931209	2691	931212
2695	931217	2696	931218	2697	931219	2700	931221	2703	931222
2706	931223	2709	931225	2711	931226	2727	940101D	2736	940103
2753	940112B	2770	940119B	2774	940120	2775	940120B	2780	940126
2790	940128	2793	940129	2797	940203	2798	940206	2799	940206B
2812	940210	2815	940211	2831	940217	2843	940222	2852	940228
2853	940228B	2855	940301	2863	940306	2864	940307	2889	940319
2890	940321	2891	940323	2894	940328	2898	940330B	2913	940406
2916	940407	2919	940410	2922	940412	2924	940413C	2925	940413
2929	940414	2931	940414B	2948	940425C	2953	940429	2958	940503
2961	940504	2984	940520	2993	940526B	2994	940526	2996	940527
2998	940529D	3001	940529B	3003	940529C	3005	940530	3011	940602B
3015	940604	3017	940606	3026	940611	3029	940616B	3032	940616
3035	940619	3039	940622	3040	940623B	3042	940623	3056	940702
3057	940703	3067	940708	3070	940710B	3071	940710	3075	940714
3076	940714B	3080	940715B	3084	940716	3085	940716B	3091	940720
3101	940728B	3102	940730	3105	940803B	3110	940806	3115	940810
3119	940812B	3120	940812	3127	940816	3128	940817	3131	940821
3134	940823B	3138	940826	3142	940829	3143	940830	3153	940902B
3156	940905	3168	940915	3171	940917	3174	940919	3177	940921B
3178	940921	3193	940925	3212	941003B	3217	941005	3220	941006
3227	941008	3237	941011	3238	941012	3241	941014	3242	941014B
3245	941017	3246	941017B	3247	941018	3255	941023	3257	941026
3259	941026B	3267	941031C	3269	941031	3276	941109	3283	941114
3287	941119	3290	941121	3292	941122	3301	941126B	3306	941128
3307	941202	3319	941214	3320	941215	3330	941228	3336	941230
3339	950102B	3345	950104	3347	950105	3350	950110	3351	950111
3352	950111B	3358	950115	3364	950118	3405	950206	3407	950207
3408	950208	3415	950211B	3416	950211C	3436	950221	3439	950223

Continued on next page

Table B.2: GRBs corresponding to the neural network class 2-II.

trigger	GRB								
3448	950301	3458	950305	3472	950317	3480	950325B	3481	950325
3488	950401	3489	950401B	3491	950403B	3493	950405	3505	950413
3509	950416	3512	950418	3514	950419	3516	950421	3523	950425
3527	950430	3552	950506	3567	950509	3569	950510	3593	950522
3608	950530	3618	950602	3634	950608	3637	950610	3648	950624
3649	950625	3654	950629	3655	950630	3658	950701B	3662	950706
3663	950711	3671	950718	3745	950808	3765	950818	3766	950819
3771	950830B	3773	950901	3776	950904	3788	950909	3801	950916
3805	950918	3811	950921	3843	951002	3853	951007	3860	951011
3870	951016	3871	951016B	3879	951020	3886	951030B	3891	951102
3893	951104	3899	951107C	3901	951107B	3903	951111	3905	951112
3906	951113	3909	951117	3912	951119	3913	951119B	3916	951121
3917	951123	3918	951124	3929	951202	3930	951203	3935	951207
3954	951213	4039	951219	4048	951220	4146	951227	4157	951228
4216	960102	4312	960111	4350	960113	4368	960114	4388	960115
4556	960124	4701	960201	4710	960202	4745	960205	4939	960219
4959	960221	5080	960229	5304	960322	5305	960322B	5379	960330
5387	960331B	5389	960331	5407	960403B	5409	960403	5411	960405B
5412	960405	5415	960409C	5416	960409B	5417	960409	5419	960411
5420	960412	5421	960414	5429	960417	5433	960418B	5434	960418C
5450	960428	5451	960430	5454	960508	5463	960516B	5464	960516
5466	960521	5470	960523	5472	960524B	5473	960524	5474	960525
5475	960527	5476	960528	5477	960529	5478	960530	5479	960531
5482	960601B	5484	960602	5486	960605	5489	960607	5492	960610
5493	960612	5495	960613	5497	960615	5512	960623	5515	960623B
5518	960625	5523	960628	5526	960703B	5530	960707	5531	960707C
5538	960713	5540	960715B	5541	960715C	5542	960716	5548	960722
5554	960730	5563	960804	5566	960806	5567	960807	5568	960808
5569	960810B	5574	960814	5575	960815	5585	960824	5591	960831B
5593	960906B	5597	960908	5601	960912	5603	960913	5604	960913B
5606	960917	5612	960923B	5614	960924	5617	960927	5621	961001B
5624	961006	5628	961009B	5632	961015	5635	961017C	5637	961019
5644	961026	5645	961026B	5646	961027	5654	961102	5667	961111B
5697	961126	5704	961202	5706	961206	5711	961212	5713	961214
5721	961223	5723	961224	5725	961225	5726	961226	5729	961228
5731	961228C	5736	970101	5773	970111	5867	970119	5989	970201
5995	970202	6004	970203	6083	970211B	6090	970214	6100	970223
6101	970224	6102	970226	6103	970226B	6111	970302B	6113	970304
6115	970306	6124	970315B	6127	970317	6139	970327	6141	970328
6147	970330	6152	970402B	6159	970405	6165	970408	6167	970409
6168	970411	6190	970417C	6194	970419	6198	970420	6222	970505
6225	970508	6226	970509	6234	970517	6235	970517B	6242	970526
6243	970529	6244	970530	6249	970603	6266	970612B	6271	970614
6272	970614B	6273	970616	6274	970616B	6279	970627	6280	970627B
6288	970629	6295	970707	6303	970713	6306	970714	6309	970716
6315	970723	6319	970725B	6320	970731	6321	970801	6329	970807B
6335	970815	6336	970816	6337	970817	6339	970818	6344	970824B
6346	970825	6349	970827	6351	970829	6353	970831	6355	970902B
6369	970907B	6375	970910	6380	970912B	6388	970919	6390	970919B
6396	970925	6397	970925B	6399	970926B	6400	970926C	6404	970930

Continued on next page

Table B.2: GRBs corresponding to the neural network class 2-II.

trigger	GRB								
6405	970930B	6413	971005	6414	971006	6422	971009B	6440	971020
6446	971023B	6450	971024B	6451	971027	6453	971029	6454	971029B
6472	971110	6489	971121	6498	971125	6504	971127	6519	971204
6521	971206B	6522	971207	6525	971207B	6528	971210	6531	971212
6533	971214	6538	971219	6539	971220	6544	971223	6560	980105
6564	980109	6566	980110	6576	980124	6577	980124B	6583	980129
6585	980202	6587	980203B	6590	980207	6592	980208	6593	980208B
6598	980213	6601	980214B	6602	980215	6605	980218	6615	980225
6619	980301	6621	980301B	6622	980301C	6629	980306	6630	980306B
6642	980315B	6648	980319	6655	980322	6657	980325	6665	980329
6670	980331	6672	980401	6674	980401B	6683	980409	6694	980420
6698	980421C	6702	980424	6707	980425	6763	980518B	6764	980519
6767	980520	6802	980601	6814	980609B	6816	980611	6877	980626B
6882	980627B	6891	980703	6892	980703B	6903	980706	6904	980706B
6930	980718	6935	980720	6938	980722	6963	980803	7012	980821
7028	980828	7030	980829	7064	980904B	7087	980913	7108	980921
7110	980922	7113	980923	7147	981009	7170	981021B	7172	981022
7178	981027	7206	981110	7207	981111	7209	981111B	7213	981117
7219	981121	7228	981125	7230	981125B	7240	981130	7247	981203
7250	981205	7255	981211	7263	981215	7285	981228	7293	990102
7295	990102C	7298	990104	7301	990104B	7310	990108	7318	990111
7319	990111B	7322	990112	7323	990113	7328	990117	7335	990120
7343	990123	7357	990128	7358	990128B	7360	990129B	7369	990204
7371	990205	7374	990206	7377	990208	7379	990210	7387	990213B
7390	990216	7403	990220	7429	990226	7433	990228	7446	990304
7451	990306	7457	990308B	7460	990308C	7464	990311	7475	990316
7477	990316B	7488	990322	7491	990323B	7493	990328	7497	990330B
7502	990403	7503	990403B	7504	990403C	7515	990411	7518	990413
7520	990415	7523	990420B	7527	990424	7528	990424B	7529	990424C
7532	990425B	7548	990505	7549	990506	7550	990506B	7551	990507
7560	990510B	7566	990515	7573	990518	7575	990518B	7576	990519
7580	990523B	7588	990528	7597	990604	7598	990604B	7605	990611C
7606	990614	7607	990615	7614	990620	7617	990622B	7630	990703
7635	990706B	7638	990707B	7642	990709B	7648	990712B	7654	990715B
7656	990716	7657	990716B	7660	990718	7677	990726	7678	990728
7683	990730	7684	990730B	7688	990802	7695	990803	7701	990806
7703	990807	7707	990810B	7711	990816	7727	990822	7729	990822B
7744	990829	7752	990904B	7762	990912	7766	990915	7769	990917
7770	990918	7780	990930	7781	991001	7786	991004	7788	991004B
7794	991009	7802	991013	7810	991018	7818	991023	7822	991025
7831	991030	7838	991103	7840	991104	7841	991105	7843	991107
7845	991108	7858	991115	7868	991121	7872	991122	7884	991127
7885	991129	7886	991129B	7900	991210C	7902	991211B	7903	991213
7906	991216	7918	991226	7923	991228B	7929	000101	7932	000103
7938	000107B	7942	000110	7948	000113	7954	000115	7969	000126
7973	000130	7976	000201	7984	000205	7987	000212	7989	000217
7994	000221	7997	000225	8001	000227	8004	000229	8008	000302
8012	000303	8019	000306B	8022	000307	8026	000310	8030	000312
8045	000320	8049	000323	8059	000331	8061	000331B	8062	000401
8063	000402	8064	000403	8066	000407	8075	000415	8084	000421

Continued on next page

Table B.2: GRBs corresponding to the neural network class 2-II.

trigger	GRB	trigger	GRB	trigger	GRB	trigger	GRB	trigger	GRB
8086	000424B	8087	000429	8098	000508B	8099	000508C	8101	000511
8110	000518	8111	000519	8116	000524	8121	000526		

Table B.3: GRBs corresponding to the neural network class 3-I.

trigger	GRB								
108	910424	138	910502B	207	910518	218	910521	228	910526B
229	910526	254	910602C	289	910607	297	910608	298	910609
373	910616	401	910620B	432	910625	444	910626	474	910702
480	910703	491	910705	526	910713	537	910714	547	910717B
551	910718	555	910719	568	910722	575	910725	603	910802
677	910814B	680	910815	690	910817	717	910823	729	910827
734	910828	752	910902	755	910904	788	910912	809	910919
830	910928	836	910929	845	911001	856	911002	878	911007
906	911016B	909	911019	936	911025	942	911027	974	911031B
1051	911113	1073	911117B	1076	911117	1088	911119	1097	911120B
1102	911120	1112	911123B	1120	911125	1129	911129	1145	911204
1154	911209B	1204	911223	1211	911224	1221	911225B	1223	911226
1289	920110C	1306	920120	1346	920203	1359	920205	1382	920209B
1384	920210C	1404	920216B	1416	920218B	1439	920226B	1453	920229
1461	920303B	1492	920318	1518	920325B	1546	920408	1566	920423
1588	920508	1634	920605	1635	920606	1636	920607	1637	920608
1659	920620B	1662	920622D	1665	920622C	1679	920628	1694	920711B
1719	920722	1741	920804	1747	920806	1760	920808	1851	920818
1953	920924	1968	921001B	2003	921023B	2035	921031	2043	921108
2044	921109	2049	921111B	2056	921115	2068	921123B	2095	921214
2099	921216	2103	921219	2114	930102	2115	930103	2125	930110
2126	930110B	2145	930124	2146	930125	2155	930201B	2161	930203B
2163	930204	2167	930206	2201	930219	2205	930219E	2206	930220
2217	930304	2220	930305B	2265	930324	2273	930329	2288	930405C
2291	930406C	2312	930421	2317	930425	2320	930428	2326	930503D
2327	930503C	2330	930506B	2332	930510	2352	930524B	2353	930526
2357	930528	2360	930530B	2365	930601	2368	930602B	2377	930606
2382	930608	2384	930609B	2395	930614C	2401	930619	2423	930701
2424	930701B	2448	930719	2449	930719B	2454	930721C	2463	930725
2487	930811	2502	930824	2512	930903	2513	930903C	2514	930905
2523	930911	2529	930913	2536	930922B	2564	931005	2583	931013
2597	931021B	2599	931022	2614	931101	2615	931101B	2623	931110
2632	931113	2649	931120	2677	931204B	2679	931205	2680	931206B
2690	931211	2693	931215B	2715	931229	2725	940101C	2757	940114
2788	940128B	2795	940201B	2800	940207	2810	940209	2814	940211B
2828	940216	2834	940219	2846	940224	2860	940305	2861	940305B
2862	940305C	2873	940310	2896	940329	2910	940404	2918	940410B
2933	940415	2945	940424	2952	940428	2966	940507	2973	940512C
2975	940512B	2977	940515B	2978	940515	2986	940521C	2988	940524B
2995	940527B	3027	940613	3037	940621C	3038	940621B	3066	940708C

Continued on next page

Table B.3: GRBs corresponding to the neural network class 3-I.

trigger	GRB								
3073	940712	3078	940714C	3088	940717C	3094	940724	3113	940808
3118	940811	3121	940812C	3144	940830B	3146	940831	3173	940918
3215	941003	3218	941005B	3248	941018B	3266	941031B	3278	941110B
3280	941111	3282	941113	3284	941115	3294	941123	3297	941126C
3308	941203	3333	941229B	3335	941230B	3340	950102	3342	950103
3349	950108	3359	950115B	3374	950123	3378	950129	3379	950129B
3410	950210	3412	950211	3437	950221B	3441	950225B	3477	950321
3487	950328	3494	950405B	3502	950410	3510	950416B	3530	950502
3545	950505	3606	950529	3611	950531	3640	950611	3642	950612
3644	950620	3665	950714	3668	950716	3722	950801	3728	950802
3733	950803	3735	950804B	3736	950805	3737	950805B	3742	950806B
3751	950810	3770	950830	3779	950907	3782	950908B	3791	950911B
3807	950919B	3810	950920	3814	950922B	3840	951001	3867	951014
3868	951015B	3888	951030C	3889	951101	3894	951104B	3895	951104C
3902	951110	3904	951112B	3910	951117B	3919	951124B	3921	951125
3926	951128	3939	951209	3940	951211	4327	960112	4660	960130
4744	960205B	4776	960207	4807	960209	4871	960214	4955	960220
5079	960229b	5206	960311	5212	960312	5277	960319	5339	960325
5423	960415C	5439	960420	5448	960426	5453	960507	5456	960508B
5461	960515	5467	960521B	5469	960523B	5471	960524C	5483	960601
5485	960604	5488	960607B	5498	960615B	5499	960615C	5500	960616B
5502	960616	5527	960703	5528	960704	5529	960705	5533	960708
5537	960713B	5546	960722B	5547	960722C	5559	960802	5561	960803
5562	960804B	5564	960805	5571	960812	5573	960813B	5576	960816
5599	960909	5605	960916	5607	960919	5619	960929B	5620	961001
5638	961020	5647	961027B	5650	961030	5664	961110	5718	961218B
5724	961224B	5730	961228B	5733	961230	5740	970103	5770	970110
6096	970219	6105	970227B	6117	970308	6120	970313	6123	970315
6131	970321	6135	970324	6136	970326	6137	970326B	6145	970329B
6153	970403	6158	970404C	6178	970414	6180	970414B	6182	970415
6188	970417	6204	970423	6205	970424	6215	970430	6216	970501
6219	970503	6223	970507	6228	970510B	6230	970514	6233	970516
6265	970612	6275	970617	6281	970627C	6292	970701	6298	970708
6299	970708B	6301	970709C	6307	970714B	6314	970720	6331	970809B
6341	970820	6342	970821	6343	970824	6347	970826	6361	970904
6368	970907	6370	970907C	6372	970908B	6376	970910B	6385	970918
6386	970918B	6395	970924	6398	970926	6401	970928	6408	971002
6411	971004	6412	971004B	6427	971012	6435	971015	6436	971015B
6439	971016	6443	971021	6445	971023	6452	971028	6462	971104
6486	971118	6488	971120	6497	971124	6534	971216	6536	971218B
6540	971220B	6542	971221	6546	971227	6547	971228	6573	980116
6579	980124C	6580	980125	6591	980207B	6606	980218B	6631	980308
6638	980312	6641	980315	6643	980315C	6645	980315D	6659	980326
6662	980327	6668	980330	6671	980331B	6679	980404B	6682	980407
6689	980416	6693	980419	6697	980421B	6700	980423	6710	980427
6715	980430	6753	980511	6757	980513	6774	980523	6782	980525
6787	980527	6788	980527B	6800	980530B	6853	980619	6870	980626
6916	980711	6931	980718B	7009	980820	7060	980903	7063	980904
7078	980910B	7102	980918	7106	980920	7133	980929	7142	981005
7148	981009B	7159	981016	7173	981022B	7187	981103	7191	981105

Continued on next page

Table B.3: GRBs corresponding to the neural network class 3-I.

trigger	GRB								
7227	981124	7283	981227	7287	981229	7290	981231	7292	981231B
7294	990102B	7297	990103	7305	990105	7344	990123B	7353	990126B
7366	990202	7367	990202B	7375	990206B	7378	990208B	7381	990210B
7427	990225	7430	990226B	7440	990302	7447	990304B	7449	990305B
7453	990306B	7455	990307	7456	990308	7472	990315B	7495	990330
7508	990404	7526	990423	7533	990426	7547	990504	7554	990508
7563	990513	7581	990523C	7584	990527	7595	990603B	7599	990605
7601	990610	7602	990610B	7626	990701B	7662	990719	7663	990720
7674	990725	7706	990810	7710	990814B	7745	990829B	7749	990902
7753	990905	7754	990906	7775	990925B	7784	991002	7789	991005
7793	991007	7800	991012	7805	991015	7813	991020	7827	991028
7862	991117	7901	991211	7912	991219	7922	991228	7939	000108
7943	000111	7963	000122	7970	000126B	7979	000202	7980	000203
7988	000213	7995	000222	7999	000226B	8018	000306	8027	000310B
8035	000313B	8041	000319	8047	000321	8072	000410	8076	000415B
8079	000418	8082	000420B	8089	000502	8097	000508	8104	000513
8120	000525								

Table B.4: GRBs corresponding to the neural network class 3-II.

trigger	GRB								
107	910423	171	910509	179	910511	204	910517B	235	910528
237	910529	414	910622	473	910702B	516	910712	549	910718C
559	910721B	606	910802B	658	910809C	673	910813	685	910816B
686	910816	741	910829	773	910908	803	910918	815	910923
820	910926	867	911004	914	911022	927	911024	946	911027B
1087	911119B	1114	911123	1123	911127C	1126	911128	1159	911210
1190	911217	1192	911217B	1197	911219	1213	911224C	1218	911225
1279	920105	1291	920110B	1390	920212	1396	920214	1443	920227
1446	920227C	1452	920229B	1551	920413	1552	920414B	1553	920414
1558	920419B	1567	920423B	1604	920511B	1626	920525C	1642	920609
1651	920617B	1657	920619B	1661	920620C	1700	920714B	1704	920717B
1714	920721D	1730	920730B	1740	920803	1806	920812B	1819	920814B
1922	920912	1993	921021	2041	921102	2047	921110	2053	921112
2079	921206B	2081	921207B	2087	921208	2102	921218	2187	930212
2189	930213B	2191	930214C	2202	930219D	2203	930219B	2204	930219C
2233	930311	2253	930317	2254	930318B	2267	930326B	2306	930416
2310	930420B	2311	930420	2344	930517B	2347	930519	2367	930602
2373	930605	2391	930612D	2392	930613	2405	930621B	2419	930627
2432	930706B	2437	930709B	2458	930724	2472	930730	2508	930901
2510	930902B	2560	931003	2569	931008C	2589	931016B	2628	931112
2640	931117	2641	931118	2691	931212	2697	931219	2719	931230
2728	940101	2749	940110	2751	940111	2753	940112B	2760	940115
2775	940120B	2799	940206B	2843	940222	2853	940228B	2900	940331B
2916	940407	2925	940413	2944	940423	2992	940526C	3026	940611
3029	940616B	3072	940711	3085	940716B	3087	940717	3091	940720

Continued on next page

Table B.4: GRBs corresponding to the neural network class 3-II.

Table B.5: GRBs corresponding to the neural network class 3-III.

trigger	GRB								
105	910421	109	910425	110	910425B	121	910429	130	910430
133	910501	143	910503	148	910505	160	910507	219	910522
222	910523	226	910525	249	910601	257	910602	288	910607B
332	910612	351	910614B	394	910619	398	910620	404	910621B
408	910621	451	910627	467	910629	469	910630	503	910709
543	910717	548	910718B	563	910721	577	910725B	591	910730B
594	910730	647	910807	659	910809B	660	910809	676	910814C
678	910814	692	910818	704	910821	761	910905	795	910914
825	910927B	829	910927	840	910930B	841	910930	869	911005
907	911016	973	911031	999	911104	1009	911106B	1025	911109
1046	911111B	1085	911118	1122	911127	1141	911202	1148	911205
1150	911207	1152	911208	1156	911209C	1157	911209	1196	911219B
1200	911221	1235	911227	1244	911228	1288	920110	1303	920116
1385	920210	1406	920216	1419	920218	1425	920221	1440	920226
1447	920227B	1449	920228	1456	920301	1458	920302B	1467	920307
1468	920308	1472	920310	1515	920323	1533	920331	1541	920406
1559	920419	1574	920430	1578	920502	1579	920502C	1580	920503
1586	920505	1601	920511	1606	920513	1609	920517	1614	920520
1623	920524	1625	920525	1628	920526	1652	920617	1653	920617C
1655	920618	1660	920620	1663	920622	1676	920627	1683	920701
1709	920718	1711	920720	1712	920720B	1717	920721	1731	920730
1733	920801	1742	920804C	1815	920814	1830	920816	1883	920830
1886	920902	1924	920913	1956	920925	1974	921003	1982	921008
1989	921015	1997	921022	2019	921029	2037	921101	2061	921118
2067	921123	2074	921203	2080	921206	2083	921207	2090	921209
2093	921211	2101	921217	2106	921227	2110	921230	2111	921230B
2112	921230C	2122	930106B	2123	930108	2138	930120	2143	930123
2149	930127	2151	930131	2156	930201	2181	930210	2188	930213
2190	930214	2193	930214B	2197	930217	2211	930301	2213	930302
2228	930309	2232	930310	2276	930331	2277	930331B	2287	930405
2298	930410	2304	930415	2309	930418B	2315	930424	2316	930425B
2321	930430	2324	930503	2328	930506C	2329	930506	2340	930514B
2345	930517	2346	930518	2371	930603	2375	930606B	2380	930607
2383	930609	2387	930612	2393	930614	2394	930614B	2428	930704
2429	930705	2430	930705B	2431	930706	2435	930708	2436	930709
2441	930711C	2443	930711	2446	930714	2447	930715	2450	930720
2452	930721B	2476	930731	2482	930805	2495	930819	2500	930822
2519	930909	2522	930910	2530	930914	2533	930916	2537	930922
2541	930926	2570	931008B	2581	931013B	2586	931014	2593	931019
2603	931024	2606	931026	2610	931030B	2611	931031	2619	931106
2634	931114	2662	931127	2664	931128C	2665	931128	2688	931209
2695	931217	2696	931218	2700	931221	2703	931222	2706	931223
2709	931225	2711	931226	2727	940101D	2736	940103	2770	940119B
2774	940120	2780	940126	2790	940128	2793	940129	2797	940203
2798	940206	2812	940210	2815	940211	2831	940217	2852	940228
2855	940301	2863	940306	2864	940307	2889	940319	2890	940321
2891	940323	2894	940328	2898	940330B	2913	940406	2919	940410
2922	940412	2924	940413C	2929	940414	2931	940414B	2948	940425C
2953	940429	2958	940503	2961	940504	2984	940520	2993	940526B
2994	940526	2996	940527	2998	940529D	3001	940529B	3003	940529C

Continued on next page

Table B.5: GRBs corresponding to the neural network class 3-III.

trigger	GRB								
3005	940530	3011	940602B	3015	940604	3017	940606	3032	940616
3035	940619	3039	940622	3040	940623B	3042	940623	3056	940702
3057	940703	3067	940708	3070	940710B	3071	940710	3075	940714
3076	940714B	3080	940715B	3084	940716	3101	940728B	3102	940730
3105	940803B	3110	940806	3115	940810	3119	940812B	3128	940817
3131	940821	3138	940826	3142	940829	3153	940902B	3156	940905
3171	940917	3174	940919	3178	940921	3193	940925	3212	941003B
3217	941005	3220	941006	3227	941008	3237	941011	3241	941014
3242	941014B	3245	941017	3246	941017B	3247	941018	3255	941023
3257	941026	3259	941026B	3269	941031	3283	941114	3287	941119
3290	941121	3292	941122	3301	941126B	3306	941128	3307	941202
3319	941214	3320	941215	3330	941228	3336	941230	3339	950102B
3345	950104	3347	950105	3351	950111	3352	950111B	3364	950118
3405	950206	3407	950207	3408	950208	3415	950211B	3436	950221
3439	950223	3448	950301	3458	950305	3480	950325B	3481	950325
3488	950401	3489	950401B	3491	950403B	3512	950418	3514	950419
3516	950421	3523	950425	3567	950509	3593	950522	3618	950602
3634	950608	3637	950610	3648	950624	3649	950625	3654	950629
3658	950701B	3662	950706	3663	950711	3745	950808	3765	950818
3766	950819	3771	950830B	3773	950901	3776	950904	3788	950909
3843	951002	3853	951007	3860	951011	3870	951016	3871	951016B
3891	951102	3893	951104	3905	951112	3906	951113	3909	951117
3912	951119	3913	951119B	3916	951121	3917	951123	3918	951124
3929	951202	3930	951203	3954	951213	4039	951219	4048	951220
4146	951227	4157	951228	4216	960102	4312	960111	4350	960113
4368	960114	4388	960115	4556	960124	4701	960201	4745	960205
5304	960322	5305	960322B	5389	960331	5407	960403B	5409	960403
5412	960405	5415	960409C	5416	960409B	5417	960409	5419	960411
5420	960412	5421	960414	5429	960417	5433	960418B	5450	960428
5451	960430	5454	960508	5463	960516B	5464	960516	5470	960523
5472	960524B	5473	960524	5475	960527	5476	960528	5477	960529
5478	960530	5479	960531	5482	960601B	5484	960602	5486	960605
5489	960607	5492	960610	5493	960612	5497	960615	5512	960623
5515	960623B	5518	960625	5523	960628	5526	960703B	5531	960707C
5540	960715B	5541	960715C	5542	960716	5548	960722	5554	960730
5563	960804	5566	960806	5567	960807	5568	960808	5574	960814
5575	960815	5585	960824	5591	960831B	5593	960906B	5597	960908
5601	960912	5603	960913	5604	960913B	5606	960917	5612	960923B
5614	960924	5617	960927	5621	961001B	5624	961006	5628	961009B
5632	961015	5644	961026	5645	961026B	5646	961027	5654	961102
5667	961111B	5704	961202	5706	961206	5711	961212	5713	961214
5721	961223	5723	961224	5725	961225	5726	961226	5729	961228
5731	961228C	5736	970101	5773	970111	5989	970201	5995	970202
6004	970203	6100	970223	6101	970224	6103	970226B	6111	970302B
6115	970306	6124	970315B	6127	970317	6147	970330	6152	970402B
6159	970405	6165	970408	6167	970409	6168	970411	6190	970417C
6194	970419	6198	970420	6222	970505	6226	970509	6235	970517B
6242	970526	6243	970529	6244	970530	6249	970603	6266	970612B
6271	970614	6272	970614B	6273	970616	6274	970616B	6279	970627
6280	970627B	6295	970707	6303	970713	6306	970714	6315	970723

Continued on next page

Table B.5: GRBs corresponding to the neural network class 3-III.

trigger	GRB								
6319	970725B	6320	970731	6321	970801	6329	970807B	6335	970815
6336	970816	6337	970817	6344	970824B	6346	970825	6349	970827
6351	970829	6353	970831	6380	970912B	6390	970919B	6396	970925
6397	970925B	6404	970930	6414	971006	6422	971009B	6440	971020
6446	971023B	6451	971027	6453	971029	6454	971029B	6472	971110
6489	971121	6498	971125	6504	971127	6521	971206B	6522	971207
6525	971207B	6528	971210	6533	971214	6538	971219	6539	971220
6544	971223	6560	980105	6564	980109	6566	980110	6576	980124
6583	980129	6585	980202	6587	980203B	6590	980207	6592	980208
6593	980208B	6598	980213	6601	980214B	6602	980215	6605	980218
6615	980225	6619	980301	6621	980301B	6622	980301C	6629	980306
6630	980306B	6642	980315B	6648	980319	6655	980322	6657	980325
6665	980329	6672	980401	6674	980401B	6694	980420	6698	980421C
6702	980424	6707	980425	6763	980518B	6764	980519	6767	980520
6802	980601	6814	980609B	6816	980611	6891	980703	6892	980703B
6903	980706	6904	980706B	6930	980718	6935	980720	6938	980722
6963	980803	7012	980821	7028	980828	7030	980829	7087	980913
7110	980922	7113	980923	7147	981009	7170	981021B	7172	981022
7178	981027	7207	981111	7213	981117	7219	981121	7228	981125
7230	981125B	7247	981203	7250	981205	7255	981211	7263	981215
7285	981228	7293	990102	7295	990102C	7301	990104B	7310	990108
7318	990111	7319	990111B	7322	990112	7323	990113	7328	990117
7335	990120	7343	990123	7357	990128	7360	990129B	7369	990204
7374	990206	7377	990208	7379	990210	7387	990213B	7390	990216
7403	990220	7429	990226	7446	990304	7457	990308B	7464	990311
7475	990316	7477	990316B	7488	990322	7491	990323B	7493	990328
7497	990330B	7502	990403	7503	990403B	7504	990403C	7515	990411
7518	990413	7520	990415	7523	990420B	7527	990424	7528	990424B
7548	990505	7549	990506	7551	990507	7560	990510B	7566	990515
7575	990518B	7588	990528	7597	990604	7598	990604B	7605	990611C
7607	990615	7614	990620	7617	990622B	7630	990703	7635	990706B
7638	990707B	7642	990709B	7648	990712B	7654	990715B	7657	990716B
7660	990718	7677	990726	7678	990728	7684	990730B	7688	990802
7695	990803	7703	990807	7707	990810B	7711	990816	7727	990822
7729	990822B	7744	990829	7762	990912	7766	990915	7769	990917
7786	991004	7788	991004B	7794	991009	7810	991018	7818	991023
7822	991025	7831	991030	7838	991103	7840	991104	7841	991105
7843	991107	7845	991108	7858	991115	7868	991121	7884	991127
7885	991129	7900	991210C	7906	991216	7929	000101	7932	000103
7938	000107B	7948	000113	7954	000115	7969	000126	7976	000201
7984	000205	7989	000217	7994	000221	7997	000225	8001	000227
8004	000229	8008	000302	8012	000303	8019	000306B	8022	000307
8026	000310	8030	000312	8049	000323	8059	000331	8062	000401
8063	000402	8064	000403	8075	000415	8084	000421	8086	000424B
8087	000429	8098	000508B	8099	000508C	8101	000511	8111	000519
8116	000524	8121	000526						

Bibliography

- Alcock, C., Farhi, E., and Olinto, A.: 1986, *Phys. Rev. Lett.* **57**, 2088
- Allen, S. W., Schmidt, R. W., and Fabian, A. C.: 2002, *MNRAS* **334**, L11
- Amati, L., Frontera, F., Tavani, M., in't Zand, J. J. M., Antonelli, A., Costa, E., Feroci, M., Guidorzi, C., Heise, J., Masetti, N., Montanari, E., Nicastro, L., Palazzi, E., Pian, E., Piro, L., and Soffitta, P.: 2002, *A&A* **390**, 81
- Armendariz-Picon, C., Mukhanov, V., and Steinhardt, P. J.: 2001, *Phys. Rev.* **D63**, 103510
- Atteia, J.-L.: 2003, *A&A* **407**, L1
- Babul, A., Paczyński, B., and Spergel, D.: 1987, *ApJ* **316**, L49
- Bagoly, Z., Mészáros, A., Horváth, I., Balázs, L. G., and Mészáros, P.: 1998, *ApJ* **498**, 342
- Balastegui, A., Ruiz-Lapuente, P., and Canal, R.: 2001, *MNRAS* **328**, 283
- Balastegui, A., Ruiz-Lapuente, P., and Canal, R.: 2003, in *AIP Conf. Proc. 662: Gamma-Ray Burst and Afterglow Astronomy 2001: A Workshop Celebrating the First Year of the HETE Mission*, pp 438–441
- Balastegui, A., Ruiz-Lapuente, P., and Canal, R.: 2005, in *Nuovo Cimento C*, Vol. 28, pp 801–804
- Ball, N. M., Loveday, J., Fukugita, M., Nakamura, O., Okamura, S., Brinkmann, J., and Brunner, R. J.: 2004, *MNRAS* **348**, 1038
- Band, D., Matteson, J., Ford, L., Schaefer, B., Palmer, D., Teegarden, B., Cline, T., Briggs, M., Paciesas, W., Pendleton, G., Fishman, G., Kouveliotou, C., Meegan, C., Wilson, R., and Lestrade, P.: 1993, *ApJ* **413**, 281
- Band, D. L.: 1999, in *Recent Developments in Theoretical and Experimental General Relativity, Gravitation, and Relativistic Field Theories*, pp 1571–+
- Blain, A. W., Kneib, J.-P., Ivison, R. J., and Smail, I.: 1999, *ApJ* **512**, L87
- Blandford, R. D. and Znajek, R. L.: 1977, *MNRAS* **179**, 433

- Bloom, J. S., Kulkarni, S. R., and Djorgovski, S. G.: 2002, *AJ* **123**, 1111
- Bloom, J. S., Kulkarni, S. R., Djorgovski, S. G., Eichelberger, A. C., Cote, P., Blakeslee, J. P., Odewahn, S. C., Harrison, F. A., Frail, D. A., Filippenko, A. V., Leonard, D. C., Riess, A. G., Spinrad, H., Stern, D., Bunker, A., Dey, A., Grossan, B., Perlmutter, S., Knop, R. A., Hook, I. M., and Feroci, M.: 1999, *Nature* **401**, 453
- Bromm, V. and Loeb, A.: 2002, *ApJ* **575**, 111
- Bruzual A., G. and Kron, R. G.: 1980, *ApJ* **241**, 25
- Caldwell, R. R.: 2002, *Phys. Lett.* **B545**, 23
- Carroll, S. M., Press, W. H., and Turner, E. L.: 1992, *ARA&A* **30**, 499
- Castro-Tirado, A. J., de Ugarte Postigo, A., Gorosabel, J., Fathkullin, T., Sokolov, V., Bremer, M., Márquez, I., Marín, A. J., Guziy, S., Jelínek, M., Kubánek, P., Hudec, R., Vitek, S., Mateo Sanguino, T. J., Eigenbrod, A., Pérez-Ramírez, M. D., Sota, A., Masegosa, J., Prada, F., and Moles, M.: 2005, *A&A* **439**, L15
- Costa, E., Frontera, F., Heise, J., Feroci, M., in 't Zand, J., Fiore, F., Cinti, M. N., dal Fiume, D., Nicastro, L., Orlandini, M., Palazzi, E., Rapisarda, M., Zavattini, G., Jager, R., Parmar, A., Owens, A., Molendi, S., Cusumano, G., Maccarone, M. C., Giarrusso, S., Coletta, A., Antonelli, L. A., Giommi, P., Muller, J. M., Piro, L., and Butler, R. C.: 1997, *Nature* **387**, 783
- Dai, Z. G., Liang, E. W., and Xu, D.: 2004, *ApJ* **612**, L101
- Daigne, F. and Mochkovitch, R.: 1998, *MNRAS* **296**, 275
- Dar, A.: 1999, *A&AS* **138**, 505
- de Vaucouleurs, G.: 1993, *ApJ* **415**, 10
- Dermer, C. D., Böttcher, M., and Chiang, J.: 1999, *ApJ* **515**, L49
- Dezalay, J.-P., Atteia, J.-L., Barat, C., Boer, M., Darracq, F., Goupil, P., Niel, M., Talon, R., Vedrenne, G., Hurley, K., Terekhov, O., Sunyaev, R., and Kuznetsov, A.: 1997, *ApJ* **490**, L17+
- Di Girolamo, T., Catena, R., Vietri, M., and Di Sciascio, G.: 2005, *Journal of Cosmology and Astro-Particle Physics* **4**, 8
- Donaghy, T. Q., Lamb, D. Q., and Graziani, C.: 2004, *AIP Conf. Proc.* **727**, 47
- Einstein, A.: 1917, *Sitzber. Preuss. Akad. Wiss.* p. 142
- España-Bonet, C., Ruiz-Lapuente, P., Shapiro, I. L., and Solà, J.: 2004, *JCAP* **0402**, 006
- Fenimore, E. E. and Ramirez-Ruiz, E.: 2000
- Firmani, C., Avila-Reese, V., Ghisellini, G., and Tutukov, A. V.: 2004, *ApJ* **611**,

1033

- Firmani, C., Ghisellini, G., Ghirlanda, G., and Avila-Reese, V.: 2005, *MNRAS* **360**, L1
- Fishman, G. J., Meegan, C. A., Wilson, R. B., Brock, M. N., Horack, J. M., Kouveliotou, C., Howard, S., Paciesas, W. S., Briggs, M. S., Pendleton, G. N., Koshut, T. M., Mallozzi, R. S., Stollberg, M., and Lestrade, J. P.: 1994, *ApJS* **92**, 229
- Fox, D. B., Frail, D. A., Price, P. A., Kulkarni, S. R., Berger, E., Piran, T., Soderberg, A. M., Cenko, S. B., Cameron, P. B., Gal-Yam, A., Kasliwal, M. M., Moon, D.-S., Harrison, F. A., Nakar, E., Schmidt, B. P., Penprase, B., Chevalier, R. A., Kumar, P., Roth, K., Watson, D., Lee, B. L., Shectman, S., Phillips, M. M., Roth, M., McCarthy, P. J., Rauch, M., Cowie, L., Peterson, B. A., Rich, J., Kawai, N., Aoki, K., Kosugi, G., Totani, T., Park, H.-S., MacFadyen, A., and Hurley, K. C.: 2005, *Nature* **437**, 845
- Frail, D. A., Kulkarni, S. R., Sari, R., Djorgovski, S. G., Bloom, J. S., Galama, T. J., Reichart, D. E., Berger, E., Harrison, F. A., Price, P. A., Yost, S. A., Diercks, A., Goodrich, R. W., and Chaffee, F.: 2001, *ApJ* **562**, L55
- Freedman, W. L., Madore, B. F., Gibson, B. K., Ferrarese, L., Kelson, D. D., Sakai, S., Mould, J. R., Kennicutt, R. C., Ford, H. C., Graham, J. A., Huchra, J. P., Hughes, S. M. G., Illingworth, G. D., Macri, L. M., and Stetson, P. B.: 2001, *ApJ* **553**, 47
- Freese, K. and Lewis, M.: 2002, *Phys. Lett.* **B540**, 1
- Friedman, A. S. and Bloom, J. S.: 2005, *ApJ* **627**, 1
- Fryer, C. L. and Woosley, S. E.: 1998, *ApJ* **502**, L9+
- Fryer, C. L., Woosley, S. E., and Hartmann, D. H.: 1999a, *ApJ* **526**, 152
- Fryer, C. L., Woosley, S. E., Herant, M., and Davies, M. B.: 1999b, *ApJ* **520**, 650
- Galama, T. J., Groot, P. J., van Paradijs, J., Kouveliotou, C., Centurion, M., Telting, J. H., Smith, P., Mackey, C., Heise, J., in 't Zand, J., Djorgovski, S. G., Metzger, M. R., Odewahn, S. C., Gal, R. R., Kulkarni, S. R., Pahre, M. A., Frail, D. A., Costa, E., Feroci, M., Steidel, C. C., and Adelberger, K. L.: 1997, *IAU Circ.* **6655**, 1
- Galama, T. J., Vreeswijk, P. M., van Paradijs, J., Kouveliotou, C., Augusteijn, T., Bohnhardt, H., Brewer, J. P., Doublier, V., Gonzalez, J.-F., Leibundgut, B., Lidman, C., Hainaut, O. R., Patat, F., Heise, J., in 't Zand, J., Hurley, K., Groot, P. J., Strom, R. G., Mazzali, P. A., Iwamoto, K., Nomoto, K., Umeda, H., Nakamura, T., Young, T. R., Suzuki, T., Shigeyama, T., Koshut, T., Kippen,

- M., Robinson, C., de Wildt, P., Wijers, R. A. M. J., Tanvir, N., Greiner, J., Pian, E., Palazzi, E., Frontera, F., Masetti, N., Nicastro, L., Feroci, M., Costa, E., Piro, L., Peterson, B. A., Tinney, C., Boyle, B., Cannon, R., Stathakis, R., Sadler, E., Begam, M. C., and Ianna, P.: 1998, *Nature* **395**, 670
- Gamow, G.: 1970, *My World Line*, Viking Press, New York, 1970
- Garnavich, P. M., Stanek, K. Z., Wyrzykowski, L., Infante, L., Bendek, E., Bersier, D., Holland, S. T., Jha, S., Matheson, T., Kirshner, R. P., Krisciunas, K., Phillips, M. M., and Carlberg, R. G.: 2003, *ApJ* **582**, 924
- Gehrels, N., Chincarini, G., Giommi, P., Mason, K. O., Nousek, J. A., Wells, A. A., White, N. E., Barthelmy, S. D., Burrows, D. N., Cominsky, L. R., Hurley, K. C., Marshall, F. E., Mészáros, P., Roming, P. W. A., Angelini, L., Barbier, L. M., Belloni, T., Campana, S., Caraveo, P. A., Chester, M. M., Citterio, O., Cline, T. L., Cropper, M. S., Cummings, J. R., Dean, A. J., Feigelson, E. D., Fenimore, E. E., Frail, D. A., Fruchter, A. S., Garmire, G. P., Gendreau, K., Ghisellini, G., Greiner, J., Hill, J. E., Hunsberger, S. D., Krimm, H. A., Kulkarni, S. R., Kumar, P., Lebrun, F., Lloyd-Ronning, N. M., Markwardt, C. B., Mattson, B. J., Mushotzky, R. F., Norris, J. P., Osborne, J., Paczyński, B., Palmer, D. M., Park, H.-S., Parsons, A. M., Paul, J., Rees, M. J., Reynolds, C. S., Rhoads, J. E., Sasseen, T. P., Schaefer, B. E., Short, A. T., Smale, A. P., Smith, I. A., Stella, L., Tagliaferri, G., Takahashi, T., Tashiro, M., Townsley, L. K., Tueller, J., Turner, M. J. L., Vietri, M., Voges, W., Ward, M. J., Willingale, R., Zerbi, F. M., and Zhang, W. W.: 2004, *ApJ* **611**, 1005
- Gehrels, N., Sarazin, C. L., O'Brien, P. T., Zhang, B., Barbier, L., Barthelmy, S. D., Blustin, A., Burrows, D. N., Cannizzo, J., Cummings, J. R., Goad, M., Holland, S. T., Hurkett, C. P., Kennea, J. A., Levan, A., Markwardt, C. B., Mason, K. O., Meszaros, P., Page, M., Palmer, D. M., Rol, E., Sakamoto, T., Willingale, R., Angelini, L., Beardmore, A., Boyd, P. T., Breeveld, A., Campana, S., Chester, M. M., Chincarini, G., Cominsky, L. R., Cusumano, G., de Pasquale, M., Fenimore, E. E., Giommi, P., Gronwall, C., Grupe, D., Hill, J. E., Hinshaw, D., Hjorth, J., Hullinger, D., Hurley, K. C., Klose, S., Kobayashi, S., Kouveliotou, C., Krimm, H. A., Mangano, V., Marshall, F. E., McGowan, K., Moretti, A., Mushotzky, R. F., Nakazawa, K., Norris, J. P., Nousek, J. A., Osborne, J. P., Page, K., Parsons, A. M., Patel, S., Perri, M., Poole, T., Romano, P., Roming, P. W. A., Rosen, S., Sato, G., Schady, P., Smale, A. P., Sollerman, J., Starling, R., Still, M., Suzuki, M., Tagliaferri, G., Takahashi, T., Tashiro, M., Tueller, J.,

- Wells, A. A., White, N. E., and Wijers, R. A. M. J.: 2005, *Nature* **437**, 851
- Ghirlanda, G., Ghisellini, G., and Lazzati, D.: 2004, *ApJ* **616**, 331
- Goobar, A. and Perlmutter, S.: 1995, *ApJ* **450**, 14
- Goodman, J.: 1986, *ApJ* **308**, L47
- Gorosabel, J., Pérez-Ramírez, D., Sollerman, J., de Ugarte Postigo, A., Fynbo, J. P. U., Castro-Tirado, A. J., Jakobsson, P., Christensen, L., Hjorth, J., Jóhannesson, G., Guziy, S., Castro Cerón, J. M., Björnsson, G., Sokolov, V. V., Fatkhullin, T. A., and Nilsson, K.: 2005, *A&A* **444**, 711
- Guetta, D. and Piran, T.: 2005, *A&A* **435**, 421
- Guetta, D., Piran, T., and Waxman, E.: 2005, *ApJ* **619**, 412
- Hakkila, J., Haglin, D. J., Pendleton, G. N., Mallozzi, R. S., Meegan, C. A., and Roiger, R. J.: 2000, *ApJ* **538**, 165
- Hanami, H.: 1992, *ApJ* **389**, L71
- Harrison, F. A., Bloom, J. S., Frail, D. A., Sari, R., Kulkarni, S. R., Djorgovski, S. G., Axelrod, T., Mould, J., Schmidt, B. P., Wieringa, M. H., Wark, R. M., Subrahmanyam, R., McConnell, D., McCarthy, P. J., Schaefer, B. E., McMahon, R. G., Markze, R. O., Firth, E., Soffitta, P., and Amati, L.: 1999, *ApJ* **523**, L121
- Hartmann, D. H., Brown, L. E., The, L., Linder, E. V., Petrosian, V., Blumenthal, G. R., and Hurley, K. C.: 1994, *ApJS* **90**, 893
- Harwit, M. and Salpeter, E. E.: 1973, *ApJ* **186**, L37+
- Hewett, P. C., Foltz, C. B., and Chaffee, F. H.: 1993, *ApJ* **406**, L43
- Hjorth, J., Sollerman, J., Møller, P., Fynbo, J. P. U., Woosley, S. E., Kouveliotou, C., Tanvir, N. R., Greiner, J., Andersen, M. I., Castro-Tirado, A. J., Castro Cerón, J. M., Fruchter, A. S., Gorosabel, J., Jakobsson, P., Kaper, L., Klose, S., Masetti, N., Pedersen, H., Pedersen, K., Pian, E., Palazzi, E., Rhoads, J. E., Rol, E., van den Heuvel, E. P. J., Vreeswijk, P. M., Watson, D., and Wijers, R. A. M. J.: 2003, *Nature* **423**, 847
- Hjorth, J., Watson, D., Fynbo, J. P. U., Price, P. A., Jensen, B. L., Jørgensen, U. G., Kubas, D., Gorosabel, J., Jakobsson, P., Sollerman, J., Pedersen, K., and Kouveliotou, C.: 2005, *Nature* **437**, 859
- Horváth, I.: 1998, *ApJ* **508**, 757
- Horváth, I., Mészáros, P., and Mészáros, A.: 1996, *ApJ* **470**, 56
- Hubble, E.: 1929, *Proceedings of the National Academy of Science* **15**, 168
- Hubble, E.: 1934, *ApJ* **79**, 8

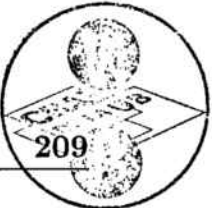
- Hubble, E.: 1936, *ApJ* **84**, 517
- Jolliffe, I. T.: 1986, *Principal Component Analysis*, Springer, New York
- Katz, J. I.: 1994, *ApJ* **432**, L107
- Katz, J. I. and Canel, L. M.: 1996, *ApJ* **471**, 915
- Klebesadel, R. W., Strong, I. B., and Olson, R. A.: 1973, *ApJ* **182**, L85+
- Knop, R. A., Aldering, G., Amanullah, R., Astier, P., Blanc, G., Burns, M. S., Conley, A., Deustua, S. E., Doi, M., Ellis, R., Fabbro, S., Folatelli, G., Fruchter, A. S., Garavini, G., Garmond, S., Garton, K., Gibbons, R., Goldhaber, G., Goobar, A., Groom, D. E., Hardin, D., Hook, I., Howell, D. A., Kim, A. G., Lee, B. C., Lidman, C., Mendez, J., Nobili, S., Nugent, P. E., Pain, R., Panagia, N., Pennypacker, C. R., Perlmutter, S., Quimby, R., Raux, J., Regnault, N., Ruiz-Lapuente, P., Sainton, G., Schaefer, B., Shahmaneche, K., Smith, E., Spadafora, A. L., Stanishev, V., Sullivan, M., Walton, N. A., Wang, L., Wood-Vasey, W. M., and Yasuda, N.: 2003, *ApJ* **598**, 102
- Kohonen, T.: 1990, *IEEC Proceedings* **78**, 1464
- Kommers, J. M., Lewin, W. H. G., Kouveliotou, C., van Paradijs, J., Pendleton, G. N., Meegan, C. A., and Fishman, G. J.: 2000, *ApJ* **533**, 696
- Kouveliotou, C., Meegan, C. A., Fishman, G. J., Bhat, N. P., Briggs, M. S., Koshut, T. M., Paciesas, W. S., and Pendleton, G. N.: 1993, *ApJ* **413**, L101
- Kulkarni, S. R., Djorgovski, S. G., Odewahn, S. C., Bloom, J. S., Gal, R. R., Koresko, C. D., Harrison, F. A., Lubin, L. M., Armus, L., Sari, R., Illingworth, G. D., Kelson, D. D., Magee, D. K., van Dokkum, P. G., Frail, D. A., Mulchaey, J. S., Malkan, M. A., McClean, I. S., Teplitz, H. I., Koerner, D., Kirkpatrick, D., Kobayashi, N., Yadigaroglu, I.-A., Halpern, J., Piran, T., Goodrich, R. W., Chaffee, F. H., Feroci, M., and Costa, E.: 1999, *Nature* **398**, 389
- Lamb, D. Q.: 1995, *PASP* **107**, 1152
- Lamb, D. Q. et al.: 2005
- Lamb, D. Q. and Reichart, D. E.: 2000, *ApJ* **536**, 1
- Larson, R. B.: 1998, *MNRAS* **301**, 569
- Lloyd-Ronning, N. M., Fryer, C. L., and Ramirez-Ruiz, E.: 2002, *ApJ* **574**, 554, (LFR)
- Maccacaro, T., Gioia, I. M., Zamorani, G., Feigelson, E. D., Fener, M., Giacconi, R., Griffiths, R. E., Murray, S. S., Stocke, J., and Liebert, J.: 1982, *ApJ* **253**, 504
- MacFadyen, A. I. and Woosley, S. E.: 1999, *ApJ* **524**, 262

- MacFadyen, A. I., Woosley, S. E., and Heger, A.: 2001, *ApJ* **550**, 410
- Madau, P. and Pozzetti, L.: 2000, *MNRAS* **312**, L9
- Mallozzi, R. S., Pendleton, G. N., and Paciesas, W. S.: 1996, *ApJ* **471**, 636
- Mao, S. and Paczyński, B.: 1992, *ApJ* **388**, L45
- Maoz, E.: 1993, *ApJ* **414**, 877
- Marzke, R. O., Geller, M. J., Huchra, J. P., and Corwin, H. G.: 1994, *AJ* **108**, 437
- Meegan, C. A., Fishman, G. J., and Wilson, R. B.: 1985, *ApJ* **291**, 479
- Meegan, C. A., Fishman, G. J., Wilson, R. B., Horack, J. M., Brock, M. N., Paciesas, W. S., Pendleton, G. N., and Kouveliotou, C.: 1992, *Nature* **355**, 143
- Meegan, C. A., Pendleton, G. N., Briggs, M. S., Kouveliotou, C., Koshut, T. M., Lestrade, J. P., Paciesas, W. S., McCollough, M. L., Brainerd, J. J., Horack, J. M., Hakkila, J., Henze, W., Preece, R. D., Mallozzi, R. S., and Fishman, G. J.: 1996, *ApJS* **106**, 65
- Mészáros, A., Bagoly, Z., Horváth, I., Balázs, L. G., and Vavrek, R.: 2000, *ApJ* **539**, 98
- Mészáros, P. and Rees, M. J.: 1993a, *ApJ* **418**, L59+
- Mészáros, P. and Rees, M. J.: 1993b, *ApJ* **405**, 278
- Mészáros, P., Rees, M. J., and Wijers, R. A. M. J.: 1998, *ApJ* **499**, 301
- Mochkovitch, R., Hernanz, M., Isern, J., and Martin, X.: 1993, *Nature* **361**, 236
- Mukherjee, S., Feigelson, E. D., Jogesh Babu, G., Murtagh, F., Fraley, C., and Raftery, A.: 1998, *ApJ* **508**, 314
- Murtagh, F. and Heck, A.: 1987, *Multivariate Data Analysis*, Dordrecht Reidel Publ.
- Narayan, R., Paczyński, B., and Piran, T.: 1992, *ApJ* **395**, L83
- Narlikar, J. V. and Apparao, K. M. V.: 1975, *Ap&SS* **35**, 321
- Nemiroff, R. J.: 1994
- Nemiroff, R. J., Norris, J. P., Bonnell, J. T., Wickramasinghe, W. A. D. T., Kouveliotou, C., Paciesas, W. S., Fishman, G. J., and Meegan, C. A.: 1994, *ApJ* **435**, L133
- Newman, M. J. and Cox, A. N.: 1980, *ApJ* **242**, 319
- Norris, J. P.: 2002, *ApJ* **579**, 386
- Paciesas, W. S., Meegan, C. A., Pendleton, G. N., Briggs, M. S., Kouveliotou, C., Koshut, T. M., Lestrade, J. P., McCollough, M. L., Brainerd, J. J., Hakkila, J., Henze, W., Preece, R. D., Connaughton, V., Kippen, R. M., Mallozzi, R. S., Fishman, G. J., Richardson, G. A., and Sahi, M.: 1999, *ApJS* **122**, 465

- Paczynski, B.: 1986, *ApJ* **308**, L43
- Paczynski, B.: 1990, *ApJ* **363**, 218
- Paczynski, B.: 1995, *PASP* **107**, 1167
- Paczynski, B. and Long, K.: 1988, *ApJ* **333**, 694
- Paczynski, B. and Rhoads, J. E.: 1993, *ApJ* **418**, L5+
- Panaiteescu, A. and Mészáros, P.: 1998, *ApJ* **492**, 683
- Panaiteescu, A. and Mészáros, P.: 2000, *ApJ* **544**, L17
- Peebles, P. J. E. and Ratra, B.: 1988, *Astrophys. J.* **325**, L17
- Pendleton, G. N., Paciesas, W. S., Briggs, M. S., Preece, R. D., Mallozzi, R. S., Meegan, C. A., Horack, J. M., Fishman, G. J., Band, D. L., Matteson, J. L., Skelton, R. T., Hakkila, J., Ford, L. A., Kouveliotou, C., and Koshut, T. M.: 1997, *ApJ* **489**, 175
- Perlmutter, S., Aldering, G., Goldhaber, G., Knop, R. A., Nugent, P., Castro, P. G., Deustua, S., Fabbro, S., Goobar, A., Groom, D. E., Hook, I. M., Kim, A. G., Kim, M. Y., Lee, J. C., Nunes, N. J., Pain, R., Pennypacker, C. R., Quimby, R., Lidman, C., Ellis, R. S., Irwin, M., McMahon, R. G., Ruiz-Lapuente, P., Walton, N., Schaefer, B., Boyle, B. J., Filippenko, A. V., Matheson, T., Fruchter, A. S., Panagia, N., Newberg, H. J. M., Couch, W. J., and The Supernova Cosmology Project: 1999, *ApJ* **517**, 565
- Petrosian, V.: 1969, *ApJ* **155**, 1029
- Petrosian, V. and Lee, T. T.: 1996, *ApJ* **467**, L29+
- Piran, T.: 1992, *ApJ* **389**, L45
- Piro, L.: 2005, *Nature* **437**, 822
- Piro, L., Garmire, G., Garcia, M., Stratta, G., Costa, E., Feroci, M., Mészáros, P., Vietri, M., Bradt, H., Frail, D., Frontera, F., Halpern, J., Heise, J., Hurley, K., Kawai, N., Kippen, R. M., Marshall, F., Murakami, T., Sokolov, V. V., Takeshima, T., and Yoshida, A.: 2000, *Science* **290**, 955
- Porciani, C. and Madau, P.: 2001, *ApJ* **548**, 522
- Preece, R. D., Briggs, M. S., Mallozzi, R. S., Pendleton, G. N., Paciesas, W. S., and Band, D. L.: 2000, *ApJS* **126**, 19
- Press, W. H., Teukolsky, S. A., Vetterling, W. T., and Flannery, B. P.: 1986, *Numerical recipes in Fortran: the art of scientific computing*, Cambridge University Press
- Prilutskii, O. F. and Usov, V. V.: 1975, *Ap&SS* **34**, 395
- Rees, M. J.: 1995, *PASP* **107**, 1176

- Rees, M. J. and Mészáros, P.: 1992, *MNRAS* **258**, 41P
- Rees, M. J. and Mészáros, P.: 1994, *ApJ* **430**, L93
- Reeves, J. N., Watson, D., Osborne, J. P., Pounds, K. A., O'Brien, P. T., Short, A. D. T., Turner, M. J. L., Watson, M. G., Mason, K. O., Ehle, M., and Schartel, N.: 2002, *Nature* **416**, 512
- Reichart, D. E. and Mészáros, P.: 1997, *ApJ* **483**, 597
- Riess, A. G., Filippenko, A. V., Challis, P., Clocchiatti, A., Diercks, A., Garnavich, P. M., Gilliland, R. L., Hogan, C. J., Jha, S., Kirshner, R. P., Leibundgut, B., Phillips, M. M., Reiss, D., Schmidt, B. P., Schommer, R. A., Smith, R. C., Spyromilio, J., Stubbs, C., Suntzeff, N. B., and Tonry, J.: 1998, *AJ* **116**, 1009
- Riess, A. G., Strolger, L.-G., Tonry, J., Casertano, S., Ferguson, H. C., Mobasher, B., Challis, P., Filippenko, A. V., Jha, S., Li, W., Chornock, R., Kirshner, R. P., Leibundgut, B., Dickinson, M., Livio, M., Giavalisco, M., Steidel, C. C., Benítez, T., and Tsvetanov, Z.: 2004, *ApJ* **607**, 665
- Rosswog, S. and Davies, M. B.: 2002, *MNRAS* **334**, 481
- Rosswog, S., Ramirez-Ruiz, E., and Davies, M. B.: 2003
- Ruffert, M. and Janka, H.-T.: 1999, *A&A* **344**, 573
- Sandage, A.: 1961, *ApJ* **133**, 355
- Sandage, A. and Tammann, G. A.: 1982, *ApJ* **256**, 339
- Sari, R. and Piran, T.: 1997, *MNRAS* **287**, 110
- Sari, R., Piran, T., and Narayan, R.: 1998, *ApJ* **497**, L17+
- Schaefer, B. E., Deng, M., and Band, D. L.: 2001, *ApJ* **563**, L123
- Schmidt, M.: 1999a, *ApJ* **523**, L117
- Schmidt, M.: 1999b, *ApJ* **523**, L117
- Spada, M., Panaitescu, A., and Mészáros, P.: 2000, *ApJ* **537**, 824
- Spergel, D. N., Verde, L., Peiris, H. V., Komatsu, E., Nolta, M. R., Bennett, C. L., Halpern, M., Hinshaw, G., Jarosik, N., Kogut, A., Limon, M., Meyer, S. S., Page, L., Tucker, G. S., Weiland, J. L., Wollack, E., and Wright, E. L.: 2003, *ApJS* **148**, 175
- Spruit, H. C., Daigne, F., and Drenkhahn, G.: 2001, *A&A* **369**, 694
- Stanek, K. Z., Matheson, T., Garnavich, P. M., Martini, P., Berlind, P., Caldwell, N., Challis, P., Brown, W. R., Schild, R., Krisciunas, K., Calkins, M. L., Lee, J. C., Hathi, N., Jansen, R. A., Windhorst, R., Echevarria, L., Eisenstein, D. J., Pindor, B., Olszewski, E. W., Harding, P., Holland, S. T., and Bersier, D.: 2003, *ApJ* **591**, L17

- Steidel, C. C., Adelberger, K. L., Giavalisco, M., Dickinson, M., and Pettini, M.: 1999, *ApJ* **519**, 1
- Takahashi, K., Oguri, M., Kotake, K., and Ohno, H.: 2003
- Tavani, M.: 1998, *ApJ* **497**, L21+
- Tinsley, B. M.: 1980, *ApJ* **241**, 41
- Totani, T.: 1999, *ApJ* **511**, 41
- Usov, V. V. and Chibisov, G. V.: 1975, *Soviet Astronomy* **19**, 115
- van den Bergh, S.: 1983, *Ap&SS* **97**, 385
- van den Bergh, S.: 1992, *PASP* **104**, 861
- van Paradijs, J., Groot, P. J., Galama, T., Kouveliotou, C., Strom, R. G., Telting, J., Rutten, R. G. M., Fishman, G. J., Meegan, C. A., Pettini, M., Tanvir, N., Bloom, J., Pedersen, H., Nordgaard-Nielsen, H. U., Linden-Vornle, M., Melnick, J., van der Steene, G., Bremer, M., Naber, R., Heise, J., in 't Zand, J., Costa, E., Feroci, M., Piro, L., Frontera, F., Zavattini, G., Nicastro, L., Palazzi, E., Bennet, K., Hanlon, L., and Parmar, A.: 1997, *Nature* **386**, 686
- Villasenor, J. S., Lamb, D. Q., Ricker, G. R., Atteia, J.-L., Kawai, N., Butler, N., Nakagawa, Y., Jernigan, J. G., Boer, M., Crew, G. B., Donaghy, T. Q., Doty, J., Fenimore, E. E., Galassi, M., Graziani, C., Hurley, K., Levine, A., Martel, F., Matsuoka, M., Olive, J.-F., Prigozhin, G., Sakamoto, T., Shirasaki, Y., Suzuki, M., Tamagawa, T., Vanderspek, R., Woosley, S. E., Yoshida, A., Braga, J., Manchanda, R., Pizzichini, G., Takagishi, K., and Yamauchi, M.: 2005, *Nature* **437**, 855
- Vlahakis, N. and Königl, A.: 2003a, *ApJ* **596**, 1080
- Vlahakis, N. and Königl, A.: 2003b, *ApJ* **596**, 1104
- von Kienlin, A. et al.: 2004, *AIP Conf. Proc.* **727**, 684
- Ward, J. H.: 1963, *Statistical Challenges of Modern Astronomy*, Springer, New York
- Warmels, R. H.: 1991, *PASP Conf. Series* **25**, 115
- Weinberg, S.: 1972, *Gravitation and cosmology: Principles and applications of the general theory of relativity*, New York: Wiley, 1972
- Wickramasinghe, W. A. D. T., Nemiroff, R. J., Norris, J. P., Kouveliotou, C., Fishman, G. J., Meegan, C. A., Wilson, R. B., and Paciesas, W. S.: 1993, *ApJ* **411**, L55
- Woosley, S. E.: 1993, *ApJ* **405**, 273
- Yonetoku, D., Murakami, T., Nakamura, T., Yamazaki, R., Inoue, A. K., and Ioka,



BIBLIOGRAPHY

- K.: 2004, *ApJ* **609**, 935
Yoshii, Y. and Peterson, B. A.: 1995, *ApJ* **444**, 15
Yoshii, Y. and Takahara, F.: 1988, *ApJ* **326**, 1